2011

Plastic Deformation and Surface Damage Mechanisms during Hot-forming of Al and Mg Alloy Sheets

Sarmistha Das
University of Windsor

PLASTIC DEFORMATION AND SURFACE DAMAGE MECHANISMS DURING HOT-FORMING OF Al AND Mg ALLOY SHEETS

By

SARMISTHA DAS

A Dissertation
Submitted to the Faculty of Graduate Studies
through Engineering Materials
in Partial Fulfillment of the Requirements for
the Degree of Doctor of Philosophy at the
University of Windsor

Windsor, Ontario, Canada
2011
© 2011 Sarmistha Das

Plastic Deformation and Surface Damage Mechanisms during Hot-forming of Al and Mg Alloy Sheets

By

Sarmistha Das

APPROVED BY

_____

K. Januszkiewicz, External Examiner
Novelis Global Technology Centre

_____

M. Madugula
Civil and Environmental Engineering

_____

H. Hu
Mechanical, Automotive and Materials Engineering

_____

A. Edrisy
Mechanical, Automotive and Materials Engineering

_____

A.T. Alpas, Advisor
Mechanical, Automotive and Materials Engineering

_____

A.R. Riahi, Co-advisor
Mechanical, Automotive and Materials Engineering

_____

D. K. Drouillard, Chair of Defense
Department of Biological Sciences

Declaration of Co-authorship / Previous Publication

Co-Authorship Declaration

I hereby declare that this thesis incorporates documentation of research performed by the author under the supervision of Professor A. T. Alpas and Dr. A. R. Riahi. The collection of electron images and diffraction patterns using transmission electron microscope was performed jointly by Dr. X. Meng-Burany and the author at General Motors Global Research and Development. The interpretation of these micrographs and their analyses were performed by the author. Dr. A. T. Morales of General Motors Global Research and Development helped with the provision of samples and brought an industrial perspective during discussions of the results analysed by the author.

Declaration of Previous Publication

This thesis includes material from two original peer reviewed journal articles that have already been published and two more journal articles to be submitted for publication in peer reviewed journals.

Publication title/full citation	Publication status	Thesis chapter
Role of plastic deformation on elevated temperature tribological behaviour of an Al-Mg alloy (AA5083): A friction mapping approach	Published	Chapter 4 and Chapter 6
High temperature deformation and fracture of tribo-layers on the surface of AA5083 sheet aluminum-magnesium alloy	Submitted	Chapter 4 and Chapter 6
Microstructural evolution during high temperature sliding wear of Mg–3% Al–1% Zn (AZ31) alloy	Published	Chapter 5 and Chapter 6
Friction and deformation mechanisms of AZ31 alloy deformed at elevated temperature	To be submitted	Chapter 5 and Chapter 6

I certify that I have obtained a written permission from the copyright owner(s) to include the published material(s) in my thesis. I certify that the above material describes work completed during my registration as graduate student at the University of Windsor.

I declare that, to the best of my knowledge, my thesis does not infringe upon anyone's copyright nor violate any proprietary rights and that any ideas, techniques, quotations, or any other material from the work of other people included in my thesis, published or otherwise, are fully acknowledged in accordance with the standard referencing practices. Furthermore, to the extent that I have included copyrighted material that surpasses the bounds of fair dealing within the meaning of the Canada Copyright Act, I certify that I have obtained a written permission from the copyright owner(s) to include such material(s) in my thesis.

I declare that this is a true copy of my thesis, including any final revisions, as approved by my thesis committee and the Graduate Studies office of University of Windsor, and that this thesis has not been submitted for a higher degree to any other University or Institution.

Abstract

Material transfer and adhesion to die surface are major tribological issues encountered during hot-forming of aluminum and magnesium alloys, reducing process efficiency. This study aimed at understanding the tribological contact interface generated between material and die surface under dynamic conditions created by simultaneous effect of temperature and strain rate. Micromechanisms of plastic deformation occurring under simulated hot-forming conditions were identified and related to the coefficient of friction (COF).

Sliding contact experiments were done using specially designed tribometer (operating temperature: 25 to 545°C, strain rate: 10^{-3} to $10^{-1}s^{-1}$). COF of AA5083(Al-4.5%Mg-0.7%Mn) and AZ31(Mg-3%Al-0.7%Zn) alloys were measured during their plastic deformation by the simultaneous effect of temperature and strain rate. The as-received and plastically deformed surfaces were characterized using optical interferometry, SEM, FIB and TEM. Additionally, the force required to break the asperity junction formed at the first contact, or junction strength, was measured for both materials at different temperatures.

Deformation mechanisms identified for AA5083 in the temperature range of 420 to 545°C and strain rate range of 5×10^{-3} to 4×10^{-2} s^{-1} included diffusional flow, grain boundary sliding (GBS) and solute drag (SD) creep. Friction maps outlining general relationships between tribological behaviour and micromechanisms controlling deformation under a set of temperature, strain and strain rate were developed. GBS induced high surface roughness, resulting in high COF. Low average roughness and retention of strength reduced COF in SD region. Dynamic recrystallization was an additional factor controlling material transfer in magnesium AZ31 alloy.

Changes in oxide layer morphology were established based on the microstructural characterization of sample's surface and subsurface. In AA5083 alloy, crack formation at temperatures <450°C or oxide ligament formation at temperature >500°C were found in the magnesium rich surface oxide. Magnesium rich surface oxide reduced COF, and low COF was found in the material having high magnesium. AZ31 alloy always showed

lower COF compared to AA5083. This was confirmed by junction strength experiment where adhesion strength was found to be low in high magnesium content material. Therefore, this investigation on the plastic deformation and surface damage mechanism, and their relation with the tribological behaviour provided better understanding of the hot-forming process.

To my maa and babu
for their unconditional love, support and encouragement.

And to my husband
for pushing me to go the extra mile.

Acknowledgements

Table of Contents

Nomenclature

COF   Coefficient of friction

CGBS   Cooperative grain boundary sliding

DC   Direct-chill cast

DMM   Deformation mechanism map

DRX   Dynamic recrystallization

EDS   Energy dispersive X-ray spectroscopy

FIB   Focussed-ion beam

GBS   Grain boundary sliding

HRTEM   High resolution transmission electron microscope

MW   Mild wear

QPF   Quick plastic forming

RT   Room temperature

Rx   Recrystallization

SD   Solute drag

SEM   Scanning electron microscope

SPF   Superplastic forming

SW   Severe wear

TEM   Transmission electron microscope

XPS   X-ray photoelectron spectroscopy

List of Symbols

b	Burgers vector
C'	Constant
d	Grain size
D	Diffusivity or diffusion coefficient
dC/dx	Concentration gradient over the diffusion distance
d_i	Initial grain size
d_g	Grain size at sliding time t
D_{gb}	Grain boundary diffusion coefficient
D_L	Lattice diffusion coefficient
D_s	Solute atom diffusion coefficient
E	Temperature compensated Young's modulus
J	Diffusive flux or quantity per second of diffusive matter passing through a unit area
k	Boltzmann's constant
$k_1 - k_5$	Material constants
k_6	Shear yield stress of substrate beneath the oxide film
p	Grain size exponent
Q	Activation energy for deformation
R	Universal gas constant
s	Interface strength
T	Temperature
T_m	Melting temperature
t_c	Oxide film thickness
W	Work of separation
α_1	Constant
γ	Surface energy

δ	Thickness of the grain boundary over which diffusion takes place
$\dot{\varepsilon}$	Strain rate
θ	Inside angle that was formed at the interface of the nano tensile structures and the materials
λ_c	Maximum length of oxide fragment during rolling
μ	Coefficient of friction between roll and the strip material during rolling
σ	Flow stress
σ_f	Tensile strength of oxide film
Ω	Atomic volume

List of Tables

List of Figures

Chapter 2 Literature Review

Chapter 3 Materials and Experimental Procedure

Chapter 4 Coefficient of Friction and Deformation Mechanisms of AA5083 Alloy

Chapter 5 Friction and Deformation Mechanisms of AZ31 Alloy

Chapter 6 General Discussion

Chapter 1 Introduction

1.1. General overview

Hot-forming is a shaping operation that is performed at temperatures above the recrystallization temperature of a given metal and which allows near-net forming of contoured parts. It is a fast and cost effective deformation processing technique for producing lightweight structural components made of aluminum [1,2] and magnesium alloys [1,3]. Hot-forming takes advantage of superplasticity of fine-grained alloys such as AA5083 and AZ31 [4-6] and uses gas pressure to force a heated blank to stretch into conformance with a die surface. One variant of hot-forming process is superplastic forming (SPF) where the materials exhibit exceptionally high tensile ductility, commonly in the range of 400 – 2000%, which provides a large design freedom. For aluminum alloy SPF operates at temperature and strain rate ranges of 460 – 545 °C and $10^{-4} – 10^{-3}$ s^{-1} [7] respectively. An important improvement over SPF is the quick plastic forming (QPF) that operates at relatively lower temperature and higher strain rate ($\sim$ 450 °C and $> 10^{-3}$ s^{-1} respectively for aluminum [7,8]) and hence reduces the forming time considerably.

The success of hot-forming lies in understanding the tribological issues occurring during the process and solving them effectively. Adhesion and material transfer to the counterface/die material are main concerns encountered during the hot-forming process of aluminum and magnesium alloys, and they influence the quality of the formed part [9,10]. Repeated action of the same die against different sample blanks leads to accumulation of the transferred material on the die surface [9,10]. Both SPF and QPF

processes operate at temperatures higher than 400 °C, where the working material is relatively soft [2,8]. As a result, any foreign material present between the blank and the die results in a surface imperfection that needs repairing to maintain the required surface finish. The adhesion of the workpiece material to the die surface increases the maintenance cost of the process, as the surface has to be cleaned by removing the adhered material mechanically [10]. Therefore, it is important to study the tribological behaviour of aluminum and magnesium alloys during hot-forming and to understand the mechanisms of adhesion for better optimization of the forming process. However, very limited investigations have been conducted so far on high temperature tribology of aluminum and magnesium alloys.

The tribological interactions during the hot-forming process are very complex in nature and involve friction, wear, material transfer, and plastic deformation simultaneously. Standard tests do not capture plastic deformation state during hot-forming, where the material is stretching and sliding at the same time, leading to a dynamic tribological condition that is difficult to represent accurately. Inability of simulating the actual tribological conditions in the hot-forming process has led to lack of understanding of mechanisms of friction and adhesion in the system. Thus, a test that represents the conditions of the hot-forming process is needed for accurately measuring friction during the process. The critical parameters of the test include the ability to conduct the test at temperatures between 400 °C and 500 °C, and strain rates between 0.001 s^{-1} and 0.1 s^{-1}. This will produce a dynamic interface in which oxides are constantly being broken and reformed [10]. The composition and mechanical behaviour of the generated surface layer on the forming material and the contacting die determine the

tribological behaviour of the system. In particular, it is important to understand how both surface layers affect friction and adhesion between the working materials. However, conventional experimental procedures for measuring the coefficient of friction (COF) in hot metal forming processes do not allow for the study of the effect of the strain rate on the system [11-16]. A study of which would require the experiment to have the ability to significantly stretch the work piece material while it is sliding past the representative tooling material. Research is therefore required to understand the phenomenon of material deformation and for accurate measurement of COF under the dynamic condition generated by the simultaneous effect of temperature and strain rate. Also, the level of friction controls material flow and the strain distribution during forming, which in turn affect the contact loads, thinning, and forming time [10]. Therefore the use of friction data in generating more accurate hot-forming process simulations will determine whether a specific geometry can be successfully formed, along with the prediction of optimal friction distribution on the forming tool.

1.2. Scope of research

This work was aimed at investigating the tribological contact interface generated under conditions similar to the hot-forming operation so that a relation can be established between the friction and the deformation mechanism of aluminum and magnesium alloys during the forming operation. In light of many factors that must be considered in describing the high temperature tribological behaviour of aluminum and magnesium alloys, this work took a comprehensive experimental approach. The experimental procedure consisted of measurement of the coefficients of friction (COF) and identification of deformation mechanisms operating at temperature and strain rate space

over which the COFs were measured. Deformation mechanisms were determined from relevant creep equations and from the optical/focussed-ion beam (FIB)/ transmission electron microscopy (TEM) observations. Friction maps that plotted COF values over the ranges of dominant deformation mechanisms were constructed, establishing relationships between tribological and mechanical properties. In addition, changes in microstructure, surface topography, and oxide properties were determined.

1.3.   Objectives of this research

The commercial success of AA5083 and AZ31 alloys are attributed to the ability of these alloys to exhibit multiple creep mechanisms under hot-forming conditions [17-30]. The general overview presented in **Section 1.1** indicates that there are some critical issues which still have to be addressed for the purpose of understanding the tribological behaviour during the hot-forming operation. Specific reference has also been made to the tribology at elevated temperature, influence of the deformation mechanism on tribological behaviour, and the role that deformation mechanisms play in developing the alloy surface morphology during high temperature deformation. Therefore, the present work was carried out with the following objectives:

(1) To study the tribological behaviour of aluminum (AA5083) and magnesium (AZ31) alloys under dynamic conditions generated by the simultaneous effect of temperature and strain rate.

 (2) To establish relationships between the tribological and mechanical properties, particularly between the COF and deformation creep mechanisms operating at elevated temperature.

(3) To investigate the evolution of alloy microstructure, surface morphology, and damage characteristics of the surface oxide layer in relation to bulk material deformation under simulated hot-forming conditions.

1.4.   Organization of the dissertation

This dissertation is organized in the following way: **Chapter 2** provides a literature survey on the hot-forming process, deformation mechanisms responsible for superplasticity observed in aluminum and magnesium alloys, the oxide layer on the surface of Al-Mg alloy, and tribology of aluminum and magnesium alloys. **Chapter 3** provides the details of the microstructures of materials that were tested, followed by descriptions of the experimental setup developed to simulate hot-forming conditions, pin-on-disk setup for investing the sliding induced damage, and junction strength experiment for measurement of adhesion strength. The chapter also includes the procedures of surface and subsurface characterization using electron microscopes, FIB microscope, EBSD technique, surface profilometer, nano-indenter, and XPS. **Chapter 4** describes the measurement the coefficient of friction (COF) of AA5083 alloy and establishes a relation between COF and deformation mechanism map (DMM). The chapter also describes the surface oxide characteristics including property, composition, quantification of surface damage, and TEM characterization of a specific surface feature. **Chapter 5** establishes a relation between COF and deformation mechanisms of AZ31 alloy. The chapter also describes the evolution of surface characteristic and bulk microstructure in relation with deformation behaviour. **Chapter 6** provides a general discussion on the COF in relation with the deformation behaviour of the material. **Chapter 7** summarizes this entire research and presents the conclusions arising from this dissertation.

Chapter 2 Literature Review

2.1. Introduction

This chapter provides a literature review on the hot-forming process of AA5083 and AZ31 sheet blanks, and review the deformation mechanisms that operate during the forming operation. The characteristics of the surface oxide present on the sheet blank are examined. In addition to that, a survey on the tribological behaviour of these materials under these conditions is provided. **Section 2.2** describes the forming process. In the next section (**Section 2.3**), deformation mechanisms responsible for superplasticity in material along with constitutive equations are discussed. High temperature deformation mechanisms specific to aluminum and magnesium alloys are discussed in **Section 2.4**. This is followed by a section (**Section 2.5**) on characteristics of oxides on the surface of Al-Mg alloy. Tribological behaviour of aluminum and magnesium alloys is discussed in **Section 2.6**.

2.2. Background on the hot-forming process

2.2.1. The forming process

Hot-forming is accomplished by clamping a sheet of superplastic material into a die and subsequently applying differential gas pressure to form the sheet to the die at a specified temperature. Usually hot-forming operation is done with an up-acting, 100-320 ton, hydraulic hot press. The temperature and the gas pressure used to form aluminum sheets are typically in the range of 450 °C to 500 °C [31] and 0.45 MPa to 3.1 MPa[7]

respectively. Heating of the die in hot-forming is achieved by the use of cartridge resistance heaters inserted into holes drilled in the die chamber. A schematic illustrating the process inside the hot press is shown in **Figure 2.1**. The sheet was heated to between 450 °C and 500 °C for hot-forming against the contoured surface of the forming tool. The sheet was held against the periphery of the tool, and air/argon pressure was applied to the back of the sheet in order to force a heated aluminum or magnesium blank to stretch into conformance with a die surface. Superplastic aluminum brackets were formed on a forming tool at 490 °C and under a gas pressure of 0.45 MPa [7]. The forming time per part was approximately 40 min.

The future advancement in hot-forming operation is intimately related to the control and improvement of the tribological conditions between the aluminum blanks and the forming tool[7]. The tribological problems that occur during these processes tend to be numerous, and include metallic particle transfer to the tool, which leads to adhesion and surface damage to both the die and the workpiece [9]. The use of solid lubricants reduces adhesion of aluminum to the die surface [32]. The most commonly used lubricants in hot-forming process are boron nitride (BN) and graphite [33]. While graphite provides excellent lubricity at low cost, it decreases the efficiency of the subsequent sheet welding process, and so must be removed from the surface after forming. The use of coatings, including PVD and plasma assisted CVD coatings based on TiAlN [34,35], thermal spray coatings based on Cr compounds, and electroless nickel-based coatings have also been considered [36][12] to reduce the die-sticking problem. Although improvements in achieving low friction at temperatures above 400 °C have

been observed in laboratory tests, these coatings usually fall short of eliminating the industrial problems.

Fundamental research aimed at understanding the factors that control friction and aluminum adhesion is essential to develop an effective lubricant or coating for improving the viability of the hot forming process that is sustainable in automotive volumes. Two variants of hot-forming process are mainly used in automotive industries and will be described in the next two sections.

2.2.2. Superplasticity and superplastic forming (SPF)

Superplasticity is the ability of a material to undergo very large uniform tensile/compressive deformation prior to failure, at a temperature well below its melting point [37]. Superplastic behaviour occurs at $T > 0.5T_m$. Typical values of the elongation to failure in uniaxial tension under superplastic conditions are of the order of a few hundred percent, and in some alloys can even exceed 1000%. The research interest in superplasticity has greatly increased in the 1960s [38,39], when it was demonstrated that in this regime, metal sheets could undergo large tensile deformation and could easily be formed to complex shapes.

SPF is one variant of hot-forming techniques where the exceptionally high ductility of the working materials allows for a large freedom of design. The main limitation towards mass application of SPF is the relatively low strain rate that is associated with conventional fine-structure superplasticity. The aerospace industry implemented SPF of parts, as there has always been a need to use high strength-to-weight materials such as aluminum and titanium. The forming of complex, one-piece components replaced the need for welding and fastening of several pieces, thereby saving

both weight and production time. Superplastically formed parts are also free of residual stresses, in addition to having no spring-back. Examples of superplastically formed aircraft pieces are landing gear doors, wing tips, engine nacelles, and stiffening panels [31,40]. In the rail industry, superplastic aluminum panels have proven to be beneficial for both interior and exterior use. Internal panels are one such example in the rail industry [31]. Also, production of complex door inner and outer panels for automotive industries, ensuring structural integrity, reducing part count, and minimizing weight, was possible by SPF [31].

2.2.3. Quick plastic forming (QPF)

The development of QPF technology enabled high volume production of various automobile body components particularly made of AA5083 [8]. As an example an automobile decklid outer panel was formed by QPF where the component was formed at 450 °C and at strain rate $> 10^{-3}$ s^{-1}. During the process the forming pressure continually increased to 3.1 MPa over a period of 260 s and maintained for the next 60 s to achieve the required shape [7]. Depending upon the size and complexity of the panel to be formed, the process can be completed in a period of about $2 - 12$ min, considerably faster than the time required for SPF (> 30 min) [7]. In the QPF process, the forming temperature is substantially reduced and the rate of forming increased from the conventional SPF process and hence the cycle time is much lower than the SPF process. The QPF process, which is similar to SPF but takes place at higher strain rates ($> 10^{-3}$ s^{-1}), works in the range of the transition from grain boundary sliding (GBS) to dislocation creep, whereas SPF is normally done at the low strain rates of the GBS regime [1,8,17-21]. QPF also takes advantage of the role of the magnesium addition to

the aluminum-base alloy, which results in control of deformation by solute drag (SD) creep in the dislocation deformation regime[18,22]. The flow stress is more strain-rate sensitive during SD creep, and this enhances ductility under QPF forming conditions [18,22-24]. Examples of superplastically formed automotive components are lift gate, decklid, and door inner and outer panel as shown in **Figure 2.2** [8,41].

2.2.4. General creep equations and typical superplastic materials

Deformation behaviour of the material during SPF/QPF can be described by the phenomenological creep equation [2]:

$$\dot{\varepsilon} = A \left(\frac{\sigma}{E}\right)^{n} \left(\frac{b}{d}\right)^{p} exp \left(-\frac{Q}{RT}\right) \tag{2.1}$$

Where A is the material constant, σ is the flow stress, n is the stress exponent, E is the temperature compensated Young's modulus, b is the Burgers vector, d is the grain size, p is the grain size exponent, Q is the activation energy for deformation, and R is the universal gas constant.

The stress exponent, n, can be obtained from the slope of a $log\dot{\varepsilon}$ vs. $log\sigma$ plot. In many cases deformation behaviour of the material is also described by the inverse of stress exponent, 1/n (strain rate sensitivity, m). For example, $n = 2$ implies deformation by GBS [42].

For superplastic behaviour, a material must be capable of being processed into a fine grain equiaxed structure ($< 10\ \mu m$), which will remain stable at the forming temperature [2,6,43]. It is important also that processing leads to a predominance of high angle boundaries (lattice misorientation $> 15°$), in order that grain boundary sliding and grain rotation, characteristic of superplasticity, can occur [2,6,44].

Numerous aluminum alloys have been shown to exhibit superplasticity; heat-treatable, high-strength aluminum alloys such as 7075, 7475, 2024, and 6061 are used in the aerospace industry [2]. A typically used Al-Mg commercial alloy is AA5083 alloy (Al-4.5% Mg-0.7% Mn). AA5083 is a relatively inexpensive alloy with medium strength, excellent cold forming, welding, and spot welding behaviour, and good corrosion resistance [2]. For superplastic deformation at 525 °C at a strain rate of 10^{-4} s^{-1}, tensile elongations of about 600% may be obtained, while elongations of 300 - 350% are observed at the commercially more attractive forming rate of 10^{-3} s^{-1} (when $m = 0.5$) [2].

Owing to low density and high specific strength, magnesium alloys have high potential as lightweight structural materials. But because of their hexagonally close packed (HCP) structure and limited number of slip systems, they exhibit poor ductility and formability at room temperature. However, some magnesium alloys show large tensile elongation at higher temperature [45,46]. At these temperatures, an additional non-basal slip system (on the pyramidal) becomes active [47,48]. The use of magnesium in automotive structural components is limited. Magnesium AZ31B has been used for structural application using the SPF process and exhibits the same enhanced elongation characteristics at elevated temperature as aluminum AA5083 alloy [2]. Magnesium AZ31 rolled sheet has good formability and strength, high resistance to corrosion and good weldability [3,49], and is used as an attractive alternative in many structural components such as door inner panel (**Figure 2.2b**) and instrument beam panel.

2.3. Deformation mechanisms for superplasticity

2.3.1. Grain boundary sliding (GBS)

GBS involves the relative translation of two grains by a shear movement parallel to their common boundary. The first evidence of relative grain movement was reported by Rosenhain [50] in 1910, which he noted by observing the difference in level of grains on an originally flat polished iron surface of a specimen strained at 1000 °C.

In many well documented studies of superplasticity in fine-grained materials, it has been observed that even after large elongations, there is no appreciable change in grain shape, and the grains remain equiaxed [6,44]. In order to explain microstructural details during superplastic deformation, many GBS models have been proposed by considering accommodation processes in conjunction with GBS.

With the application of tensile stress, diffusion occurs along the grain boundaries as grain boundary interfaces slide past each other. Thus, there is a strong dependence on the grain size. Also, the entire grain rotates during this process. This typically results in the grains remaining equiaxed and random in texture [6,40].

2.3.1.1. *Types of GBS mechanisms*

Two types of GBS mechanisms were reported in the literature, Rachinger sliding [51,52] and Lifshitz sliding [53]. Rachinger sliding is a mechanism where grains retain their original shape even after large elongations, as shown schematically in **Figure 2.3a**. Rachinger sliding occurs by the movement of extrinsic dislocations along grain boundaries, and the climbing of accumulated dislocation within a grain controls the rate of sliding [51,52]. In Rachinger sliding, the shape change of the specimen occurred by

neighbour-switching event without any permanent change in shape of the grains themselves. On the other hand, Lifshitz sliding is considered to be due to stress-directed flow of vacancies either through the grain interiors (Nabarro-Herring creep) [54,55] or along the grain boundaries (Coble creep) [56]. A schematic illustration of Lifshitz sliding is shown in **Figure 2.3b**. In **Figure 2.3b**, grains become elongated in the tensile direction due to the directional flow of vacancies from grain boundaries experiencing tensile stresses to those which have compressive stresses.

During superplastic deformation, large strains are achieved with grains retaining their equiaxed shape, which is similar to Rachinger sliding. Therefore, it is considered that Rachinger sliding is involved in superplastic deformation [52]. However, as suggested recently by Chokshi [57], Lifshitz sliding can also lead to retention of an equiaxed grain size by grain rearrangement and switching, which resulted from the grain growth that occurred during superplastic deformation.

Several microscopic models were proposed to explain the superplastic deformation behaviour of polycrystalline materials. These models can be generally divided into two groups: GBS accommodated by diffusional flow and GBS accommodated by slip, as described in two sections (**Sections 2.3.1.3 and 2.3.1.4**) following the next section.

2.3.1.2.　　 *Diffusional flow*

Diffusional creep may occur, through the grain boundaries, Coble creep (favoured at lower temperatures) or through the grains themselves, Nabarro-Herring creep (favoured at higher temperatures).

Creep at high temperatures $(T \sim T_m)$ and very low stresses in fine-grained materials was attributed 50 years ago by Nabarro and Herring [54,55] to the diffusion of vacancies through the grains from one grain boundary to another. Excess vacancies are created at grain boundaries perpendicular to the tensile axis with a uniaxial tensile stress. The constitutive equation under the diffusion of vacancies through the grain boundaries can be described as:

$$\dot{\varepsilon} = k_1 \left(\frac{D_{gb}}{d^2}\right) \left(\frac{Eb^3}{kT}\right) \left(\frac{\sigma}{E}\right) \text{ (grain boundary diffusion [56])} \tag{2.2}$$

Where D_{gb} is grain boundary diffusion coefficient, b is the Burgers vector, d is the grain size, E is the Young's modulus, k is Boltzmann's constant, and k_1 is material constant.

These excess vacancies diffuse from the grain boundaries lying normal to the tensile direction toward those parallel to it, as illustrated in **Figure 2.4**. Grain boundaries act as perfect sources and sinks for vacancies; thus grains would elongate without dislocation slip or climb. The constitutive equation for diffusional flow with a predominant diffusion through the grain interior:

$$\dot{\varepsilon} = k_2 \left(\frac{D_L}{d^2}\right) \left(\frac{Eb^3}{kT}\right) \left(\frac{\sigma}{E}\right) \text{ (lattice diffusion [54,55])} \tag{2.3}$$

Where D_L is lattice diffusion coefficient, k is Boltzmann's constant, and k_2 is material constant.

2.3.1.3. *GBS accommodated by diffusional flow*

Ashby and Verrall [58] proposed a 2-D model based on GBS with diffusional accommodation, and this was explained from a grain switching event for a four-grain unit without appreciable deformation of grains (**Figure 2.5**). The schematic illustration of the grain switching mechanism in **Figure 2.5** showed during intermediate stages grains

change their original shape by diffusional flow occurring by mass transfer through grain boundaries. Also, the inter-grain distance perpendicular to the tensile direction contracts and the grain boundaries come closer and engaging the grains in lateral direction where as in the other direction (along the tensile direction) the grains move apart. This model was modified later to incorporate a more realistic diffusion path, which considers the vacancy concentration associated with the normal traction distribution at any location on the grain boundary [59,60].

However, as pointed out by Gifkins [61], the grain switching models proposed by Ashby–Verrall and Lee do not account for the increase in surface area at large elongations. Increase in surface area at large elongation has been analyzed by Hazzledine and Newbury [62] based on a continuous model of grain switching event. They suggested that in order to account for the increase in surface area during superplastic deformation, new grains should emerge on the surface. Later, Gifkins [61] suggested another model (**Figure 2.6**), which takes into account the increase in surface area during deformation. This model considers the formation of a shallow gap on a free surface due to the sliding of grains. Later as the gap increases, the emerging grain fills the gap. The dihedral angles are maintained by boundary migration, which results in the boundaries of the four grains becoming curved.

However, as noted by Langdon [63], Gifkins model is two dimensional because it demands that the surface grain boundaries be perpendicular to the specimen surface. Langdon [63] proposed another GBS model in which the grain rearrangement takes place in such a way that they retain equiaxed while they permit an increase in surface area by the exposure of grain boundary facets at the sliding boundaries as shown in **Figure 2.7**.

This model suggests that the grains move apart by sliding to expose both boundary facets and internal grains as in **Figure 2.7b** and there is a continuous rounding at grain corners to produce the type of configuration shown in **Figure 2.7c**.

Based on the analysis on many superplastic materials, Luthy et al. [64] confirmed that most of the GBS models developed so far have been found to correlate well with experimental data, and led to a constitutive equation for GBS accommodated either by lattice diffusion or grain boundary diffusion as in E**quations 2.4 and 2.5** respectively.

$$\dot{\varepsilon} = k_3 \left(\frac{D_L}{d^2}\right) \left(\frac{\sigma}{E}\right)^2 \text{ (lattice diffusion controlled [42])} \qquad (2.4)$$

$$\dot{\varepsilon} = k_4 \left(\frac{D_{gb}b}{d^3}\right) \left(\frac{\sigma}{E}\right)^2 \text{(boundary diffusion controlled [42])} \qquad (2.5)$$

Where $\dot{\varepsilon}$ is strain rate, D_L is lattice diffusion coefficient, D_{gb} is grain boundary diffusion coefficient, b is the Burgers vector, d is the grain size, σ is the flow stress, E is the Young's modulus, and k_3, k_4 are material constants. In **Equations 2.4 and 2.5**, the stress dependence of the power law is given by n = 2 (also implies strain rate sensitivity m = 0.5), which corresponds to the GBS mechanism.

2.3.1.4. *GBS accommodated by slip*

GBS can occur also by dislocation slip, which occurred due to dislocation pileups within the grain and also due to pileups in the grain boundary. The model of dislocation pileups in the grain interior was first proposed by Ball and Hutchinson [65] based on the sliding of a group of grains. The Ball and Hutchison model is schematically represented in **Figure 2.8**. In this mode, grains whose boundaries are suitably aligned will slide as groups during deformation. The shear stress on the group becomes concentrated on any

grain or protrusion that obstructs motion of the group. The local stresses would generate dislocations in the blocking grain and dislocations would pileup at the opposite grain boundary until their back stress prevents further generation of dislocations and thus further sliding by the group. Mukherjee [66] also mentioned a similar GBS model by considering the sliding of individual grains. These models are based on the assumption that when GBS is obstructed, the dislocations will be emitted at triple points or ledges along grain boundaries due to stress concentration. These dislocations traverse through the grain by glide process and are annihilated at the opposite grain boundary by climb of grain boundary dislocations. Because the dislocation glide and climb are sequential processes, the slowest process controls the strain rate. By assuming climb is slower than glide, these models suggest climb of dislocation as the rate controlling process. Based on this, both models predict a stress exponent of n = 2 (m = 0.5) arising from the stress concentration due to the dislocation pileups, an inverse grain size dependence of p = 2 (**Equation 2.1**), and an activation energy which is equal to that for grain boundary diffusion (activation energy of boundary diffusion of aluminum is 82 kJ/mol [67]).

Fukuyo et al. [68] suggested another model for GBS accommodated by dislocation climb or glide for solid solution superplastic alloys. For fine-grained solid solution alloys, the model predicts dislocation climb to be the rate controlled process with $n = 2$ ($m = 0.5$) and the activation energy $Q = Q_l$, activation energy for lattice diffusion.

The model of dislocation pileup in grain boundary plane was suggested by Gifkins [69] and considered the movements of grain boundary dislocations that pileup at triple points to be responsible for GBS. The stress concentration that results from sliding is being relaxed by dissociation of the leading grain boundary dislocations, either moving

into the other two boundaries making up the triple point or by dissociating into lattice dislocations [69]. These new dislocations climb or glide until they annihilate or combine to form different grain boundary dislocations. The sequence of these processes leads to grain rotation and grain rearrangement.

2.3.2. Dislocation glide controlled creep

Deformation in certain solid solution materials at intermediate stresses and certain combination of strain rate can often be described by three regions [70-72] and is illustrated in **Figure 2.9**. With increasing stress, the stress exponent, n, changes from value 5 to 3 and again to 5 in region I, II, and III respectively. Region II with stress exponent 3 is viscous glide of dislocation [70] also known as SD creep mechanism. This is due to the fact that in this regime, the dislocations interact in several possible ways with the solute atoms, and their movement is impeded by the solute atmosphere. Distribution of the solute atoms (interstitial or substitutional) around a moving dislocation would cause a perturbation force that acts on the dislocation opposite to the applied stress. Due to this opposing force the motion of dislocations slows down. This force can be regarded as viscous drag, which allows a steady state motion under a steady state stress [73], and the mechanism known as viscous glide or SD creep mechanism. There are two competing mechanisms over this stress range, dislocation climb and viscous glide, and viscous glide is slower and thus rate controlling. The constitutive equation that describes SD mechanism is given in the form of **Equation 2.6**.

$$\dot{\varepsilon} = k_5 \left(\frac{D_s}{b^2} \right) \left(\frac{\sigma}{E} \right)^3 \hspace{4cm} (2.6)$$

Where D_s is solute atom diffusion coefficient, b is the Burgers vector, d is the grain size, E is the Young's modulus, k is Boltzmann's constant, and k_5 is material constant.

There are several possible SD processes in region II, where n = 3 [74-76]. Cottrell and Jaswon [75] proposed that the dragging process is the segregation of solute atmospheres to moving dislocations. The dislocation speed is limited by the rate of migration of the solute atoms. Fisher [76] suggested that in solid solution alloys with short-range order, dislocation motion destroys the order. The generation of dislocation pileups of high density gives the possibility of pushing leading dislocations through the regions of short-range ordering. Therefore, in the course of their cooperated movement, the dislocations of pileups destroy the short-range ordering. Weertmen [74] suggested that movement dislocation is limited in long-range-ordered alloys because the implied enlargement of an anti- phase boundary results in an increase in energy.

The transition between regions II (n = 3, viscous glide) and III (n = 5, climb controlled creep) has been the subject of several investigations [74,77-79]. It is generally agreed that it is due to the breakaway of dislocations from solute atmospheres. Thus, glide becomes faster than climb, and the latter is then rate controlling in region III.

A behaviour unique to deformation under SD condition is the inverse creep transient, which is demonstrated schematically in **Figure 2.10** for tests in which deformation rate is varied abruptly [18]. In inverse creep transient behaviour, upon an increase in strain rate, the flow stress undergoes a large, abrupt increase and then gradually decreases toward a steady-state value at the new increased strain rate. With the decrease in strain rate, flow stress shows a large, abrupt decrease and then gradually increases to a steady-state value at the new reduced strain rate.

2.4. Deformation mechanisms of aluminum and magnesium alloys

2.4.1. High temperature deformation mechanisms in Al and Al-Mg alloys

Details of the elevated temperature deformation mechanisms of an aluminum alloy depend on the solute content and grain size of the alloy, but the general trends governing temperature, strain, and strain rate dependence of the deformation behaviours of these alloys are well known. To represent various deformation mechanisms that operate in pure aluminum, a deformation mechanism map (DMM) was constructed on stress vs. temperature axes by Frost and Ashby [67]. The zones of different mechanisms were identified, based on the stress exponent (n) value. **Figure 2.11** shows the DMM generated by Frost and Ashby for pure aluminum of grain size 10 μm. The range of strain rate and temperature over which the hot forming operation takes place is narrow. Another form of DMM was constructed by Kim et al. [80] where the grain size and the stress are varied and the temperature is held constant. One such DMM for aluminum alloy at a temperature of 527 °C is shown on grain size vs. stress axes in **Figure 2.12**. This map identifies different deformation mechanisms under the circumstances where the initial grain size varies largely. The superplastic AA5083 alloy is expected to show a steady grain size under all superplastic deformation conditions.

At temperatures near the melting point ($T > 0.8T_m$) of the alloy, and very low normalized stresses ($\sigma/E < 5 \times 10^{-7}$), creep normally occurs as a result of vacancy diffusion, a phenomenon that causes strain accumulation by grain elongation. This mechanism is known as Nabarro-Herring creep [54,55] and is characterized by lattice diffusion that occurs at the grain interiors (see **Figure 2.4**), where as Coble creep, for which the grain boundaries are the preferential diffusion paths, is normally observed at

$T < 0.8T_m$ [67]. A dependence on the third power of the grain size is characteristic of Cobble creep. In both cases, the steady-state strain (creep) rate increases linearly with the applied stress, producing a stress exponent, $n = 1$. Another creep mechanism that operates at high temperatures but at very low stresses (with a resulting stress exponent of $n = 1$), is the Harper and Dorn linear viscous creep [81] that accounts for deformation rates much higher than those achieved by diffusional flow. One possible mechanism proposed for Harper-Dorn creep is climb-controlled deformation, in which the dislocation density is not changed with stress [82,83]. Harper-Dorn creep is independent of grain size [77] and is unlikely to occur in fine-grained materials like AA5083 [83,84]. Dislocation creep controls plastic deformation at mid-range homologous temperatures ($T > 0.5T_m$) and moderate normalized stresses ($\sigma/E > 5\times10^{-5}$), at which point a diffusion-controlled climb mechanism becomes responsible for strain accumulation. Dislocation creep results in a power-law relationship, where the creep rate shows sensitivity to the applied stress with a typical exponent of $n \sim 5$ [78].

The superplasticity of aluminum alloys, particularly with small grain sizes and low solute contents (Al-5Mg-1.2Cr, Al-6.3Mg-0.5Mn, Al-10Mg-0.5Mn), has been associated with GBS [6,52,85,86]. The earlier version of the DMM constructed by Frost and Ashby [67] did not show the region of GBS. However, the DMM constructed by Kim et al. [80] shows the region of GBS as lying between the regions of diffusional flow and power-law creep as in **Figure 2.12**. Large total strains exceeding 300% occur at a given combination of temperature and strain rate within the range of $T = 450\ °C – 545\ °C$ and $d\varepsilon/dt = 10^{-4} – 5 \times 10^{-3}\ \text{s}^{-1}$ [4-6,43]. GBS is generally characterized by an activation energy that is equal to the activation energy for either grain boundary diffusion or lattice self-

diffusion and a stress exponent of $n = 2$. Proposed models of GBS include boundary sliding accommodated by diffusional flow, akin to Coble creep (Ashby-Verrall model [58], see **Figure 2.5**), and GBS that occurs in a mantle-like region at the grain boundaries [69]. GBS is favoured in alloys with equiaxed grains < 10 μm and the presence of second phase particles that inhibit grain growth.

A solid solution may influence diffusional flow by changing the rate of diffusion [55]. In addition, the solid solution can impose a drag on dislocations to slow the rate of creep. Their redistribution can also lead to creep transients (see **Figure 2.10)**. Taleff et al. [23] utilized the concept of SD creep mechanism and discussed the mechanisms of superplasticity in coarse grained Al-Mg alloys (Al-2.8Mg, Al-5.5Mg, Al-3Mg-0.25Mn, and Al-3Mg-0.5Mn) in which a large lattice misfit strain is introduced when Mg is in the aluminum lattice, causing a large local lattice strain. In Al-Mg alloys with a magnesium concentration above 2 wt %, the operation of the SD creep that shows no grain size dependence becomes a critical factor in extending the range of temperatures and strain rates in places where commercial 5000 series alloys exhibit a superplastic response. In fact, recent studies [17,20,87,88] have shown that temperatures of about 450 °C and fast strain rates ($d\varepsilon/dt \geq 10^{-3}$ s^{-1}) during hot forming often involve deformation by SD creep. The activation energy reported for SD creep mechanism was found to be 136 kJ/mol, whereas activation energy for GBS was reported as 110 kJ/mol [89]. Zener-Hollomon type analyses of experimental data gathered from coarse-grained Al-Mg alloys exhibiting SD creep have revealed that the stress exponent, n, has a value between 3 and 4 [17,20,23] as shown in **Figure 2.13** [18]. The Zener-Hollomon parameter ($Z = \dot{\varepsilon}exp(Q/RT)$) combines the effects of strain rate and temperature on a single parameter.

However, observed value of n alone does not confirm the existence of SD creep. As a proof of SD controlling deformation, Kulas et al. [17] showed inverse creep transient, a behaviour unique to deformation under SD condition. Step at fast strain rates, which correspond to high flow stresses, illustrate inverse transients, shown in **Figure 2.14** [17]. A newer version of DMM (**Figure 2.15**) was generated on the logarithm of true stress vs. temperature axes for fine grain direct-chill cast (DC) 5083 material, where the region of GBS and SD creep, along with power law breakdown (PLB), are shown [17]. Even though SD creep operates at low temperature and high strain rates, under certain operating conditions of hot forming (at 450 °C and 10^{-5} s^{-1} < $d\varepsilon/dt$ < 10^{-2} s^{-1}), SD creep and GBS occur concomitantly [21,90]. The details of earlier experimental work on high temperature deformation of Al-Mg alloy are given in **Table 2.1**.

2.4.2. High temperature deformation mechanisms in AZ series magnesium alloys

It is well known that magnesium, with a hexagonal unit cell and limited number of slip systems, exhibits low ductility unless deformation is carried out at elevated temperatures (> 327 °C). At these temperatures, an additional non-basal slip system (on the pyramidal) becomes active [47,48]. The deformation mechanisms operating in pure magnesium was shown by Frost and Ashby [67] in the form of a DMM. The DMM of magnesium shows a large region of dynamic recrystallization (DRX) [67]. Recently Kim et al. [91] constructed a newer version of DMMs, where grain size and stress dependence on deformation mechanisms were shown at a constant temperature (300 °C, 350 °C, and 400 °C) for magnesium AZ31 alloy. One such map on grain size vs. modulus compensated stress axes constructed at a temperature of 400 °C is shown in

Table 2. 1.   High temperature deformation data for Al-Mg alloy.

Material	Grain size, μm	T, °C	Strain rate range, s⁻¹	m	n	Q, kJ/mol	Maximum Elongation, % (T, °C and strain rate, s⁻¹ etc.)	Comments	Ref.
5083	6.9 - 8	450, 500	3×10^{-4} - 6×10^{-2}	0.25 - 0.5	2 - 4	110 for GBS, 136 for SD	300 (at Zener-Hollomon parameter, $z < 3 \times 10^{-5}$ s⁻¹)	450 °C, 3×10^{-2} s⁻¹ - SD, 450 °C, 3×10^{-4} s⁻¹ - GBS transition to SD	[89]
5083	9	335	10^{-4} - 0.1	0.2 - 0.6	2 - 5	140 (close to self-diffusion)	400 (at 535 °C and 10^{-4} s⁻¹)	Texture, grain refinement through discontinuous R_x, transition from dislocation to GBS at $\sigma/E < 6 \times 10^{-4}$	[87]
5083	6.5 (at 425 °C), 10 (at 525 °C)	450	10^{-4} - 3×10^{-1}	0.45 (at 5×10^{-4} s⁻¹), <0.25 (at 5×10^{-2} s⁻¹)	2 - 4	-	390	Transition from GBS to SD at $> 10^{-2}$ s⁻¹, in GBS failure by cavity linkage, in SD failure by flow localization at high strain rate	[21]
5083	7 - 7.7	425 - 500	3×10^{-5} to 1×10^{-1}	0.25 - 0.5	2 - 4	123-135 (at $\sigma/E = 6 \times 10^{-4}$, SD), 101 - 109 (at $\sigma/E = 3 \times 10^{-4}$, GBS)	-	GBS and SD creep, GBS occurs at high temperature and low strain rate	[17]
5083 (0.02 - 0.6Cu)	6.5 - 8.0	425 - 500	3×10^{-5} to 6×10^{-2}	0.31 - 0.36	3	136 (at $\sigma/E > 3 \times 10^{-4}$, SD), 110 (at $\sigma/E < 3 \times 10^{-4}$, GBS)	300 (450 °C)	Cu addition reduce flow stress and improve ductility when deformation is by GBS, elongation to failure decreased from 450 °C to 500 °C	[20]

Continued .. GBS – Grain boundary sliding; SD – Solute drag.

Material	Grain size, μm	T, °C	Strain rate range, s^{-1}	m	n	Q, kJ/mol	Maximum Elongation, % (T, °C and strain rate, s^{-1} etc.)	Comments	Ref.
5083	6.5	500 - 565	3×10^{-5} to 1×10^{-2}	0.4 - 0.65	1 - 2	-	600 (at 550 °C)	At strain rate $< 1 \times 10^{-3}$ s^{-1} GBS is the primary deformation process	[43]
5083	20	300 - 450	10^{-5} to 10^{-1}	0.33	3	123	elongation to failure: 160 (450 °C and 10^{-3} s^{-1})	Viscous glide of dislocation	[88]
Al-Mg (2.8-5.5% Mg)	30 - 450	200 - 500	10^{-4} to 2	0.29 - 0.32	3	136	325 (400 °C, 1×10^{-4} s^{-1})	Deformation controlled by SD creep	[23]

GBS – Grain boundary sliding; SD – Solute drag.

Figure 2.16 [91]. There have been many reports on the superplastic deformation characteristics of Mg- Al- Zn alloys (AZ31, AZ61 and AZ91), based on which the superplastic deformation in AZ series magnesium alloy are considered in the subsequent paragraphs.

Solberg et al. [26] studied superplasticity in the conventionally cast and rapidly solidified extruded AZ91 magnesium alloy. Conventionally cast material had a duplex microstructure of alternating bands of coarse (20 µm) and fine grains (3 µm), whereas the rapidly solidified alloy had a uniform microstructure of grain size of 1.2 ± 0.4 µm. Elongations above 1000% were reported for rapidly solidified alloy when tests were carried out at a strain rate of 3.3×10^{-3} s^{-1} and 275 °C and 300 °C. Based on the calculated activation energy of 25 and 45 kJ/mol at constant strain rate and constant stress, it was suggested that grain boundary diffusion was the rate controlling mechanism. During the initial stages of superplastic deformation of AZ91 alloy, grain refinement due to DRX was reported, and the alloy exhibited a maximum elongation of 604% at 300 °C and 1.5×10^{-3} s^{-1} [92]. This large elongation was attributed to significant GBS due to the grain refinement.

Takuda et al. [29] investigated the possibility of grain refinement for superplasticity of coarse grained (17 µm) Mg- 1.86Al- 0.79Zn alloy. The tensile tests were conducted with an initial strain rate of 8.3×10^{-5} s^{-1} – 8.3×10^{-2} s^{-1} at temperatures in the range of 200 – 500 °C. The measured strain rate sensitivity, m, was found to be less than 0.3 for all of the above testing conditions, and a maximum elongation of 200 % was observed at 400 °C and at 8.3×10^{-4} s^{-1}.

Mukai et al. [93] investigated the high temperature deformation characteristics of coarse- and fine-grained AZ31 alloy. They observed that the deformation mechanism in two alloys was different. A coarse-grained (75 μm) alloy exhibited a strain rate sensitivity of 0.33, giving a maximum elongation of 130 % at 5×10^{-5} s^{-1} and 350 °C. The activation energy was estimated to be 127 kJ/mol and from the evidence of m = 0.33, glide controlled dislocation creep was suggested as the deformation mechanism for coarse-grained alloy. Mukai et al. [93] achieved superplastic deformation with a maximum elongation of > 600 % at 1×10^{-4} s^{-1} and at 325°C in fine-grained (3 μm) extruded AZ31 bar. This alloy exhibited $m = 0.5$, and $Q = 96$ kJ/mol. Based on these observations, it was inferred that the deformation occurred by GBS accommodated by slip controlled grain boundary diffusion.

Wu and Liu [30] investigated a maximum elongation of 320 % was reported during superplasticity of coarse-grained AZ31 alloy with a mean grain size of 300 μm at 500 °C and at strain rate of 1×10^{-3} s^{-1}. Calculated strain rate sensitivity and activation energy in the strain rate regime below 1×10^{-3} s^{-1} was found to be 0.39 and 145 kJ/mol respectively, and the deformation mechanisms were interpreted as lattice diffusion controlled process.

Superplastic behaviour of the wrought AZ31 alloy with grain sizes 6 and 16 μm were studied by Somekawa et al. [94], with strain rate varying from $10^{-4} - 10^{-2}$ s^{-1} at temperatures of 200, 300 and 400 °C respectively. Based on the calculated value of $m = 0.5$ for both fine- and coarse-grained materials in the low strain rate range at 400 °C, GBS was suggested as the deformation mechanism.

Tan and Tan [25] proposed a two-stage deformation method to enhance the superplasticity of average grain sized 12 μm AZ31 alloy sheet. The method was based on the capability of the material to undergo DRX. The optimum condition for grain refinement was indentified to be 250 °C, at a strain rate of 1×10^{-4} s^{-1} to a strain level of 60 %, and the ductility was found to be 140 %. The strain rate sensitivity was calculated to be 0.5, and GBS accommodated by dislocation slip was the suggested deformation mechanism. When pre-deformed samples with refined grain size of 6 μm were tested at 400 °C and at 1×10^{-4} s^{-1}, the ductility was found to be improved from 250 to 320 %. A strain rate sensitivity of 0.3 was observed and the data were attributed to viscous glide, also known as SD creep mechanism.

Del Valle et al. [95] investigated the deformation mechanisms responsible for high ductility in coarse grained AZ31 alloy with an initial grain size of 17 μm. Tensile tests to failure were performed at 300 °C and 375 °C and at initial strain rates ranging from $3 \times 10^{-5} - 5 \times 10^{-2}$ s^{-1}. They identified two deformation regimes. In the lower strain rate regime, the strain rate sensitivity decreased with deformation from 0.59 to 0.45, and the activation energy varied from 91 to 106 kJ/mol. A maximum ductility of 320 % was reported when the specimen was deformed at 375 °C and at 5×10^{-5} s^{-1}. Based on the observations of large elongation, significant grain elongation, and the retention of basal fibre texture, the suggested mechanism was concurrent operation of GBS and dislocation slip.

The mechanical behaviour and microstructural evolution of AZ31 with a heterogeneous grain structure of equiaxed grains (4 μm) and elongated grains (200 μm) was investigated by Yi et al. [96]. The tensile tests were carried at room temperature (RT)

to 250 °C with an initial strain rate of 5.5×10^{-4} s^{-1}. A maximum elongation of 149 % was reported at 250 °C, which suggests the simultaneous operation of GBS and grain refinement by DRX.

Mabuchi et al. [97] calculated activation energy of 121 kJ/mol for powder metallurgy AZ91 alloy with grain size $1 - 3$ μm and 104 kJ/mol for Ingot metallurgy AZ91 with grain size $4 - 5$ μm when deformed at $250 - 450$ °C and with constant strain rate range $2 \times 10^{-5} - 1 \times 10^{-1}$ s^{-1}. Because these values were found to be higher than the activation energy of grain boundary diffusion, they suggested the rate controlling mechanism as a combination of lattice and grain boundary diffusion processes. However, equal channel angular extrusion processed AZ91 alloy with grain size of 1 μm showed a large elongation of 661 % at 200 °C and at 6.2×10^{-5} s^{-1} and with a strain rate sensitivity of 0.3, which suggested that the low temperature superplasticity for the AZ91 alloy was due to viscous glide (also known as SD) of dislocations [98].

Watanabe et al. [99] studied the superplastic characteristics in 10 μm grain-sized AZ61 magnesium alloy at temperatures ranging from $250 - 400$ °C with constant strain rate ranging from $1 \times 10^{-6} - 1 \times 10^{-3}$ s^{-1}. Strain rate sensitivity (m) of 0.5 was reported for a true strain of 0.1, and the alloy exhibited a maximum elongation of 461% at 375 °C and at 3×10^{-5} s^{-1}. The activation energies were found to be 90 kJ/mol at $250 - 300$ °C and 140 kJ/mol at $325 - 400$ °C. They suggested that GBS accommodated by slip was the deformation mechanism controlled by grain boundary diffusion at $250 - 300$ °C and lattice diffusion at $325 - 400$ °C. At 350 °C and at 1.0×10^{-4} s^{-1}, GBS by lattice diffusion was also reported for 6 μm fine-grained AZ31 alloy to be the deformation mechanism [100].

Lin and Huang [101] have carried out grain refinement in AZ31 alloy by a one-step high ratio extrusion process, which resulted in high strain rate superplasticity (HSRSP) and low temperature superplasticity (LTSP). The initial grain size of 70 μm was significantly reduced up to 2.5 μm. With an initial strain rate ranging from 1×10^{-4} – 1×10^{-1} s^{-1} the alloy exhibited HSRSP and/or LTSP at 200 – 300 °C. A maximum elongation of 900 and 600 % was reported when the alloy tested at 1×10^{-4} s^{-1} and at 553 and 200 °C, respectively. At higher strain rates of 2×10^{-3} s^{-1} and 1×10^{-1} s^{-1}, elongation was maintained at 300 % and 210 % respectively at 300 °C. The strain rate sensitivity was found to be 0.4, which suggested that GBS and SD creep might have contributed to deformation.

From the tensile tests carried out by Lee and Huang [102] at 200 – 450 °C and at 6.0×10^{-4} s^{-1} to 1.0×10^{-1} s^{-1} on extruded AZ31 plate having equiaxed grains 1.7 μm, a maximum elongation of 740 % was observed at 300 °C and at 1.0×10^{-3} s^{-1}. The observation of higher elongations at different testing conditions indicated that the AZ31 alloy was capable for LTSP and HSRSP. The strain rate sensitivity was measured to be 0.45 – 0.6 suggesting that GBS was the dominant deformation mechanism.

Fine-grained superplasticity of AZ61 having an average grain size of 3.5 μm was investigated by Perez-Prado et al. [103]. Ductility tests were conducted at temperatures ranging from 100 – 400 °C and at initial strain rate 1.0×10^{-4} s^{-1} – 1.0×10^{-3} s^{-1}. A maximum ductility of 700 % was reported when the tensile sample was deformed at 250 °C and at 1.0×10^{-4} s^{-1}. The strain rate sensitivities calculated at strain rates ranging from 2×10^{-5} – 2×10^{-2} s^{-1} at 250 °C identified two regimes. At strain rates higher than 3×10^{-4} s^{-1}, m = 0.23 and at lower strain rates, m = 0.59, the suggested deformation

mechanisms were dislocation slip and GBS, respectively. GBS was also suggested by their observations of equiaxed grains even after large elongations and significant decrease in texture intensity. The measured activation energies were found to be 121 kJ/mol in the dislocation regime and 104 kJ/mol in the GBS regime, and a combination of lattice and grain boundary diffusion was proposed as the rate controlling mechanism.

Yin et al. [104] examined superplasticity of AZ31 alloy sheet with a grain size of 4.5 µm. The initial grain size of 15 µm was refined to 4.5 µm by hot rolling followed by annealing conducted at 320 °C. Tensile tests were conducted in the temperature range of 250 – 450 °C and at strain rates ranging from 7×10^{-4} s^{-1} – 1.4×10^{-1} s^{-1}. A maximum elongation of 363 % was reported at 7×10^{-4} s^{-1} and at 400 °C. The strain rate sensitivity was found to be 0.5 suggesting that GBS was the dominant deformation mechanism.

The details of each individual work that is grain size, stress exponent, activation energy, deformation mechanism, and so on, are summarized in the form of a table as in **Table 2.2**. Many studies identified the deformation mechanisms by evaluating the values of strain rate sensitivity only, and only in some cases was the deformation mechanism validated with the study of post deformation microstructure. Deformation mechanisms in magnesium alloys have been briefly analyzed and are described in the next paragraph.

According to the DMM of pure magnesium [67], diffusional flow is the governing elevated temperature deformation mechanism at low applied stresses (that is, for normalized shear stress, $\tau/\mu < 3 \times 10^{-4}$, where τ and μ are the shear strength and shear modulus of the material). Power law creep, where deformation is controlled by dislocation glide and climb, becomes dominant at temperatures $T/T_m > 0.4$ with the application of high stresses $\tau/\mu > 3 \times 10^{-4}$. GBS, a shear process promoted by an increase

Table 2. 2. High temperature deformation data for AZ series magnesium alloy.

Material	Grain size, μm	T, °C	Strain rate range, s^{-1}	m	n	Q, kJ/mol	Maximum Elongation (%), Strain rate (s^{-1}) T (°C)	Comments	Ref
AZ91	20 and 3	250 - 300	3.3×10^{-3}	> 0.3	3	25 - 45	$180, 3.3 \times 10^{-3}, 275$	At 3.3×10^{-3} - Grain boundary diffusion. At 300 °C and 1.5×10^{-3} - GBS of small grains generated by DRX	[26]
Mg-1.86Al-0.79Zn	19	200 - 500	8.3×10^{-5}- 8.3×10^{-2}	< 0.3	3	-	$345, 8.3 \times 10^{-4}, 400$	Recrystallization of pre-deformed alloy reduced grain size and enhanced ductility	[29]
AZ31	75	300 - 350	1×10^{-5}- 1×10^{-3}	0.33	3	127	$190, 5 \times 10^{-5}, 350$	Superplasticity in coarse grain material by viscous glide mechanism	[93]
AZ91	23	300	1.5×10^{-3}	-	-	-	$604, 1.5 \times 10^{-3}, 300$	GBS mechanism due to small grains generated by DRX	[92]
AZ31	300	350 - 500	1×10^{-3}- 1	0.39	2	145	$320, 1\times10^{-3}, 500$	Lattice diffusion controlled process	[30]

Continued ..

Material	Grain size, μm	T, °C	Strain rate range, s⁻¹	m	n	Q, kJ/mol	Maximum Elongation (%), Strain rate (s⁻¹) T (°C)	Comments	Ref
AZ31	16	200 - 400	1×10^{-4} - 1×10^{-2}	0.5	2	-	-	GBS mechanism	[94]
AZ31	12	250 - 400	1×10^{-4}	0.5	2	-	320, 1×10^{-4}, 400	Optimum condition for grain refinement - 250 °C, 1×10^{-4} GBS of refined grains At T > 400 °C - Viscous glide mechanism	[25]
AZ31	17	300 - 375	3×10^{-5} - 5×10^{-2}	(0.59-0.45) 0.17	2, 6	91 143	320, 5×10^{-5}, 375	GBS and DS at lower strain rate climb controlled DS at higher strain rate	[95]
AZ31	4 and 200	27 - 250	5.5×10^{-4}	-	-	-	150, 5×10^{-4}, 250	Simultaneous occurrence of GBS and DRX	[96]
PMAZ91	1 - 3	270 - 400	2×10^{-5} - 1×10^{1}	0.5	2	121	275, 1×10^{-2}, 300	Combination of Lattice and GB diffusion process	[97]
IMAZ91	4 - 5	250 - 300				104	410, 5×10^{-4}, 250		

Continued ..

Material	Grain size, μm	T, °C	Strain rate range, s^{-1}	m	n	Q, kJ/mol	Maximum Elongation (%), Strain rate (s^{-1}) T (°C)	Comments	Ref
AZ91	1	175 - 200	2×10^{-5}- 1×10^{-3}	0.3	3	-	661, 6.2×10^{-5}, 200	Viscous glide creep mechanism	[98]
AZ61	10	250 - 400	1×10^{-6}- 1×10^{-3}	0.5	2	90 at 523-300 °C, 143 at 325 -350 °C	461, 3×10^{-5}, 375	GBS accommodated by slip controlled by GB diffusion at lower temp, lattice diffusion at higher temp	[99]
AZ31	3	300 - 400	1×10^{-4}- 1×10^{-1}	0.5	2	96	600, 1×10^{-4}, 325	GBS mechanism accommodated by slip	[93]
AZ31	2.5	200 - 350	1×10^{-4}- 1×10^{-1}	0.3 - 0.4	2 - 3	-	900, 1×10^{-4}, 280	At 300 °C and 2×10^{-3} - 1×10^{-1} - GBS and Viscous glide operates simultaneously	[101]
AZ31	10 6	350 - 400 200 - 400	1×10^{-5}- 1×10^{-3}, 1×10^{-4}- 1×10^{-2}	0.5	2	-	404, 1×10^{-5}, 450	GBS mechanism	[27]
AZ61	6	300 - 400	1×10^{-4}- 1×10^{-2}	0.45	2	132	920, 1×10^{-4}, 350	GBS mechanism accommodated by slip controlled by lattice diffusion	[100]

Continued ..

Material	Grain size, μm	T, °C	Strain rate range, s⁻¹	m	n	Q, kJ/mol	Maximum Elongation (%), Strain rate (s⁻¹) T (°C)	Comments	Ref
AZ31	1.7	200 - 450	6×10^{-4} - 1×10^{-1}	0.45 - 0.6	2	-	740, 1×10^{-3}, 300	GBS mechanism	[102]
AZ61	6	100 - 400	1×10^{-4} - 1×10^{-1}	0.59 / 0.23	2 / 4	121 / 104	700, 2×10^{-4}, 250	GBS mechanism at lower strain rate regime / Dislocation slip at high strain rate regime	[103]
AZ31	4.5	150 - 450	7×10^{-4} - 1.4×10^{-1}	0.47		-	363, 7×10^{-4}, 400	GBS mechanism	[104]

GBS – Grain boundary sliding; SD – Solute drag; DRX – Dynamic recrystallization.

in the temperature and/or a decrease in the strain rate, is another commonly observed high temperature deformation mechanism [91,99,105-107]. As indicated previously, GBS is either controlled by lattice diffusion or grain boundary diffusion [91,99,106,108,109]. The high strain rate sensitivity of magnesium is often associated with the operation of GBS mechanisms [106], and in microstructures with small grain size, it leads to superplastic behaviour [25,91,99,105]. GBS has often been reported [91,99,105-107] as the main mechanism of plastic deformation in pure magnesium and magnesium alloys deformed at a temperature range between 250 and 400 °C. Since superplasticity is a high temperature phenomenon, grain coarsening is one major concern while deforming magnesium alloys. In the coarse-grained (grain size, $d > 100$ μm) Mg-Al-Zn alloys [91,107,110,111], glide and climb controlled dislocation creep operate in the temperature range of 300 – 400 °C. It was also reported that SD creep was responsible for the superplastic behaviour observed in some coarse-grained alloys, Mg-Al-Zn alloys [25,107,111]. Grain coarsening can be prevented by a duplex microstructure with two phases or by dispersing a small fraction of the second phase in finely distributed form. Many studies have addressed the DRX [25,67,96,105,112-115] that was observed during the deformation of magnesium alloys at temperatures, $T/T_m > 0.76$ (temperature > 450 °C for pure magnesium) and high strains ($\varepsilon = 0.4 – 2.0$).

To summarize, extended ductility observed in AZ31 alloy was attributed to the predominance of one of these two deformation mechanisms: GBS for small grain sizes (< 10 μm) [25-28,93,99] or viscous glide controlled creep in which gliding dislocations are dragged by the solute atmosphere for rather large grain sizes (> 20 μm) [25,29,30,93]. Tan et al. reported that coarse grains originated from initial DRX grains and had grown as

a result of a higher deformation temperature ($T > 400$ °C). The value of m was found between 0.3 and 0.5, inferring that the fine grains deformed by GBS, whereas coarse grains deformed by viscous glide [25,93]. It has also been found that in some cases dynamic recrystallization leads to in-situ grain refinement and thus enhanced plastic deformation in an initial coarse-grained material [37,99]. Also, effective grain refinement by DRX observed during the deformation of magnesium alloys, which led to the improvement of GBS, enhanced the superplastic behaviour of the material [25,28,96,101,116].

2.4.3. Dynamic recrystallization in magnesium alloy

Recrystallization refers to a process of restoration in which new dislocation-free grains formed within the deformed or recovered structure, and the original deformed grains will be consumed by newly nucleated and grown undeformed grains [114,117]. Recrystallization that occurs during the deformation is called dynamic recrystallization (DRX); on the other hand, recrystallization that occurs after the deformation is called static recrystallization. Recrystallization can also be divided into continuous and discontinuous processes. Discontinuous recrystallization (DDRX) has clear nucleation and growth stages, and dislocations are removed by eliminating high angle grain boundaries [117]. Continuous recrystallization (CDRX) has no identifiable nucleation and growth stages, and dislocations still remain in the recrystallized grains, which is generally considered as a recovery process whereby low angle boundaries transform to high angle boundaries [116-120].

Unlike for aluminum alloy, DRX is very common in magnesium due to its low stacking fault energy, where recovery is very low. New fine grains nucleate at the old

grain boundaries. A necklace structure of recrystallized grains may be formed. Tan et al. [25,28] have found evidence for the transformation from low angle grain boundaries (<15º) to high angle grain boundaries (>15º) during dynamic recrystallization. The neighbouring grains in the undeformed specimen which had small misorientation angles of 1~2º between each other showed large angle of 28º after DRX. **Figure 2.17** shows the TEM micrograph of DRX specimen and two neighbouring subgrains with corresponding diffraction patterns, which show large misorientation angles 28º between subgrains, which is attributed to DRX [28].

Several DRX mechanisms in magnesium ZK60 at different temperatures had been proposed previously and are schematically shown in **Figure 2.18** [116]. At a low temperature of 150 °C, basal slip and twining played an important role on DRX [116,118]. At intermediate temperatures (200 – 250 °C), continuous DRX was associated with cross slip and predominantly activated near the original grain boundary. Dislocation rearrangements by cross slip and climb generate a low angle boundary network in the vicinity of the original boundary. Continuous absorption of dislocations in the low angle boundaries result in CDRX, that is, in formation of new grains (as in **Figure 2.18b**) [116]. At high temperature (300 – 450 °C) microscopic strain localization at the slip lines causes formation of bulges of grain boundaries, which leads to nucleation of DRX grains (as in **Figure 2.18c**) [116].

The volume fraction of the DRX grains increased with increase in temperature. Also, with increase in strain rate, the DRX grain size for the alloy at the same strain became smaller. The dislocation density of the alloy at high strain rate was higher, which made it easier to form finer subgrains and DRX grains [114].

2.5. Oxide layers on Al-Mg alloy surfaces

The surface of aluminum alloy sheets contains a tribo-layer known as the disturbed layer that forms during the prior thermo-mechanical treatment particularly during hot rolling of the sheet. The disturbed layer of non-uniform thickness varies between 1.5 and 8.0 μm. These layers are characterized by rolled-in oxide patches and a distribution of ultra fine aluminum grains mixed with the comminuted fragments of fractured second phase particles [121,122]. Severe plastic strain in the near-surface region during rolling is responsible for the formation of a near-surface deformed layer that contained fine grains of oxide particles of 100–200 nm in diameter [123]. The schematic representation in **Figure 2.19** shows the subsurface layer containing the microcrystalline oxides mixed with small-grained metal [121].

Studies aimed at understanding the high temperature oxidation behaviour of fresh surface of Al-Mg alloys revealed that these alloys tend to develop a thin, amorphous layer of Al_2O_3 during the early stages of oxidation [124]. Once heated above 400 °C, the amorphous layer transforms into crystalline γ-Al_2O_3, with the outward diffusion of magnesium atoms into the surface and promoting the formation of MgO islands on the surface and $MgAl_2O_4$ at the interface between the oxide and the bulk aluminum [125], as shown in the schematic model in **Figure 2.20**. These surface layers are generally observed to consist of a mixture of $MgAl_2O_4$, MgO, and Al_2O_3 (amorphous and/or crystalline), with the concentration of MgO being the highest at the surface, and the size of the oxide particles in the subsurface layer ranging from 3.0 to 30.0 nm [125-127]. Diffusion coefficient for magnesium in aluminum increased with increase in temperature and a value of diffusion coefficient was found to be 1.04×10^{-9} $cm^2 s^{-1}$ at 425 °C [128].

The diffusion of magnesium to the surface of the alloy occurs rapidly and the concentration of magnesium increases with time [124]. Alloy containing higher bulk magnesium showed more magnesium diffusion and oxide formation at the surface [129]. Riahi et al. [130] showed an increase in magnesium content from 0.7 % to 4.7 %, the thickness of oxide layer increased from 35 nm to 100 nm.

2.5.1. Surface oxide failure mechanism modes

The oxide scales that form on metallic surfaces act as hard, protective layers that prove advantageous in some high temperature applications. In many practical applications however, these oxides are stressed either by an externally applied load, or by oxide growth stresses, which cause cracks to form that result in their failure. The thermal stresses induced by a mismatch of thermal expansion coefficients of the oxide layer and substrate [131] is another known mechanism of oxide failure. When the substrate is subjected to creep deformation, the surface oxide crack density initially increases with strain [127] and eventually reaches a saturation point. This behaviour has been illustrated in a model for viscous sliding of oxide segments against a substrate subjected to creep [127].

Evans [132] demonstrated that under tensile loading, sliding could occur at the oxide-metal interface, which results in oxide delamination and subsequent spallation. Le et al. [133] showed the spacing between adjacent cracks increases with oxide film thickness during aluminum rolling, exposing nascent aluminum. The reaction between the fresh metal surfaces and the atmosphere during the subsequent hot deformation process depends on the thickness of the initial oxide layer. The maximum aspect ratio of the oxide fragment that does not break was derived [133] as:

$$\frac{\lambda_c}{t_c} = \frac{2\sigma_f}{k_6(1-4\mu^2)}$$ (2.7)

where λ_c is maximum length of oxide fragment, t_c is oxide film thickness, σ_f is tensile strength on oxide film, k_6 is shear yield stress of substrate, and μ is coefficient of friction (COF) between roll and the strip material.

In addition, the fresh metal may be extruded to the surface through these cracks because the bulk metal has a lower flow stress and a higher ductility than the oxide scale at hot working temperatures [133].

2.5.2. Plasticity and creep of oxide layer

The number of active slip systems is fewer than five in most oxides. Two independent slip systems at a temperature of 987 °C were found in Al_2O_3, and therefore the secondary slip systems must be activated in order to observe plastic deformation in the oxide [127]. The stress required to activate the secondary slip systems decreased more rapidly with increasing temperatures than that required to initiate micro-cracks. So, at higher temperature considerable deformation by dislocation glide becomes possible.

Deformation mechanisms operating in Al_2O_3 and MgO are summarized in the form of DMMs, as shown in **Figures 2.21a and 2.21b**. Diffusion creep becomes the controlling mechanism at high temperatures and relatively low stresses in MgO (modulus compensated stress < 10^{-4}) [67]. The stress changes the chemical potential of the atoms on the surfaces of the grains in a polycrystalline material in such a way that there is flow of vacancies from grain boundaries experiencing tensile stresses to those which have compressive stresses. Flow of vacancies that takes place at the grain boundaries can be described as Coble-type creep [56] by

$$\frac{d\varepsilon}{dt} = \frac{\alpha_1 D_{gb}\delta\sigma\Omega}{d^3 kT}$$

(2.8)

Where α_1 is a constant, D_{gb} is the grain boundary diffusion coefficient, σ is the applied stress, Ω is the atomic volume, k is Boltzmann's constant, T is temperature, d is the average grain size, and δ is the thickness of the grain boundary over which diffusion takes place.

Equation 2.8 shows that a refinement of grain size by a factor of two is expected to increase the steady state creep rate by a factor of eight. Therefore, the oxide with smaller grain size is expected to show high plastic deformation even at low temperature and low stresses.

2.5.3. Characteristics surface features on aluminum alloys upon high temperature deformation

The formation of fibrous structures running in the tensile direction has been observed on the fracture surfaces of Al-Mg alloys tested at temperatures between 250 °C and 550 °C [134-137]. Topographic studies on Al-Cu-Mg alloys (AA2090) [134] indicated that bundles of fibres formed on oxidized surfaces and at grain boundaries that experienced sliding. The fibres were 0.5 – 1.0 μm in diameter and extended up to 15 μm. The appearance of these fibres suggests very large strains, e.g. superplasticity in the local regions. Zelin [134] and Chang et al. [138] reported that the formation of these fibres was associated with dynamic oxide growth that resulted from the interaction between freshly exposed material and oxygen. Proposed mechanisms for fibre superplasticity include viscous flow induced by the presence of liquid phase along the grain boundaries [136,137,139], dislocation movement facilitated by the oxygen atoms [136,140], and

submicron size of grains that promoted local superplastic deformation [137,141], prompting a phenomenon called *superplasticity in micro-volume*. Although the mechanisms of their formation are still open to discussion, the high ductility fibres that form on the surfaces of the AA5083 alloy are of particular interest in characterizing the tribological properties of this alloy at elevated temperatures.

2.6.   Tribology of aluminum and magnesium alloys at elevated temperature

When two solids are placed in contact the plastic flow occurs at the point of real contact until the area is sufficient to support the normal load. At these contact regions metallic junctions are formed as a result of a process of cold welding. These junctions are responsible of adhesion and friction observed in material [142]. The adhesion is the measure of tensile strength of the junction and the friction is a measure their shear strength [142]. It was shown that friction force increased with the increase in adhesion and hence friction has been considered as a measure of adhesion between them [15,142]. Thus, the friction behaviour of the alloy deformed at elevated temperature and at various strain rates is one of the main factors to consider while studying the adhesion mechanism.

2.6.1. Aluminum alloys

Tribological data from the interaction between aluminum and steel at elevated temperature are rather limited to date [13-15,143-146]. The summary of existing literature on tribological behaviour of aluminum alloy is given in **Table 2.3**. Hanna [15] reported a maximum COF of 0.55 (as in **Figure 2.22**), when AA5083 sample was tested

Table 2. 3.   Summary of high temperature tribological properties of aluminum alloys.

Material	Type of test	T, °C	Experimental conditions	Counter-face	Lubricant	Coefficient of friction (conditions)	Wear rate	Comments	Ref.
7475 extruded	Ball-on-disc	300 –450	10 N (max. load), 500 rpm (max. speed)	H11 hot-work tool steel ball	dry	1.3 (450 °C), 0.8 (300 °C), 0.53 (25 °C)	Not measured	Plowing friction contributed towards the high COF at elevated temperature	[14]
5083	Reciprocating tribo test machine	RT -450	10 - 100 N (load)	P20 steel block	With and without Boron Nitride (BN)	< 0.005 (BN, 200 - 300 °C), 0.14 (BN, 400 °C), 0.55 (Without BN, 450 °C)	Not measured	Experiments were done mainly to determine the onset of adhesion and to evaluate the coating and lubrication effectiveness	[15]
A356	Block-on-ring	RT -150	42 N (load), 0.16 - 1.24 m/s(sliding speed)	S45C steel ring	dry	-	wear rate increased at 150 °C when speed > 0.64 m/s	Wear occurred accompanied by plastic deformation	[144]
6061	Ring-on-flat	RT -500	10 N (load)	SAE 52100 bearing steel	dry	0.65 (25 °C), 0.25 (150 °C)	0.004 mm³/m (10 N, 100 °C, mild wear), 0.3 mm³/m (10 N, 500 °C, severe wear)	Transition to SW occurs at temperatures >150 °C. SW occurs by gross plastic deformation and material transfer to the counterface	[147]

Continued..

Material	Type of test	T, °C	Experimental conditions	Counter-face	Lubricant	Coefficient of friction (conditions)	Wear rate	Comments	Ref.
A356, 6061	Ring-on-flat	RT - 460	11.55 N (load), 0.1 m/s (speed)	SAE 52100 bearing steel ring	dry	0.6 (mild wear), 1.2 (severe wear)	0.001 mm³/m (mild wear), max. 0.4 mm³/m (severe wear at 250 °C)	Transition temperature: 175 - 190 °C (6061 alloy), 225 - 230 °C (A356)	[146]
7475, 5083	disc-on-flat	450 - 530	1-8 MPa (normal pressure), 450 - 530 °C (temperature)	tool steel	with and without graphite	0.1 (at high normal pressure), 0.45 (at low normal pressure)	Not measured	COF is not affected by temperature under lubricated condition, at low pressure friction attributed to interaction of surface asperities, and ploughing of surface, At high pressure sublayer plastic deformation controls friction	[145]
Pure aluminum	Forward extrusion	RT	-	AISI H13	dry	0.84 at RT	Not measured	Friction model works well for cold extrusion of aluminum in dry condition	[154]
Pure Al, 5005, 5052, 5082	Pin-on-disc	440	0.5 N (Load), 8.75×10^{-6} m/s (speed)	AISI 52100-grade steel disc	dry	Junction strength: 0.7 N (pure Al), 0.25 (Pure Mg)	Not measured	MgO decreased the junction strength, low adhesion tendency of the alloys with high Mg content	[130]

MW – Mild wear; SW – Severe wear.

under dry condition using a reciprocating tribotester (load – 50N, speed 0.11 Hz). On the other hand, Singh et al. [143,147] had studied elevated temperature tribology of aluminum 6061 alloy and reported an increase in COF from 0.5 to 2 when the temperature was increased from room temperature to 400 °C. In the same study the author had described the relationship between wear and the microscopic variable of deformation as in **Figure 2.23**. The figure reveals the range of conditions under which mild wear and severe wear occur. According to the map, the mild wear should involve plastic deformation by dislocation glide. Severe wear should proceed by creep of subsurface material within the temperature range of $0.5T_m < T < 0.65T_m$ and may involve micromechanisms such as climb and glide (power-law breakdown) [143]. Activation energy of 87 kJ/mol for the severe wear regime was calculated in the same work from the slope of a wear rate vs. reciprocal temperature plot [143]. Based on the theoretical model, the calculated COF during the metal forming process was found to be always less than the value of 0.577 [148], which is very close to the value reported by Hanna [15]. On the other hand, elevated temperature experiments on aluminum 7475 alloy by Wang et al. [14] also showed a trend similar to the one found by Singh and coworkers [143]. Wang et al. [14] have suggested that the high COF value at elevated temperature could be attributed to the increased plowing friction caused by the severe plastic deformation.

Riahi et al. [130] have used pin-on-disk tribometer to study the effect of the magnesium content of 5000 series aluminum alloys on their adhesion behaviour to steel surface. The authors have determined the junction strength between the Al–Mg alloys and the steel counterface by measuring the tangential force required to break the adhesive junctions formed during initial sliding contact. The junction strength in Al-Mg alloy was

found to be dependent on magnesium content of the material, as in **Figure 2.24**. Low adhesion tendency was found in the material with high magnesium content.

2.6.2. Magnesium alloys

Deformation and damage mechanisms in magnesium alloys subjected to sliding contact at elevated temperatures have not been investigated extensively. Sliding-induced damage mechanisms on samples worn at room temperature are also scarce [149-153], as summarized in **Table 2.4**. Evidence based on the sliding wear experiments of AZ91 alloy suggests that the material removal processes are dominated by localized plastic deformation and the production of long, continuous grooves on the contact surfaces, which are suggestive of self-mated sliding from adherent deposits of magnesium detached from contact surface and transferred to the counterface [149]. Hiratsuka et al. [150] examined the dry sliding of pure magnesium against alumina at room temperature and observed two different types of wear mechanism, namely oxidational wear that occurred during tests run in air, and severe plastic deformation with high wear rates that was observed in vacuum.

Chen and Alpas [151] classified the wear behaviour of AZ91 alloy into two regimes: a mild wear (MW) regime, in which a steady-state wear rate is observed, and a severe wear (SW) regime, which featured a continuously increasing wear rate. The results were summarized in the form of a wear map that delineated the load and speed ranges of the wear micromechanisms that controlled wear rates (**Figure 2.25**) [151]. The transition from MW to SW was controlled by a critical surface temperature (= 74 °C) criterion that was a function of applied load and test speed. It was shown that the onset of severe wear

Table 2. 4.   Summary of tribological properties of magnesium alloys.

Material	Type of test	T, °C	Experimental conditions	Counter-face	Lubricant	Coefficient of friction (conditions)	Wear rate	Comments	Ref.
AZ31	Reciprocating tribo tester	RT-450	10 - 100 N (load)	P20 steel block	With and without Boron Nitride (BN)	0.4 (Without BN, 450 °C)	Not measured	Determined onset of adhesion	[15]
Pure magnesium	Pin-on-disc	RT	9.8 N(Load), 0.16 m/s (sliding velocity)	Alumina disc	dry	0.6 (in air), 0.25 (in vacuum)	Specific wear: 90×10^{-9} mm²/N (in air), 13×10^{-9} mm²/N (in vacuum)	Two types of wear mechanism: oxidational wear in air, metallic wear in vacuum	[150]
AZ91	Block-on-ring	RT	1-350 N(load), 0.1-2.0 m/s (sliding velocity)	AISI 52100 bearing steel flat	dry	-	6×10^{-3} mm³/m (at 1 m/s, 20N, mild wear), 45×10^{-3} mm³/m (at 1 m/s, 133 N, severe wear)	The contact surface temperature was found to be a function of load and velocity. The transition from MW to SW was controlled by a critical surface temperature criteria (>74 °C), rather than a load or sliding speed criterion	[151]

Continued...

Material	Type of test	T, °C	Experimental conditions	Counter-face	Lubricant	Coefficient of friction (conditions)	Wear rate	Comments	Ref.
AZ91	Pin-on-disc	RT	10 - 100 N (load), 0.25 - 1 m/s (sliding speed)	M35 hardened tool steel disc of 160 mm dia.	dry	0.015 (10 N, 0.25 m/s), 0.57 max. (100 N, 1 m/s	2.6×10^{-5} g/m max. (100 N, 1m/s)	Abrasion, delamination and gross plastic deformation were identified as prevailing wear mechanisms. Abrasive wear activated at lower loads and sliding speeds	[152]
Pure Mg and AZ31	Pin-on-disc	RT	12 - 36 N (load), 0.5 - 1.5 m/s (sliding speed)	AISI 52100 steel disc	dry	-	4.5×10^{-5} g/m max. (Pure Mg, 36 N, 0.5 m/s)	The authors have improved the wear property of Pure Mg and AZ31 by introducing 2 wt.% Al_2O_3. Abrasion, oxidation and delamination were observed during dry sliding wear of pure Mg and AZ31	[153]

MW – Mild wear; SW – Severe wear.

coincides with this critical surface temperature. Two material removal mechanisms operated in the SW regime, the first being extensive surface damage that resulted from the plastic deformation of material layers adjacent to contact surface. With further increase in load and speed, sliding-induced surface melting became significant. Under the processing conditions of QPF ($T > 400$ °C and strain rates $> 1 \times 10^{-3}$ s^{-1}) it is likely that the surface contact promotes SW conditions.

Hanna [15] has seen that the affinity between magnesium and steel is very low compared to that between aluminum and steel. However, the characteristics of the interaction are different under lubricated condition. The COF of AA5083 was greatly reduced compared to AZ31 alloy after applying BN (Boron nitride) lubricant on the respective surfaces, as in **Figure 2.22**. According to the author, the low strength of AZ31 alloy (20 – 25 % lower than that of AA5083 above 350 °C) resulted in a higher COF than that of AA5083.

The conventional experiments for studying friction in metal forming processes include the unidirectional ball-on-disk test [14], reciprocating flat-on-flat tests [15], drawbead tests [13], forward extrusion process [154], load-scanning test [155], and so on. Schematic representations of ball-on-disk (**Figure 2.26a**), flat-on-flat (**Figure 2.26b**), and drawbead test (**Figure 2.26b**) show the contact area where the COF was measured during the test. However, inability to simulate the contact surface similar to hot-forming condition, where material is stretched along with sliding, made the reported experiments not completely representative to the forming process.

2.7. Summary of Literature Review

The conclusions and helpful suggestions rising from the literature survey on high temperature deformation and tribological behaviour of aluminum and magnesium alloy literature survey are as follows:

1. AA5083 and AZ31 alloys are two superplastic materials widely used to produce structural components using hot forming operation, which is a high temperature shaping process that operates at temperatures above the recrystallization temperature of the material.

2. It was found the during high temperature deformation especially under the conditions close to hot-forming process two deformation mechanisms were found in aluminum alloy – GBS and SD creep mechanism. In AZ31 alloy, along with GBS and SD creep DRX played an additional role during high temperature deformation.

3. Various studies had investigated the effect of temperature on tribological behaviour of aluminum alloy. COF was found to increase with the increase in temperature for both aluminum and magnesium alloys. Increase in COF was attributed to the increased plowing friction caused by the severe plastic deformation at elevated temperature. Also, it was shown that it was the contact surface temperature that determined the transition from mild wear to severe wear.

In the literature there are several studies on the elevated temperature tribological behaviour of aluminum and magnesium alloys and also on elevated temperature

deformation behaviour of these alloys. However, the relation between the tribological behaviour and deformation mechanisms has yet to be established. Also until now, there is no work in the open literature on the effect of strain rate on the tribological behaviour of these alloys. Strain rate is another factor to be considered while investigating the tribological behaviour of the hot-forming operation. To understand the complexity involved in the tribological contact interface generated during hot-forming operation, it is important to investigate the effect of temperature and strain rate on COF. It is also important to establish a relation to the deformation mechanisms operating in the applied strain rate and temperature range.
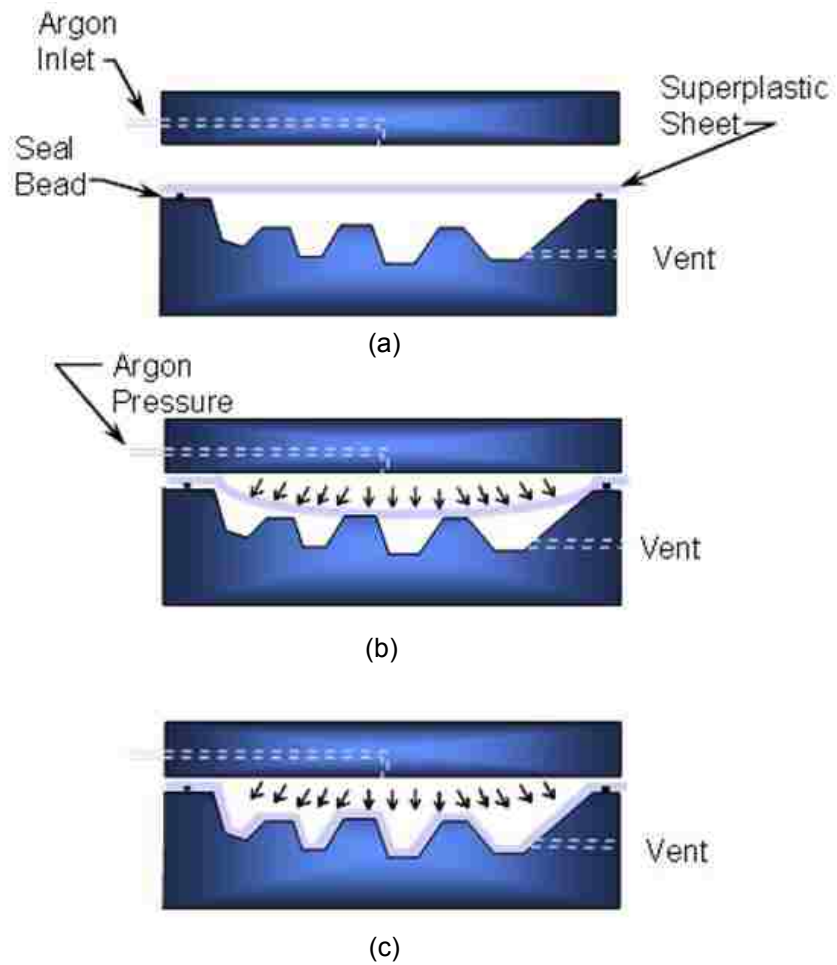
Figure 2. 1. Schematic representation of the hot-forming process – (a) sheet of metal is sealed around its periphery between an upper and lower die. The dies and sheet are maintained at the SPF temperature. (b) the sheet is heated to its superplastic temperature range, gas pressure is injected through inlets in the upper die (c) the lower cavity is maintained under vacuum or can be vented to the atmosphere and at the same time gas pressure is used to form the sheet down over the tool.

(a)

(b)

Figure 2. 2. (a) Lift gate and door outer panel from AA 5083 (Al - 5% Mg - 1% Mn) sheet and (b) Door inner panel from AZ31 (Mg- 3% Al- 1% Zn) sheet [8].

Before deformation　　　　　　**After deformation**

(a)

Before deformation　　　　　　**After deformation**
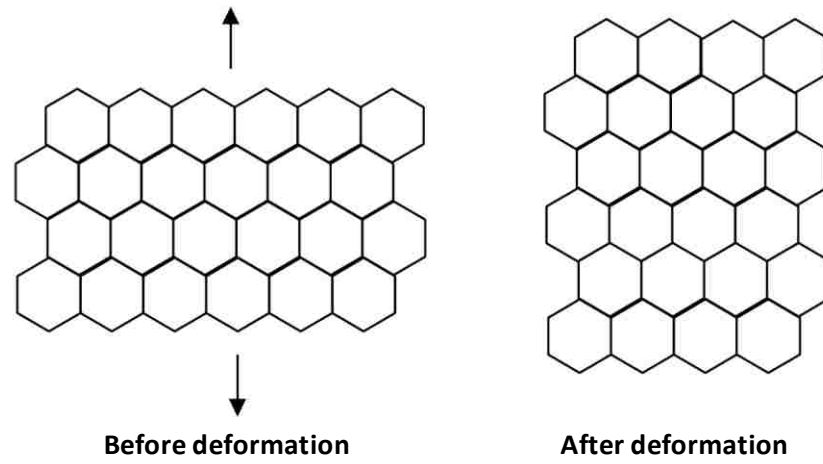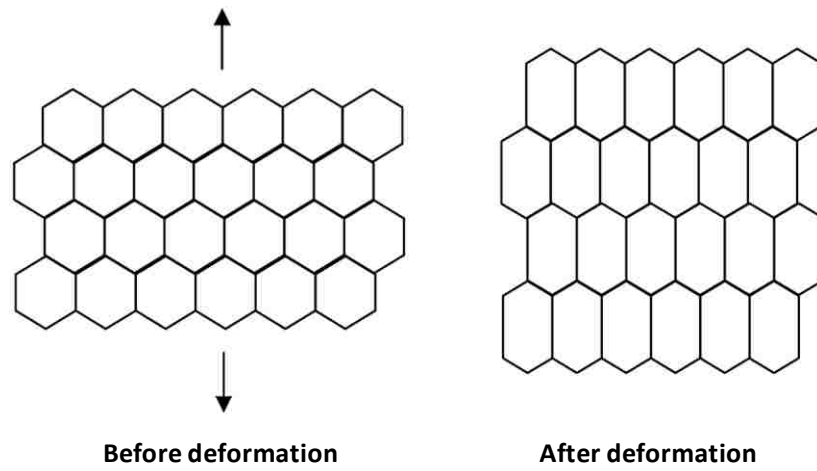
(b)

Figure 2. 3. Schematic illustration of grain rearrangement during (a) Rachinger sliding [51] and (b) Lifshitz sliding [53].
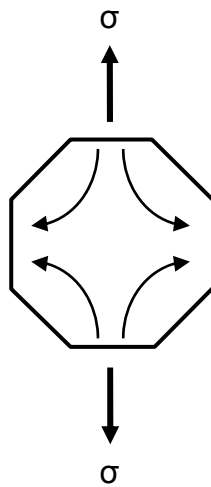
Figure 2. 4. Nabarro-Herring model of diffusional flow [54]. Arrows indicate the flow of vacancies through the grains from boundaries lying normal to the tensile direction to parallel boundaries. Thicker arrows indicate the tensile axis.
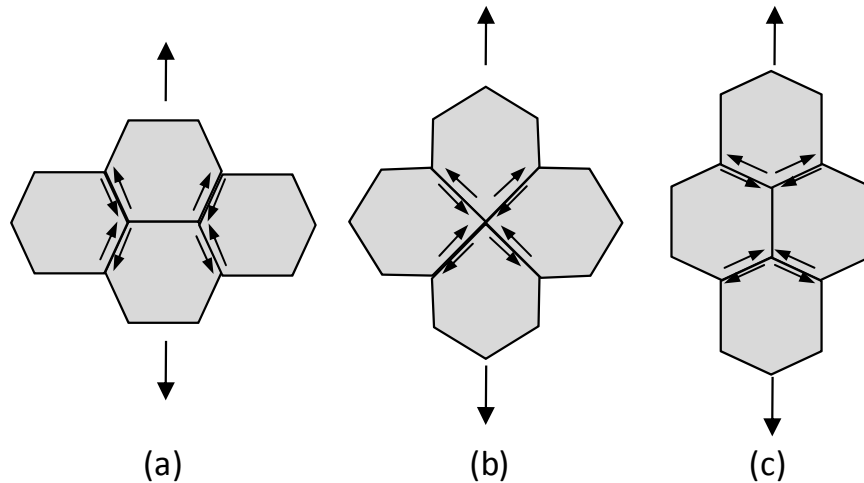
Figure 2. 5. The principle of the model of Ashby and Verrall [58] for grain rearrangement by diffusion: (a) $\varepsilon = 0$; (b) $\varepsilon = 0.275$; (c) $\varepsilon = 0.55$. In this model, grains change their original shape by diffusional flow occurring by mass transfer through grain boundaries. Also, the inter grain distance perpendicular to the tensile direction contracts and engaging the grains in lateral direction where as in the other direction (along the tensile direction) the grains move apart.
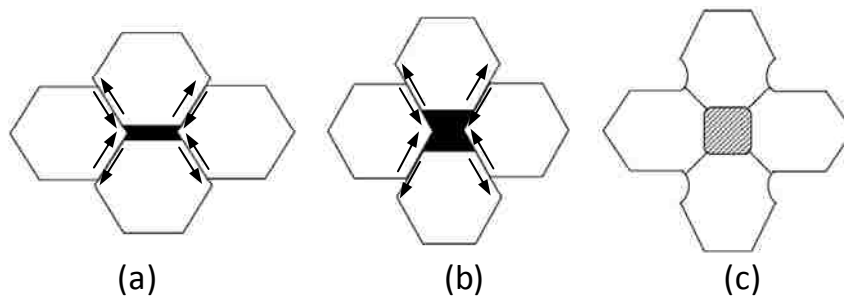
Figure 2. 6. The stages of Gifkins model for grain rearrangement in superplasticity [61] – (a) sliding of grains by diffusion along the grain boundary, (b) formation of a shallow gap due to the sliding of grains and (c) as the gap increases, the emerging grain fills the gap.
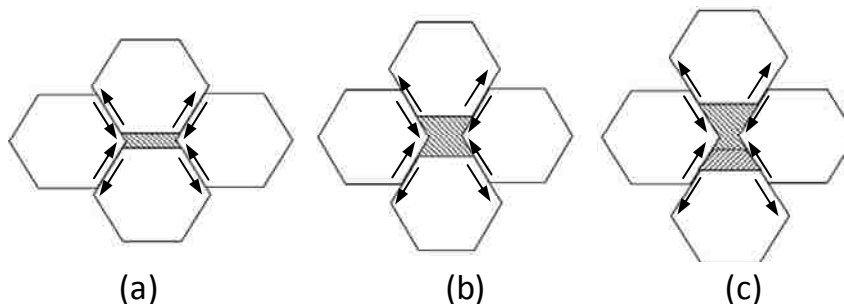
Figure 2. 7. Schematic illustration of Langdon's model [63] for grain rearrangement in thress steps (a), (b) and (c) during superplastic deformation. The grain rearrangement takes place by the exposure of grain boundary facet at the sliding boundaries, which in turn can account for an increase in surface area with deformation.
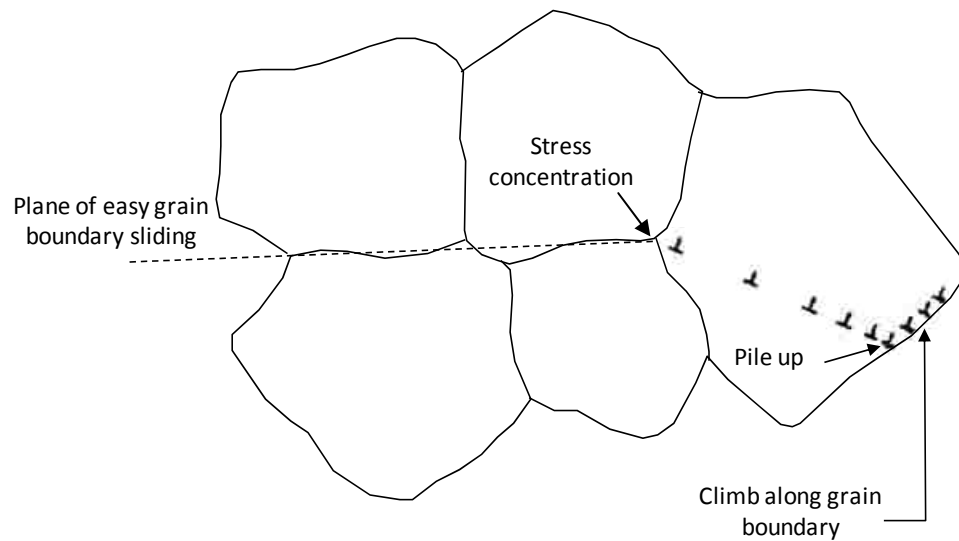
Figure 2. 8. Schematic illustration of the mechanism of superplasticity developed by Ball and Hutchison [65]. At any instant during deformation, of grains whose boundaries are suitable aligned will slide as groups. The shear stress on the group becomes concentrated on any grain or protrusion that obstructs motion of the group. The local stresses would generate dislocations in the blocking grain and dislocations would pileup at the opposite grain boundary until their back stress prevents further generation of dislocations and thus further sliding by the group.
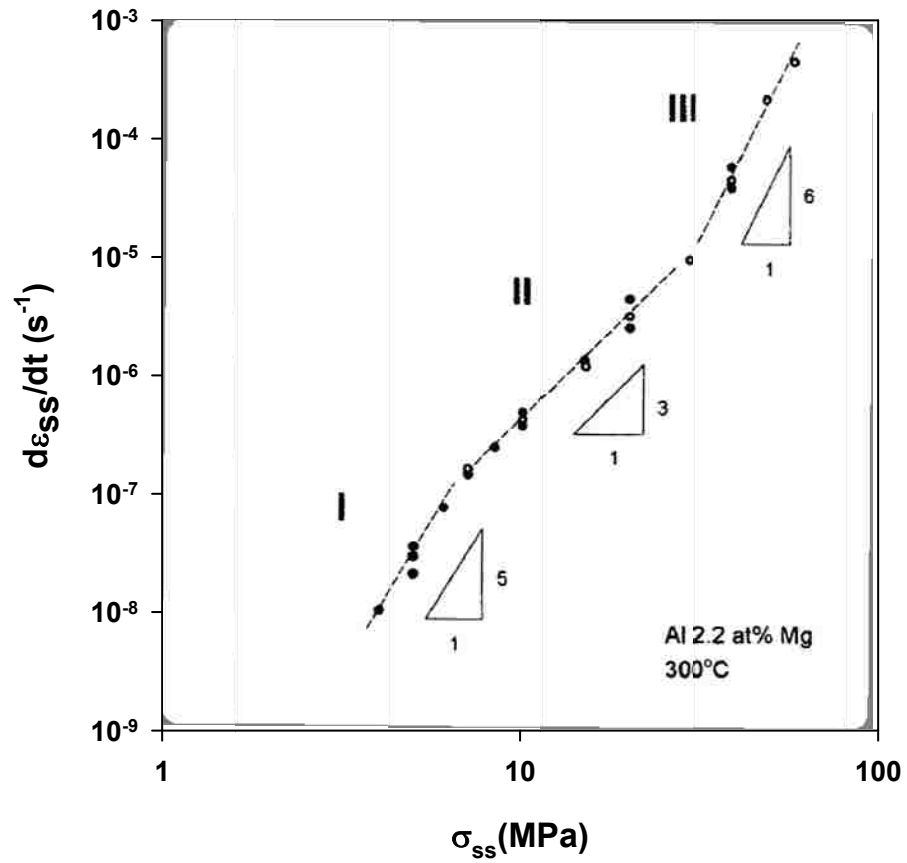
Figure 2. 9. Steady-state creep rate versus applied stress for an Al-2.2at%Mg alloy at 300 °C. Three different creep regimes, I, II, and III, are evident [70-72].
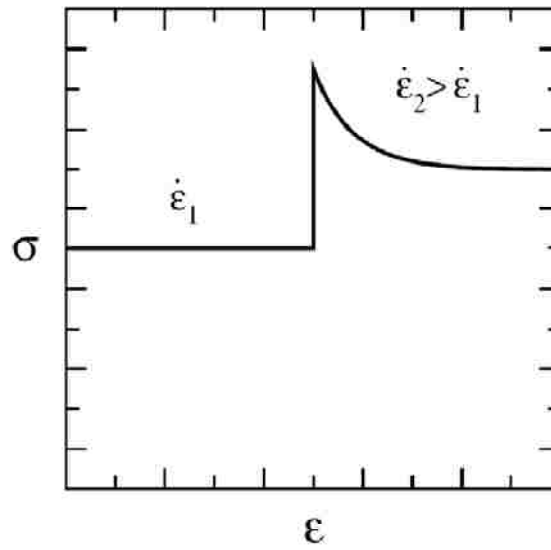
(a)
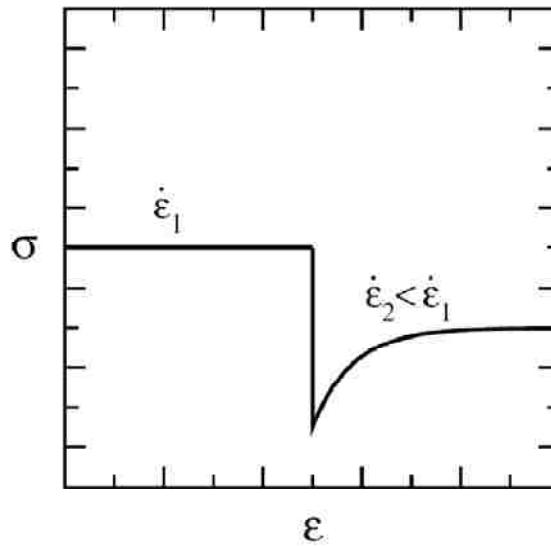
(b)

Figure 2. 10. Inverse creep transients are demonstrated for rate-controlled experiments in schematics for (a) a rate increase and (b) a rate decrease [18]. In inverse creep transient behaviour, upon an increase in strain rate the flow stress undergoes a large, abrupt increase and then gradually decreases toward a steady-state value at the new increased strain rate. With the decrease in strain rate, flow stress shows a large, abrupt decrease and then gradually increases to a steady-state value at the new reduced strain rate.
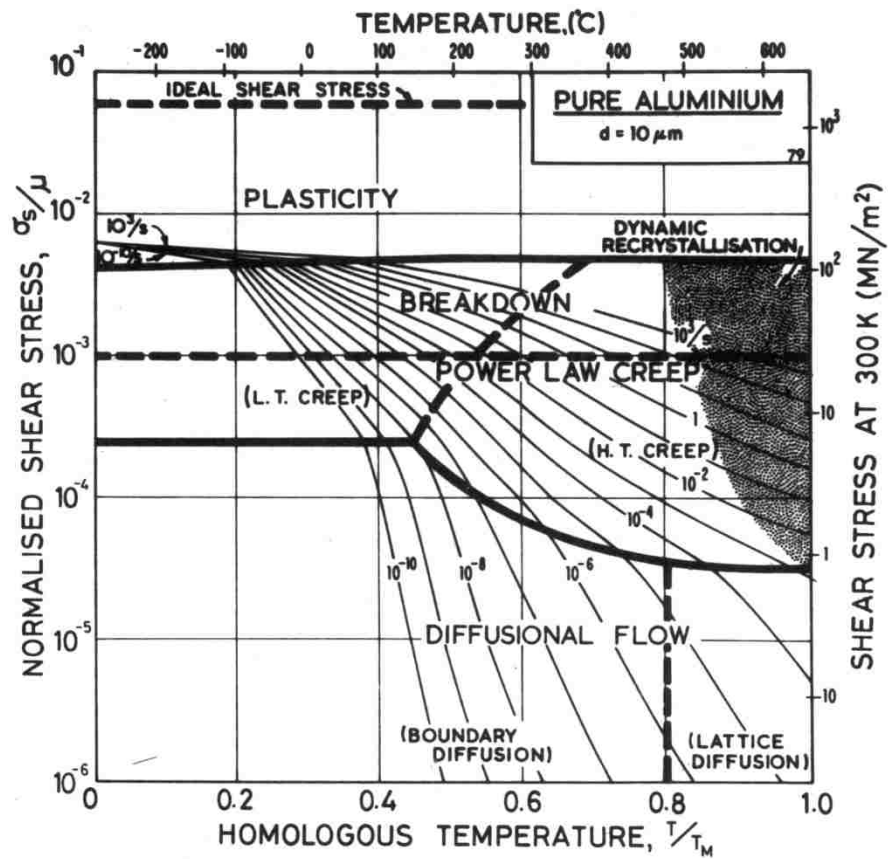
Figure 2. 11. Deformation mechanism map (DMM) for pure aluminum of grain size 10 μm, showing boundary and lattice diffusion controlled diffusional flow, dynamic recrystallization and power law creep [67].
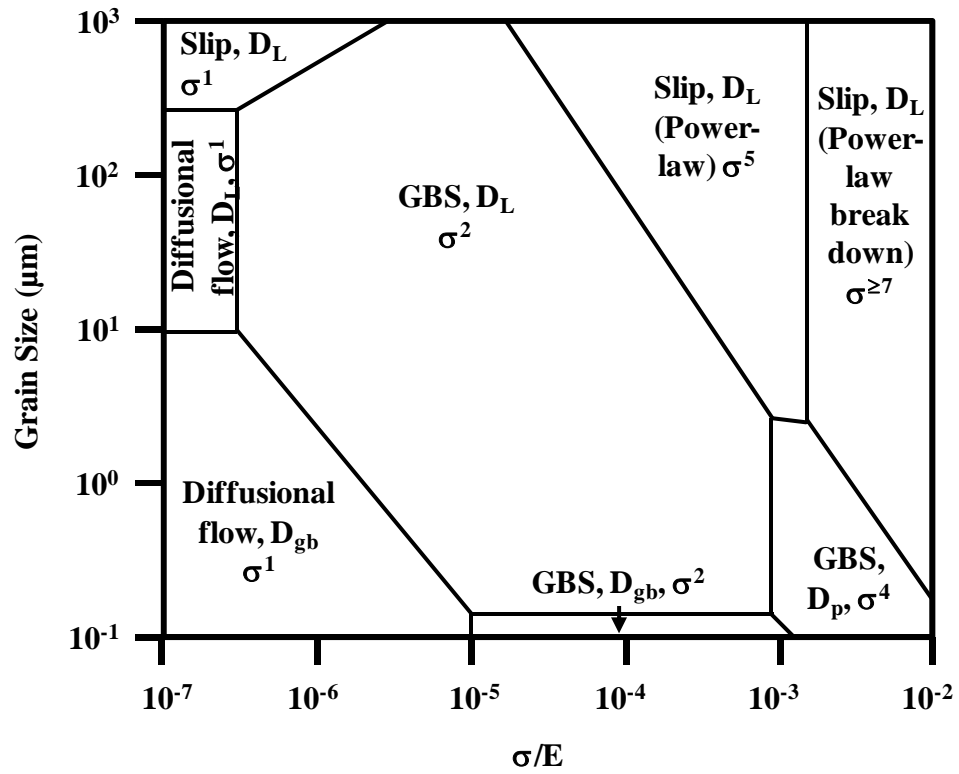
Figure 2. 12. DMM for aluminum alloy at 527 °C [80].
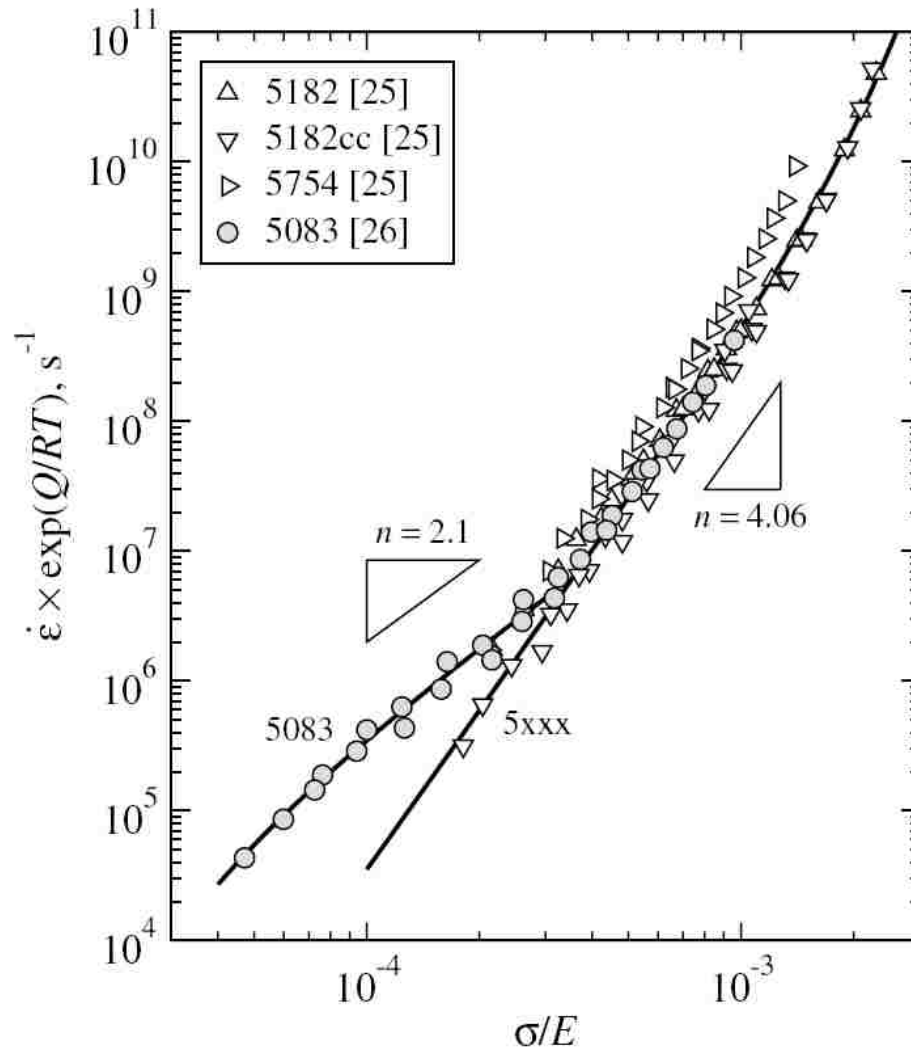
Figure 2. 13. Data for creep deformation in commercial 5000-series alloys are plotted as the logarithm of the Zener-Hollomon parameter versus the logarithm of modulus compensated stress [18]. The exponent 2 and 4 are representative of GBS and SD creep mechanism respectively.
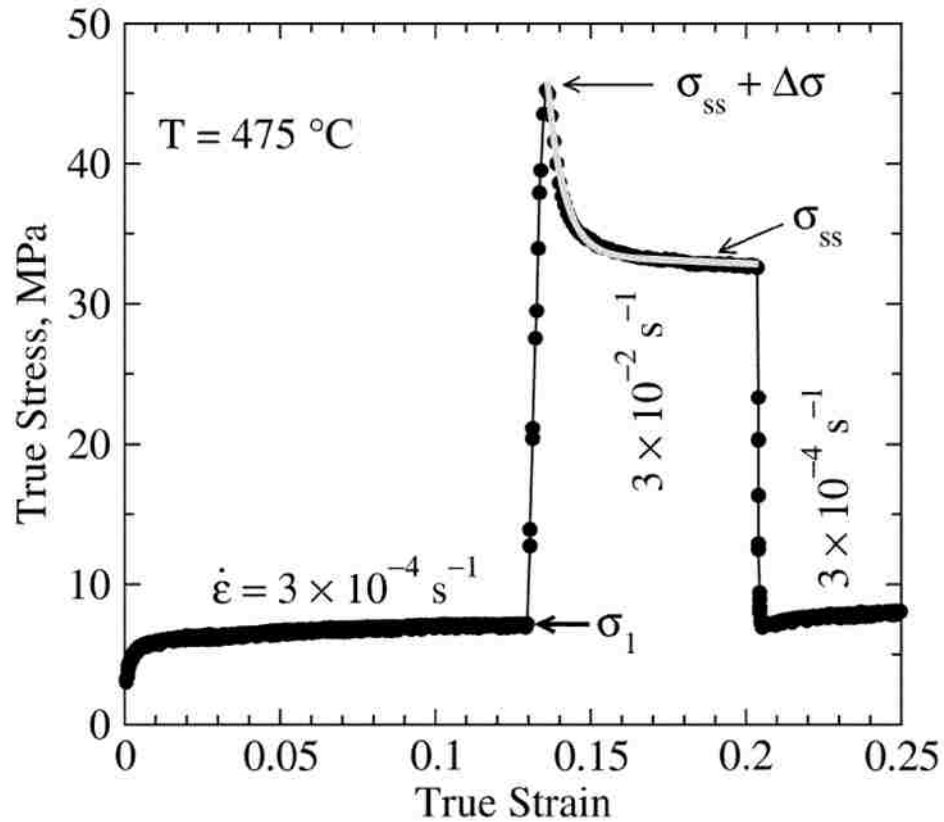
Figure 2. 14. Transients characteristic of SD creep are shown for 5083 alloy [17]. The plot shows a clear transient in step upon the rate increase to a fast rate of 3×10^{-2} s^{-1}, where SD creep governs deformation, but shows only a negligible transient upon the subsequent change to a slow rate, where GBS creep controls deformation. σ_{ss} is the stress state when SD creep governs deformation.
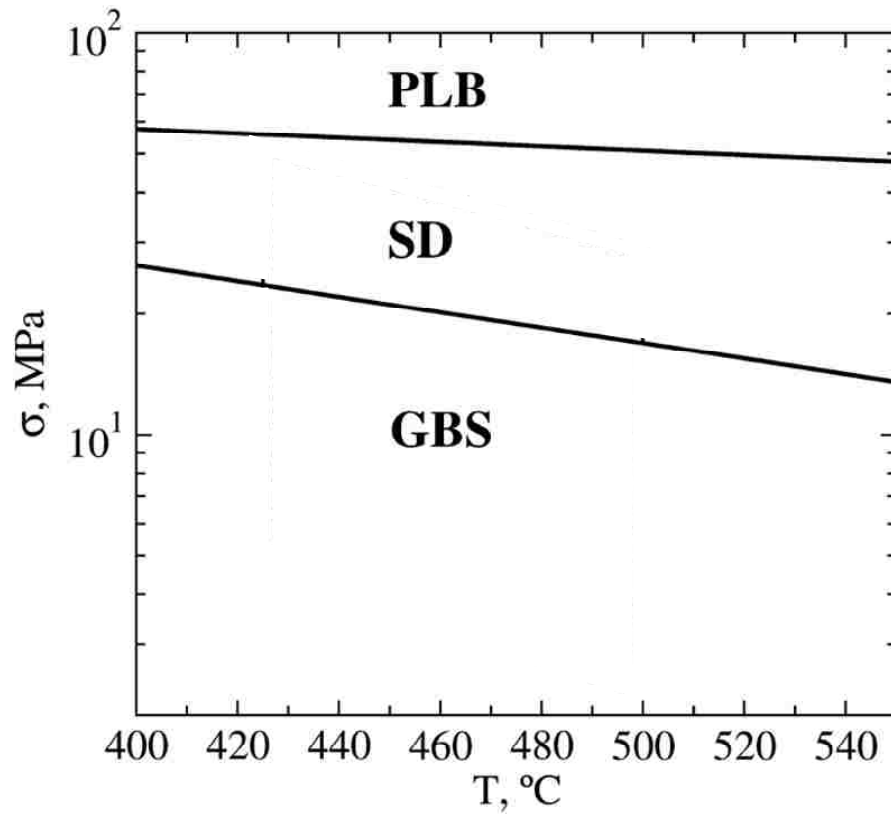
Figure 2. 15. DMM for the fine-grained direc-chill cast AA5083 material [17]. The map shows the solute drag (SD), grain boundary sliding (GBS) along with power law breakdown (PLB) region on temperature vs. stress axes.
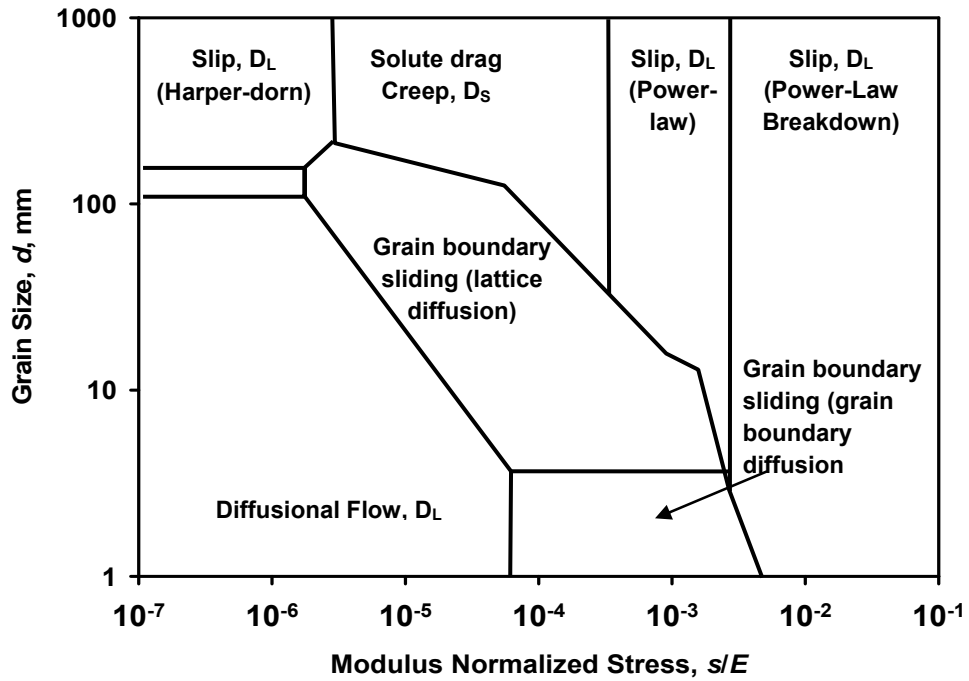
Figure 2. 16. DMM constructed for magnesium AZ31 alloy at 400 °C [91] shows the regions of different deformation mechanisms based on the alloy grain size and modulus compensated stress.
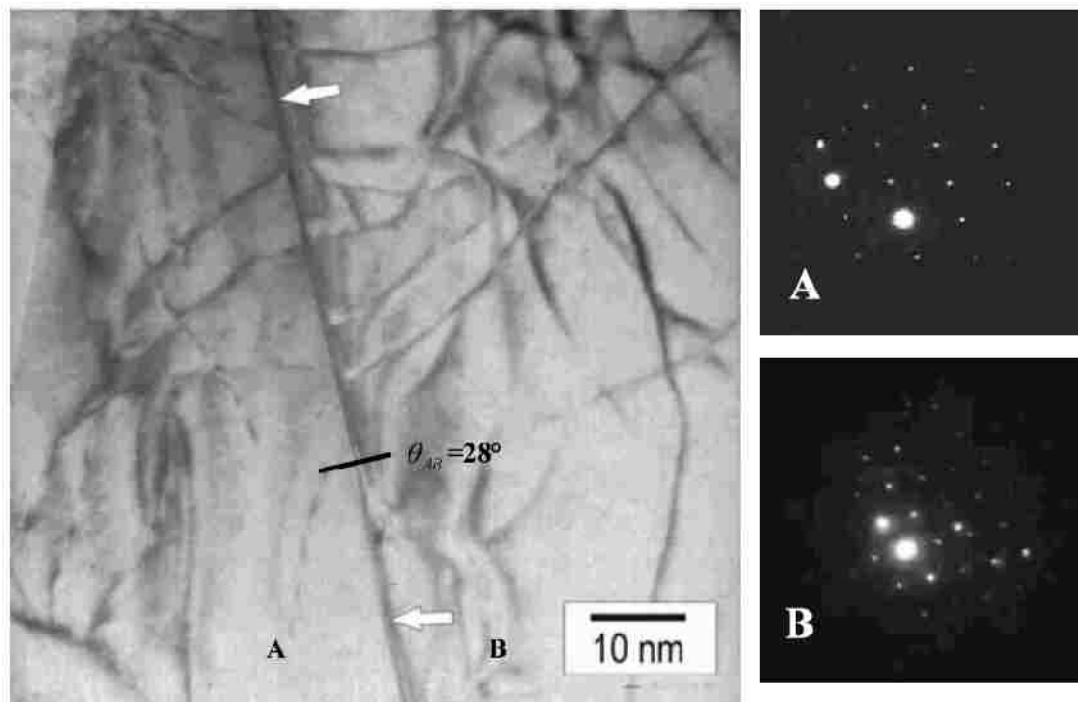
Figure 2. 17. TEM micrograph of two neighbouring subgrains A and B taken from a DRX specimen strained to 60 % at 250 °C and 1×10^{-4} s^{-1}. Misorientation angle, θ_{AB} estimated from the diffraction patterns is also shown. The white arrows indicate the location of subgrain boundary [28]. The figure infers that subgrain boundary misorientation increased during high temperature deformation and low angle grain boundaries transformed into high angle boundaries. The large increase in grain misorientation observed was attributed to dynamic continuous recrystallization.
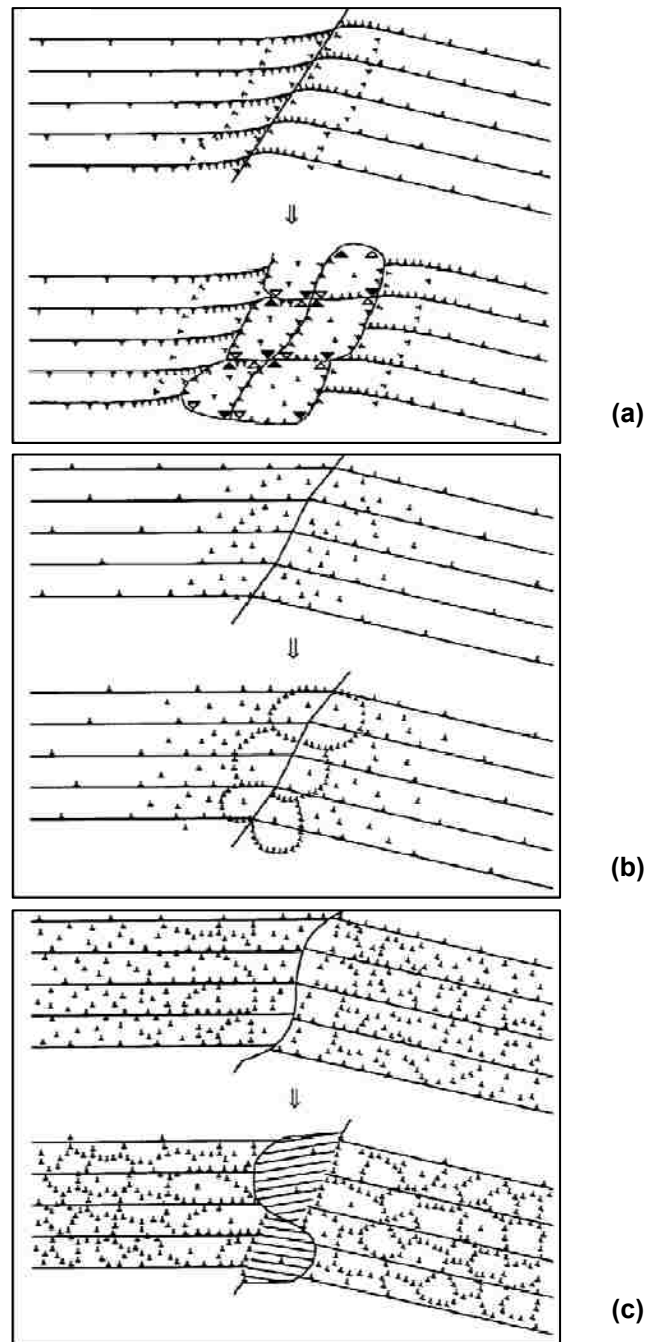
Figure 2. 18. Schematic representations of the nucleation process in DRX: (a) at $T =$ 150 °C: combined effect of basal slip and twining resulted in DRX grains, (b) at $T = 200$ – 250 °C: dislocation rearrangements by cross slip and climb generate a low angle boundary network in the vicinity of original boundary. By absorbing the dislocations continuously the low angle boundaries changed to DRX grains, and (c) at $T = 300$ – 450 °C: microscopic strain localization at the slip lines causes formation of bulges of grain boundaries which leads to nucleation of DRX grains [116].
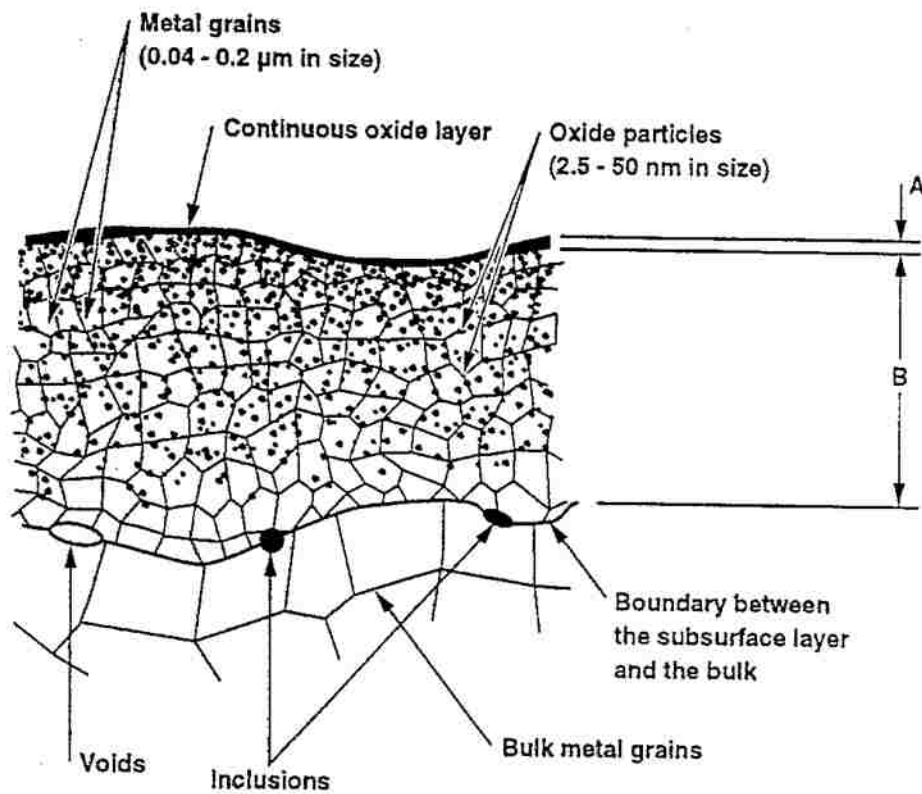
Figure 2. 19. Schematic representation of the subsurface layer containing the micriocrystalline oxides mixed with the small grained metal and covered with the continuous surface oxide: (A) thickness of the continuous surface oxide, 250 – 1600 Å; (B) thickness of the mixed subsurface layer, 1.5 – 8 μm [121].
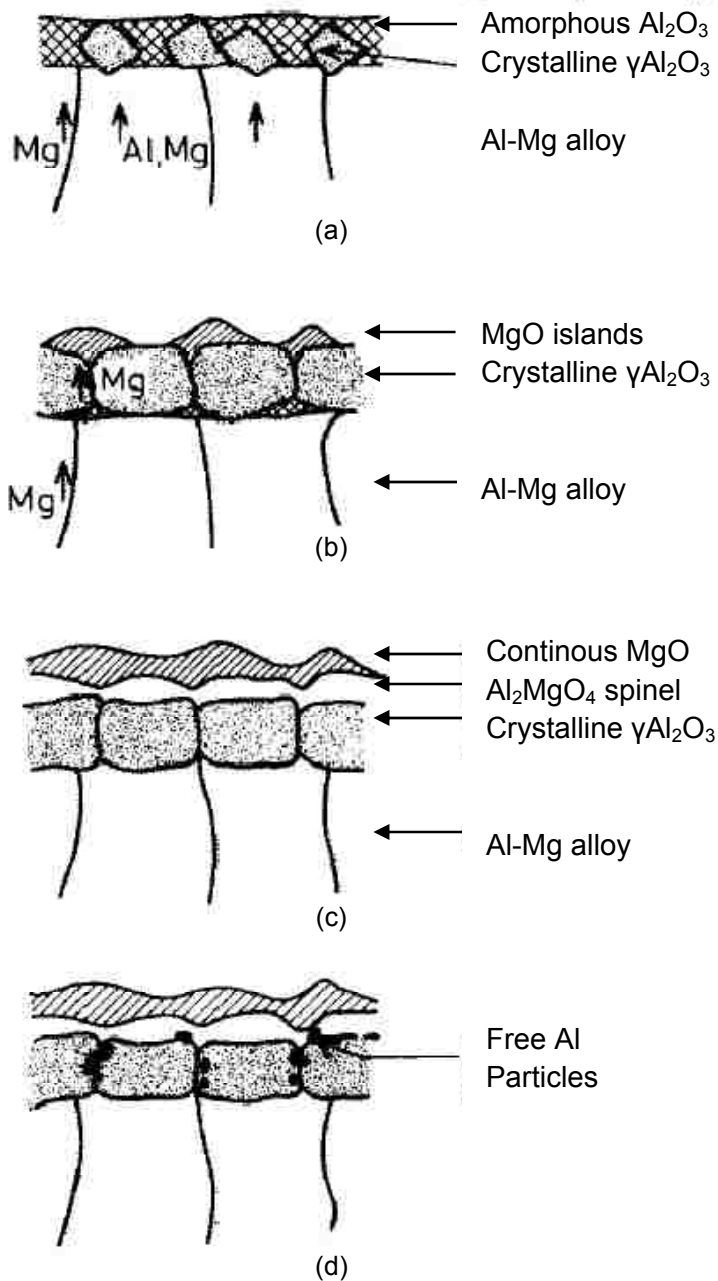
Figure 2. 20. Schematic model of the growth of the oxide film on Al-Mg alloys during heat treatment [125] – (a) oxide crystallites nucleate and the thickness increases by grain boundary diffusion of aluminum and magnesium to the free surface, (b) The difference in diffusivity of the species ensures that the surface becomes magnesium-rich and MgO islands forms on the surface, (c) Al_2O_3 in the film is reduced by the outwardly diffusing magnesium to form the spinel $MgAl_2O_4$, and (d) this leaves free aluminum within the oxide and also leaves MgO islands that join to form an aluminum-free surface.
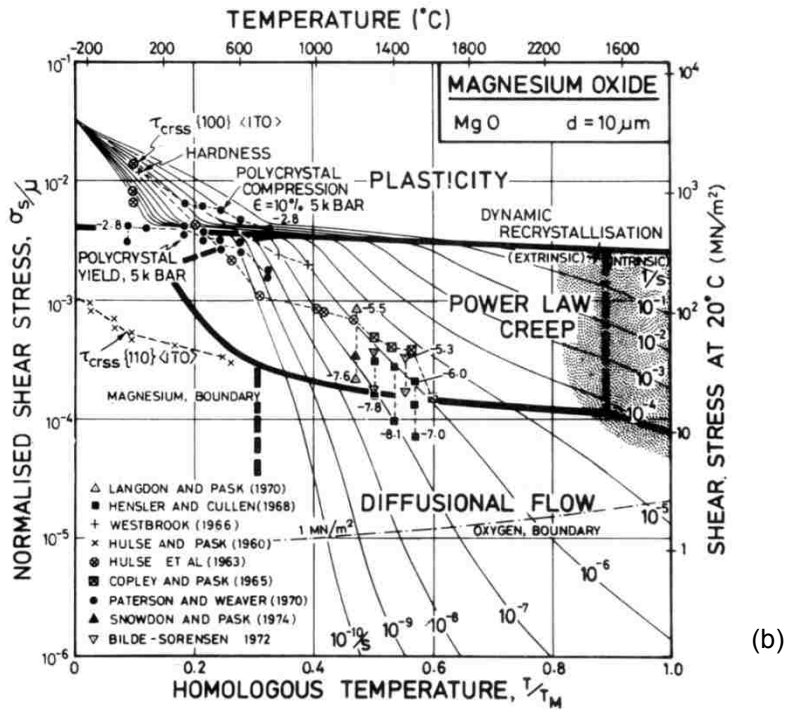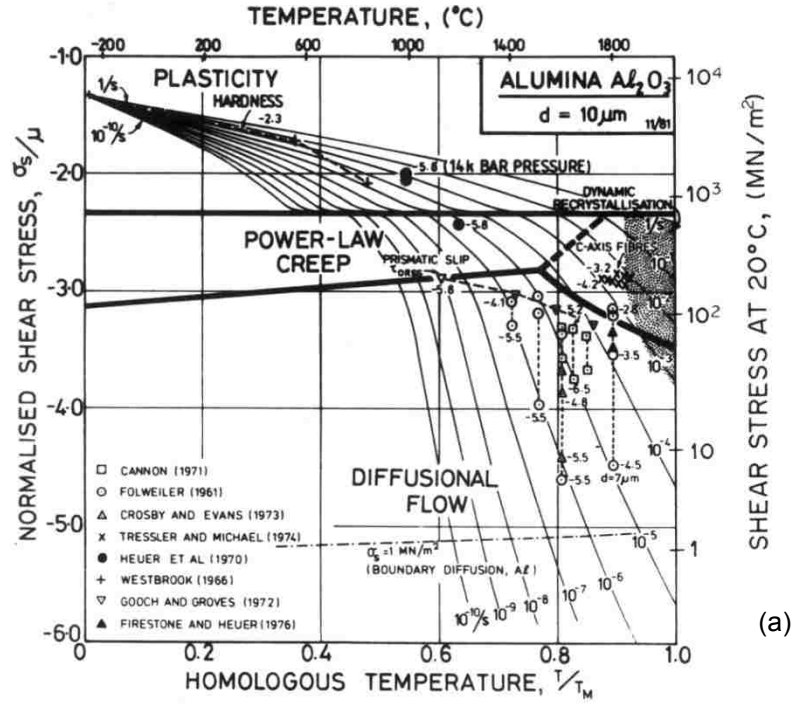
Figure 2. 21. (a) DMM for Al_2O_3 with a grain size of 10 μm. (b) DMM for MgO with a grain size of 10 μm [67].
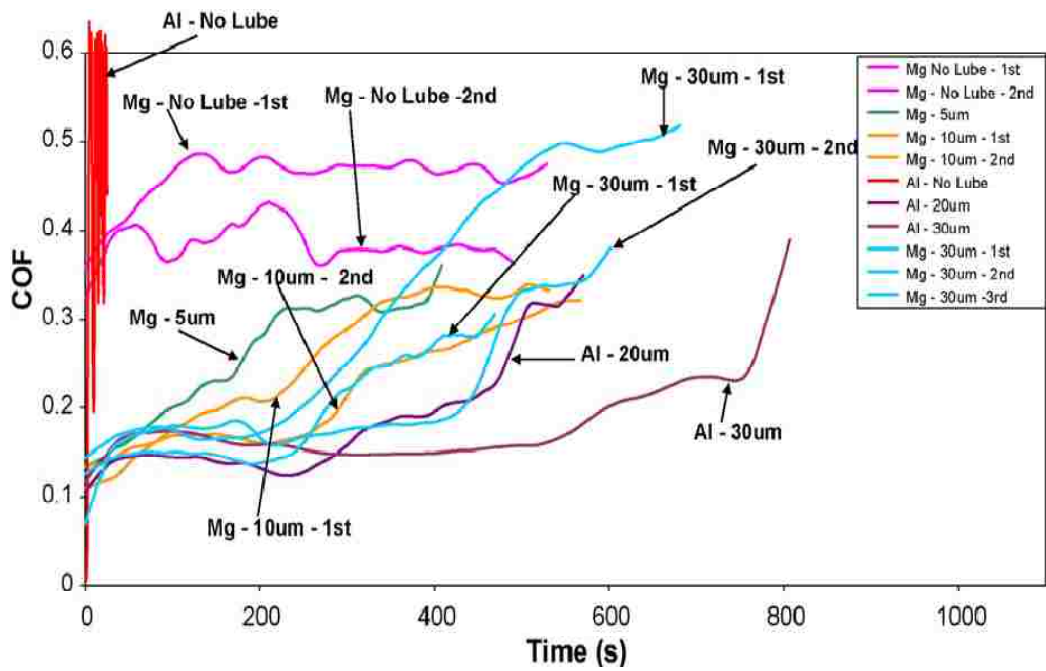
Figure 2. 22. Friction coefficient results of Al 5083 and Mg AZ31B with lubrication for sheet at 450 °C, 50 N load and 0.11 Hz sliding speed with different BN lube thickness [15].
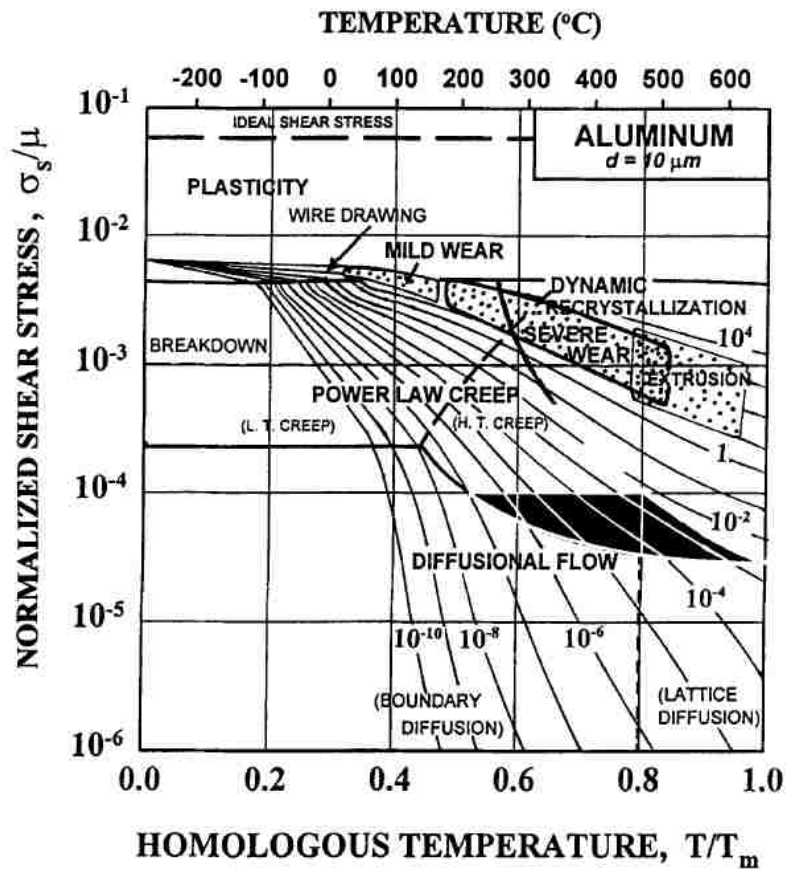
Figure 2. 23. The DMM for aluminum [67]. The regimes of mild and severe wear are shown and compared with the regimes of metal forming processes. The dynamic recrystallizatwn region confined to $T > 0.8T_m$ in the original map is extended to lower temperatures to incorporate observations made on the 6061 Al [143].
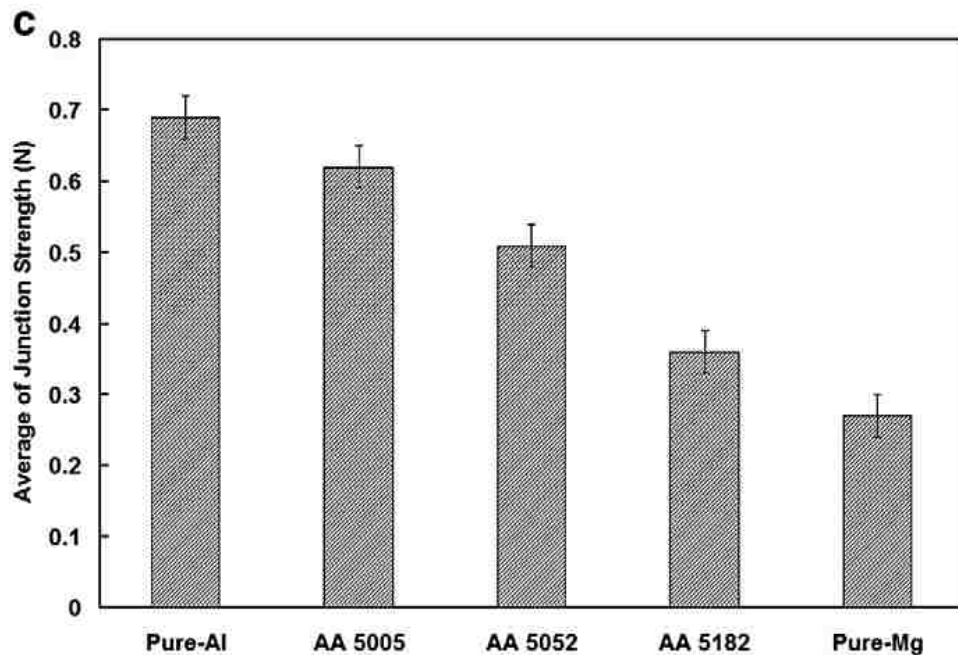
Figure 2. 24. The average value of junction strength for each alloy (maximum tangential stress reached before the failure of adhesive junction) [130].
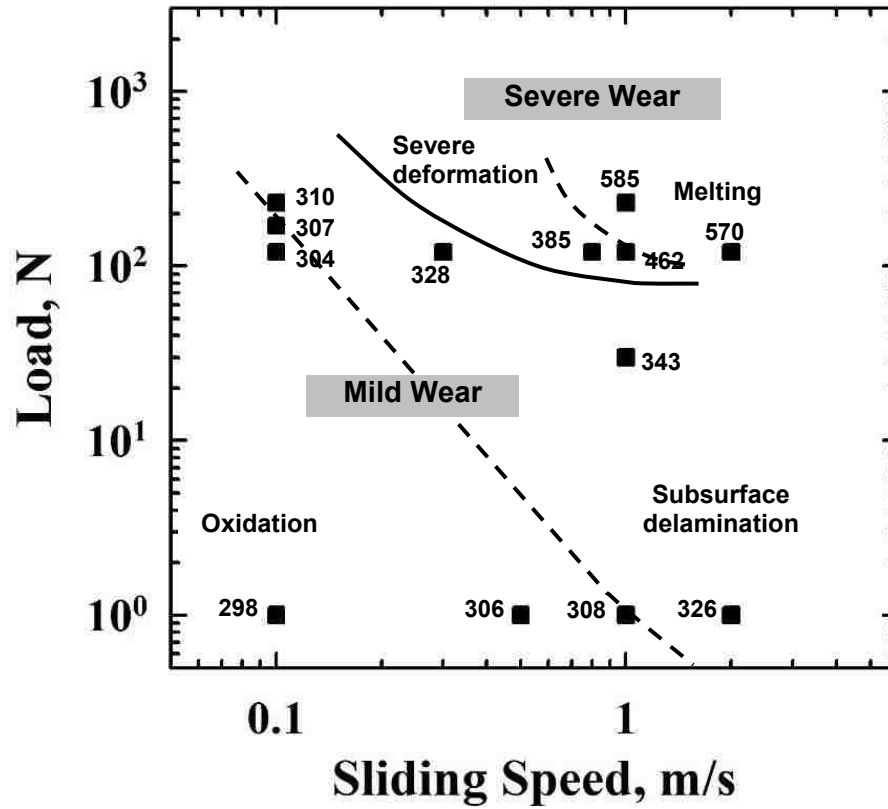
Figure 2. 25. Wear map for magnesium AZ91 alloy [151] showing mild and severe wear regimes and the principal wear mechanisms controlling the wear rates in each regime. Data points indicate measured contact surface temperatures (in K).

Load

Disc

Friction measured at
the contact between
ball and disc

(a)

Flat

Flat

Friction measured at
the contact between
cylinder and flat

(b)

F_2

F_1

Roller

Friction considers the interfacial
(c) behaviour of both side of the strip
and calculated using the drawing
force F_1 and clamping force F_2
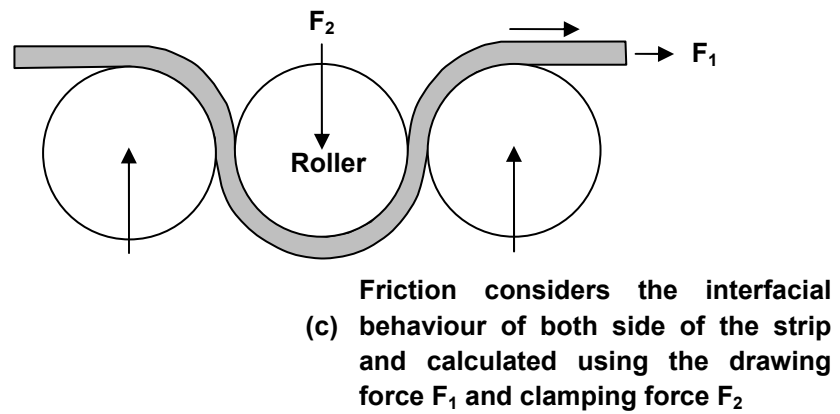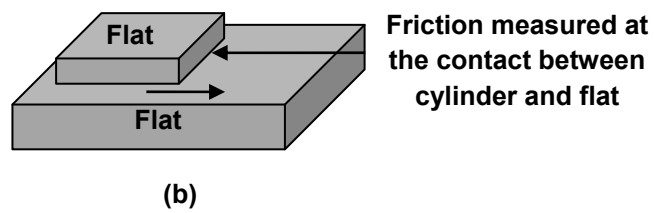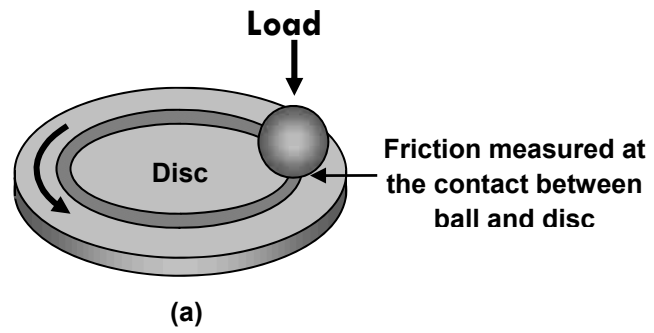
Figure 2. 26. Schematic representation of conventional experiments for studying friction
in metal forming process (a) ball-on-disk, (b) flat-on-flat and (c) drawbead test.

Chapter 3 Materials and Experimental Procedures

3.1. Introduction

In this chapter, the materials tested and the methodology employed in the analyses are described. Experiments were intended to simulate conditions very close to hot-forming process. Similar strain rates and temperatures of hot-forming were used simultaneously while the material was in sliding contact. The mechanisms of plastic deformation and surface damage in relation with COF were systematically investigated.

Section 3.2 presents microstructures and compositions of AA5083 and AZ31 alloys used in the present experiments. **Section 3.3** describes the development of hot-forming simulator, which consists of three main parts – a loading system, a friction measurement assembly and an observation system. The same section also provides a detailed description of measurement of COF and mechanical properties of the bulk AA5083 alloy under simulated hot-forming conditions.

In **Section 3.4**, the sliding induced damage was investigated on the material without any externally applied tensile load by using a pin-on-disk tribometer. **Section 3.5** describes the measurement of junction strength (force required to break the initial adhesive contact) of for Al-Mg alloys.

Section 3.6 describes the procedures and the analytical methods employed in the characterization of the worn surfaces and subsurface microstructures used for characterizing the surface and sub-surface deformation.

3.2. Materials and microstructures

3.2.1. Microstructure and properties of the AA5083 alloy

Strips of 5.0 mm wide and 1.5 m long were sectioned from 1.2 mm thick cold-rolled AA5083 alloy (Al-4.5wt.%Mg-0.7wt.%Mn) sheet obtained in the H18 condition (75 % cold reduction of fully annealed starting material). The AA5083 alloy composition is shown in **Table 3.1**. The microstructure of the as-received alloy is shown in an SEM cross-section micrograph in **Figure 3.1a**. The elongated grains of the alloy were 1.3 ± 0.4 µm long in the rolling direction and 0.3 ± 0.1 µm wide. The section of the strip shown in **Figure 3.1a** provides evidence of the presence of Al_6Mn precipitates.

Table 3. 1. Composition of the AA5083 alloy.

Elements	Mg	Mn	Si	Fe	Cr	Cu	Al
Weight %	4.5	0.7	0.1	0.25	0.09	0.02	The balance

AA5083 strips were tested using a high temperature tribometer, which is capable of applying tensile strains at known strain rates and temperatures (see **Section 3.3.1**). A typical cross-sectional microstructure of the AA5083 strip that was tested at a temperature of 420 °C and a strain rate of 4×10^{-2} s^{-1} using this tribometer (without placing the strip into sliding contact) is shown in **Figure 3.1b**, and illustrates the equiaxed grain structure of the material at this temperature. The average grain size in the near surface section was approximately 3.6 ± 2.1 µm. **Figure 3.1c** shows the microstructure of a strip tested at 545 °C and a strain rate of 4×10^{-2} s^{-1}, where equiaxed grains with a diameter of 4.8 ± 2.5 µm near the free surface of the sheet can be seen.

Once the equiaxed grain size was attained, the grain morphology and size did not change significantly with strain rate and temperature (**Figures 3.1b and c**). The volume fraction of Al_6Mn particles was $1.6 - 2.0$ %. The Al_6Mn particles, 0.35 ± 0.15 μm long and 0.13 ± 0.03 μm wide, retained their shape and did not fracture during elevated temperature tests. Evidence of grain boundary sliding (GBS) that produced a step on the surface of the sample tested at 545 °C was also observed in **Figure 3.1c**. The deformation mechanisms responsible for generating these microstructures are described in detail later in **Chapter 4.**

The surface of the as-received alloy was covered with an oxide layer, thickness of which varied between a few hundred nanometers and one micron as shown in **Figure 3.2a**. **Figure 3.2a** also reveals that the surface oxide consisted of nanocrystalline grains $10 - 100$ nm in size. TEM analyses using a Gatan image filter (GIF) performed at equal depth intervals through the oxide layer was used to obtain elemental concentration distribution of the layer's constituents. The magnesium concentration profile in **Figure 3.2b** indicates that its concentration near the sheet surface was approximately three times higher compared with that of the bulk. According to the selected area diffraction patterns (SADP) taken from material adjacent to the surface $MgAl_2O_4$, MgO and Al_2O_3 were identified as the main constituents of the oxide layers adjacent to the surfaces of the as-received sample (**Figure 3.2c**).

3.2.2. Microstructure and properties of the AZ31 alloy

The material tested was Mg–3wt.%Al–0.7wt.%Zn wrought alloy designated as AZ31. **Table 3.2** shows the quantity of other alloying elements present in AZ31 alloy. The hardness of the samples tested was measured as 73.6 ± 2.2 HV on the Vickers scale

using a load of 1.0 N. The room temperature microstructure of the AZ31 sheet along the rolling and the transverse directions is shown **in Figure 3.3a.** The average grain size was 13.9 ± 2.2 μm. These measurements were made on the surface parallel to the rolling direction (the contact surface during the wear tests), using a linear intercept method [156]. Al_8Mn_5 intermetallic particles appeared as light grey constituents with a particle size of 5.3 ± 1.3 μm, but no $Al_{12}Mg_{17}$ phase was observed.

Table 3. 2.   Composition of the AZ31 alloy.

Elements	Al	Zn	Mn	Fe	Ca	Cu	Mg
Weight %	3.0	0.7	0.38	0.03	0.03	0.04	The balance

A typical cross-sectional microstructure (near surface) of the AZ31 alloy strip that was tested at a temperature of 350 °C and a strain rate of 4×10^{-2} s^{-1} is shown in **Figure 3.3b**, which illustrates the equiaxed grain structure of the material at this temperature. The average grain size at this deformation condition was approximately 5.7 ± 1.1 μm. **Figure 3.3c** shows the microstructure of a strip tested at 450 °C and a strain rate of 4×10^{-2} s^{-1} where the grain size was measured to be 18.5 ± 2.5 μm. From the micrographs in **Figures 3.3b and c**, it can be observed that the grain size in AZ31 alloy is clearly a function of temperature. The deformation mechanisms in conjunction with this variation in microstructure are described in detail later in **Chapter 5**.

3.2.3. Counterface material

AA5083 and AZ31 alloy materials were tested against cylindrical surface of a 12.0 mm diameter pin made of P20 tool steel. The hardness of P20 tool steel is

318 ± 4.1 HV and the composition is given in **Table 3.3**. The P20 steel pin surface was polished with 3.0 μm diamond paste and cleaned ultrasonically in acetone.

Table 3. 3.   Composition of the P20 steel (sliding pins).

Element	C	Cr	Mn	Ni	Si	Mo	S	Fe
Weight %	0.35	1.90	0.83	0.40	0.70	0.49	≤0.01	The balance

3.3. Measurement of COF using hot-forming simulator

3.3.1. Description of the hot-forming simulator

There is no single and widely accepted experimental procedure to measure friction during conventional sheet metal forming processes [10,13,16]. This is even more apparent in elevated temperature forming processes, where industry experience is limited. Many of the existent tests do not capture the deformation state, where the material is stretched and subjected to sliding at the same time. Thus, a test that allows for the accurate measurement of friction during high temperature plastic deformation is needed.

The critical capabilities of the equipment needed to simulate forming processes, like QPF, include the ability to test at temperatures between 400 °C and 500 °C, and strain rates between 10^{-3} s^{-1} and 10^{-1} s^{-1}. Equally important is the ability to continually stretch the aluminum sheet while it is sliding against the die surface – a state that produces a dynamic interface in which the surface morphology is constantly modified as a result of the operating plastic deformation mechanisms. In addition to that, as discussed previously, surface oxides are continually broken and reformed, or in cases where they remain ductile, they may show a large deformation, or even superplasticity. All these

complex bulk and surface events have an effect on the COF. Hence, the equipment should be capable of measuring COF of the material while being deformed.

In order to address these issues, a new high temperature tribometer has been built at University of Windsor in collaboration with General Motors R&D and with the help of Technical Support Centre at the university. The device has been described in the previous paper [157]. The tribometer with pin-on-strip configuration is capable of simulating the sliding contact during forming operations (**Figure 3.4a**). This tribometer was used to measure the COF during contact between the pin surface representing the tool material, and a metallic strip stretching at different strain rates and temperatures. The tribometer consists of three main assembly parts (**Figure 3.4b**), which are described as follows:

I. A loading system that consists of two linear actuators, each connected to one end of the strip to be tested: The actuators are synchronized in such a way that they apply tensile stress along the longitudinal axis of the strip at the required deformation (strain) rate, while the strip moves in a forward direction at a predetermined speed. This is achieved by the use of a synchronized slave actuator that can be assigned to pull the strip at a higher speed than the master actuator. In this way, while the strip moves forward and each point on the top surface of the strip comes in contact with the pin; the material in contact is subjected to plastic deformation. Thus a constant strain rate of various magnitudes can be applied to the strip by adjusting the difference in linear velocities of the actuators. Tensile load during each experiment was measured using a 1000.0 N maximum capacity load cell (Omega LCMCD-100) with a sensitivity of ± 0.1 N attached between the strip holder and the actuator. **Figure 3.4a** shows the location of the load cell to measure the tensile

load on the strip.

II. A friction measurement assembly to measure the COF of the strip being stretched against a loaded steel pin in contact with the strip **(Figure 3.4c)**: The ability to heat the strip in contact with the pin to a constant temperature is noteworthy. The strip was heated while passing through the stainless steel roller heated using a 500 W cartridge heater inserted inside the roller. The hot roller, which had an outer diameter of 20 mm, was in contact with the bottom face of the strip in motion while the P20 steel pin was in contact with the top surface. The pin contact configuration was selected in such a way that a uniform line contact was maintained while the strip was subjected to tensile deformation. Three thermocouples were inserted in the holes circumferentially inside the roller 120° from each other and situated 0.5 mm below the outer surface of the cylinder's middle length to evenly control the temperature of the roller. The strip temperature during experiments was determined from the average temperature reading simultaneously obtained from these three thermocouples. The temperature of the upper surface of the strip was 3 – 5 °C lower than the average thermocouple reading. The heating time of the AA5083 strip before reaching a constant temperature and entering the hot zone was approximately 15 s. Each section of the strip remained in the hot zone at the set temperature for 3 – 5 s. The COF between the P20 steel pin in contact with the top face of the strip was measured using the force measurement system, which consisted of another load cell with a sensitivity of ± 0.05 N. The hot roller was placed on a bearing system that allowed it to rotate freely, while a boron nitride lubricant (purchased from VWR International AG) was applied to its surface to

minimize friction. It was calculated that a constant strain of 0.06 was applied to the strip surface during bending. No lubricant was used on the top part of the strip so that a dry contact was maintained between the P20 steel pin and the metallic strip during the COF measurements. In this work, the COF between the stretching strip and the P20 steel pin was measured at a normal load of 0.27 N.

III. A camera system that records the in-situ deformation of the grids inscribed on the sample surface: This was used to determine the strain within the hot-zone and elsewhere within the strip. Details of strain measurements using the grid system are given in the following section.

3.3.2. Measurement of COF

As indicated above, the two synchronized actuators were programmed to pull the strip at a constant differential speed of ΔV. The linear velocity of Actuator 1 was fixed at $V = 1.0$ mm/s in all the experiments. As the strip moved over the roller heated to the test temperature, a constant temperature was maintained over a certain length. This constant temperature zone was termed as the 'hot zone' (refer **Figure 3.5a)** where the COF and strain rate measurements were made. The temperature of the rest of the strip was lower than that in the hot zone. No further deformation occurred once the strip passed the hot zone. The average COF values were measured at a given temperature and strain rate after 20 s from the start of the experiments once a stable deformation condition was reached.

The camera system installed over the top face of the strip was used to measure in-situ major and minor strains in the hot zone by measuring changes in the initial diameter (2.5 mm) of circular grids inscribed on the strip's surface (**Figure 3.5a**). The calculated major and minor strains from two consecutive grids at the location of the strip's hot

deformation zone are shown in **Figure 3.5b**. The instantaneous (true) strain rate for the strip shown in **Figure 3.5a** tested at 545 °C was $d\varepsilon/dt = (\varepsilon_1 - \varepsilon_2)/\Delta t = 4 \times 10^{-2}$ s^{-1} (where $\Delta t = 2.5$ s).

AA5083 strips were placed in dry contact with the P20 steel pin and tested under constant strain rates applied in the range of 5×10^{-3} s^{-1} and 4×10^{-2} s^{-1} at different temperatures ranging from 420 °C to 545 °C. The strip was cleaned with a clean fabric soaked in acetone prior to each test. The experiments were conducted with the absence of any lubricant and the reported COF values thus represent those measured under dry sliding condition. Typical COF vs. sliding time plots were obtained at two different strain rates of 1×10^{-2} s^{-1} and 4×10^{-2} s^{-1} at 545 °C, and are shown in **Figure 3.6**. The COF measured at a strain rate of 1×10^{-2} s^{-1} (at a constant strain of 0.4) resulted in an average value of 1.0 ± 0.21. At the same temperature, the AA50803 strip subjected to the same total strain but deformed at a higher rate of 4×10^{-2} s^{-1} revealed a higher COF of 2.09 ± 0.34. A comparison between the COF curves subjected to strains of 0.1 and 0.4, but at the same strain rate of 4×10^{-2} s^{-1}, **Figure 3.6**, indicates that there is negligible effect on the COF due to the amount of strain applied to the strip at a fixed strain rate. The role of the applied strain rate on the bulk and surface deformation and damage is described later in **Chapter 4**.

3.3.3. Measurement of mechanical properties of the bulk material

Not all experiments were performed while the P20 steel pin was in contact with the strip. A series of 'non-contact' tests were conducted using the same high temperature tribometer to measure the flow stress of the strip at each temperature at the strain rates used in the COF tests. This information, together with the measured strain rates was used

to determine the creep rates and the stress exponents. The deformation mechanisms operating in the AA5083 alloy at different temperatures and strain rates were determined with electron microscopy and by analyzing the experimental creep data and reported in **Section 4.5**.

3.4. Investigation of sliding induced damage using pin-on-disk test apparatus

Sliding wear tests were conducted without any externally applied strain using a pin-on-disk type tribometer (CSM Instruments), and a schematic diagram illustrating the experimental configuration is given in **Figure 3.7a**. The majority of the sliding wear tests were conducted at 400 °C, for up to 5×10^2 sliding cycles. Sliding tests were also performed at lower temperatures for the purpose of determining wear rates as a function of test temperature (and also to obtain the grain growth rates). All tests were run under ambient atmosphere using a constant load of 5.0 N and a constant sliding speed of 1.0×10^{-2} ms^{-1}. Contact surfaces were ground and polished by standard metallographic procedures to a roughness of 0.1 µm and cleaned ultrasonically in acetone prior to putting them in contact with the counterface. The counterface was made of AISI 52100 steel with the following composition (in wt%): 1.45 % Cr, 1.00 % C, 0.35 % Mn, 0.23 % Si, 0.025 % P (max.), 0.025 % S (max.) and the balance Fe. Steel balls with a 6.0 mm diameter and a hardness of 890.0 ± 8.5 HV were polished to a surface roughness of 0.1 µm.

A reference marker, i.e., a thin plate of AZ31 inserted in the wear test sample normal to its contact surface, as shown in **Figure 3.7b**, was used to measure the sliding

displacement gradient generated in the material below the worn surface. The equivalent

plastic strain, ε, was determined using $\varepsilon = (\sqrt{3})-1 (\tan \theta)$ [158-160], where θ is the angle

between the tangent line to the marker and the axis perpendicular to the sliding surface

(i.e., the original position of the marker) as shown in **Figure 3.7c**.

The worn surfaces were investigated using WYKO NT1100 optical surface

profilometer. Representative surface profiles of the worn surfaces of AA5083 and AZ31

alloy materials at two temperatures of 300 °C and 400 °C after one sliding cycle are

shown in **Figures 3.8a to d**. The volumetric wear loss that occurred as a result of sliding

for a given number of cycles was calculated by averaging the wear track's cross-sectional

area at four equally spaced locations along the track, then multiplying it by the track

perimeter (47.1 mm). Volumetric wear losses were plotted as a function of the number of

sliding cycles and sliding distance. The cumulative increase in volumetric wear loss as a

function of the number of sliding cycles at 400 °C is plotted for AZ31 alloy as shown in

Figure 3.9a, where a linear relationship was observed. Wear rates (mm^3/m) were

determined from the slope of the volume loss versus the sliding distance plots. The

measured wear rate values are plotted against temperature from both AA5083 and AZ31

alloys as shown in **Figure 3.9b**. This plot was useful to establish the quantitative measure

of wear rate with temperature in aluminum and magnesium alloy.

The variation in wear rates with the temperature in AZ31 alloy can be examined

in two separate regions distinguished according to the differences in the slopes of wear

rate versus temperature plot. A low slope region corresponding to wear rates between

1.0×10^{-2} and 6.0×10^{-2} mm^3/m was observed in the temperature range between 298 and

300 °C, while a high slope region existed above 327 °C, where the wear rates reached as

high as 2.2×10^{-1} mm^3/m at 400 °C. The worn surfaces of the samples tested in the low slope region were oxidized, and the spallation of the oxidized surface layers was responsible for material loss. This work focuses on the high wear rate region where extensive surface damage occurred as a result of plastic deformation. The temperature range used during dry sliding test is also close to the operating temperature of hot-forming process.

3.5. Measurement of adhesion strength using junction strength experiments

The experimental setup to conduct the adhesion tests performed in this work followed the procedure that was described previously by Riahi et al. [130]. In the setup, shown in **Figure 3.10a**, a pin on disk type configuration was used where the sample materials to be studied are used as pin and the disk is made out of P20 steel. Each sample is heated by a cartridge heater embedded inside the sample holder. The sample holder connects to 3 mm diameter steel tube inserted with a 50 W cartridge heater. While the sample was heated to 400 °C the counterface P20 tool steel/glass was held at room temperature. The time required for the sample to reach the desired temperature is approximately 10 min. After the sample reached the desired temperature the sample tip was pressed against the steel surface under a normal load of 0.12 N and 0.5 N. After keeping the sample in contact with the steel disk surface for 15 s in order to generate the junction, the disk started to rotate at a very low velocity. The tangential force required to slide the disk increased until a maximum value was reached, after which the force dropped. The maximum value represents the force required to break the asperity junction

formed at the first contact and hence termed as 'junction strength'. The change in the tangential force, F_t, was measured throughout the experiment and used to calculate the coefficient of dynamic friction.

Deformation and oxide formation on the surface of AA5083 and AZ31 alloy during sliding contact were observed in-situ by replacing the counterface steel disk with a 2 mm thick quartz glass. The objective lens of a microscope was placed underneath the glass disk such that the video of contact surface deformation can be recorded as shown in **Figure 3.10b**.

3.6. Surface and sub-surface characterization

3.6.1. Microstructural characterization

A JEOL 840 scanning electron microscope (SEM), and a ZEISS NVision 40 CrossBeam workstation (focused ion beam, FIB) were used to study the microstructures of the surfaces and cross-sectional layers. Cross-sectional trenches were ion milled on the deformed surface using the CrossBeam workstation to investigate deformation induced damage in the vicinity of the surface. Care was taken to avoid ion-beam damage to the surface by depositing a layer of carbon. A trench was milled, using a Ga ion beam at an accelerating voltage of 30.0 kV with beam currents ranging from 13 nA to 700 pA. Final polishing was done at a lower ion-beam current of 80 pA to reduce any possible damage to the microstructure by the high energy beam.

FIB H-bar method was used for preparing the TEM samples. From the strip sample a plate of 15 mm long, 1.5 mm wide was first cut with a low speed diamond saw. The plate was then mechanically polished to a thickness of approximately 30 μm with

SiC abrasive papers. A smaller semicircular sample with a 1.5 mm radius was cut from this plate. Cutting was done in such a way that the strip surface constituted the 3 mm flat edge of the semicircular sample to be examined by the TEM. The semicircular sample was then thinned using FIB milling by removing material from each parallel side of the sample. The details of the H-bar sample preparation method consisted of the steps schematically illustrated in **Figures 3.11a to d**:

(i) The sample was mechanically polished from both sides to a thickness of 30 μm (as indicated by the dotted lines in **Figure 3.11a**).

(ii)The area to be sectioned was coated with a 2 μm wide and 2 μm thick strip of C in order to protect the sample surface from ion beam damage (**Figure 3.11b**).

(iii) Ion milling and polishing were first performed on one side of the sample starting from the edge and moving towards the centre of the sample, to reduce the thickness of the side parallel to the tensile direction (**Figure 3.11c**) until the region of interest protected by the C layer was reached.

(iv) Ion milling and polishing were then performed on the other side of the area protected by the C layer. Upon finishing this step the sample reveals the H-shape geometry when viewed from top (**Figure 3.11d**). The cross-sectional sample was polished using a low ion beam current of 80 pA, while continually monitoring the sample position until a thickness of 100 nm was obtained.

TEM cross-sectional microstructures of the samples prepared using a FIB H-bar method were observed by a JEOL JEM-2100F field emission electron microscope operating at 200.0 kV. Selected area diffraction patterns (SADP) were also taken to

identify oxide structures. Also, a Gatan Image Filter (GIF) was used to perform the elemental mapping of the oxides.

3.6.2. Electron back scattered diffraction (EBSD) measurements

EBSD measurements were carried out on the AA5083 samples deformed at two temperatures of 420 °C and 545 °C and strain rate of 4×10^{-2} s^{-1}. Measurements were also taken on the samples annealed for 5 min at temperatures of 420 °C and 545 °C, and their textures were considered as the reference texture.

EBSD measurements were performed on RD-ND plane (**Figures 3.12a to b**) over an area of 0.38 mm (in the rolling direction) by 0.38 mm (in the normal direction) containing on an average of 1500 grains in total using the EDAX TSL-OIM Data Collection 4.0 system attached to a LEO scanning electron microscope (Carl Zeiss SMT Inc., Peabody, MA). Prior to the measurements the samples were ground using 500, 800, 1200, and 2400 grit paper, subsequently polished using 6.0, 3.0, 1.0 μm diamond suspension and finally with 0.05 μm colloidal silica for 5 minutes each under 22.0 N force, and then etched using 0.5 pct hydrofluoric acid in water base for 10 to 30 s. Prior to the analysis, the data was rotated using OIM analysis software in such a way that they represent the TD-RD plane.

Volume fraction of ten different orientations (see **Table 3.4**) for each sample were calculated using a misorientation angle of 11°, which is also referred as the optimum misorientation angle to be used to get a comparable volume fraction data of texture components from X-ray and EBSD data [161]. Additionally, certain orientation components were grouped by the representative plane and the volume fraction of the group was calculated. Cube, R-cube and H orientation components lie on the same (001)

plane and considered as one group. Similarly Goss, Brass, P and Rx orientation components are one group lying on (011) plane. Locations of most common orientation components in (111) pole figure for aluminum are shown in **Figure 3.12c**.

Table 3. 4.   Texture components selected for analysis

Number	Designation	Euler Angles	Orientation {hkl}⟨uvw⟩
1	Cube	(0.0, 0.0, 0.0)	{0 0 1}⟨1 0 0⟩
2	R-cube	(18.4, 0.0, 0.0)	{0 0 1}⟨3 -1 0⟩
3	H	(45.0, 0.0, 0.0)	{0 0 1}⟨1 -1 0⟩
4	Goss	(0.0, 45.0, 0.0)	{0 1 1}⟨1 0 0⟩
5	Brass	(35.3, 45.0, 0.0)	{0 1 1}⟨2 -1 1⟩
6	P	(70.5, 45.0, 0.0)	{0 1 1}⟨1 -2 2⟩
7	Rx	(62.8, 45.0, 0.0)	{0 1 1}⟨8 -11 11⟩
8	S	(52.9, 74.5, 33.7)	{2 3 1}⟨3 -4 6⟩
9	Copper	(90.0, 35.3, 45.0)	{1 1 2}⟨-1 -1 1⟩
10	CG	(0.0, 26.6, 0.0)	{0 1 2}⟨1 0 0⟩

3.6.3. Surface profilometry

A WYKO NT 1100 optical surface profilometer were used for characterization of the surface topographies of the samples subjected to deformation at different temperatures and strain rates. The profilometer characterization includes measurement of the surface roughness of the samples, height of the steps formed at the grain boundaries of the deformed surface and also volume loss during pin-on-disk type sliding tests. The WYKO NT 1100 was used in vertical scanning interferometry (VSI) mode. In this mode

unfiltered white light reflected from a reference mirror combines with the light reflected from the sample to produce interference fringes where the fringe with best contrast occurs at best focus. The device then measures the degree of fringe modulation to acquire the surface profile.

3.6.4. Measurement of mechanical properties of the surface oxide

The mechanical property (Young's modulus and hardness) of the oxide layer were measured using Hysitron TI 900 Triboindenter equipped with a Berkovich nano-indenter. In this technique, an indenter is loaded and unloaded into a sample to a certain load in a controlled manner. Indentation was done using a maximum load of 2 mN. After each indentation the image of the indent was captured using the same indenter in the scanning probe microscopy (SPM) mode. A load of 2 µN and a scan area of 5 µm were used for imaging each indent. Indentation under an ideal case is expected to provide an indent shape with 3-fold-mirror-symmetry when viewed from top. Observation of the indents by means of SPM imaging mode were used to identify the indentations that were abnormal and hence eliminated from the calculation of mechanical properties of the oxide. The hardness and elastic modulus values of the surface oxide were extracted from its indentation load-displacement curve using the analysis methods developed by Oliver and Pharr [162,163].

3.6.5. Measurements of elemental composition of surface oxide

The surfaces of AA5083 in as-received condition and after deformation were examined using X-ray photoelectron spectroscopy (XPS) using PHI Quantera Scanning X-ray Microprobe. A focused, monochromatinc Al K-alpha X-ray beam, 200 µm in diameter, was used for analyses. XPS was combined with Ar-ion etching to provide

composition vs. depth information (depth profiles). Depth profile etch rates were calibrated as 14.3 nm/min using SiO_2 thin-film standard. Because different materials etch at different rates, the depth scales on the depth profiles can only be used for relative comparisons.
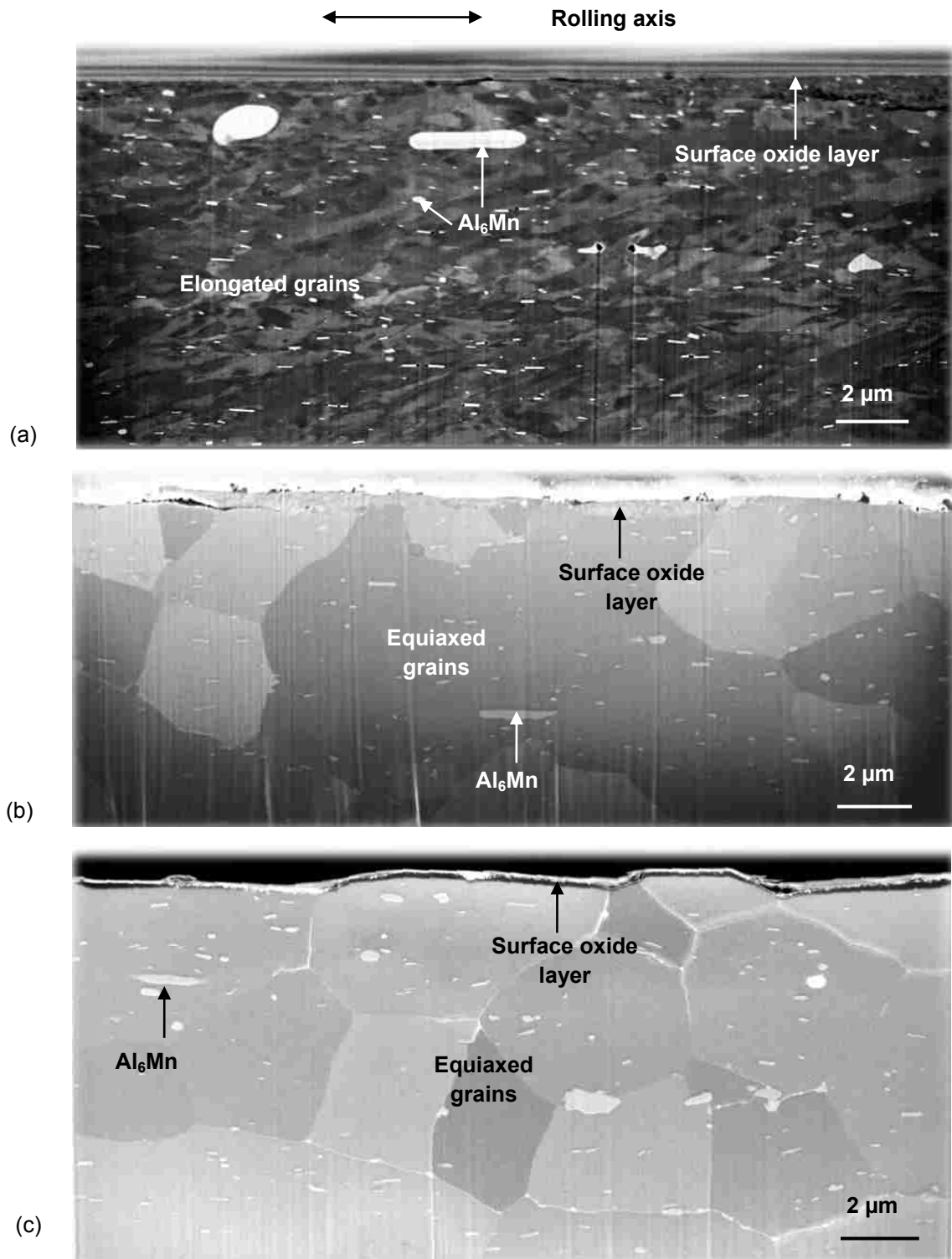
Figure 3. 1. Cross-sectional FIB/SEM micrographs of (a) elongated Al grains in a cold rolled AA5083 strip; (b) equiaxed grains in the strips stretched at 420 °C and 4×10^{-2} s^{-1}; and (c) at 540 °C and 4×10^{-2} s^{-1}.
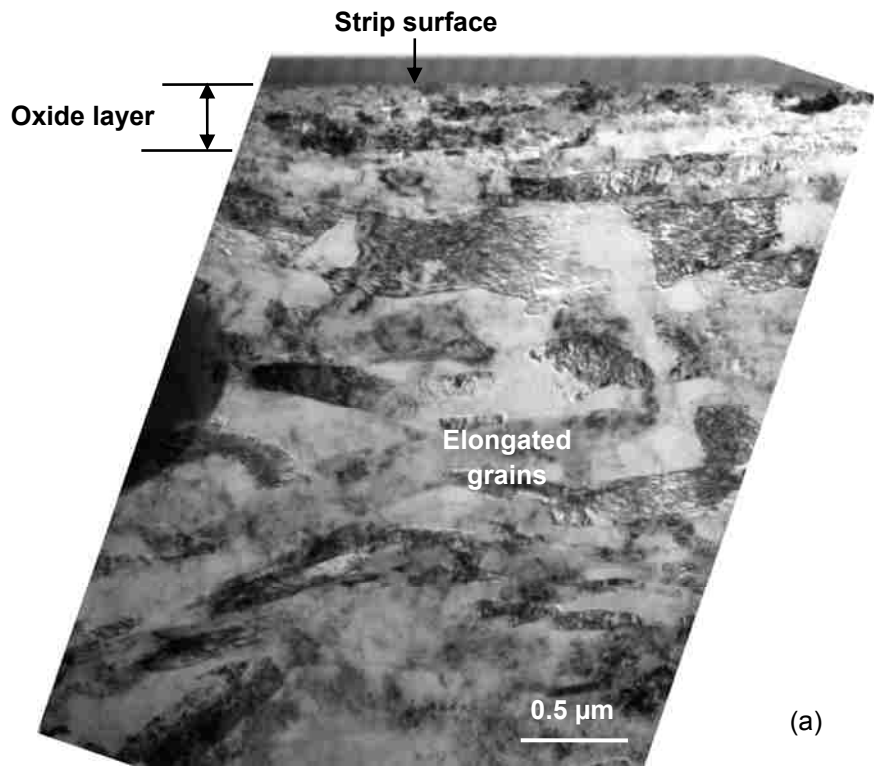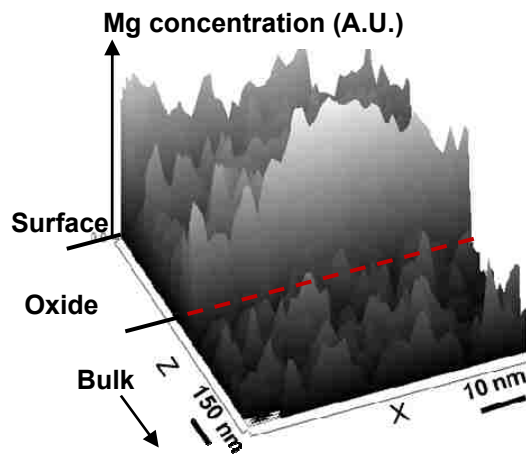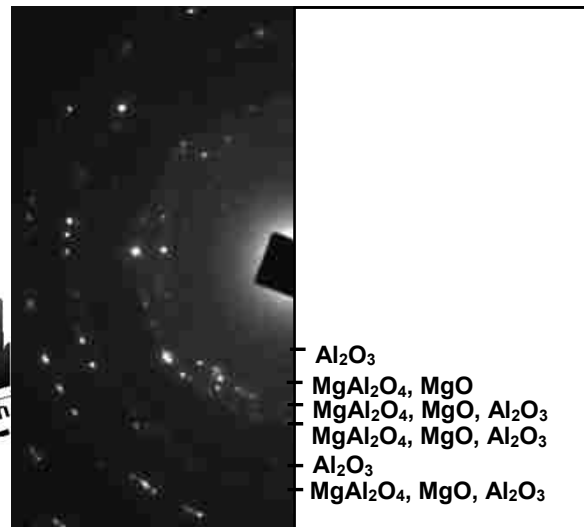
Figure 3. 2. (a) Cross-sectional TEM micrograph showing the oxide layer on the surface of a cold rolled AA5083 strip; (b) GIF elemental map showing that the Mg concentration near the surface was approximately three times higher than that in the bulk; and (c) SADP of the oxide layer that identifies $MgAl_2O_4$, MgO and Al_2O_3. The SADP was taken using an aperture of 250 nm in diameter.
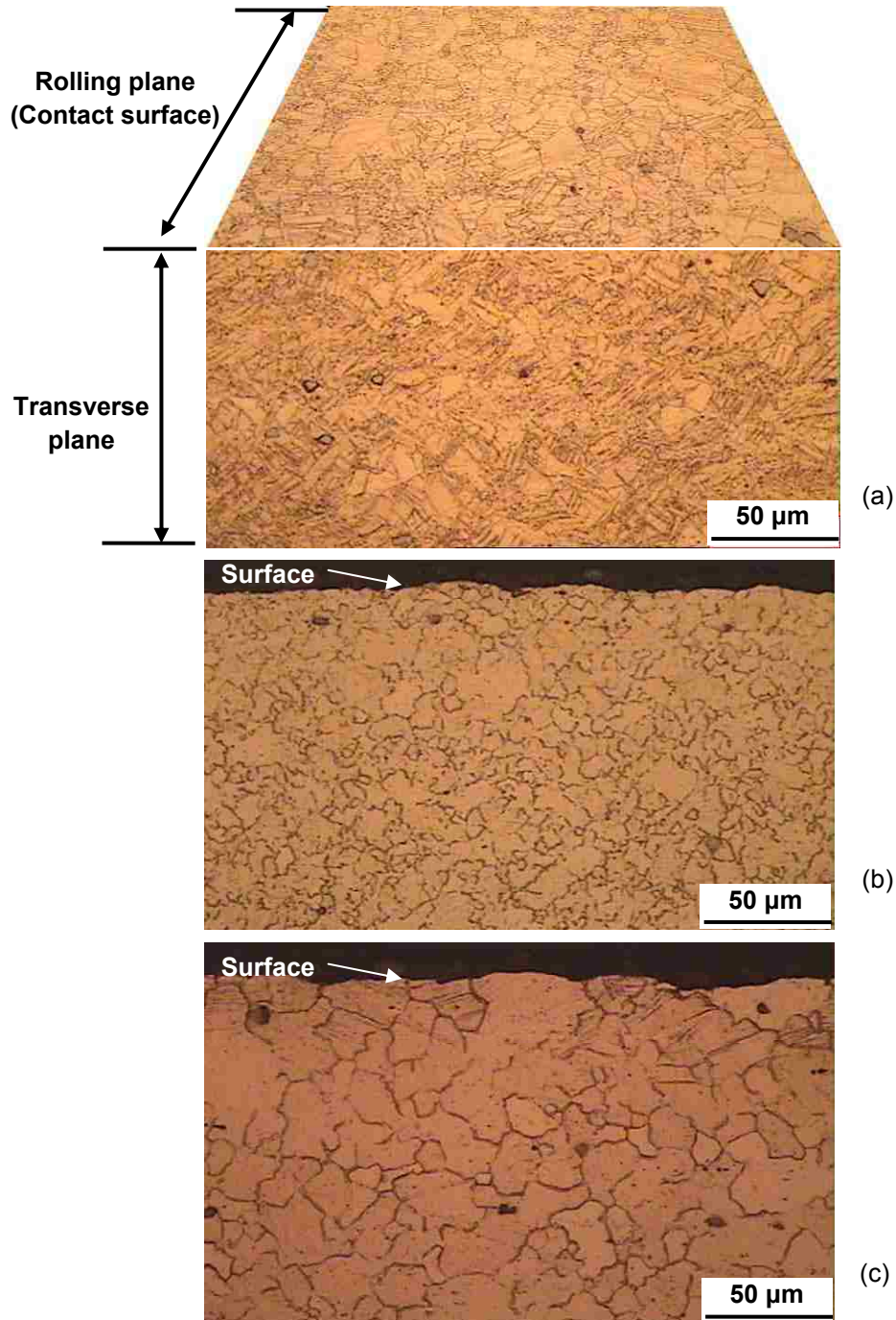
Figure 3. 3. (a) Composite optical micrograph of as-received AZ31 alloy sample showing the microstructure of the surface placed in contact with the counterface (rolling plane) and the subsurface (transverse plane). Micrographs of the sample deformed at (b) 350 °C and 4×10^{-2} s^{-1} and (c) 450 °C and 4×10^{-2} s^{-1}. The samples were etched with acetic-picral solution (5 g picric acid, 6 ml acetic acid, 10 ml water, and 100 ml ethanol).
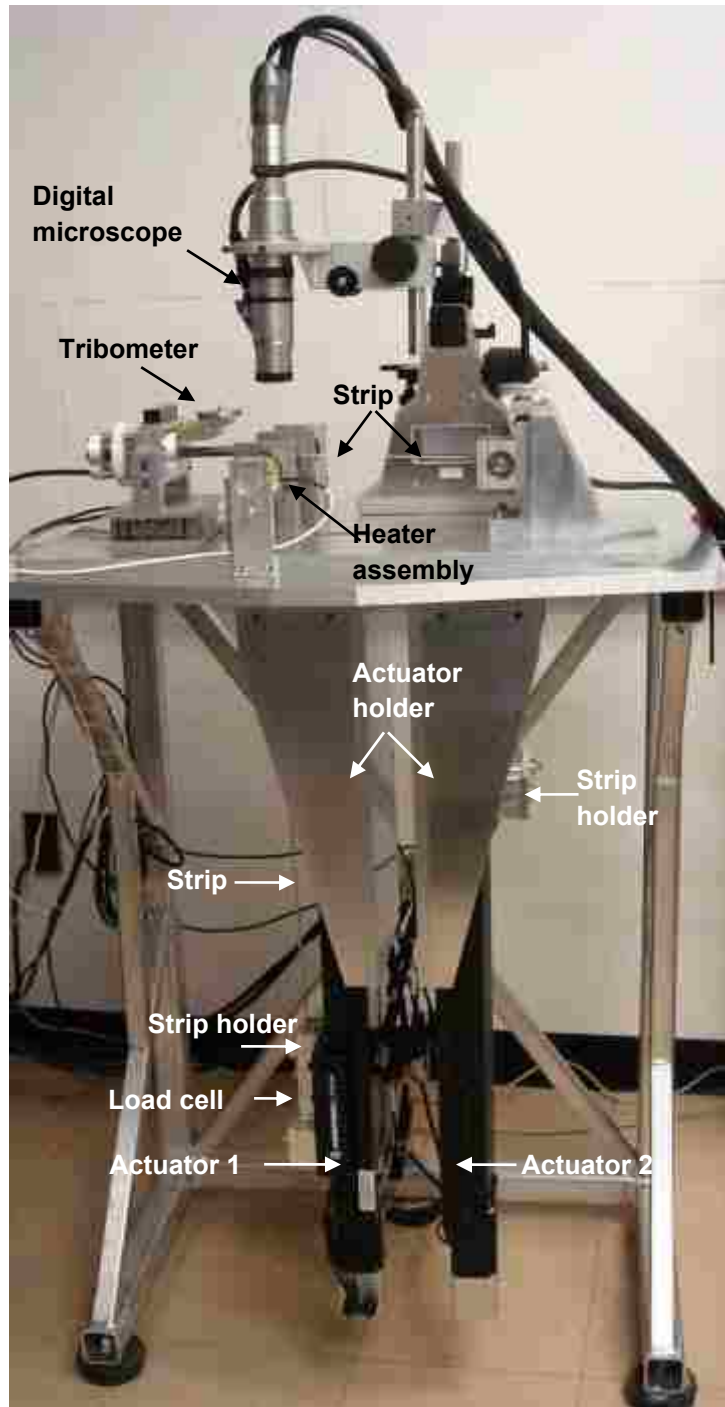
Figure 3. 4. (a) Photograph of the high temperature tribometer designed to simulate the sliding contact during forming operations, (b) isometric view of the experimental setup that shows the AA5083 strip under sliding contact against the P20 steel pin being stretched by the linear actuators; (c) photograph of the tribometer and heater assembly.

(b)

(c)
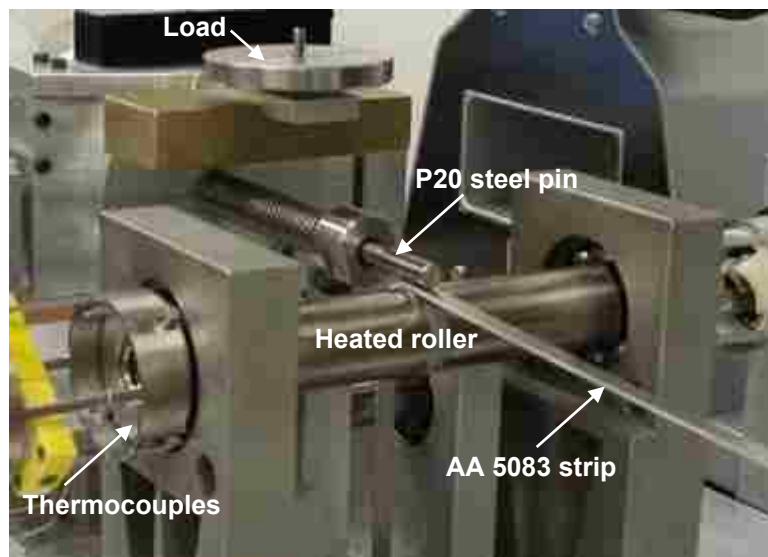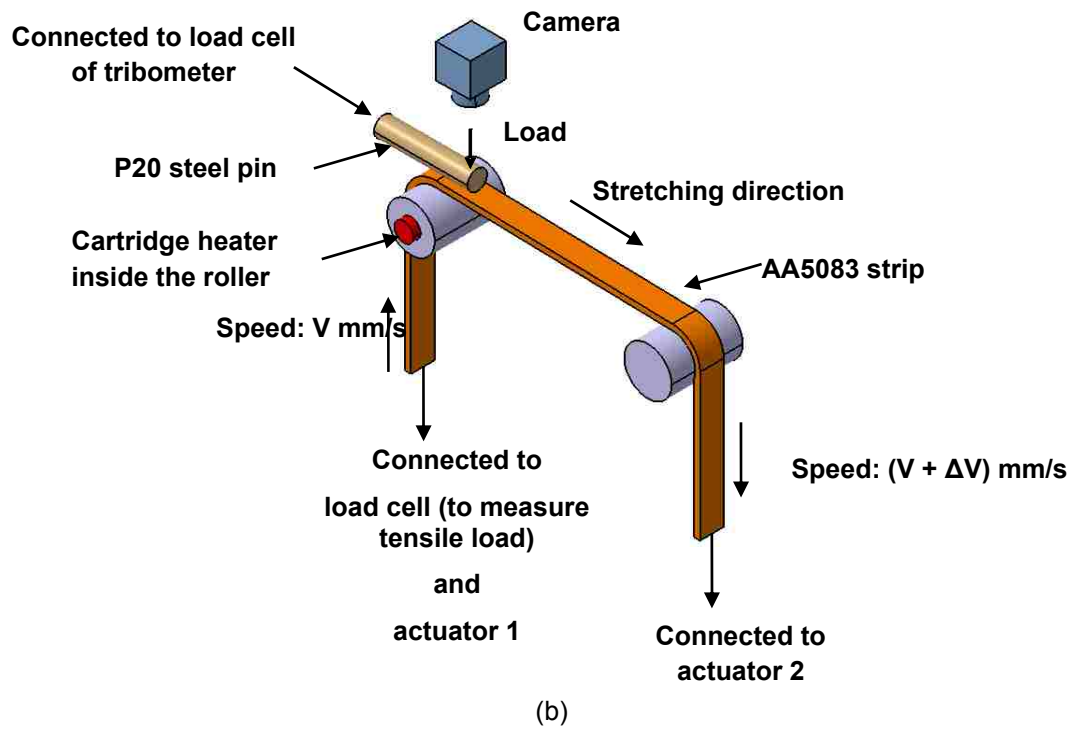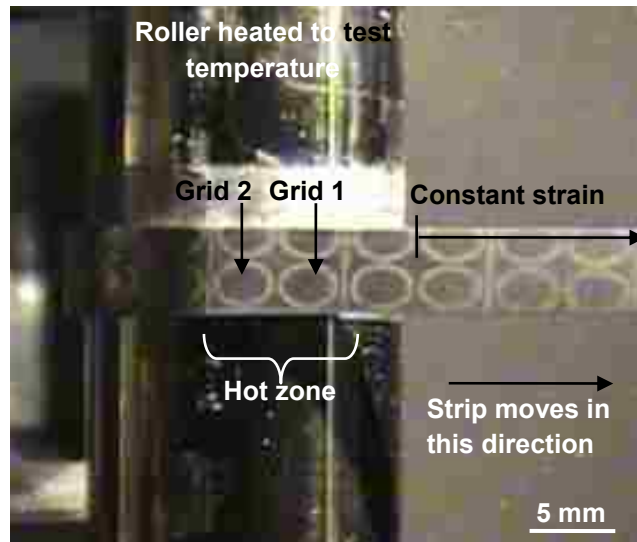
(a)
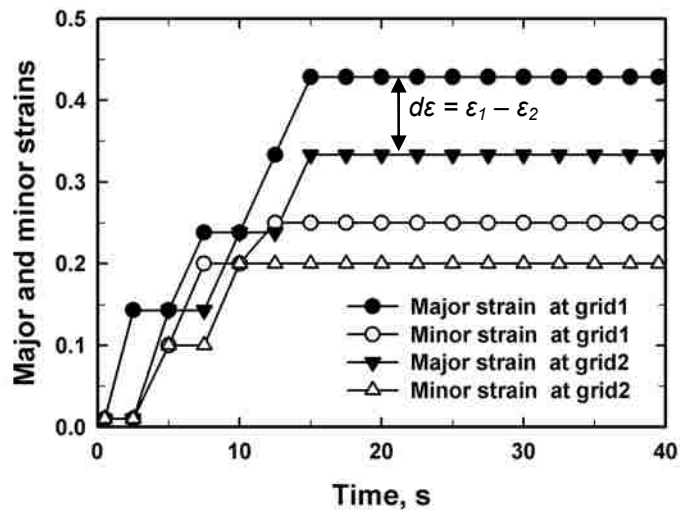
(b)

Figure 3. 5. (a) AA5083 strip inscribed with grids that shows elongation along the direction of the applied strain while being pulled; and (b) major and minor strain of the strip, measured from two consecutive grids (shown in plate (a)) within the hot zone.
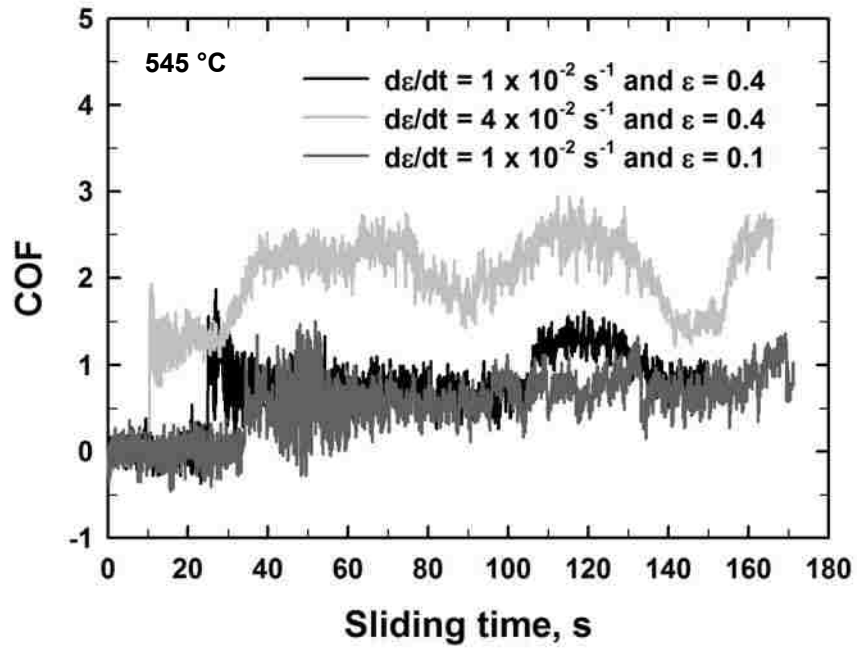
Figure 3. 6. COF vs. sliding time plot at 545 °C that shows the measured COF during experiments at two different strains and strain rates.
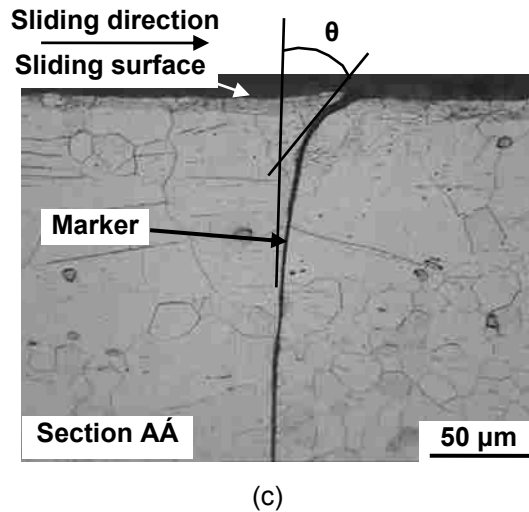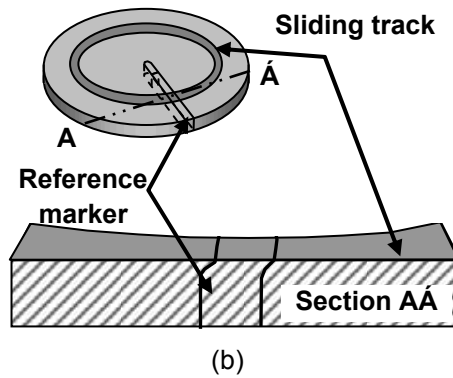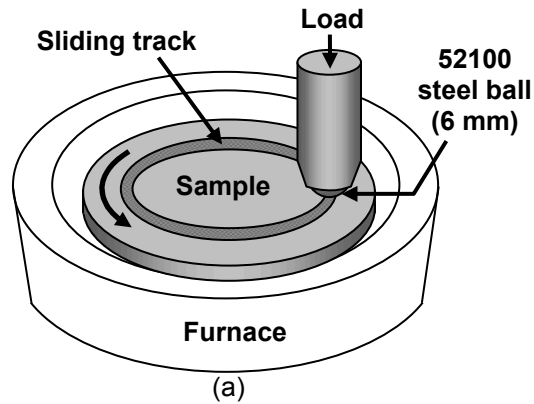
Figure 3. 7. (a) Schematic representation of high temperature pin-on-disk experimental set-up; (b) Geometry of the marker inserted in the sample (disk) and the cross-section AA´ representing the displacement of the marker underneath the contact surface after the sliding wear test and (c) Cross-sectional optical micrograph showing the displacement of the marker towards the sliding direction after sliding for 50 cycles at 400 °C.
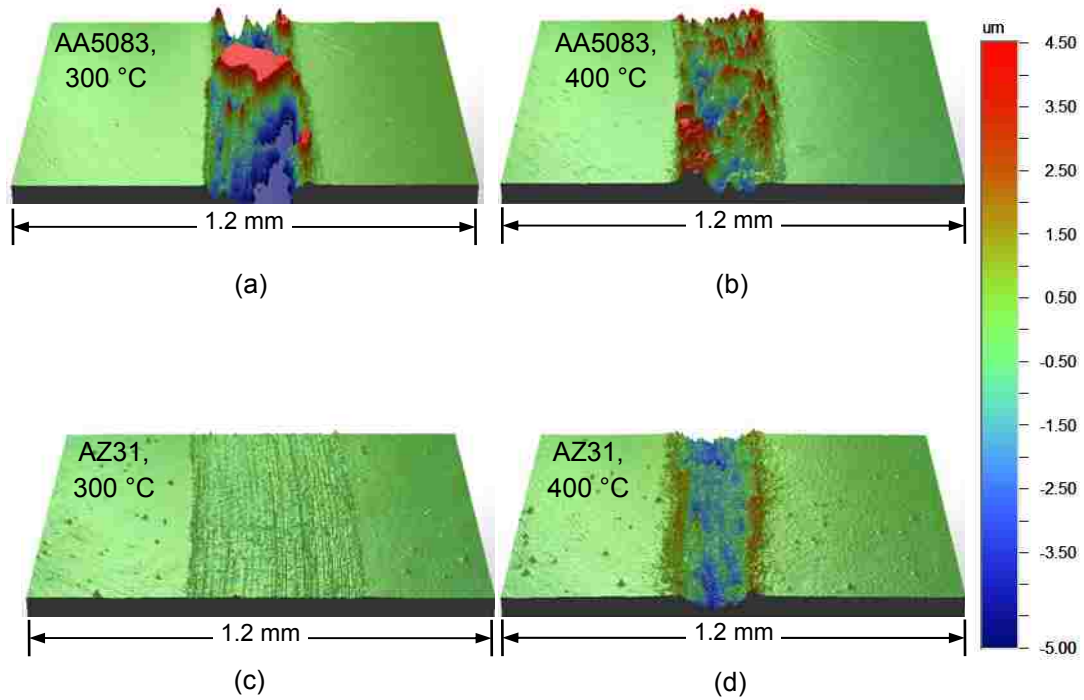
Figure 3. 8. The wear track profiles of AA5083 and AZ31 alloys at 300 °C and 400 °C (The width of all the profiles is 1.2 mm) (a) AA5083 at 300 °C, (b) AA5083 at 400 °C, (c) AZ31 at 300 °C and (d) AZ31 at 400 °C. The profiles in AA5083 indicate with the increase in temperature, increased adhesion result in discontinuous and uneven wear profile with chunks of material sticked to the disk. The profile in AZ31 alloy is generally continuous and at 400 °C shows deep groove in the middle indicating occurrence of plastic deformation.
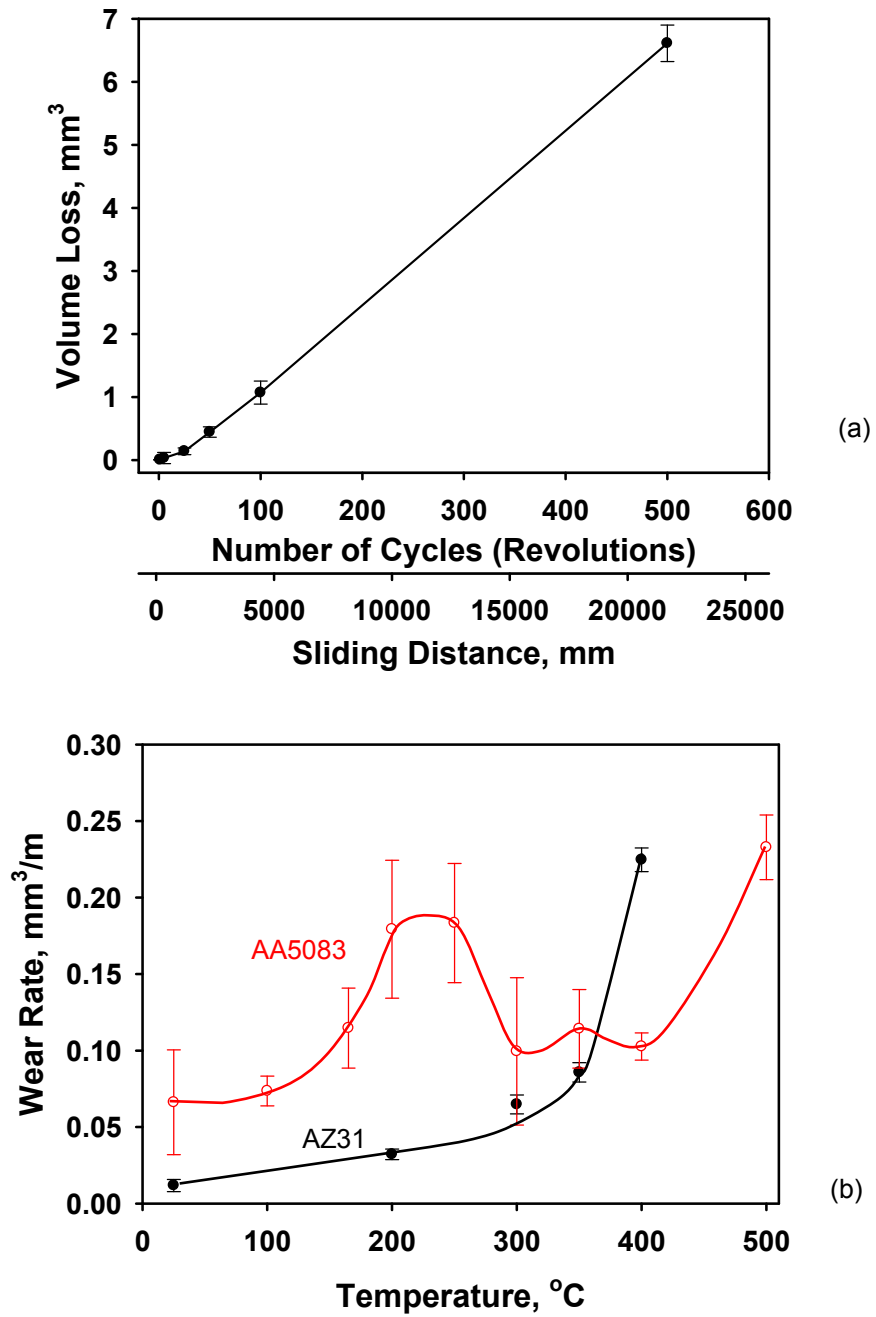
Figure 3. 9. (a) Volume loss versus sliding distance plot of AZ31 alloy showing an increase in volume loss with sliding cycles at 400 °C (5.0 N, 0.01 m/s); (b) The wear rate plot of AA5083 and AZ31 alloys against steel at temperatures 25 – 500 °C.
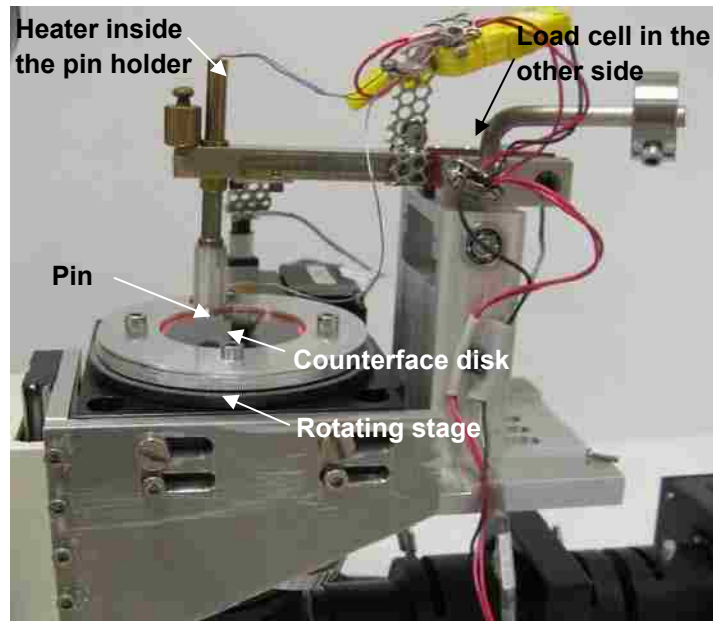
(a)
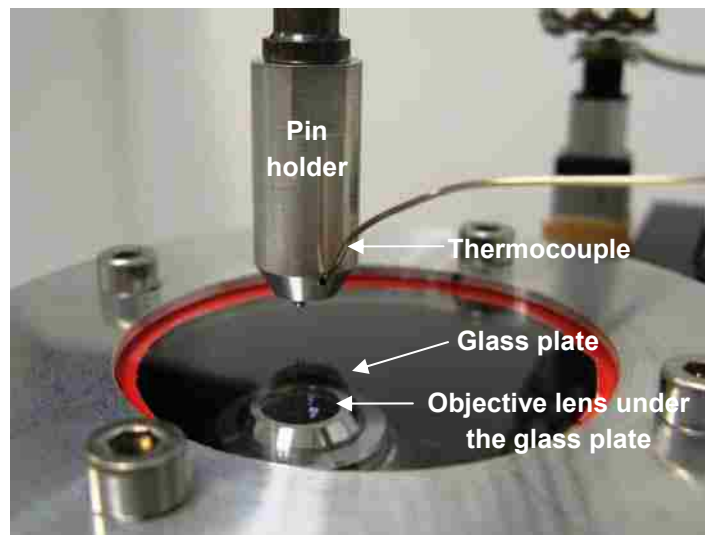
(b)

Figure 3. 10. (a) Experimental set-up for junction strength experiment and (b) close-up view of the setup for in-situ observation.
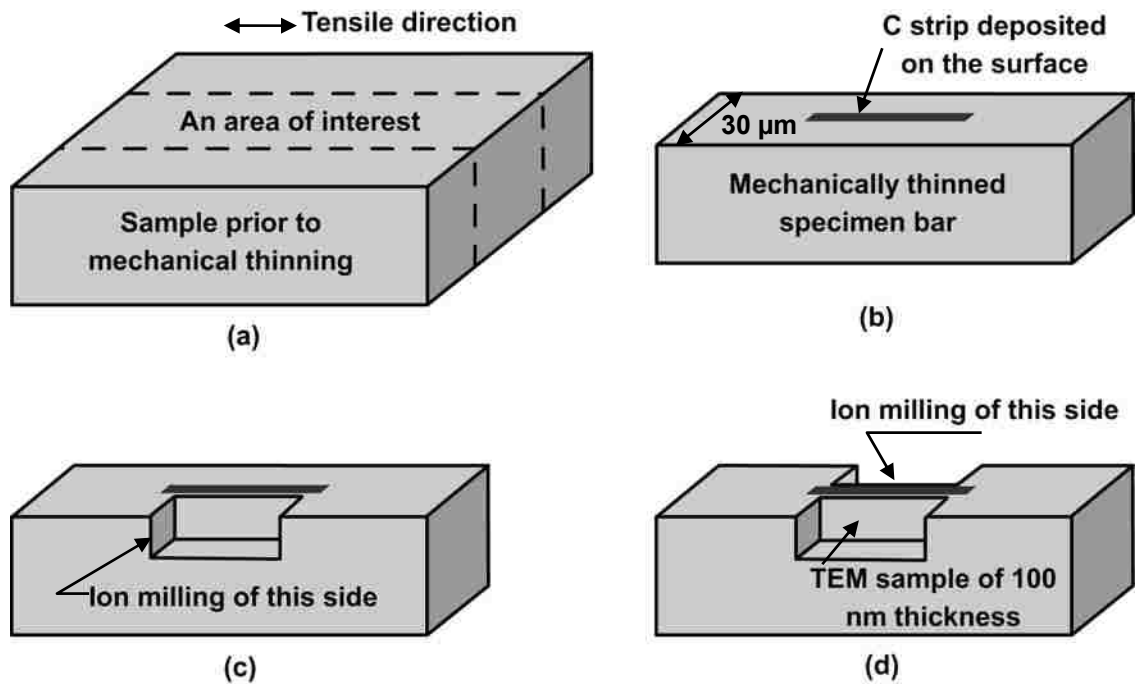
Figure 3. 11. Illustration of the steps used for the FIB H-bar procedure for TEM sample preparation: (a) The sample was mechanically polished from both side. (b) A C strip deposited on an area of interest in the wear track. (c) Ion milling of one side of the strip starting from the edge of the slab and heading towards the location protected by the C strip, followed by polishing using an ion beam with low current. (d) Ion milling parallel to the sample's opposite side to create the H-bar configuration (when viewed from top) and finally polishing the cross-sectional TEM sample to a thickness of approximately 100 nm using an ion beam with a low current [164].
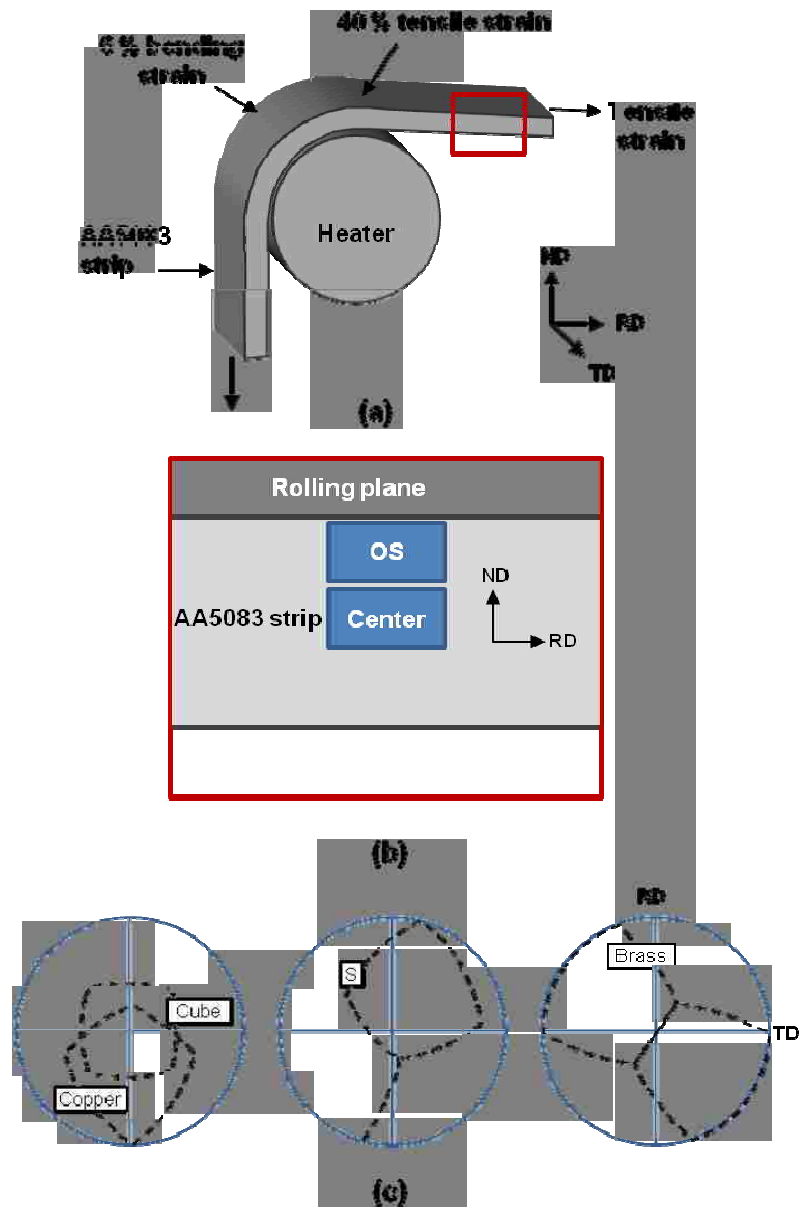
Figure 3. 12. (a) Schematic representation showed the sample annealed and deformed by simultaneously applied 6 % bending strain and 40 % tensile strain at a strain rate of 4×10^{-2} s^{-1} creating a complex strain path. (b) the location of EBSD measurements (close to outer surface (surface) and Centre) with respect to the sample reference. (c) Location of most common orientation components in (111) pole figure for aluminum.

Chapter 4 Coefficient of Friction and Deformation Mechanisms of AA5083 Alloy

4.1. Introduction

This chapter presents the results of experiments conducted in order to study the properties of interface generated between the AA5083 alloy and the steel counterface under a dynamic condition generated under high temperatures and different strain rates. The friction experiments were performed at temperature between 420 °C and 545 °C, and strain rate ranges between 10^{-3} s^{-1} and 10^{-2} s^{-1}. The purpose of these experiments was to simulate the conditions close to the hot-forming operations, where the workpiece was subjected to tensile forces while under sliding contact.

In **Section 4.2** results on the effect of temperature and strain rate on COF for AA5083 alloy are presented. **Section 4.3** deals with the surface morphologies that developed during high temperature deformation and describes the effects of temperature and strain rate on the properties of surface oxide. Variation in surface roughness generated as a result of different surface morphologies is described in **Section 4.4**. The section will also discuss the generation of surface damage map. The composition and mechanical properties of the surface oxide and the damage features observed within the oxide layer are presented in **Section 4.5**. The deformation mechanisms under the temperature (420 – 545 °C) and strain rate ($5 \times 10^{-3} - 4 \times 10^{-2}$ s^{-1}) conditions used during friction experiments are discussed in **Section 4.6**, which includes identification of the operating deformation mechanism based on mechanical data, microstructural evidence

and texture analysis. **Section 4.7** provides an overall summary of the friction behaviour of AA5083 alloy deformed at elevated temperature.

4.2.   Variation of coefficient of friction (COF) with temperature and applied strain rate

The COF of the AA5083 alloy measured at room temperature against the P20 steel pin without applied tensile strain and under 6 % bending strain (see **Section 3.3.1**) was 0.29 ± 0.11. **Figure 4.1a** shows COF variations with strain rate at two different temperatures characteristic of the hot-forming process (420 °C and 545 °C). The average COF values are plotted against the instantaneous strain rate measured in the part of the strip inside the hot zone (see **Section 3.3.2**). The reported values are averages of two tests at each temperature and strain rate. The COF value increased with strain rate at each of the two temperatures, and the increase was higher at 545 °C. The mean COF value was 0.95 at $T = 420$ °C and $d\varepsilon/dt = 5 \times 10^{-3}$ s^{-1}. The COF increased to 1.16 at a higher strain rate of 4×10^{-2} s^{-1}. Temperature had a significant effect on COF; increasing the temperature from 420 °C to 545 °C at a strain rate of $4 \times 10^{-2} s^{-1}$, the COF value increased by 80 % to 2.09.

In **Figure 4.1b**, the friction data is represented by plotting the average COF values as a function of the test temperature, but at two different constant strain rates of $5 \times 10^{-3} s^{-1}$ and $4 \times 10^{-2} s^{-1}$. **Figure 4.1b** indicates that the COF values were higher when the strips were subjected to higher strain rates.

The effects of strain rate and temperature on COF are mapped on temperature – strain rate axes, shown in **Figure 4.1c**. This map enables visualization of the combined

effect of temperature and strain rate conditions on the COF of AA5083 alloy.

4.3. Surface oxide deformation and damage during high temperature deformation

4.3.1. Pre-existing surface oxide

The surface morphology of AA5083 in the as-received condition is shown in **Figure 4.2**. The surface was covered with a compacted oxide layer with a morphology typical of rolled aluminum surfaces. The damage due to rolling manifested itself as continuous lines extending parallel to the rolling direction and the formation of surface cracks normal to the rolling direction. These cracks were almost equally spaced and usually 20 – 100 µm long and 1 – 5 µm wide. Groups of such oxide cracks were formed in some portions of the strip, whereas other portions were free of cracks altogether. The composition of the surface oxide was discussed in detail in **Section 3.2.1**. During the COF measurements the P20 pin came in contact with a surface that has undergone tensile deformation. Examples of surface morphologies taken from deformed strips that have not yet contacted the P20 pin are discussed in **Sections 4.3.2 and 4.3.4**.

4.3.2. Oxide layer after deformation at 545 °C

Figure 4.3a shows the typical surface morphology of an AA5083 alloy strip deformed at 545 °C and 4×10^{-2} s^{-1}. The alloy's grain boundaries, as well as the steps formed at the grain boundaries became visible on the surface due to the sliding of the grains relative to each other. The out-of-plane sliding of the grains, responsible for the formation of a faceted appearance, indicate that the alloy was subjected to deformation by

GBS [134]. The top surface of grain boundaries was covered with an oxide layer. The oxide layer that covered the surface, experienced damage with cracks forming at the surface layer in certain locations as indicated on the figure. Also, formation of thin and fibrous structures was visible at the location of the surface oxide just above the top face of the grain boundaries. These fibrous structures, termed as ligaments from this point onward, consisted of very thin fibres (about 0.1 - 0.2 μm in diameter) that extended to few microns. While some ligaments extended up to 3 μm in length, most were stretched to only about 1 μm. The location of the ligaments coincided with the grain boundaries of the bulk alloy that exhibited sliding. This appearance is akin to microfibres that were observed on the fracture surfaces of aluminum [136,137], suggesting local superplasticity in the oxide layer.

A higher magnification view of the deformed surface clearly shows how GBS between grains A and B (as labelled in **Figure 4.3b**) led to the formation of a prominent grain boundary step. The grain boundaries lying on the surface were covered with the oxide layer. The formation of 2 μm long ligaments from the oxide is shown in **Figure 4.3b** to coincide with sections of the oxide lying at the boundary where steps were formed by GBS. Another example of oxide ligaments with an average length of 1.5 μm is observed in the step formed between grains B and C, also due to out-of-plane sliding of grains relative to each other. Individual oxide ligaments had a diameter < 200 nm, but in general, ligaments formed bundles consisting of a few to hundreds (in cases where grain boundaries exhibited sliding in groups) of individual fibres. A few ligaments were fractured (ruptured), while a majority of the ligaments sustained large amounts of deformation without exhibiting rupture due to the mechanism of micro-superplastic

behaviour reported previously [134,137,140]. It is noted however that in all the previous studies [134,137,140,141,165], the ligaments were observed on the portion of freshly generated fracture surfaces that become exposed to air during the fracture process. In the present study, however, formation of ligaments was observed with in the pre-existing oxide layer on the surface of AA5083 alloy (**Figure 4.3a**).

The oxide layer of the sample deformed at 545 °C as shown in **Figure 4.4a**, which illustrates in detail the morphology of a stretched oxide ligament and the large cavities that formed between the ligaments were sectioned by FIB milling across the ligaments. **Figure 4.4b** is the cross-section showing the oxide layer, which became detached from the underlying bulk grains in locations where ligaments were observed. The cross-sectional morphology of the large cavities that formed at the interface between the oxide layer and the bulk grain boundaries can also be seen in this micrograph. Some cavities even extended through the bulk grain boundaries beneath the oxide layer. For a better visualization of the formation of ligaments, a schematic representation of the cross-sectional micrograph in **Figure 4.4b** is also shown in **Figure 4.4c**.

4.3.3. Effect of strain rate on surface oxide

Oxide ligaments were observed at temperatures as low as 460 °C and strain rates above 2×10^{-3} s^{-1}. When tested at low strain rates at $T > 460$ °C, the oxide layer remained ductile, with very few cracks, as shown in **Figure 4.5a**. Very few ligaments were also formed. The length of these ligaments was short. Grain X and grain Y in **Figure 4.5a** are shown schematically in **Figure 4.5b**, where a location of a short ligament formed between the two grains is indicated. The number of ligaments and their length

were a function of the temperature and strain rate used and will be described in detail in **Section 4.5.3**.

4.3.4. Oxide layer after deformation at 420 °C

The morphology of the surface that was covered with a pre-existing oxide layer after deformation at 420 °C and 4×10^{-2} s^{-1} had a less faceted appearance. The extent of the out-of-plane displacement of the near surface grains, seen underneath the oxide layer, was also smaller (**Figure 4.6a**) when compared with strips deformed at higher temperatures. This implies that GBS at 420 °C was not as extensive as at 545 °C. **Figure 4.6a** shows that the oxide layer fractured more frequently at 420 °C and the resulting cracks, running normal to the direction of applied strain, were both longer and wider. Oxide ligaments, while not totally absent, were fewer in number. None of the oxide ligaments' length observed on the surface (see **Figure 4.6a**) was exceeded 1.0 μm.

Figure 4.6b features the cross-section of the oxide layer of a sample tested at 420 °C taken from the location indicated in the plan view of the SEM micrograph of **Figure 4.6a**. The cross-sectional micrograph indicates that the cracks running normal to the tensile axis propagated along the whole thickness (1 μm) of the oxide layer before reaching the oxide layer/bulk alloy interface. Voids (0.3 – 0.5 μm in diameter) within the surface oxide layer and its interface with the bulk alloy are also evident. The micrograph in **Figure 4.6b** is also shown schematically in **Figure 4.6c**, where the void formation at the interface between the surface oxide and aluminum grains could be seen. In addition to that, the cracks formed in the surface oxide and the exposure of bulk aluminum due to these oxide cracks are illustrated in the figure.

In summary, considerable differences were observed between surface characteristics at 420 °C and 545 °C. While the oxide exhibited high plasticity during the strip's deformation at 545 °C and local oxide superplasticity was evident in the form of ligament formation, the oxide deformed at 420 °C proved to be less ductile, with damage proceeding mainly as the result of crack formation. A detailed analysis of the characteristics of the surface oxide is presented in **Section 4.4**.

4.4. Surface oxide characteristics

4.4.1. Properties of surface oxide

Room temperature mechanical properties of the surface oxide were measured on the as-received material as well as on the material deformed at 420 °C and 545 °C, and under an applied strain rate of 4×10^{-2} s^{-1} using Hysitron TI 900 Triboindenter. Indentation load vs. displacement plots for all three samples are shown in **Figure 4.7a**. The images corresponding to each indentation in **Figure 4.7a** were taken using scanning probe microscopy (SPM) mode of the indenter. The images showed that the shape of the indents was following 3-fold mirror symmetry. Young's modulus and hardness values of the oxide layers extracted from the load vs. displacement plots using Oliver and Pharr technique [162,163] are shown in **Figures 4.7b and c** respectively. The hardness was reduced when the deformation temperature was increased. The reduction in hardness is due to the varying composition of the surface oxide upon high temperature deformation. The hardness values of nanocrystalline $MgAl_2O_4$-Al_2O_4 and $MgAl_2O_4$-MgO composites (made from MgO and Al_2O_3) were found between 2.89 and 7.79 GPa [166]. In the same work it was also reported that the hardness value of the composite made from MgO and

Al$_2$O$_3$, decreased with the increase in MgO content. Therefore, the decrease in hardness of the oxide layer in the present investigation might be due to the change in composition i.e. increased amount of MgO content in the layer.

4.4.2. Composition of surface oxide

Magnesium diffusion to the surface increased with increase in temperature. The Mg concentration at the surface was captured in the XPS composition vs. depth profiles of the pre-existing oxide and the oxides at 420 °C and 545 °C (**Figures 4.8a to c**). The highest concentration of Mg was found in the sample tested at 545 °C (**Figure 4.8c**) at a depth of 1.5 nm below the surface. Higher amount of Mg concentration was also found in this sample at any depth up to 35 nm below the surface. High Mg concentration at 545 °C supported the fact that Mg diffusion to the surface increased with increase in temperature.

Elemental composition from XPS data at the surface and at the depth of 35 nm were used to generate the bar charts shown in **Figures 4.8d and e**. Magnesium concentration increased significantly from the initial surface (7 % Mg) to the surface at 420 °C (12 % Mg) and 545 °C (23 % Mg). However, an opposite trend was found in case of aluminum, where the amount of aluminum decreased 16 % at the initial surface to 9 % at the surface of the sample deformed at 545 °C. Surfaces with high magnesium content were also associated with high oxygen concentration, suggesting presence of magnesium rich oxides on the surface at elevated temperature and being highest at the surface deformed at 545 °C. According to Fick's first law of diffusion [167], the diffusive flux (J) or quantity per second of diffusive matter passing normally through a unit area is proportional to the concentration gradient and can be written as:

$$J = -D\frac{dC}{dx} \tag{4.1}$$

where D is diffusivity or diffusion coefficient, which is a characteristic of the medium and varies exponentially with temperature. dC/dx is concentration gradient over the diffusion distance.

Diffusion coefficient for magnesium in aluminum increased with increase in temperature and a value of diffusion coefficient was found to be 1.04×10^{-9} $cm^2 s^{-1}$ at 425 °C [128]. It was also reported that once heated above 400 °C, the outward diffusion of Mg atoms into the surface increased promoting the formation of MgO islands on the surface and $MgAl_2O_4$ at the interface between the oxide and the bulk aluminum [125].

4.4.3. Quantification of oxide cracks and oxide ligaments

Statistical analyses were conducted to quantify the average length of the ligaments as well as the percentage of oxide area they covered. The average width of the cracks that appeared on the oxide surfaces was determined. The oxide damage mechanisms were quantified using the following measurable damage parameters: i) crack width, ii) oxide ligament length and iii) area percentage (%) of oxide ligaments. An increase in temperature (at high strain rate) promoted the formation of oxide ligaments and suppressed the formation of cracks. The distribution of the cracks in the oxide was non-uniform making the crack width unsuitable as a quantitative measure of surface features. The average oxide ligament length and surface crack width are plotted against the test temperature in **Figure 4.9** at a constant strain rate of 4×10^{-2} s^{-1}. The average width of the oxide cracks decreased from 8.2 ± 2.3 μm at 420 °C to 5.5 ± 1.6 μm at

545 °C. The length of the oxide ligaments increased from 0.9 ± 0.2 µm at 420 °C to 2.5 ± 0.5 µm at 545 °C.

The area fraction of oxide surface covered by ligaments was calculated at temperatures between 420 °C and 545 °C on strips tested at different strain rates between 5×10^{-3} and 4×10^{-2} s^{-1}. By plotting the pct oxide ligaments on temperature vs. strain rate axes, an oxide damage map was generated, as shown in **Figure 4.10**. **Figure 4.10** shows that high temperatures ($T > 460$ °C) and high strain rates ($d\varepsilon/dt > 1.5 \times 10^{-2}$ s^{-1}) promoted the formation of oxide ligaments. A 'superplastic ligaments' region is identified when these features cover an area that is greater than 10 %, where the ductile nature of the oxide accommodates the applied strain without fracture. Deformation at $T \leq 450$ °C and at all strain rates caused extensive cracking of the oxide; accordingly, the region was identified as 'oxide damage by crack formation'. The area fraction of the surface covered by oxide ligaments was lower than 1 % at $T > 460$ °C when tested at low strain rates, and only a few cracks appeared on the oxide surface indicating that the oxide was still showing ductile behaviour. This region was highlighted as 'oxide damage by plastic deformation'. The oxide damage mechanisms will be discussed in relation to the deformation mechanisms of the AA5083 alloy in **Chapter 6**.

4.4.4. TEM characterization of ligaments

Detailed analyses of the microstructure and composition of oxide ligaments were necessary to understand how these ligaments were formed. The microstructure of the oxide ligaments was investigated using cross-sectional TEM. The FIB-milled cross-section **Figure 4.11a** shows a subsurface microstructure that is typical at 545 °C. The micrograph suggests that elevation of grain D over grain E formed surface step. Due to

the formation of surface step, the surface oxide that existed on top of the grain boundary between grain D and grain E experienced a localised stretching and formed oxide ligaments at that location. The TEM image of the same grains and ligaments shown in **Figure 4.11a** is given in **Figure 4.11b,** from which a higher magnification TEM micrograph capturing the surface offset between grains D and E is presented in **Figure 4.11c**. The oxide ligament in this particular cross-section is 400 nm long and approximately 100 nm thick. The small crystals seen in the microstructure of the ligament provide evidence of its nanocrystalline grain structure. The ligament's SADP from the location identified by the dotted circle is shown in **Figure 4.11d**, where the rings were indexed as {111}, {200}, {220} and {222} MgO, with a space group of Fm-3m. The same rings can also be indexed as {311}, {400}, {440} and {533} of the fcc $MgAl_2O_4$ spinel phase, with a space group of Fd-3m. The diffraction peaks obtained from the ligaments, **Figure 4.11e**, were compared with those taken from the oxides of the as-received alloy (see **Figure 3.2c in Chapter 3**) by using the intensity profile of each SADP ring obtained by the rotational average method, and plotting this against the inverse d-spacing. The {222}, {220} and {116} reflections of γ-Al_2O_3 present in the as-received oxide layer was absent in the ligament structure suggesting that this perhaps got converted to MgO and the $MgAl_2O_4$ spinel at the test temperature. The concentration of each oxide layer initially consisting of Al_2O_3, MgO and $MgAl_2O_4$ did not remain constant with temperature; outward diffusion of Mg atoms enhanced Mg concentration in the oxide layer, and hence concentration of MgO and $MgAl_2O_4$ increased during the high temperature oxidation process. As MgO appears to reduce the COF as compared to Al_2O_3

this conversion appears to be beneficial. The role of MgO in reducing COF will be discussed in **Section 6.4.1**.

The high resolution TEM (HRTEM) micrograph in **Figure 4.12** shows that the ligament has an extremely fine grain microstructure since the oxide grain diameters measured varied between 3 and 7 nm. The nanocrystalline grains had an equiaxed morphology and were not elongated in the direction of the strain.

The d-spacing between the crystal planes inside the individual grains were measured to be about 0.211 nm and 0.203 nm, corresponding to the {200} planes of MgO and the {400} planes of $MgAl_2O_4$, respectively. **Figure 4.12** shows the morphology of MgO and $MgAl_2O_4$ grains in a plane parallel to the length of the ligament. Since the grains are equiaxed on this plane, it can be assumed that they have approximately equivalent dimensions in the transverse direction. Similar high resolution micrographs taken from the cross-section of several other ligaments showed an average ligament grain size of 4.5 ± 0.7 nm. The grain boundary regions between the oxide grains in **Figure 4.12** constitute about 30 % of the total cross-sectional area. The small size of the magnesium oxide grains and diffuse nature of the grain boundaries enhance atomic diffusion during deformation. A detailed discussion of the deformation mechanism of oxide ligaments will be given in **Section 6.4.2.2**.

4.4.5. Adhesion and material transfer to P20 steel

The magnesium rich oxide layers were transferred to P20 steel surface (counterface) when slid against AA5083 alloy surface. The material that was transferred and attached to the counterface during the COF measurement test was sectioned and viewed by FIB. **Figure 4.13a** shows a schematic of the P20 steel pin indicating the

location of transferred material attached to the contact side of the cylindrical surface of the pin. A typical transferred material layer generated under the experimental condition of $T = 545$ °C and $\dot{\varepsilon} = 4 \times 10^{-2}$ s^{-1} is also shown in **Figure 4.13a**. The cross-sectional micrograph in **Figure 4.13b** corresponds to the section taken along the dotted line in **Figure 4.13a**. A higher magnification view of the interface in **Figure 4.13b** is given in **Figure 4.13c**. **Figure 4.13c** shows ligament like junctions formed at the interface between transferred material and the P20 steel surface.

The FIB cross-section shown in **Figure 4.13** was further polished and thinned down to 100 nm in thickness to be viewed under TEM. A bright field image of interface in **Figure 4.14a** shows one such area with ligament like structures making the junction between the transferred material and the P20 steel surface. Based on the contrast in the bright field image and the energy dispersive X-ray spectroscopy (EDS) dot map of element magnesium (**Figure 4.14b**), the interface area in the micrograph, which was rich in magnesium based oxides was indentified and termed as 'interface oxide'. EDS analysis was performed at 20 spots across the interface along the dotted line AB in **Figure 4.14a**. Combining the data at each location, elemental concentration profiles across the interface were determined and shown in **Figure 4.14c**. The '0' value in X-axis represents the location 'A'. Aluminum and iron concentrations profiles were as expected i.e. aluminum concentration was highest at location A (corresponding to transferred material) and 0 % aluminum was found at location B. Similarly, iron concentration is highest at point B and lowest at point A. However, oxygen and magnesium profiles showed high concentration of these two elements at the interface. EDS dot map generated for magnesium element at the same location shows enrichment of magnesium at the interface. Therefore, it was the

magnesium rich oxide, present on the surface of AA5083 samples, first transferred and formed the first layer of the interface between the P20 steel pin and the transferred material.

It was observed that the surface damage characteristics depend on the alloy's deformation behaviour. To correlate the surface damage characteristics with the bulk deformation behaviour, the mechanisms operating in the bulk material were investigated and will be discussed in **Section 4.5**.

4.5. Deformation mechanisms of the bulk material at high temperature

The mechanisms operating in the bulk material were identified from the stress-strain rate measured from the experimental data (discussed in **Section 4.5.1**), and were validated with the help of microstructural characterization (discussed in **Section 4.5.3**) and texture analysis (discussed in **Section 4.5.4**).

4.5.1. Mechanisms identified based on stress-strain rate data

The change in tensile load applied to the AA5083 strip with time was determined for different constant strain rates at a given temperature. Typical data is given in **Figures 4.15a and b** for tests conducted at 450 °C and 545 °C, respectively. The flow stress of the AA5083 was calculated using the cross-sectional area of the sample when it passed through the hot zone (see **Figure 3.4d in Chapter 3**) within a time interval, *dt*, shown in these figures and given in **Table 4.1**. The flow stress values are plotted in temperature and strain rate space in **Figure 4.15c)**. The relationship between the imposed

strain rate and modulus-compensated flow stress of the strip was determined using the general phenomenological creep equation (**Equation 4.1**) from the data plotted in **Figure 4.16**.

$$\dot{\varepsilon} = A \left(\frac{\sigma}{E}\right)^n exp\left(-\frac{Q}{RT}\right)$$
(4.1)

Where A is the material constant, σ is the flow stress, n is the stress exponent, E is the temperature compensated Young's modulus, Q is the activation energy for deformation, and R is the universal gas constant.

Table 4. 1.　　Flow stress of the bulk material at 450 °C and at 545 °C.

Strain rate, s^{-1}	Flow stress, MPa	
	450ºC	540ºC
4×10^{-2}	55.6	26.3
3×10^{-2}	-	24.7
2×10^{-2}	42.8	16.5
1.5×10^{-2}	35.7	-
1×10^{-2}	-	10.7
5×10^{-3}	13.3	5.8

The stress exponent, n, was obtained from the slope of a $\log\dot{\varepsilon}$ vs. $\log\sigma$ plot in **Figure 4.16**. The values of n, thus calculated are found to be in range of 1 to 3. As described earlier, a stress exponent of $n = 2$ is indicative of creep by grain boundary sliding (GBS), which is a well characterized creep mechanism operating in AA5083 alloy with small grain size [4-6,17,20,43,52,85,86]. The value of n of approximately 2 was

calculated for a temperature range of 460 °C – 545 °C and strain rate range of 2×10^{-2} s^{-1} – 4×10^{-2} s^{-1}. Accordingly, GBS was the operative mechanism in this temperature and strain rate range.

An effective way of summarizing the observed creep mechanisms for AA5083 was achieved by constructing a stress exponent map in temperature and strain rate space to delineate the operating plastic deformation mechanisms in the present experimental conditions (**Figure 4.17**). At low strain rate ($\leq 1.5 \times 10^{-2}$ s^{-1}) and at all temperature conditions stress exponent value of $n = 1$ indicated diffusional flow as a dominant creep mechanism. At temperature range of 460 °C – 545 °C and strain rate range of 2×10^{-2} s^{-1} – 4×10^{-2} s^{-1} stress exponent value of $n = 2$ identified as GBS operated regime. At low temperature (< 450 °C) and high strain rate (4×10^{-2} s^{-1}), SD creep operated regime was identified based on the stress exponent value $n = 3$.

4.5.2. Quantification of surface roughness

This section provides quantification of the surface roughness caused by the alloy's deformation behaviour. The surface morphology of the as-received samples and the samples tested at high temperatures were studied with a digital optical interferometer. The distribution of the surface heights and the frequency of surface height distributions were plotted in the form of histograms (**Figures 4.18a to d**). Measurements were made on areas of 120 μm × 90 μm, which contained 70 – 100 surface grains depending on the testing condition. The histograms show the relative frequency of the height distribution, which obey Gaussian probability distribution. **Figure 4.18a** shows the surface height distribution obtained from the samples tested at 420 °C at four strain rates of 5×10^{-3}, 1×10^{-2}, 2×10^{-2} and 4×10^{-2} s^{-1}. The arithmetic mean deviation of the surface height, R_a

(average roughness), and its standard deviation increased with the strain rate. At higher temperatures (**Figures 4.18b to d**), the Gaussian behaviour is preserved, but the distribution is spreaded with increasing temperature. The R_a values also increased with the temperature.

Five different locations on two sets of samples were considered for measuring R_a, and the values were given in **Table 4.2**. The lowest R_a of 0.29 µm was found for deformation at 420 °C at a strain rate of 5×10^{-3} s^{-1}. The R_a increased to 0.52 µm at a higher temperature and strain rate of 545 °C and 4×10^{-2} s^{-1}, respectively. Thus, the temperature and strain rate conditions resulting in high R_a values also contributed to high COF values.

Table 4. 2.   Surface roughness at different temperatures and strain rates.

Strain rate, s^{-1}	Roughness, µm			
	420 ºC	450 ºC	500 ºC	545 ºC
5×10^{-3}	0.29	0.28	0.24	0.35
1×10^{-2}	0.39	0.35	0.27	0.37
2×10^{-2}	0.37	0.43	0.40	0.49
4×10^{-2}	0.37	0.44	0.49	0.52

In summary a considerable increase in roughness was observed with increase in temperature and strain rate. The variation in roughness is affected by the evolution of the surface characteristics, which depends on the alloy's deformation behaviour.

4.5.3. Microstructural evidence of deformation mechanism

Microscopic evidence for GBS is given in **Figures 4.19a and b**, which show an FIB cross-section taken from an AA5083 strip tested at 545 °C. The sliding displacement that took place between Grain 1 and Grain 2 (marked in **Figure 4.19a)** resulted in the formation of a surface offset. A high magnification micrograph of the same set of grains, in **Figure 4.19b**, shows the formation of a step on the oxide layer as a result of sliding of the surface grains relative to each other. The grain interiors appear to have a low dislocation density, and the grains retained their original shape during GBS, consistent with the observation of equiaxed grains after creep deformation.

At low temperatures and high strain rates, the stress exponent increased to higher values than that of rest of the deformation conditions (**Figure 4.17**). The n value observed at temperatures between 420 °C to 450 °C and at strain rates greater than 3×10^{-2} s^{-1} was approximately 3.5, suggesting that the mechanism of solute drag (SD) creep was operating under these conditions [17,20]. SD creep is associated not only with higher n values (between 3 and 4) compared with GBS, but also with inverse creep transients [17]; specifically an abrupt drop in flow stress following a sudden strain rate change, which could be attributed to dislocations detaching from obstacles on slip planes. In general terms, any dislocation glide obstructed by precipitates and Mg atoms in AA5083 during creep (at relatively low temperatures and high strain rates) promote climb into the subgrain boundaries that are formed within the grains, which, in turn, accommodate the imposed strain. **Figure 4.19c** shows the surface grains on a AA5083 strip tested at 420 °C and 4×10^{-2} s^{-1}. The formation of a substructure (cells of 200 nm in diameter) can be observed in the high magnification micrograph shown in **Figure 4.19d**. While this

microstructure alone is not proof of SD creep as an operating mechanism, but together with the measured stress exponent of 3 and higher flow stress values of 56 – 69 MPa compared with 25 – 43 MPa for GBS, as shown in **Figure 4.15**, is evidence of SD creep operating under these conditions. Subgrains were not formed during GBS, and grain interiors were virtually free of dislocations (**Figure 4.19a**).

In addition to the microstructural evidence, the texture developed in the material due to deformation at elevated temperatures also supported the two deformation mechanisms (GBS and SD creep) operating in AA5083 alloy and will be discussed in the **Section 4.5.4**.

4.5.4. Texture evolution in the material with temperature

This section discusses the evolution of texture with temperature. Analysis was done based on the pole figures and fraction of different orientations (see **Table 3.4** in **Chapter 3**) in the material tested at 420 °C and 545 °C and strain rate of 4×10^{-2} s^{-1}. The preferred orientation of grains in a polycrystalline material is referred to as crystallographic texture also known as fiber texture. The complete description of texture requires determining the crystallographic plane aligned in the rolling plane of the sheet and the direction in that crystallographic plane aligned into the direction of rolling. The fiber texture is also described by the definition of the crystallographic direction aligned parallel to the fiber axis.

The pole figure of the as-received material is given in **Figure 4.20a**, which shows a rolling texture that is strong S ({2 3 1}⟨3 -4 6⟩), Brass ({0 1 1}⟨2 -1 1⟩) and Copper ({1 1 2}⟨-1 -1 1⟩) component and a weak cube ({0 0 1}⟨1 0 0⟩) component. Because the

samples to be analysed were deformed at two different temperatures, the texture of the material at those two respective temperatures were considered as the reference point. For example, the texture of the material annealed at 420 °C is considered as the starting texture for the material deformed at 420 °C and 4×10^{-2} s^{-1}. Then the texture of the material deformed at 420 °C using hot-forming simulator was determined. At the centre line of the strip, which followed its neutral axis, experienced 0 % bending strain, whereas the location close to the outer surface experienced a bending strain of 6 %. The (111) pole figures of the annealed only, and annealed and deformed samples are shown in **Figures 4.20b to d**. The pole figure in **Figure 4.20b** shows the existence of ⟨111⟩ fibre texture (parallel to RD). The fibre texture was strengthened upon deformation as in **Figures 4.20c and d**. The texture components were compared by plotting them as a bar chart in **Figure 4.20e**. The volume fraction of (001), S component and Copper component decreased and (011) remained same and the CG component ({0 1 2}⟨1 0 0⟩) increased slightly. In the starting material it has a total 0.081 volume fraction of (001) plane components, which consisted with cube ({0 0 1}⟨1 0 0⟩) and rotated-cube ({0 0 1}⟨3 -1 0⟩) texture component. Development of cube texture upon heating is most prominent in pure aluminum however with alloying addition the intensity decreased [168]. The (011) components remained unchanged at the surface and centre after plastic deformation of the strip. A small decrease in S and small increase in CG components were found from surface to the centre. Though the copper component ({112}⟨-1-11⟩) decreased from the initial texture, strengthening of ⟨111⟩ fibre parallel to RD was observed at the surface as well as at the centre of the strip. Strengthening of ⟨111⟩ fibre is might be due to strengthening of {101}⟨111⟩ orientation.

The texture of the material annealed at 545 °C was considered as the starting texture for this temperature. The (111) pole figures of the samples at 545 °C are shown in **Figure 4.21**. The figure shows a weakening of texture from the **Figure 4.21a** to **Figure 4.21c**. This is due to the fact that GBS operating at this temperature providing a random texture. Slight strengthening of the texture in **Figure 4.21b** compared to the pole figure in **Figure 4.21a** (comparison made between the intensity numbers in these pole figures) are due to the bending strain applied while deformation. **Figure 4.21d** shows the comparative volume fraction data at 545 °C. In summary, low intensity in the pole figure indicated GBS as the dominant mechanism of deformation in AA5083 alloy when stretched at 545 °C and 4×10^{-2} s^{-1}. High volume fraction of texture components indicated more dislocation activity during plastic deformation of the sample at 450 °C and 4×10^{-2} s^{-1}.

Knowing the texture of the material, the relative COF at two temperatures can be predicted. Farhat [169] reported that (111) texture development in the aluminum adjacent to contact surface during sliding reduces the friction of sliding contact. Formation of (111) texture parallel to the worn surface reduced the resistance to the sliding motion since (111) plane is the slip plane of FCC materials. As a result this may cause the COF to drop. In the present case, random texture at 545 °C may not have a direct influence on friction. On the other hand, the random texture is indicative of GBS mechanism which controls the surface roughness, and hence would increase friction. Development of ⟨111⟩ fibre texture formation (parallel to RD) at lower temperature of 420 °C would help in maintaining low COF.

4.6. Summary on friction behaviour of AA5083 alloy

Friction experiments conducted using hot-forming simulator made it possible to recognize the role of temperature and strain rate on friction behaviour of AA5083 alloy. An increase in the COF with an increase in the temperature and strain rate was observed (see **Figure 4.1**). It was found that the plastically deformed material under various conditions of temperatures and strain rates exhibits different surface characteristics. With the increase in temperature and the strain rate, the surface roughness of the sample increased significantly. A metallographic examination of the deformed surface revealed the presence of grain boundary steps (as in **Figure 4.3a and b**) that caused the roughness increase in the sample when deformed at 545 °C and 4×10^{-2} s^{-1}. In summary this chapter provides the relationship between the plastic deformation and surface damage mechanisms and their relation with the tribological behaviour of AA5083 alloy.
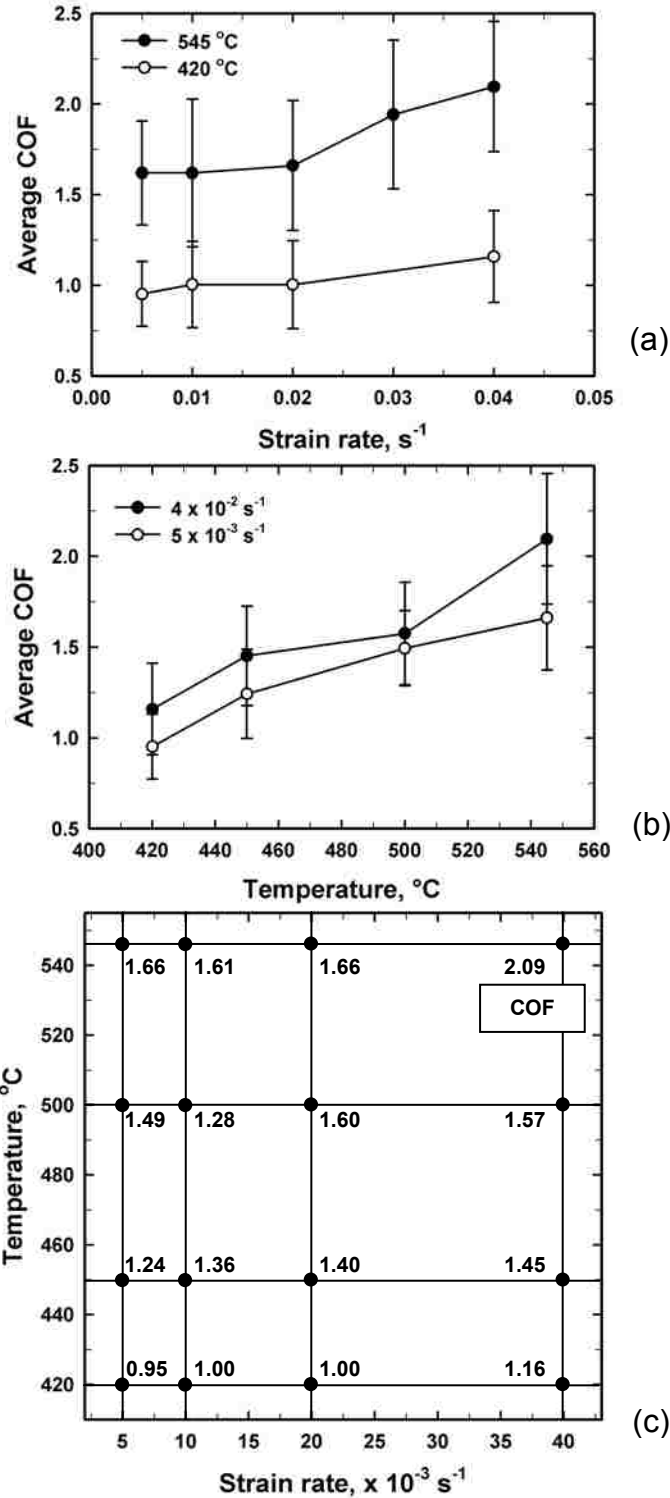
Figure 4. 1. (a) Average COF vs. strain rate plot; (b) average COF vs. temperature plot; and (c) average COF values plotted on temperature vs. strain rate axes. Error bars indicate range of fluctuations in mean COF values measured over 100 s time test period on each strip (following the initial 20 s heating period) at a constant temperature and strain rate.
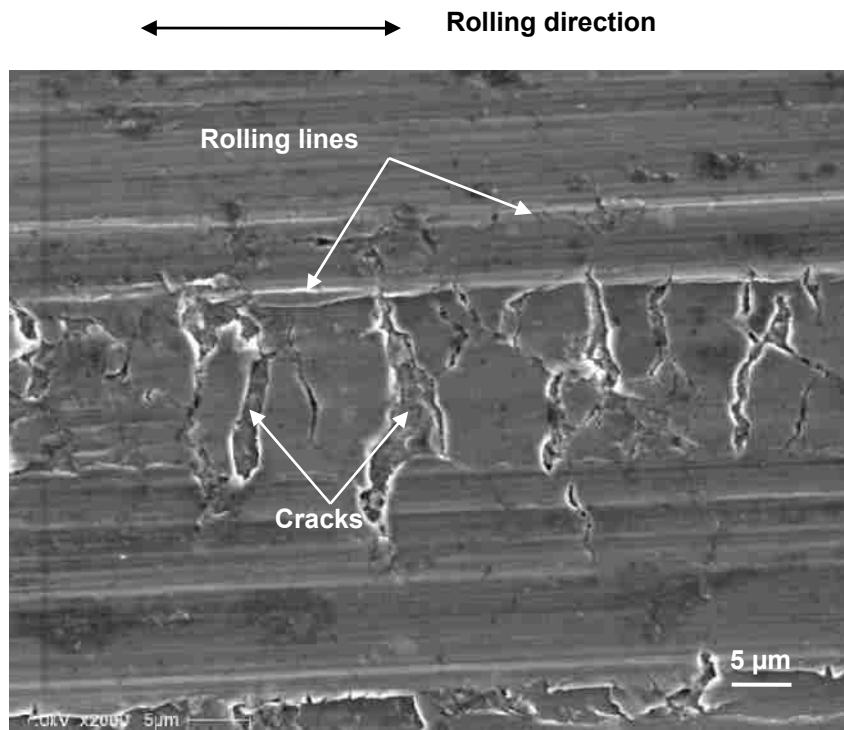
Figure 4. 2. Secondary electron image showing the surface morphology of as-received AA5083 strip surface.
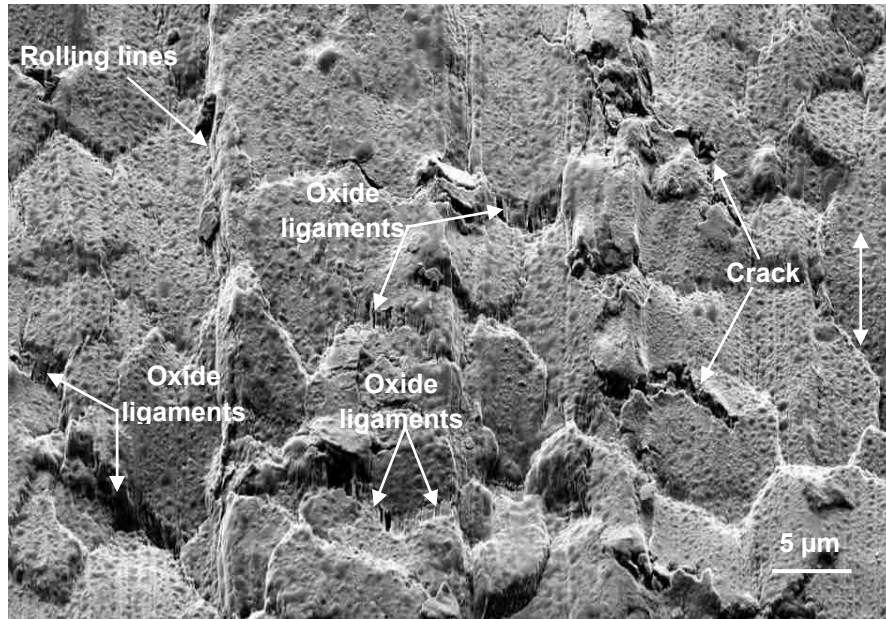
(a)
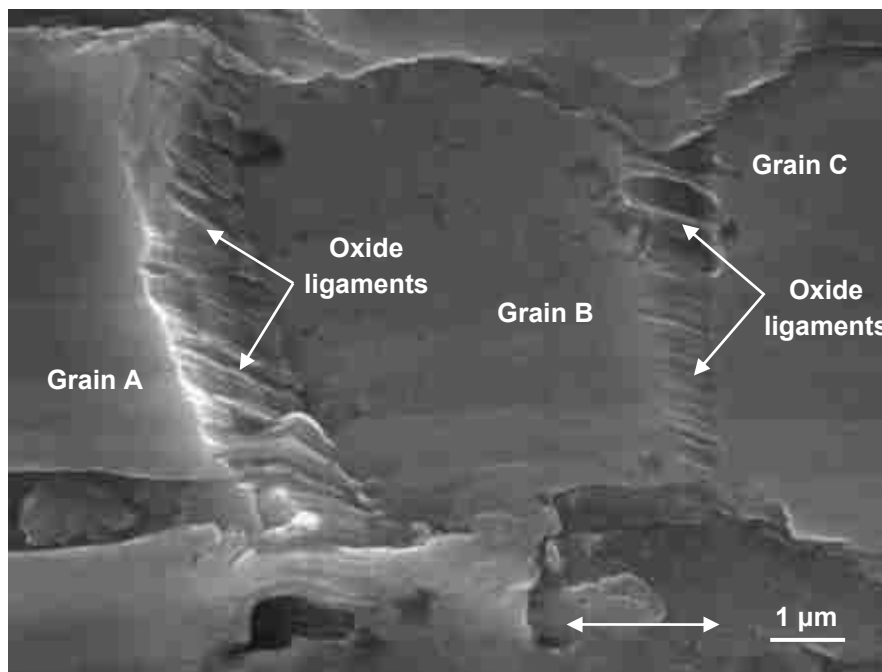
(b)

Figure 4. 3. (a) Secondary electron image showing the surface morphology of the sample deformed at elevated temperatures (545 °C and 4×10^{-2} s^{-1}). (b) A higher magnification view of the sample surface deformed at 545 °C and 4×10^{-2} s^{-1}. The two sided arrow in these and succeeding figures show the tensile direction. Surfaces are covered by oxide layers, and GBS beneath oxide layers is evident.
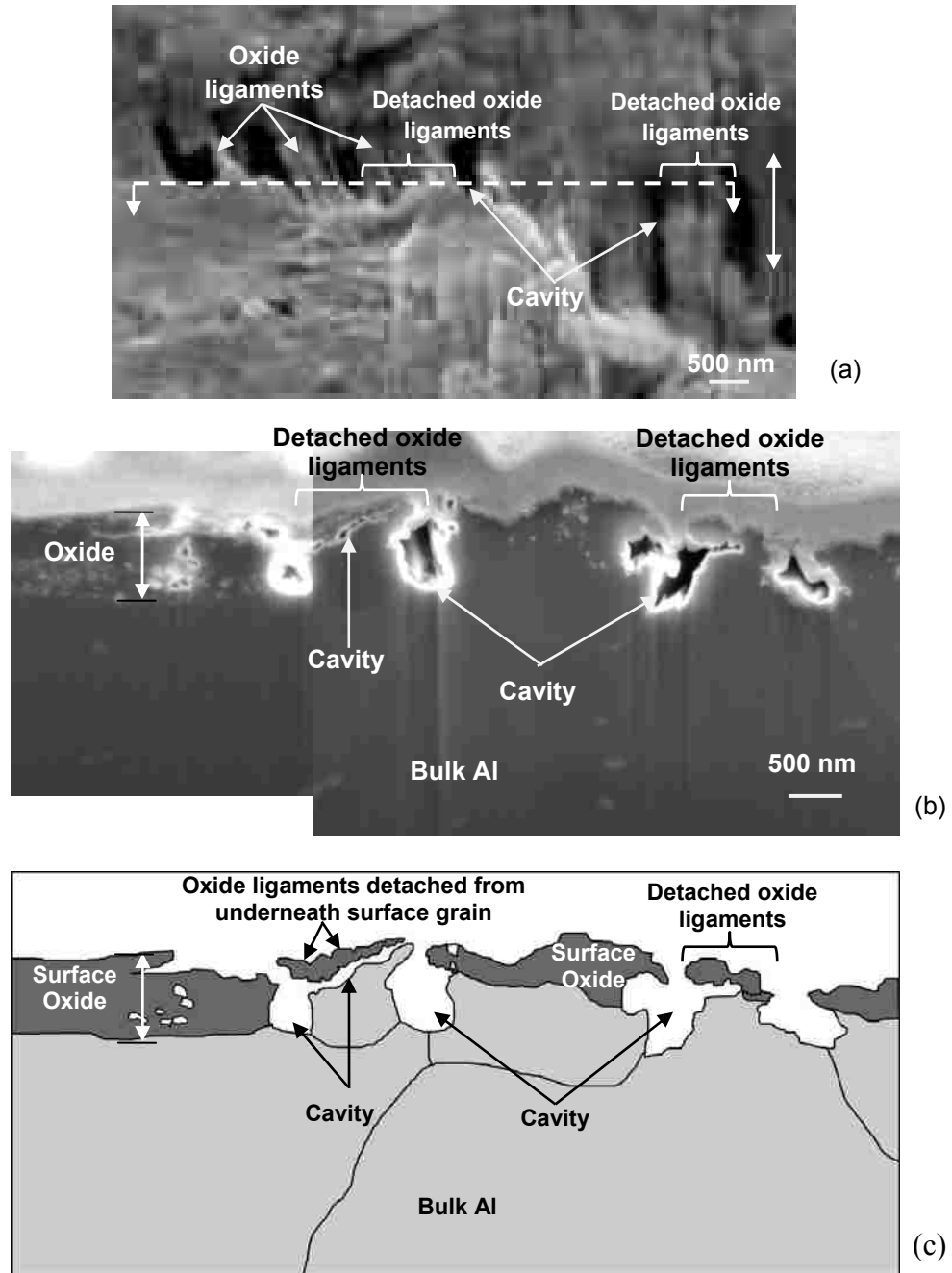
Figure 4. 4. (a) FIB/SEM micrographs of the sample deformed at 545 °C and 4×10^{-2} s^{-1}. The two sided arrow indicates the tensile direction. Plastically deformed surface oxide forms superplastic ligament-like structures at the grain boundaries and tended to align in the tensile direction; (b) FIB cross-section of the sample with superplastic ligaments taken along the dotted line in plate (a). The micrograph shows groups of detached oxide ligaments at two locations (the sheet normal represents the long axis of the ligament). (c) Schematic representation of the micrograph in plate (b) showing the group of ligaments detached from the underneath grains.
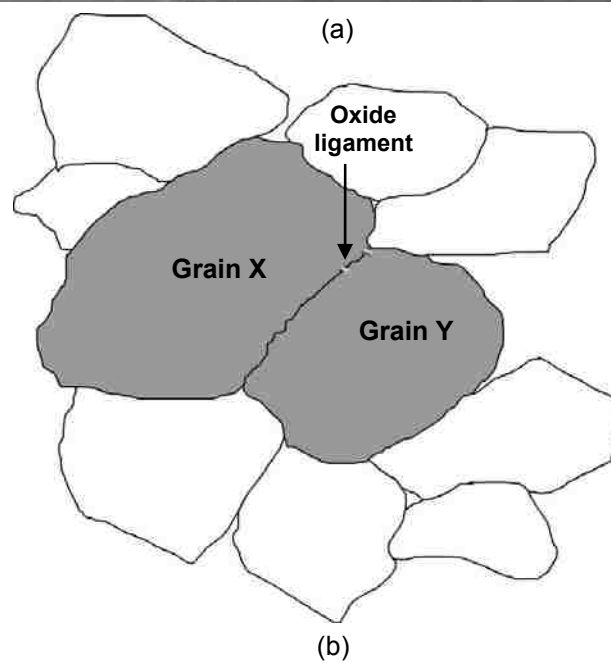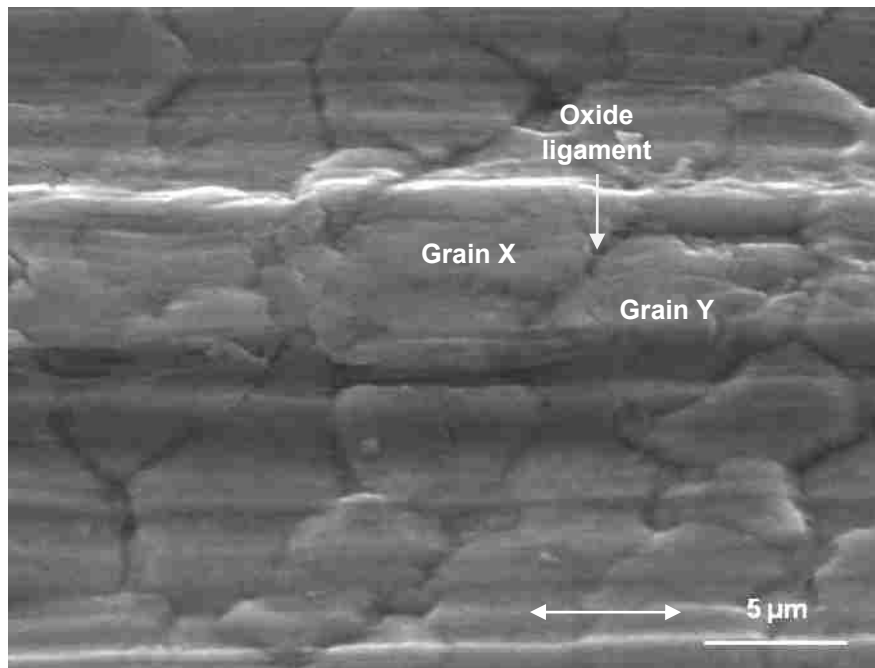
Figure 4. 5. (a) SEM micrograph of the deformed surface corresponding to the condition (545 °C and 1×10^{-2} s^{-1}) where a few oxide ligaments were observed at the grain boundaries. (b) Schematic representation of the grains in plate (a) showing a small oxide ligament between grain X and grain Y.
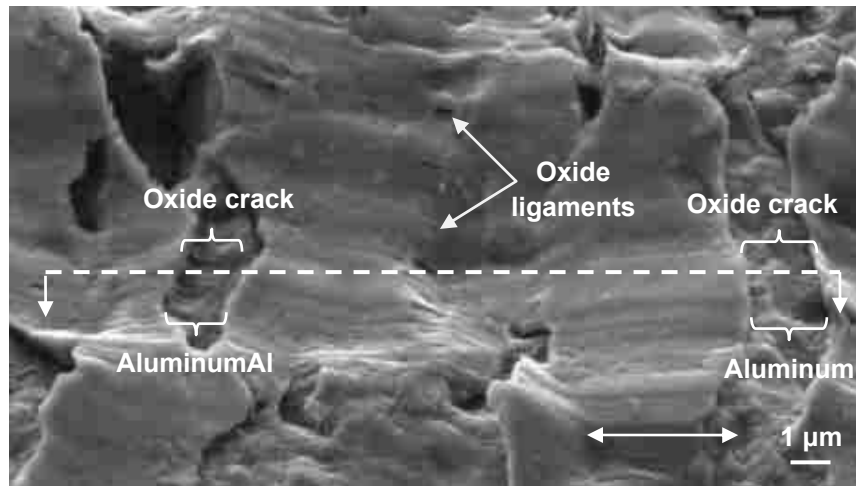
(a)
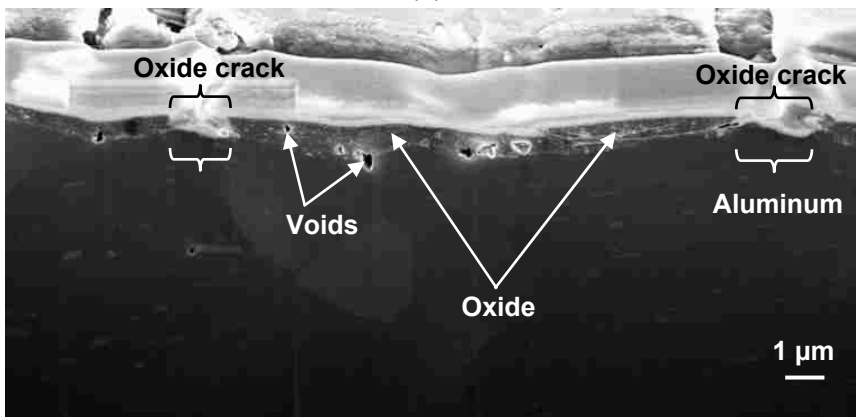
(b)
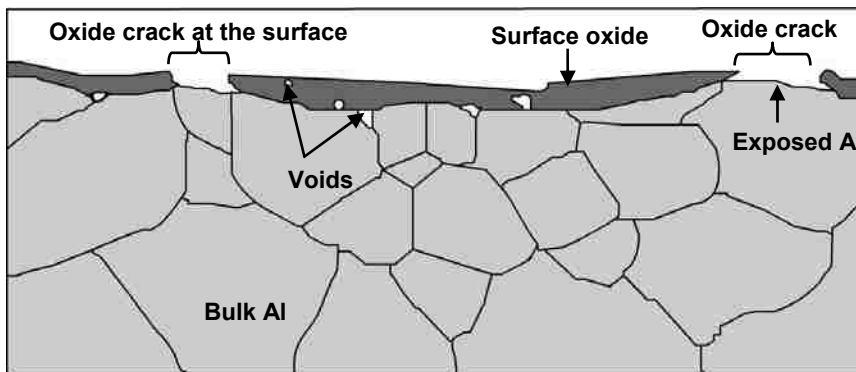
(c)

Figure 4. 6. (a) FIB/SEM micrographs of the sample deformed at 420 °C and 4×10^{-2} s^{-1}. Cracks in surface oxide indicate the brittle nature of the oxide at low temperatures; (b) cross-section of the sample taken along the dotted line in plate (a) revealing aluminum exposure due to the cracks in the surface oxide. (c) Schematic representation of the micrograph in plate (b) outlines the surface oxide, voids formed at the interface between the surface oxide and Al grain, exposed Al due to the oxide cracks at the surface.
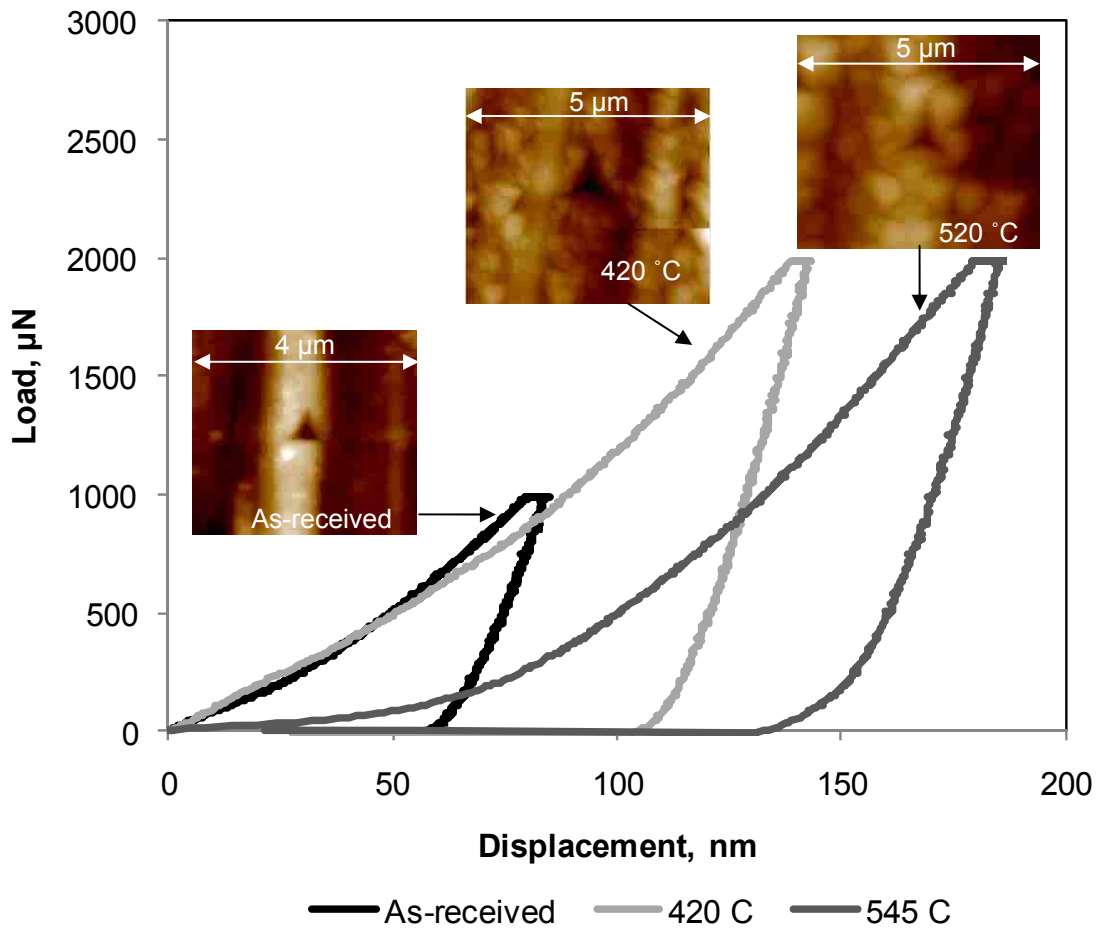
(a)

Figure 4. 7. Typical load vs. displacement plots of room temperature indentations tests on the surface of as-received material, surface deformed at 420 °C and 4×10^{-2} s^{-1}, and surface deformed at 545 °C and 4×10^{-2} s^{-1}. Corresponding images at the top were taken using scanning probe microscopy (SPM) mode of Hysitron Triboindenter. Mechanical properties measured from load-displacement plots of the oxide on the surface of all three samples mentioned above – (b) Young's modulus and (c) Hardness.

(b)

(c)
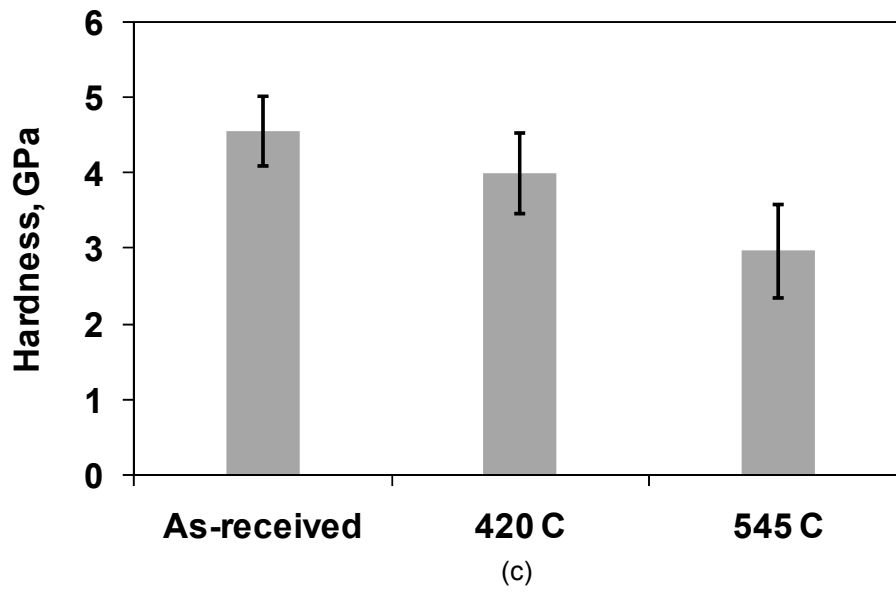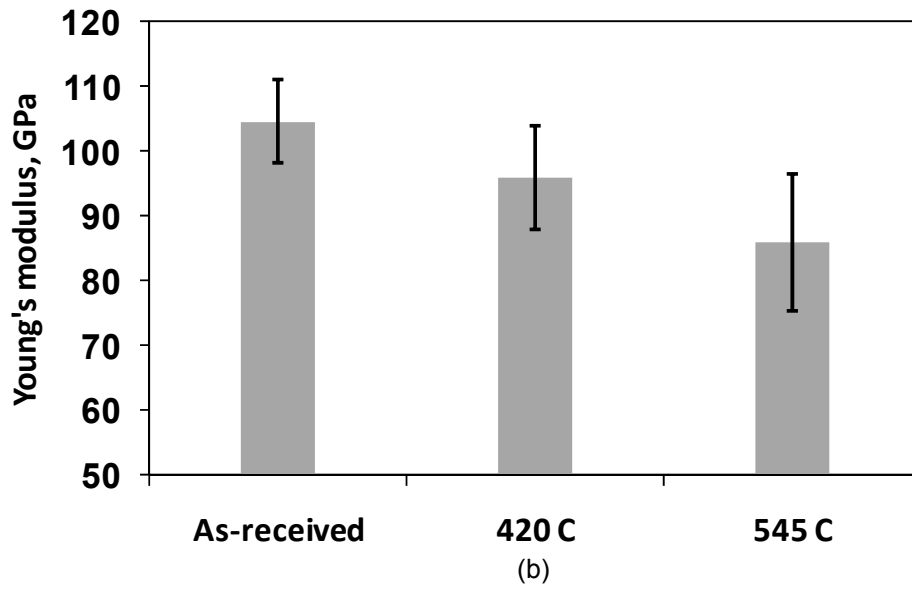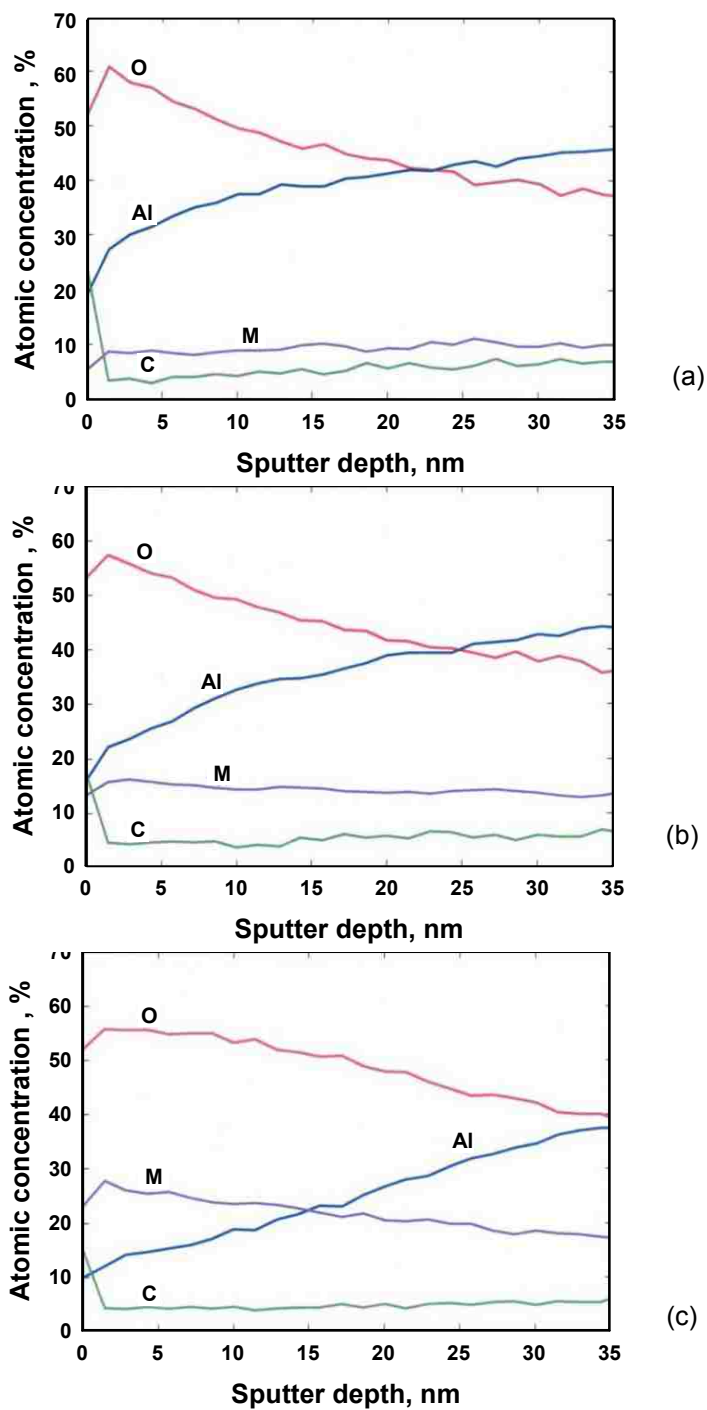
Figure 4. 8. XPS depth profile on the surface (a) initial surface, (b) surface deformed at 420 °C and 4×10^{-2} s^{-1} and (c) surface deformed at 545 °C and 4×10^{-2} s^{-1}. The highest concentration of magnesium was found on the surface deformed at 545 °C and 4×10^{-2} s^{-1}. XPS results illustrating the element concentration varied with deformation temperatures at (d) the surface and (e) 35 nm below the surface.
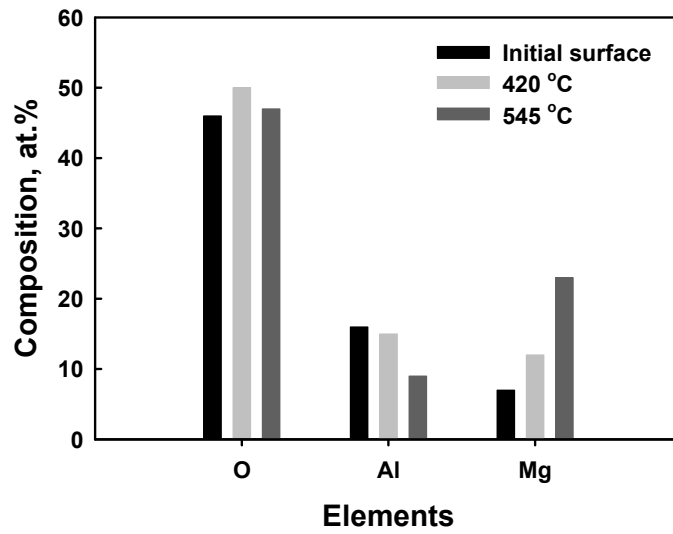
(d)
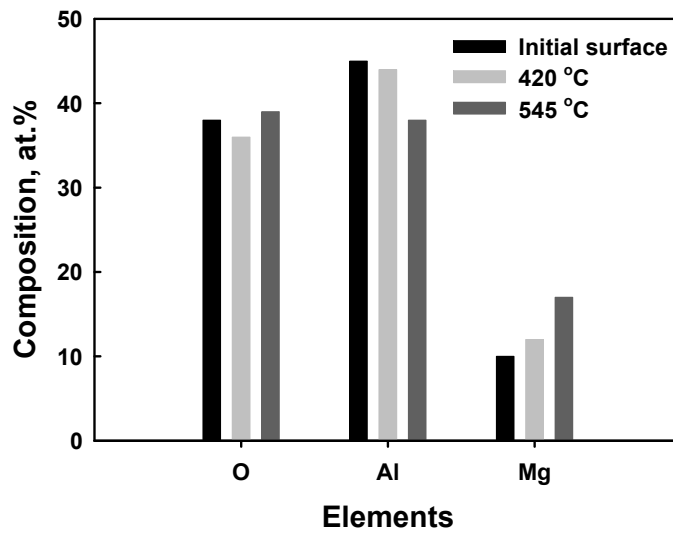
(e)
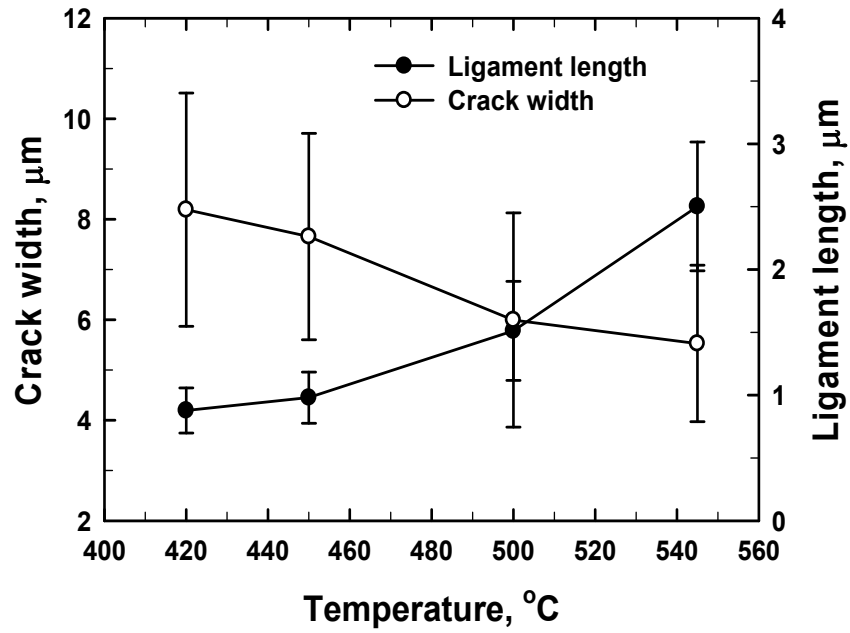
Figure 4. 9. Crack width and ligament length vs. temperature plot at 4×10^{-2} s^{-1} shows that the length of the superplastic ligaments increases with temperature.
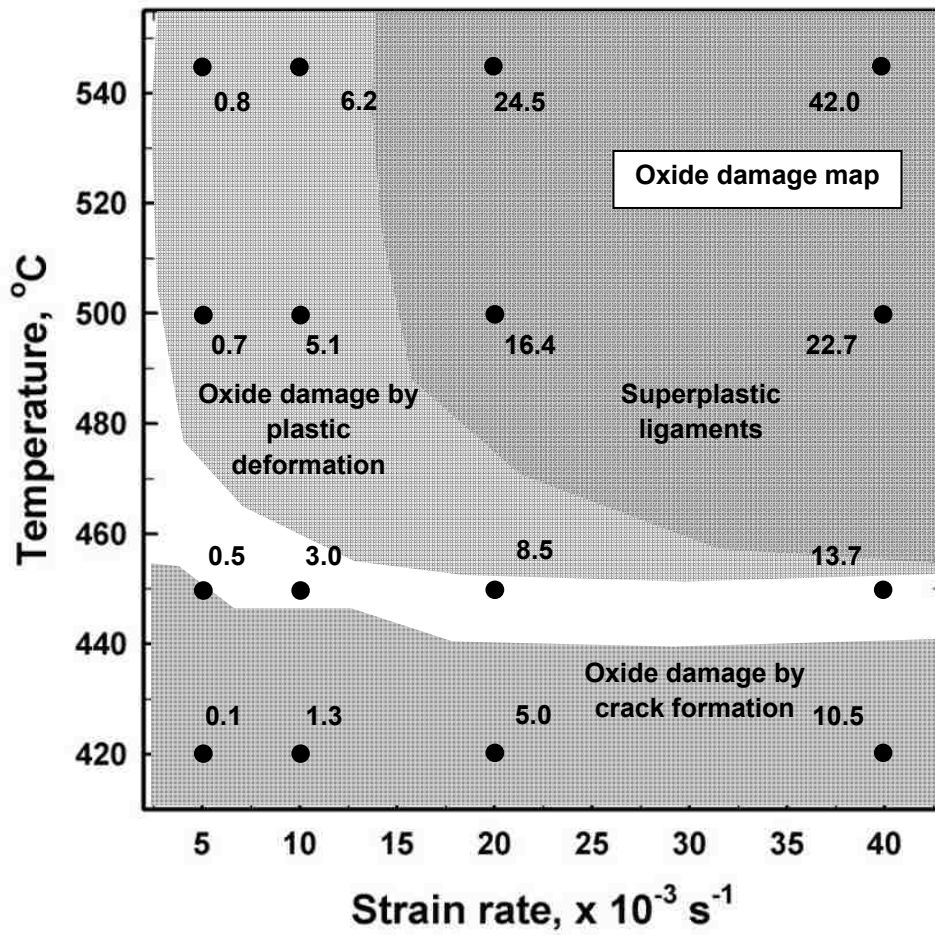
Figure 4. 10. Oxide damage map on temperature vs. strain rate axes where the data points shown are the % oxide ligaments.
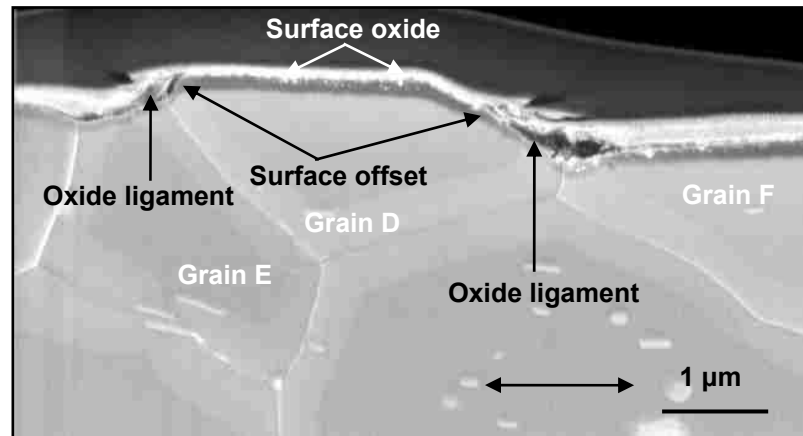
(a)

Figure 4. 11. (a) FIB cross-section of deformed surface taken along the tensile axis to illustrate the superplastic ligament formed at the surface offset that resulted from GBS. (b) TEM micrograph of deformed surface (at 545 °C) along the tensile axis; (c) high magnification image taken from region 'A' in plate (b) showing the formation of superplastic ligaments at the grain boundary between grains A and B; (d) SADP pattern taken from the superplastic ligament in plate (c) (with different rings in the SADP pattern indexed as MgO and $MgAl_2O_4$ spinel phase). (e) Selected area diffraction intensity profile taken from initial oxide layer and superplastic ligament structure.

Surface **Ligament** **Surface oxide**

A

Surface oxide **Grain E** **Grain D**

2 µm

(b)

~400 nm

SADP HRTEM

Surface oxide

Ligament

Grain D

Grain E

Grain boundary

100 nm

(c)

200_{Al}

111_{Al}

$MgAl_2O_4$, MgO
$MgAl_2O_4$, MgO

$MgAl_2O_4$, MgO
$MgAl_2O_4$, MgO

(d)

(e)
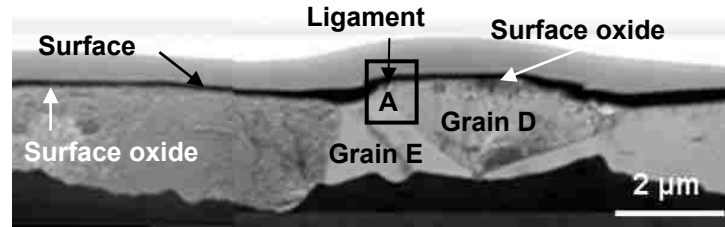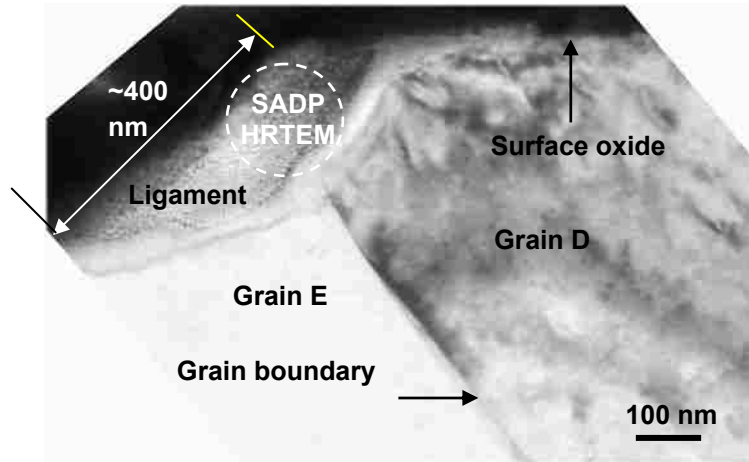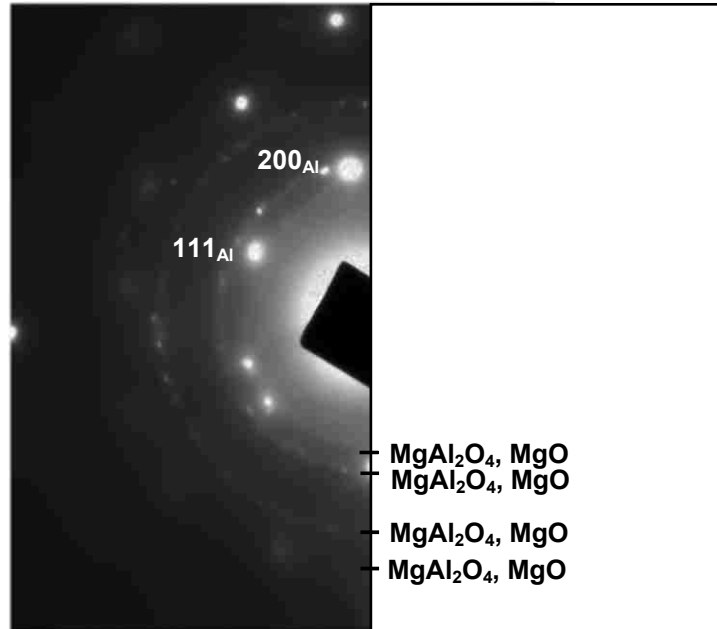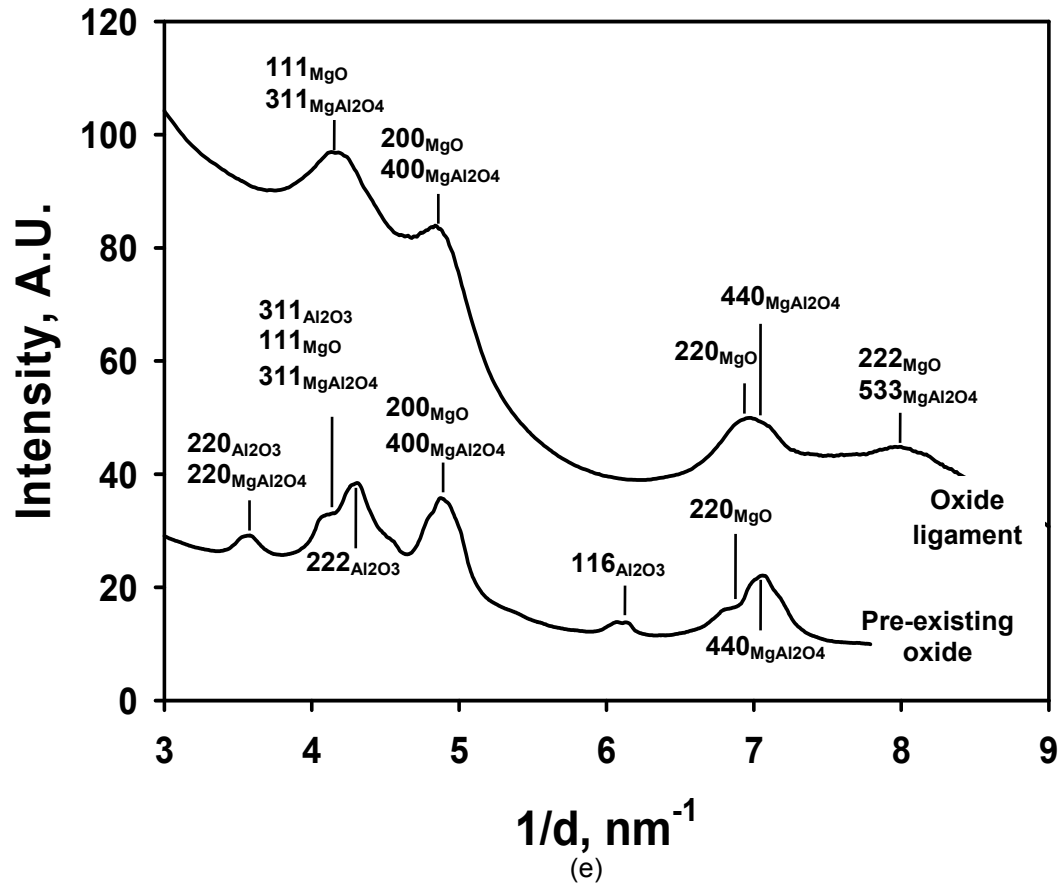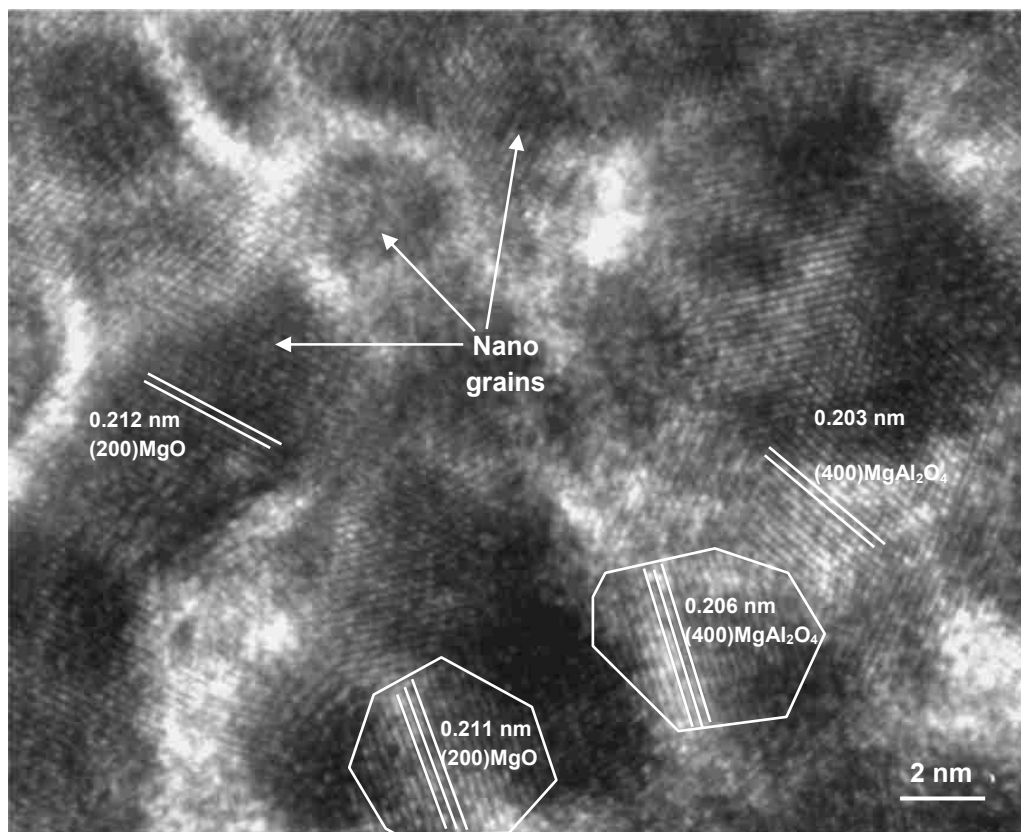
Figure 4. 12. HRTEM micrographs taken from the superplastic ligament in plate (c). Main phases in the superplastic ligament are found to be particles (4.5 ± 0.7 nm) of MgO and $MgAl_2O_4$.
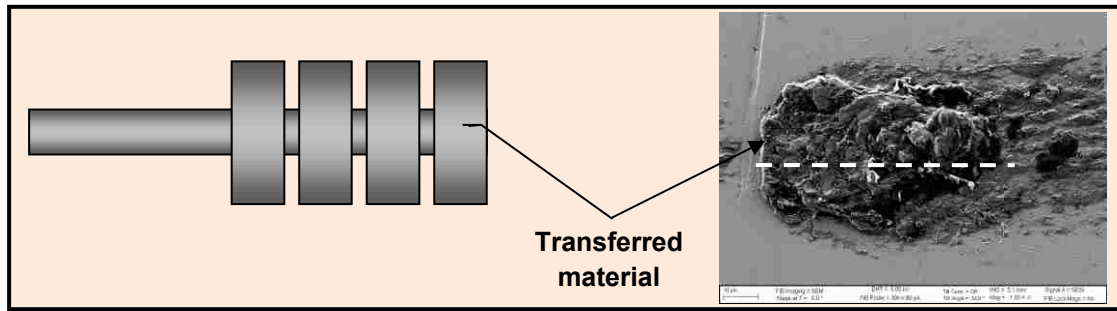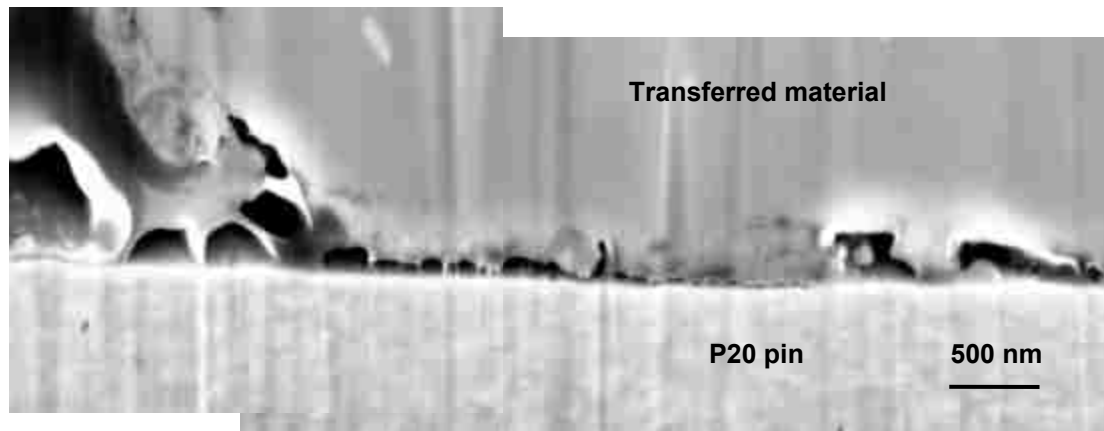
Figure 4. 13. (a) Schematic representation of the P20 steel pin showing the location of transferred material, (b) FIB cross-section of the transferred material showing the material attached to the pin surface. (c) Magnified image taken from the micrograph in plate (b) shows the interface between the transferred material and the P20 pin. (The direction of pin sliding against AA5083 surface is along the cylindrical axis and towards the right side of the pin.)
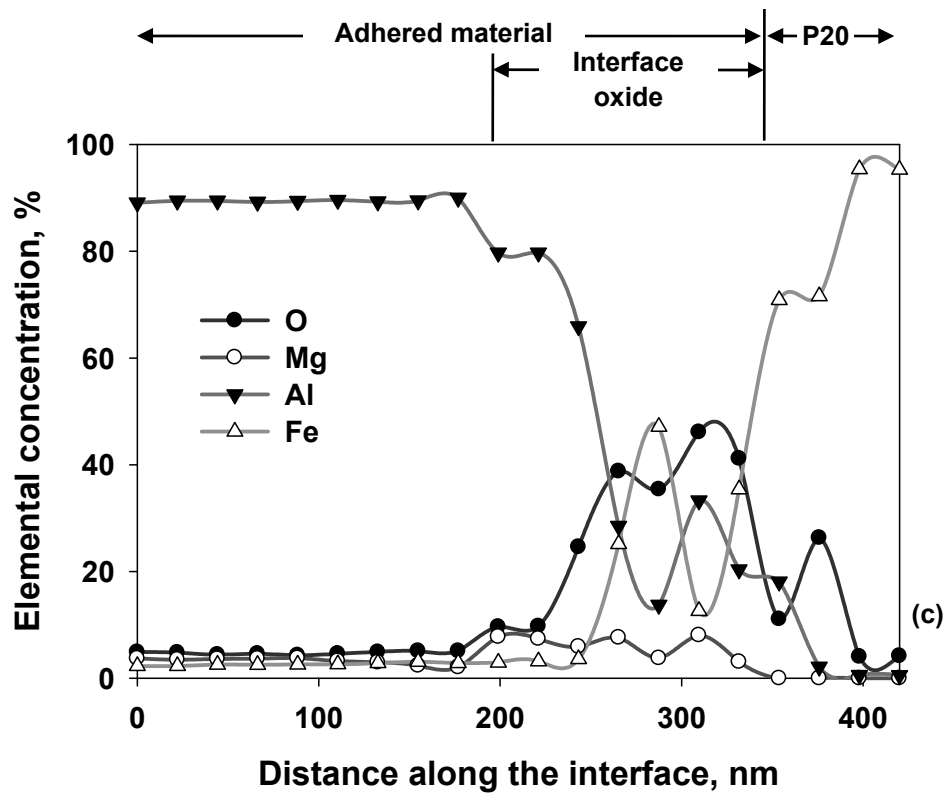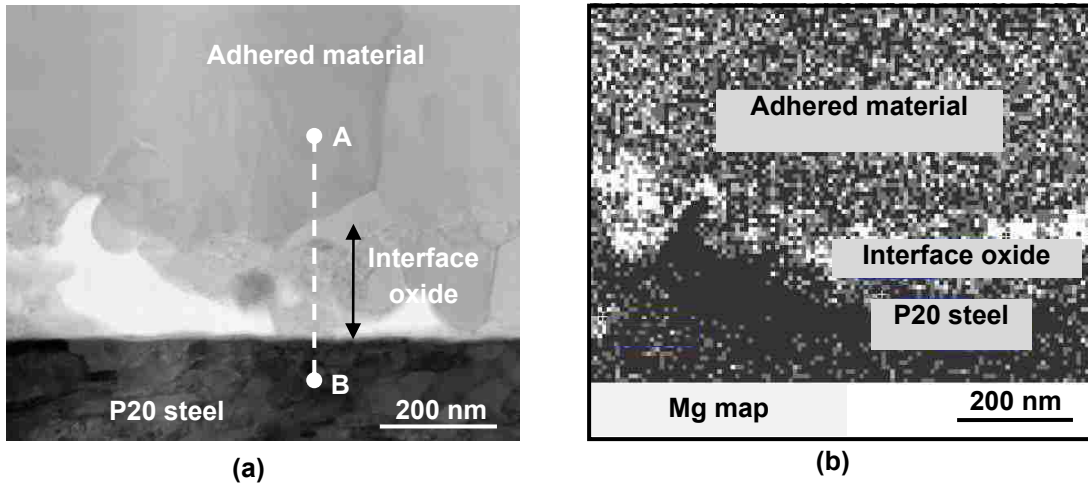
Figure 4. 14. (a) Bright field image of the transferred material showing the interface oxide, (b) Mg dot map taken from plate (a) shows the oxides are rich in magnesium; (c) Elemental concentration across the interface along the dotted line AB in plate (a) shows presence of high oxygen and magnesium and less aluminum in the interface oxide. The '0' value in X-axis represents the location 'A'.
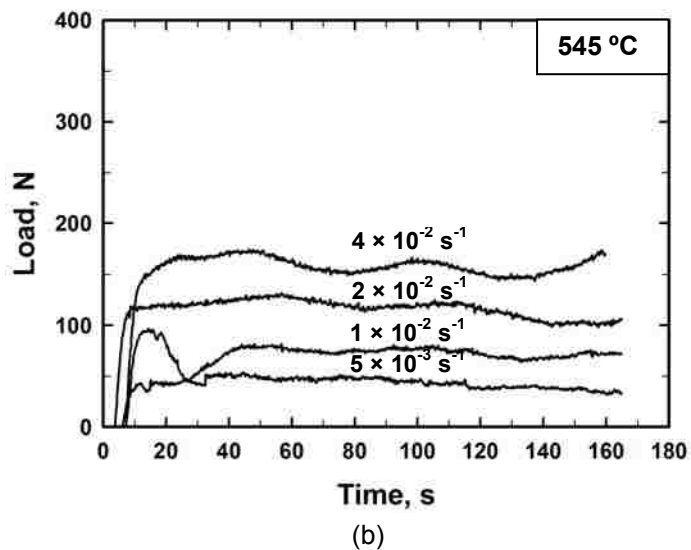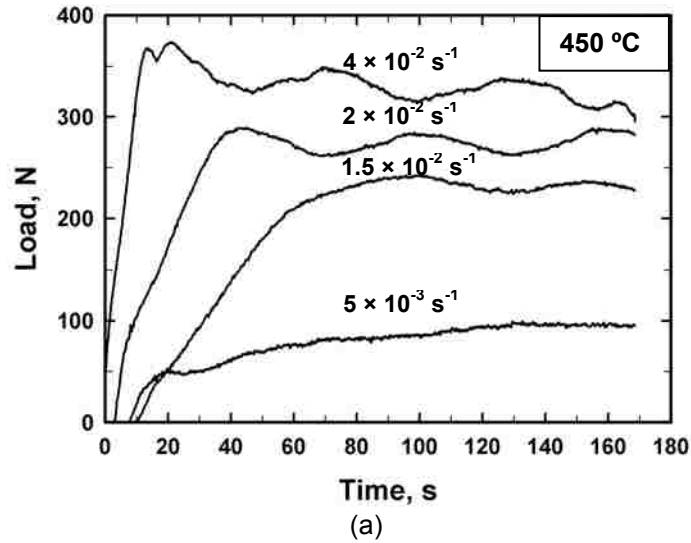
Figure 4. 15. Tensile loads applied to AA5083 strips at different strain rates at (a) 450 °C; and (b) 545 °C. (The time axis indicates the duration of the test, during which a different section of the forward moving strip – 170 mm in length – passes through the hot zone, as shown in Figure 3.5a. The flow stress of the strip was measured at the section that enters the hot zone at $t = 140$ s. True strain rate was determined from the strain differences within a time interval of dt). (c) Flow stress calculated from experimental data in Figures 4.15a and b and plotted on temperature vs. strain rate axes.
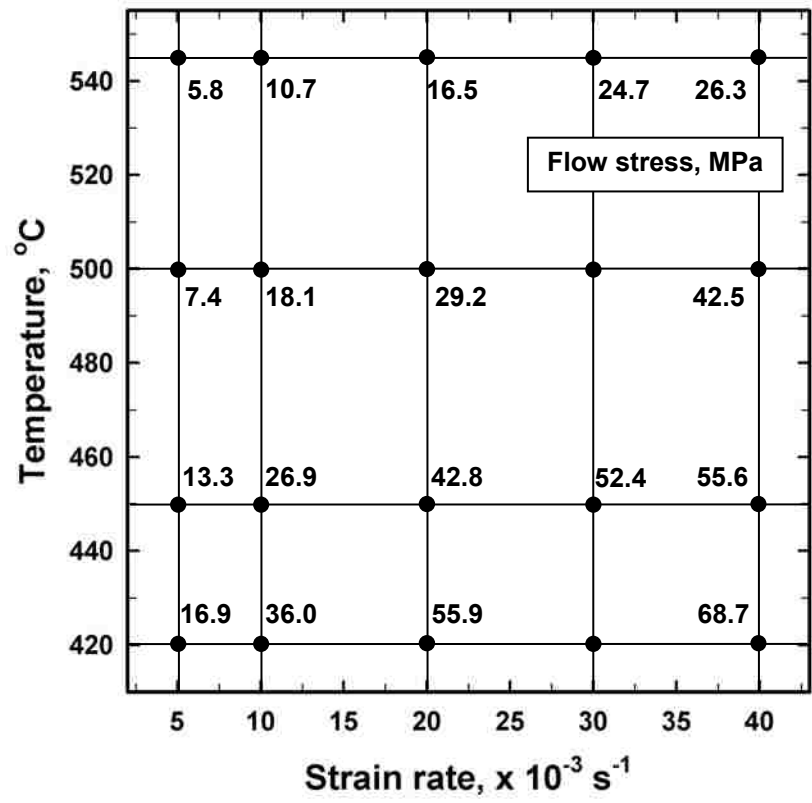
(c)
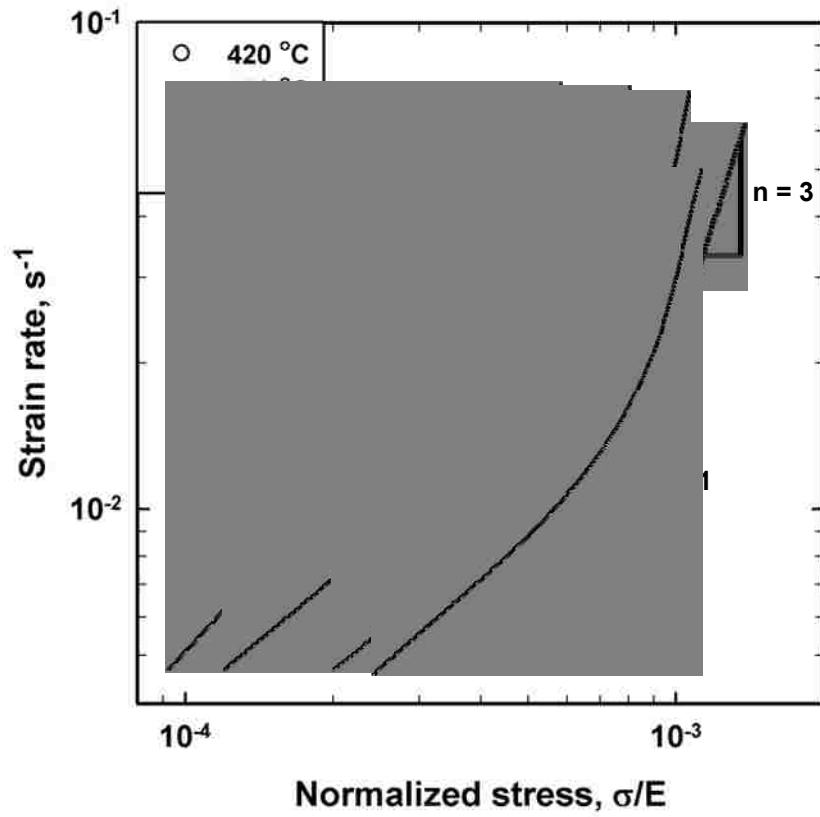
Figure 4. 16. Strain rate vs. modulus compensated flow stress plots following the general creep equation where '*n*' is the stress exponent.
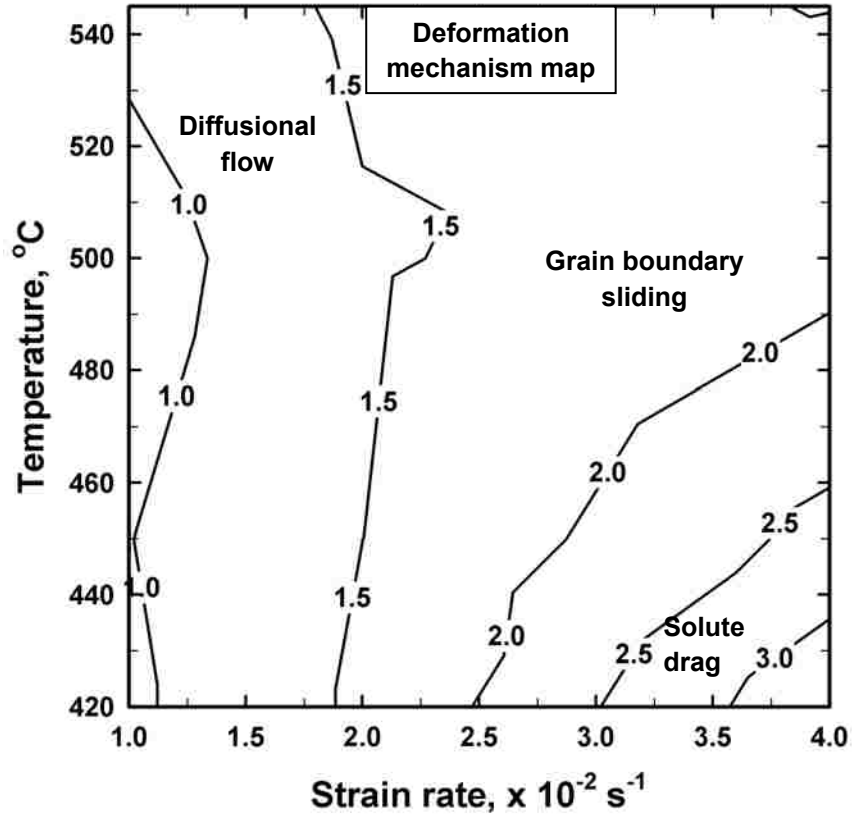
Figure 4. 17. Deformation mechanism map (DMM) for AA5083 plotted on temperature vs. strain rate axes, where the regions of dominance for each mechanism are identified based on the stress exponent value, *n*. The contours are for constant stress exponent values.
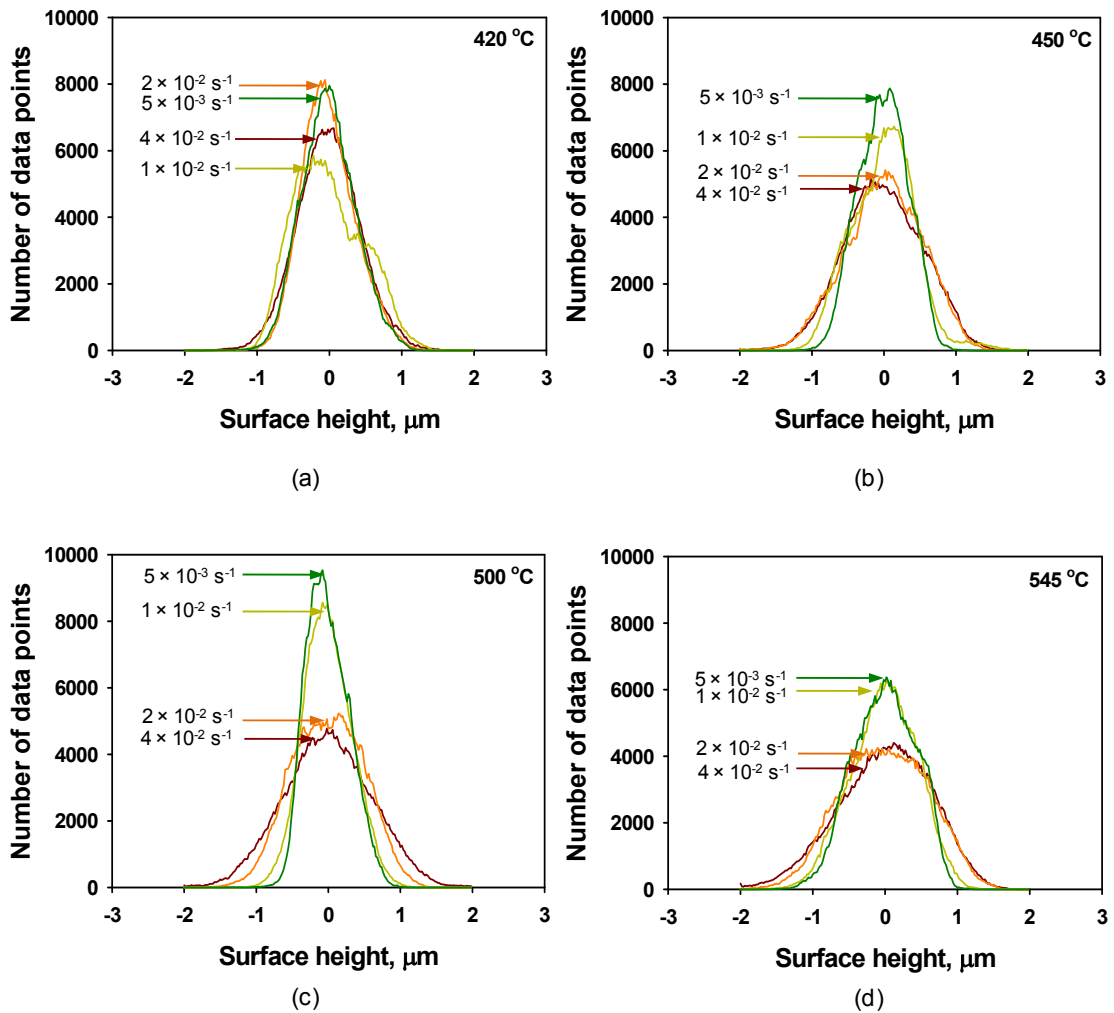
Figure 4. 18. Surface height distribution profiles for surfaces deformed at four temperatures (a) $T = 420$ °C, (b) $T = 450$ °C, (c) $T = 500$ °C and (d) $T = 545$ °C. Measurements at each surface were taken from areas of 120 μm × 90 μm, which were sufficiently large to contain typical surface features, and encompassed 70 − 100 grains.
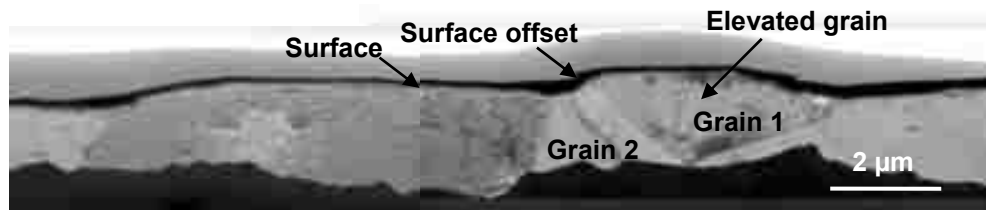
(a)
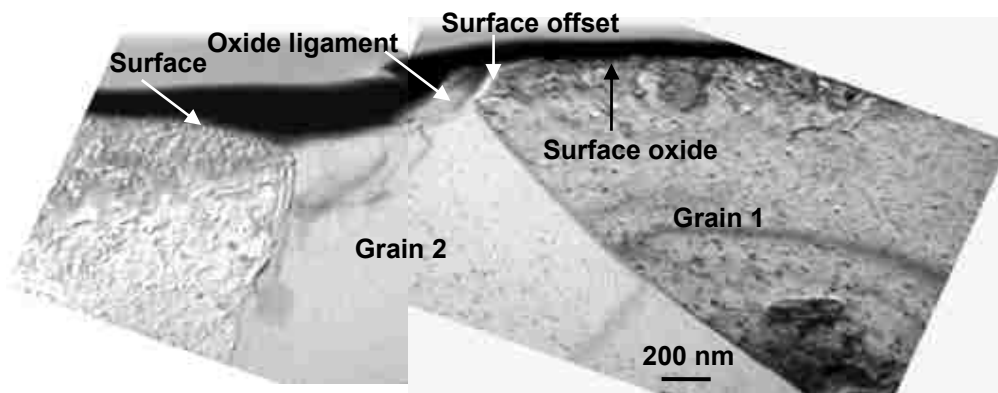
(b)

Figure 4. 19. (a) Cross-sectional TEM Micrographs showing the subsurface microstructure of AA5083 alloys deformed at 545 °C at 4×10^{-2} s^{-1}; (b) high magnification image taken from plate (a) showing that Grain 1 is at a higher elevation than Grain 2, which indicates the occurrence of relative sliding between them. (c) cross-sectional TEM micrographs showing the subsurface microstructure of AA5083 alloys deformed at 420 °C and 4×10^{-2} s^{-1}; and (d) a high magnification image taken from plate (c) that shows the formation of a subgrain structure.
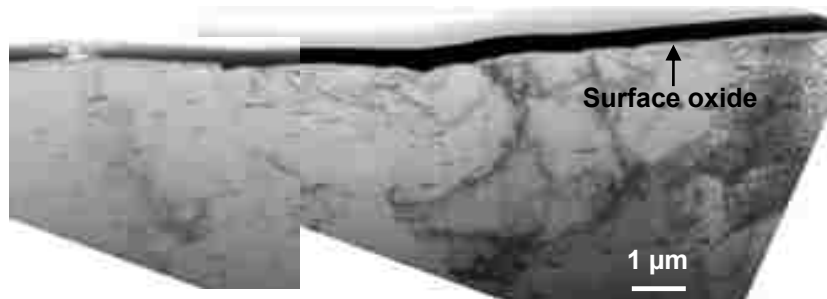
(c)
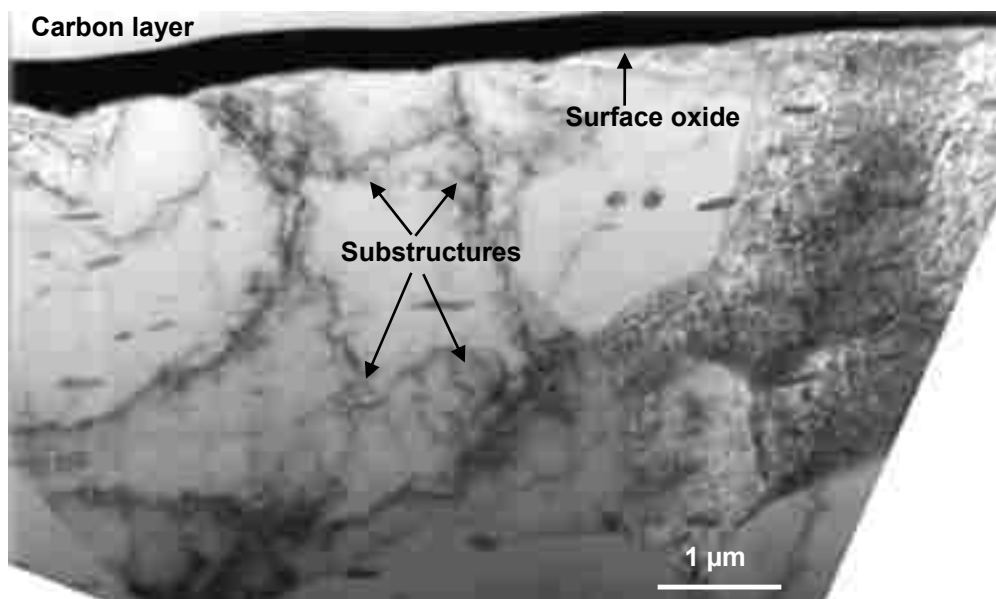
(d)
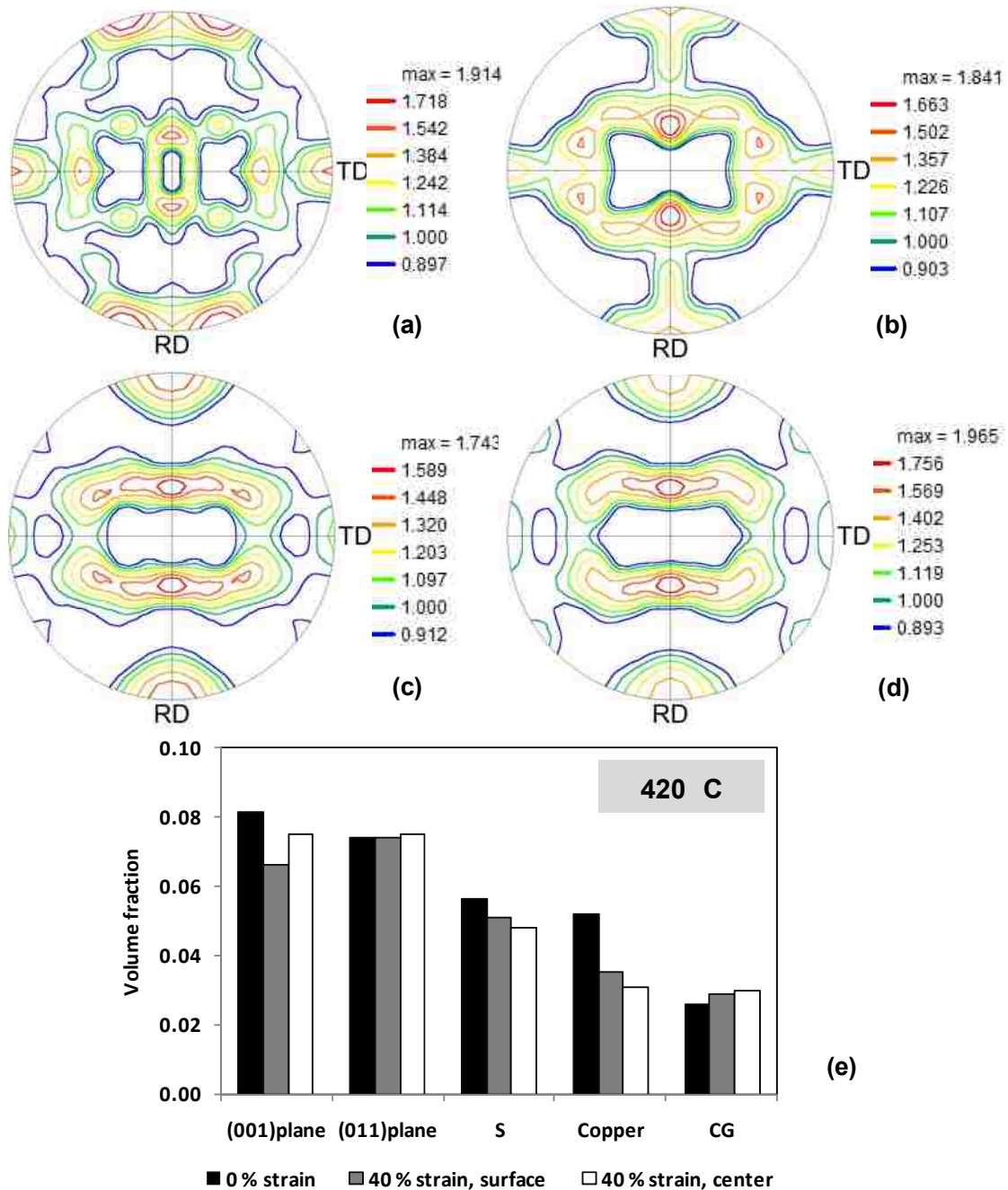
Figure 4. 20. (a) (111) pole figure of as-received sample. (111) pole figures for series of samples at 420 °C (b) sample without any application of strain (c) and (d) sample deformed using hot-forming simulator by simultaneous application of 6 % bending strain and 40 % tensile strain. Pole figure in plate (c) and plate (d) were taken from the OD and the centre area respectively (as explained in Figure 3.12). (e) Volume fraction of different orientation components in the material at 420 °C.
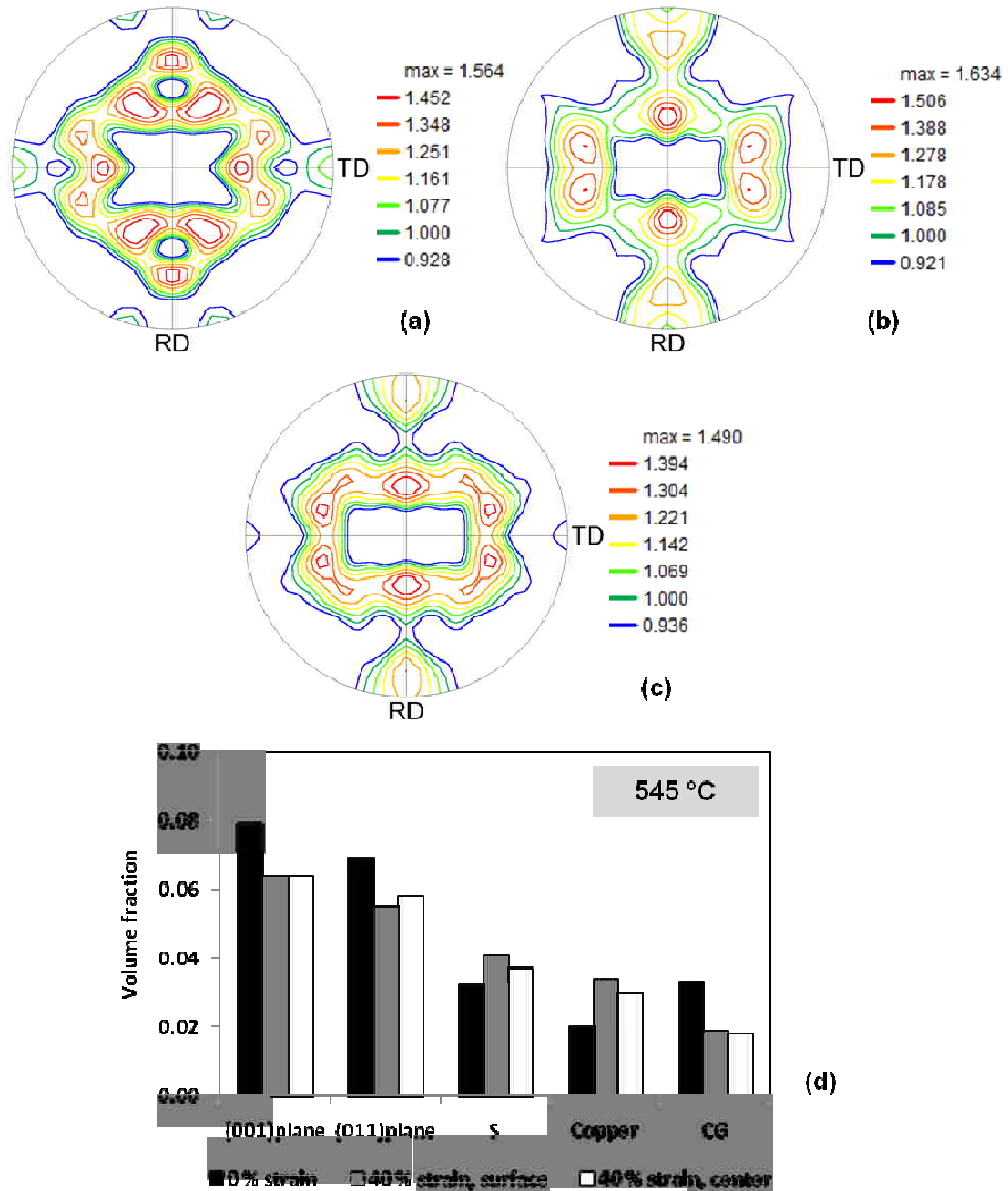
Figure 4. 21. (111) pole figures for series of samples at 545 °C (a) sample without any application of strain (b) and (c) sample deformed using hot-forming simulator by simultaneous application of 6 % bending strain and 40 % tensile strain. Pole figure in plate (b) and plate (c) were taken from the OD and the centre area respectively (as explained in Figure 3.12). (d) Volume fraction of different orientation components in the material at 545 °C.

Chapter 5 Friction and Deformation Mechanisms of AZ31 Alloy

5.1. Introduction

This chapter describes the relationship between COF and deformation mechanisms in the AZ31 alloy, a typical light weight Mg alloy. This alloy is a superplastic material used to produce automotive components (such as deck lids and door inner panels) by hot forming.

Section 5.2 presents the results on the variation in the COF of the AZ31 alloy with temperature and strain rate. **Section 5.3** describes the evolution of the surface, that is, surface roughness, surface morphology, and microstructure. Characterization of oxide present on the alloy sheet surface and how this can be related to the COF are also considered in the same section. **Section 5.4** describes the microstructural evolution and morphologies that developed during high temperature deformation. Deformation mechanisms operating in the material under the experimental temperature (250 – 450 °C) and strain rate ($5 \times 10^{-3} - 4 \times 10^{-2}$ s^{-1}) conditions are identified and discussed in **Section 5.5**. In the same section, deformation mechanisms are related to the microstructural evolution of the bulk material. **Section 5.6** discusses the deformation mechanisms that operated during the high temperature sliding process (without subjecting the samples to external strain). Microstructural evolution and material transfer process due to sliding induced damage are also discussed in the same section. Finally, a brief summary on the relationship between COF and deformation mechanisms is provided in **Section 5.7**.

5.2. Variation in coefficient of friction (COF) with temperature and strain rate

The COF of the AZ31 alloy tested against the P20 steel was 0.25 ± 0.06 when measured at room temperature without applying external strain. Typical COF vs. sliding time plots, obtained at two different temperatures (300 °C and 450 °C) and at two different strain rates of 1×10^{-2} s^{-1} and 4×10^{-2} s^{-1}, are shown in **Figures 5.1a and b**. COF measured at a strain rate of 4×10^{-2} s^{-1} and temperature of 450 °C resulted in an average COF of 0.89 ± 0.20, which was the highest COF value measured under present experimental conditions. At a low strain rate of 1×10^{-2} s^{-1}, the COF value varied between 0.34 ± 0.13 at 300 °C and 0.59 ± 0.16 at 450 °C. The average COF values at different temperatures and at two strain rates are plotted in **Figure 5.1c**. The values reported are taken by averaging COF data from two experiments. The standard deviation in the plot represents the variation in COF value over a 100 s time span. **Figures 5.1a and c** show that for the tests at 450 °C, COF became more sensitive to the applied strain rate. At a high strain rate of 4×10^{-2} s^{-1}, the COF increased from 0.55 ± 0.14 at 300 °C to 0.89 ± 0.20 at 450 °C. For the representation of the effect of temperature and strain rate under various conditions, the COF values are plotted as map on temperature vs. strain rate axes as shown in **Figure 5.1d**. The data in **Figure 5.1d** is later used for generating the COF-deformation mechanism map (COF-DMM) in **Chapter 6**.

5.3. Surface evolution and COF

In order to understand the variation in COF with temperature and strain rate, the surface characteristics generated under these deformation conditions were studied and discussed in **Sections 5.3.1-5.3.3**.

5.3.1. Microstructural evolution of the surface

The morphologies of the as-received surface as well as the surface deformed at elevated temperature were viewed under the SEM and are shown in **Figure 5.2**. The micrograph in **Figure 5.2a** shows the presence of patches of oxide layer on the surface of the as-received material. **Figure 5.2b** shows a typical surface microstructure of the sample deformed at $T = 450$ °C and $\dot{\varepsilon} = 4 \times 10^{-2}$ s^{-1}. The micrograph shows a number of islands of oxides lying on the surface. Ligaments up to a 2 µm long can be seen between these oxide islands. These ligaments are formed in such a way that their long axes were aligned along the tensile direction of the sample as shown in a higher magnification view in **Figure 5.2c**. Also, at certain locations the grains underneath the oxide layer could be identified by their facetted appearance as in **Figure 5.2d**. The facetted appearance at the surface is due to the out-of-plane sliding of the surface grains. However, ligament structures in this alloy were found only between the fractured oxide islands (**Figure 5.2c**). Very few ligaments were observed on oxide layers between the grains showing the facetted appearance generated due to out-of-plane sliding of grains (**Figure 5.2d**). Out-of-plane sliding of the surface grains occurred throughout the sample surface. However, their facetted appearance was masked by the oxide islands and became visible only in the areas without broken oxides on the surface as in **Figure 5.2d**. Unlike aluminum alloy, the

evidence of grain boundary sliding (GBS) is not very obvious in AZ31 alloy, where the surface is covered with a layer of non-uniform initial oxide. The ligaments formed at the surface cracks were also observed at temperature as low as 250 °C when deformed under the applied strain rate of 2×10^{-2} s^{-1} as shown in **Figure 5.2e**. However, at this temperature a few cracks were observed at the surface. Irrespective of the deformation temperature, the ligaments were formed between the fractured and separated oxide islands as in **Figures 5.2c and e**.

In summary, the surface of AZ31 alloy was covered with a layer of broken oxides when deformed at elevated temperature ($\geq$ 250 °C). These oxides on the deformed surface were completely fractured and separated at 450 °C and 4×10^{-2} s^{-1} and appeared as oxide islands, whereas at low temperature of 250 °C and strain rate of 2×10^{-2} s^{-1}, the damage to the surface oxide was limited to cracks, and only a few oxide islands were observed on the surface. Local oxide superplasticity was evident in certain locations (between the oxide islands and at the cracks) in the form of ligaments. A detailed analysis of the characteristics of the surface oxide is presented in **Section 5.3.2**.

5.3.2. Characterization of surface oxide

The surface morphology of the sample deformed at 450 °C and 4×10^{-2} s^{-1} is shown in **Figure 5.3a**, where cracks in the surface oxides running in the direction normal to the stretching direction are visible. The FIB–milled cross-section taken along the dotted line in **Figure 5.3a** is shown in **Figure 5.3b**. The oxide layer on the surface was non-uniform in thickness, with thickness changing from 200 nm to 1 µm in the same cross-section of 15 µm wide. Between the fractured oxides, the ligaments were also seen as indicated in the microstructure. The TEM micrograph of one such area with a ligament

is shown in **Figure 5.3c**. A high magnification image taken from **Figure 5.3c** is shown in **Figure 5.3d**. **Figure 5.3e** shows the selected area diffraction pattern (SADP) of the ligament taken from the location identified by the dotted circle in **Figure 5.3d**. Diffraction rings in the SADP were indexed as {111}, {200}, {220}, and {311} MgO, with a space group of Fm-3m. These rings in SADP are also very close to {311}, {400}, {440}, and {533} of the fcc $MgAl_2O_4$ spinel phase, with a space group of Fd-3m. The AZ31 alloy has 3 % aluminum. The activation energy of aluminum diffusion in magnesium (143 kJ/mol [24]) and magnesium self-diffusion (135 kJ/mol [67]) are very close. Therefore, enrichment of the spinel phase in the surface layer due to outward diffusion of aluminum is most likely to occur. The ring patterns in SADP (**Figure 5.3e**), taken using an aperture of 250 nm in diameter, are an indication of the nanocrystalline nature of these oxide grains in the oxide ligament structures on the surface of AZ31 alloy.

Microstructural evolution of the surface of the sample under different temperature and strain rate conditions resulted in changes in the surface roughening. Variation in surface roughness due to deformation of the surface oxide and the surface grains at different temperatures and strain rates will be discussed in the next section.

5.3.3. Quantification of surface roughness

The surface morphology of the as-received samples and those tested at high temperatures were studied with a digital optical interferometer. The distribution of the surface heights were plotted in the form of histograms (**Figures 5.4a to d**). **Figure 5.4a** shows the surface height distribution obtained from the surface subjected to $T = 300$ °C at four strain rates of 5×10^{-3} s^{-1}, 2×10^{-2} s^{-1}, 3×10^{-2} s^{-1} and 4×10^{-2} s^{-1}. The arithmetic mean deviation of the surface height distribution is the measure of surface roughness, R_a.

The average surface roughness measured over 300 μm × 225 μm area at five different locations and data are plotted on temperature and strain rate axes as shown in **Figure 5.4e**. A roughness map has been generated by connecting the similar R_a data with iso R_a contours plotted on temperature and strain rate axes as shown in **Figure 5.4f**. The surface roughness under the deformation conditions generated in temperature range between 250 °C and 450 °C and the strain rate range of $5 \times 10^{-3} - 4 \times 10^{-2}$ s^{-1} varied between 0.61 μm and 1.66 μm. At a low temperature of 250 °C, the surface roughness increased from 0.61 μm (at 5×10^{-3} s^{-1}) to 1.24 μm (at 4×10^{-2} s^{-1}). However, at temperatures ≥ 300 °C, the variation in roughness was found in the range of $1.19 - 1.66$ μm. The out-of-plane sliding of surface grains underneath the surface oxide layer did not contribute significantly to increase in surface roughness. This is because the surface roughening due to the damage in the surface oxide was much more extensive than the roughening resulting from GBS.

Roughness of the polished surface (without the pre-existing oxide layer) was also measured after deformation at different temperatures (250 − 450 °C) and two strain conditions (1×10^{-2} s^{-1} and 4×10^{-2} s^{-1}) and plotted as shown in **Figure 5.5**. **Figure 5.5** shows that the roughness of the surface increased with increase in temperature as well as with increase in strain rate. The highest roughness of 0.92 ± 0.06 μm was observed on the surface of the material deformed at 450 °C and 4×10^{-2} s^{-1}.

The surface roughness of the AZ31 alloy with the pre-existing oxide layer did not show a direct correlation with the COF of the alloy. Experiments were also done on the polished surface, where the initial pre-existing surface oxide was removed by mechanical polishing, which would help in identifying the role of the surface oxides and GBS on

COF. Variation in COF and surface morphology evolution of polished samples with temperature and strain rate are discussed in **Sections 5.3.4 and 5.3.5**.

5.3.4. Effect of surface oxide on COF

The initial oxide layer of the AZ31 alloy was mechanically removed by grinding with 240g, 600g, and 1200g sand paper followed by 1 μm diamond polishing. **Figure 5.6a** shows the variation of COF between polished sample and P20 steel pin with temperature at two strain rates. The COF values in this plot showed a slight increase with the temperature as well as with the strain rate. The COF data measured on the polished surface and the as-received surface were compared by plotting them together in **Figures 5.6b and c**. At strain rate of 1×10^{-2} s^{-1}, COF of the as-received surface is lower than the COF of the polished surface under all temperature conditions. When the applied strain rate increased to 4×10^{-2} s^{-1}, COF of the as-received sample remained low up to a temperature of 400 °C. Therefore, the pre-existing oxide layer reduced COF up to a temperature of 400 °C, where GBS is masked by the same oxide layer. However, at a temperature of 450 °C and a strain rate of 4×10^{-2} s^{-1}, the as-received sample showed higher COF than that of polished surface as in **Figure 5.6c**. At this deformation condition, the pre-existing oxide layer did not act as a protective layer. In fact, the oxide islands present on the deformed surface, as seen in **Figures 5.2a and b**, might act as abrasive and increase the COF of the sliding pair.

5.3.5. Microstructural evolution of the polished surface

Microstructural features of the worn surface after a single pass sliding experiments using hot-forming simulator on the polished surface of AZ31 alloy are

shown in **Figures 5.7a to f**. The figure shows the width of the wear track increased with the temperature and also with the strain rate. More specifically, the contact width of the wear track increased from 13.8 ± 2.0 µm at 300 °C and 1×10^{-2} s^{-1} to 22.1 ± 0.3 µm at 300 °C and 4×10^{-2} s^{-1}, as shown in **Figure 5.7g**. Similarly, for the strain rate of 4×10^{-2} s^{-1}, changing the temperature to 450 °C made the contact width as wide as 47.3 ± 3.5 µm. Increase in strain rate increased the surface roughness (see **Figure 5.5**). The increase in the width of the wear track was attributed to the increase in surface roughness. Also, the wear track at high temperature (> 350 °C) was intermittent compared to the continuous wear track observed at low temperature of 300 °C as shown in **Figure 5.7**. The surface of the AZ31 alloy deformed by cooperative grain boundary sliding (CGBS), which occurred through the movement of grain groups as an entity. The CGBS mechanism generates a wavy pattern on the deformed surface as shown in **Figures 5.8a to d**. **Figures 5.8a to d** showed surface profiles of the polished surface after deformation at two temperatures of 350 °C and 450 °C and at two strain rates of 1×10^{-2} s^{-1} and 4×10^{-2} s^{-1}. It was reported that CGBS usually occurred during the initial stage of superplastic deformation in some superplastic Al or Ti base alloys [170,171]. 2-D profiles taken along the dotted lines in **Figures 5.8a to d** are shown in **Figure 5.8e**. The wavy patterns of the deformed surface due to CGBS are well captured in this figure. For instance, the profile of the surface deformed at 450 °C and 4×10^{-2} s^{-1} strain rate showed three major peaks. Each individual big peak in the profiles was also consisted with a few small peaks, which formed due to GBS of individual grains within the large peak. Spacing between the small peaks also matches well with the size of the individual grains (see **Section 5.4**). The elevated grains on the surface due to deformation through

CGBS were in contact while sliding against the counterface. The elevated grains led to the increase in surface roughness with increase in strain rate and temperature of deformation (see **Figure 5.5**). The increase in surface roughness is the cause of high COF observed at high temperature and high strain rate as in **Figure 5.6**. The bulk material exhibiting signs of CGBS also showed a gradient in microstructure with temperature and strain rate and will be discussed in the next section.

5.4. Microstructural evolution of the bulk material and generation of grain size map

Microstructures of the bulk material after each experiment were examined optically in the subsurface plane, parallel to the transverse plane. The microstructure of the as-received alloy (see **Chapter 3**) was transformed into recrystallized microstructure upon heating > 250 °C. The microstructure became coarser at higher temperature. The average grain size was measured using the linear intercept method, and grain size of 6.12 ± 0.59 μm and 11.80 ± 0.87 μm were found in the material when heated to 300 °C and 450 °C respectively. The microstructures of the samples deformed at various temperatures and strain rates are presented in **Figure 5.9**.

At low temperatures (300 °C) and low strain rates (5×10^{-3} s^{-1}), the grains are 6.61 ± 0.69 μm in diameter with an equiaxed shape. When the test temperature was increased and the strain rate kept constant, the grain size increased up to a maximum value of 12.7 μm at 450 °C. A microstructural feature that can be noted in **Figure 5.9** is the effect of deformation condition on the grain boundary morphology. At low temperatures ($\leq$ 350 °C), the grain boundaries became serrated when the strain rate of

deformation was increased, and as a result, the grains became irregular in shape. However, at high temperature of 450 °C, no serration at the grain boundary was observed when deformed at a high strain rate of 4×10^{-2} s^{-1}. The formation of serrated boundaries was also observed previously in AZ31 alloy at a temperature range of 250 °C – 350 °C [118,172]. In that study the author described the bulging of a grain boundary due to dynamic recrystallization, which led to microscopic strain localization in slip lines near the grain boundaries. They assume that the interfering dislocation slip systems on both sides of the boundary contribute to the manifestation of the grain boundary serrations. This effect was also found in other hot deformed magnesium alloy systems such as Mg-rare earth alloys after creep tests at 300 – 350 °C [118,172].

The average grain size of the deformed material after the test at a given temperature and strain rate was measured from three different locations using the linear intercept method. **Figure 5.10a** shows the grain size vs. temperature plots at two strain rates of 1×10^{-2} s^{-1} to 4×10^{-2} s^{-1}. The plot shows that the grain size of the material showed an increase in behaviour with temperature increase irrespective of the strain rate of deformation. In order to identify the effect of strain rate on grain size, the grain sizes of the deformed materials were also plotted against strain rate as in **Figure 5.10b**. In the plot, an increase in grain size from 12.63 ± 0.64 μm at 5×10^{-3} s^{-1} to 18.50 ± 1.17 μm at 4×10^{-2} s^{-1} was observed when the deformation was carried out at 450 °C. However, at low temperature of 300 °C, the grain size value decreased from 6.6 μm at 5×10^{-3} s^{-1} to 4.0 μm at 4×10^{-2} s^{-1}. Grain size values of the deformed microstructures in the present investigation are plotted on temperature vs. strain rate axes as shown in **Figure 5.10c**. The microstructures in **Figure 5.9** and the grain size data in **Figure 5.10c** showed a

general trend in increase in grain size with increase in temperature. However, at temperatures < 400 °C, the grain size decreased with an increase in the strain rate. At 350 °C, the increase in strain rate from 5×10^{-3} s^{-1} to 4×10^{-2} s^{-1} refined the grain size from 8.81 ± 0.49 µm at 5×10^{-3} s^{-1} to 5.70 ± 0.69 µm at 4×10^{-2} s^{-1}. At about 400 °C the grain size became less sensitive to the change in strain rate. The grain size at this temperature remained in the range of $8.92 - 10.53$ µm for all strain rates. The average grain size data in the temperature range of 250 °C – 450 °C and strain rate range of 5×10^{-3} s$^{-1} - 4 \times 10^{-2}$ s^{-1} was used to generate a grain size map and will be discussed in the **Section 5.4.1**.

A grain size map has been generated on temperature and strain rate axes (**Figure 5.11**) based on the grain size data in **Figure 5.10c**. The contours in the map in **Figure 5.11** represent the iso-grain size data. The grain size of the deformed AA5083 alloy in the present investigation did not show a substantial increase or decrease with the deformation temperature and strain rate. The AZ31 alloy in the present investigation did not show a similar trend. The grain size of the magnesium AZ31 alloy changed with deformation condition as shown in **Figures 5.9 to 5.11**.

Based on the grain size and morphology, three regions—recrystallization, dynamic recrystallization, and grain growth—are identified in the grain size map in **Figure 11c**. At low strain rates, $< 1 \times 10^{-2}$ s^{-1}, and at all temperature conditions, the grain size of the deformed material remained close to the microstructure of static recrystallization. At temperature < 400 °C and at strain rate $> 1 \times 10^{-2}$ s^{-1}, the grain size of the deformed material reduced as a result of dynamic recrystallization. At temperature > 400 °C and strain rate $> 1 \times 10^{-2}$ s^{-1}, grain growth of recrystallized grains dominates.

Variation in microstructure with temperature and strain rate observed in the bulk material affects deformation behaviour of the material. The next section will discuss the deformation mechanisms in AZ31 alloy and also the role of microstructural evolution on the deformation behaviour of the alloy.

5.5. Deformation mechanisms based on stress- strain rate data

The load required to generate tensile deformation in AZ31 sample was recorded during each experiment for the present temperature and strain rate ranges. Typical load vs. time data for tests conducted at 300 °C – 450 °C and strain rates ranging from 5×10^{-3} s^{-1} to 4×10^{-2} s^{-1} are given in **Figures 5.12a to d**.

The flow stress of AZ31 alloy was calculated using the cross-sectional area of the sample when it passed through the hot zone (see **Chapter 3**) within a time interval, *dt*. The flow stress values are plotted on temperature and strain rate space as in **Figure 5.12e**. To characterize the effect of strain rate on plastic flow behaviour, the strain rate was plotted as a function of variation in flow stress and shown in **Figure 5.13**. The relationship between the imposed strain rate and temperature-compensated flow stress of the strip can be described using the general phenomenological creep equation (**Equation 5.1**).

$$\dot{\varepsilon} = A \left(\frac{\sigma}{E}\right)^{n} exp\left(-\frac{Q}{RT}\right)$$
(5.1)

Where A is the material constant, σ is the flow stress, n is the stress exponent (reciprocal strain rate sensitivity, $1/m$), E is the temperature compensated Young's modulus, Q is the activation energy for deformation, and R is the universal gas constant.

The slope of the data shown in **Figure 5.13** is equal to the stress exponent, *n*. A value of n of approximately 2 was calculated for a temperature range of 250 °C – 450 °C and strain rate range of 2×10^{-2} s^{-1} – 4×10^{-2} s^{-1}. As described earlier, a stress exponent of *n* = 2 is indicative of creep by GBS, which is a well characterized operating creep mechanism in fine grain AZ31. At low temperature (250 °C) and high strain rates ($> 3 \times 10^{-2}$ s^{-1}), the stress exponent value was found > 4, suggesting dislocation activity dominated over GBS mechanism.

Deformation mechanisms in AZ31 alloy are summarized by constructing a stress exponent map in temperature and strain rate space. The stress exponent map is generated by plotting the values of stress exponent data on temperature vs. strain rate axes as shown in **Figure 5.14**. The contours in the plot represent the iso-exponent values. At low strain rates, $< 1 \times 10^{-2}$ s^{-1}, diffusional flow (viscous creep) with a stress exponent of *n* = 1 becomes dominant.

The constitutive equation for superplastic flow, taking the grain size into account, can be described as [173]

$$\dot{\varepsilon} = A \left(\frac{\sigma}{E}\right)^{n} \left(\frac{b}{d}\right)^{p} exp\left(-\frac{Q}{RT}\right) \tag{5.2}$$

Where *b* is the Burgers vector, *d* is the grain size, and *p* is the grain size exponent. The value of grain size exponent, *p*, was reported earlier as 3 in superplastic materials including magnesium AZ31 alloy [109] and AZ91 [97] alloy. The activation energy of operating mechanisms was calculated by plotting the grain size dependent strain rate vs. reciprocal temperature at two normalized stress values. The relationship between the average grain size (from **Figure 5.10c**) compensated strain rate, $\dot{\varepsilon}d^{3}$, and reciprocal

temperature is illustrated in **Figure 5.15**. Here, $\dot{\varepsilon}d^3$ is determined at two fixed normalized stress values of 4×10^{-3} and 7×10^{-3} (indicated with dotted lines in **Figure 5.13**). The activation energies at two normalized stress values were calculated from the plot, which were found to be 79 kJ/mol and 130 kJ/mol at the normalized stress of 4×10^{-3} and 7×10^{-3} respectively. The activation energy for grain boundary diffusion in magnesium was reported as 92 kJ/mol [67], which is close to the activation energy found at a normalized stress of 4×10^{-3}. Similarly, the activation energy of 130 kJ/mol found under the present deformation condition at a normalized stress of 7×10^{-3} is close to the reported activation energy for lattice diffusion in magnesium (135 kJ/mol [67]). Therefore, over a large range of temperature and strain rate, GBS operates either by grain boundary diffusion or by lattice diffusion. DRX grains produced during high temperature deformation intensify GBS mechanism in the material.

Three dominant mechanisms were identified based on the flow stress and strain rate data, and the microstructural evolution in **Figures 5.9 to 5.11** supports the operating mechanisms. The occurrence of dynamic recrystallization led to fine grain structure, and consequently, GBS was favoured by the fine grain microstructure and became the dominant mechanism of plastic deformation of the material. An increase in temperature made it difficult for the material to deform by GBS due to the large grain size. Under these conditions the AZ31 alloy deformed by dislocation glide controlled creep (or viscous glide creep).

5.6. Sliding induced damage and material removal

Evidence of GBS along with dynamic recrystallization was also found when

deformation in material was induced by sliding contact without subjecting the materials to external tensile strain. This was achieved using pin-on-disk experiments, where a very high sliding induced strain was observed in the subsurface of the wear track. The following two subsections will discuss the material removal process and surface and subsurface microstructural characteristics generated during sliding induced damage process.

5.6.1. Material removal and transfer process

The surface profile of the counterface material that came into contact with the worn AZ31 test sample surface in pin-on-disk test is shown in **Figure 5.16a** and provides evidence of material transfer. Significant accumulation of transferred material on the counterface can be seen after sliding for a single cycle. The secondary electron image of the transferred material is shown in **Figure 5.16b**. The EDS analyses confirmed that the composition of the transferred material included magnesium, aluminum and zinc—all originating from the AZ31 (**Figure 5.16c**). As the number of sliding cycles increased, new material layers were deposited on previously transferred material—an accumulation process that resulted in the formation of debris fragments with a lamellar structure. In order to observe the microstructure of the transferred material, the debris particles were mounted in an epoxy mould along their longitudinal axes and polished until their cross-sections were exposed. The optical micrographs in **Figures 5.17a and b** display a typical debris microstructure, revealing the presence of deformation bands extending parallel to each other as well as the formation of small, equiaxed, recrystallized grains between them. In this cross-section, the recrystallized grain size was 6.1 ± 1.4 μm, and the thickness of recrystallized zones varied between 10 – 15 μm.

5.6.2. Worn surface and subsurface microstructure

The worn surfaces of AZ31 samples tested at 400 °C were chemically etched to reveal the structure of the near surface grains that were developed during sliding contact. Etching the wear track with an acetic-picral solution for two seconds (without mechanical polishing) removed the damaged top layer and exposed the grain structure immediately underneath. **Figure 5.18a** shows the plan view of the wear track, where the equiaxed morphology of the exposed grains, with an average size of 6.9 ± 3.6 μm, are displayed. It is noted that the grains inside the wear track were smaller than those outside the wear track (12.7 ± 2.16 μm), which suggests the occurrence of recrystallization during sliding contact at this temperature. **Figure 5.18b** shows the cross-sectional view of the same wear track, which reveals the subsurface grain morphology as a function of depth below the contact surface. Again, the presence of some recrystallized grains on the top layer adjacent to the contact surface can be seen. In the region immediately below the recrystallized surface grains, the microstructure is characterized by a region of grain growth that extends within a depth of approximately 10 to 50 μm below the wear track. **Figure 5.19** is a cross-sectional composite micrograph that shows details of the microstructure developed after sliding for 50 cycles. This section was cut at an angle of 5 degrees to the contact surface as a way of enhancing the details of the near surface microstructure. The typical features of the sliding-induced deformation microstructure are clearly depicted in this micrograph: A zone of recrystallized grains that extends up to $10 - 15$ μm below the contact surface and the grain growth zone underneath the recrystallized grains that penetrates to a depth of 80 μm are among the important aspects of the microstructure.

Apart from dynamic recrystallization, evidence of GBS was also found during the sliding induced damage process. GBS was found in regions neighbouring the edges of the wear track, where the pileups of plastically deformed material formed elevated plateaus. **Figure 5.20a** shows the three-dimensional optical surface profile of this region, where the grain boundaries are clearly distinguished. Analysis of the surface profiles revealed that the grains shown in **Figure 5.20a** were either elevated or sunken in relation to the neighbouring grains. A two-dimensional section taken across this region (**Figure 5.20b**) indicates an average step height of 0.15 μm between the adjacent grains. The formation of these steps was attributed to sliding of the grain boundaries.

5.7. Summary of observations on deformation and friction behaviour of AZ31 alloy

One of the main differences in the estimation of the flow stress in AZ31 alloy over AA5083 alloy is that the flow stress of the magnesium alloy was sensitive to the concurrent grain growth. In AZ31 with an increase in temperature, the grain size increased from 6.6 μm at 300 °C to 13.6 μm at 450 °C. Temperature and strain rate conditions that generated the highest grain size (in the temperature and strain rate range studied) corresponded to a stress exponent value of $n = 3$ as shown in **Figure 5.14**. GBS was the dominant deformation mechanism over a large temperature and strain rate range and associated with the fine grain structure. At temperatures > 400 °C, where $n > 3$, the material appeared to deform more readily by glide controlled dislocation creep. Glide controlled dislocation creep (also termed viscous glide creep) was observed previously in the coarse grained AZ31 alloy [93]. Grain coarsening at high temperature (> 400 °C)

brings about a transition to dislocation dominated flow from GBS, which operates only in fine-grained material.

At high temperatures the bulk material started to exhibit a bimodal grain structure, and two mechanisms might be operating simultaneously. The dislocation glide creep mechanism operates within the large grains. In addition, the AZ31 alloy deformed by CGBS, which occurred through the movement of grain groups as an entity. An increase in strain rate increased the formation of slip bands within the large grains, as can be seen from the microstructure of the deformed surface in **Figures 5.6a and b,** where the grains which were not in contact show the formation of slip bands. An increase in slip band formation with increase in stress (equivalent of strain rate increase) was reported previously by Kottada et al. [174].

Occurrence of CGBS through the movement of grain groups generated multiple large peaks on the surface and induced roughening of the deformed surface. These large peaks that appeared at a level higher than the surrounding area made contact with the steel pin during the experiment and caused the intermittent wear track as in **Figures 5.6a and b**.

Dynamic recrystallization was also found in the subsurface of the wear track as well as in the material that was transferred to the counterface during unidirectional sliding experiments using pin-on-disk set-up (**Figures 5.18 and 5.19**). However in those experiments, very high sliding induced surface and subsurface strains were generated, which resulted in the detachment of that layer from the underneath material and transferring of the layer to the counterface (see **Chapter 6** for a detailed analysis). In

single pass stretching experiments, the sliding induced subsurface strain under a low load of 0.12 N was not sufficient to produce significant grain growth underneath the sliding track. The externally applied strain is uniformly accommodated in the deformed material without generating a strain gradient. In fact, the small grains and retention of strength at low temperature resulted in low COF under those conditions. With an increase in temperature, flow strength of the material decreased and hence increased the COF. Existence of surface oxide seemed to lower the COF at temperatures up to 400 °C. When the deformation temperature exceeds 400 °C, the surface oxide does not act as a protective layer, and COF of the initial surface was found to be higher than that of the surface without the pre-existing layer at 450 °C.
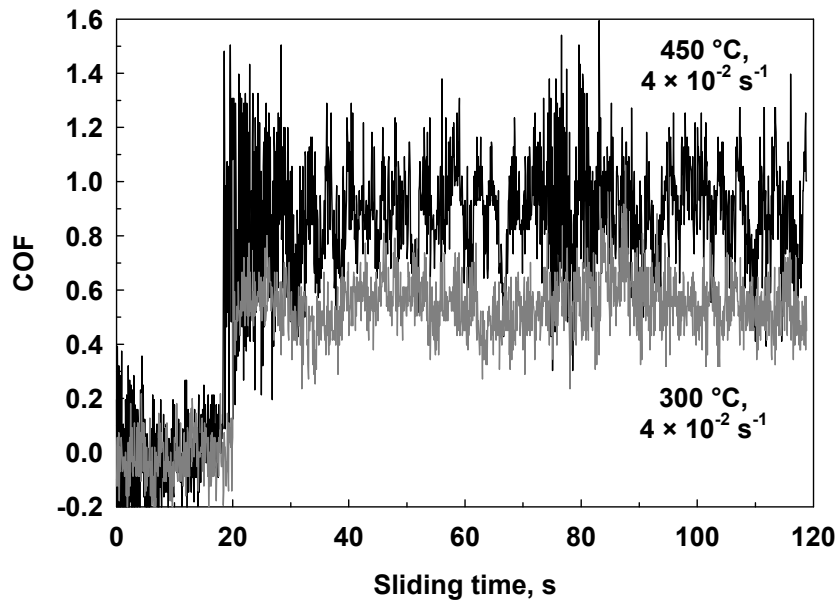
(a)
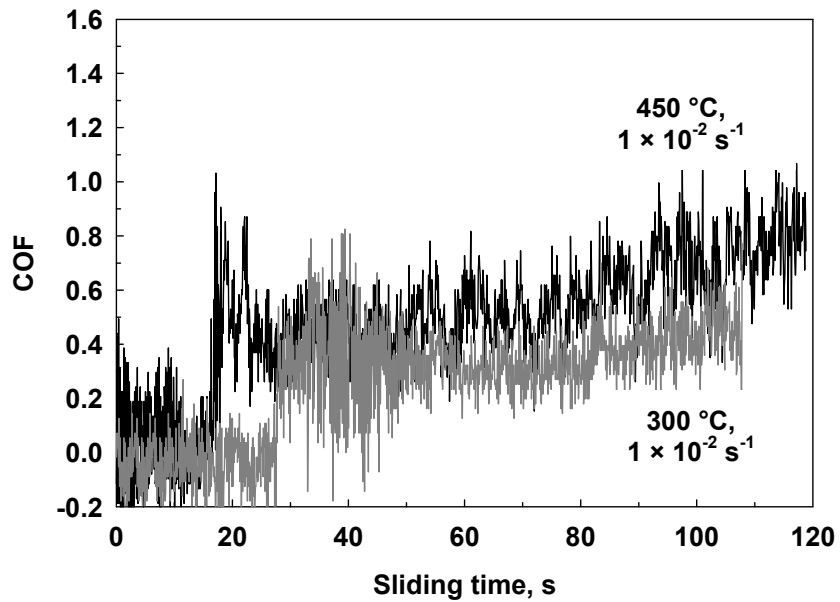
(b)

Figure 5. 1. COF vs. sliding time plot at two temperatures and strain rates of (a) 4×10^{-2} s^{-1} and (b) 1×10^{-2} s^{-1}. (c) Average COF vs. temperature plot, where error bars indicate range of fluctuations in mean COF values measured over 100 s time test period on each strip; (d) Average COF values plotted on temperature vs. strain rate axes.

(c)

(d)
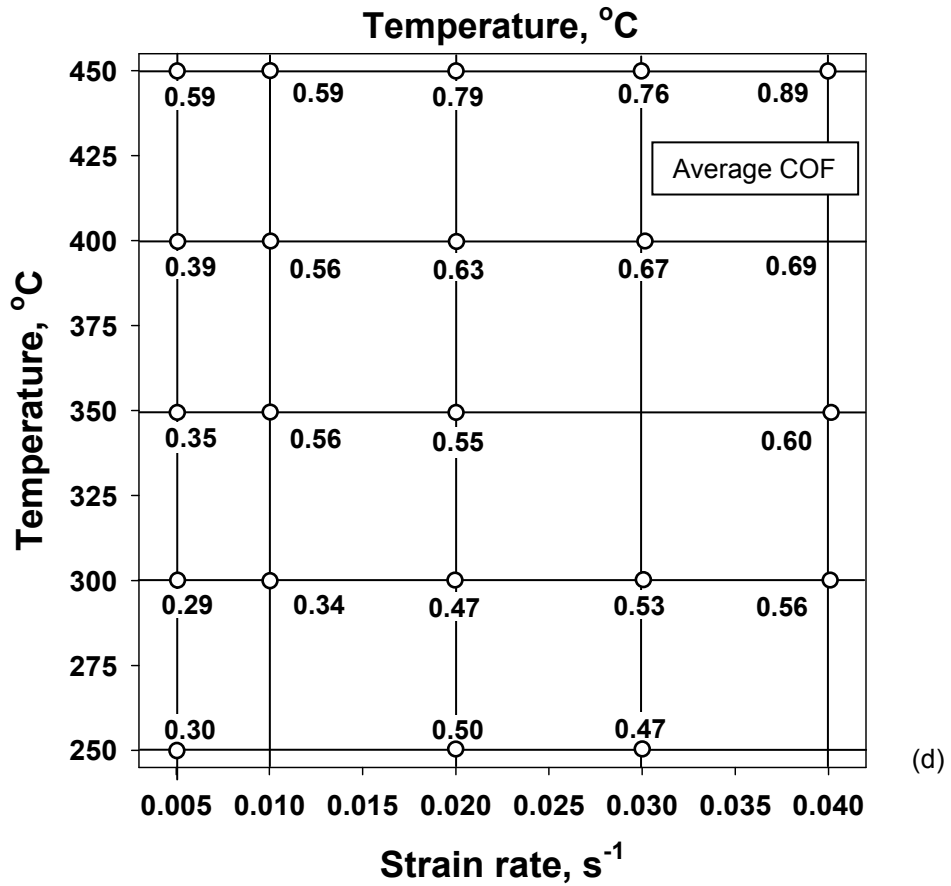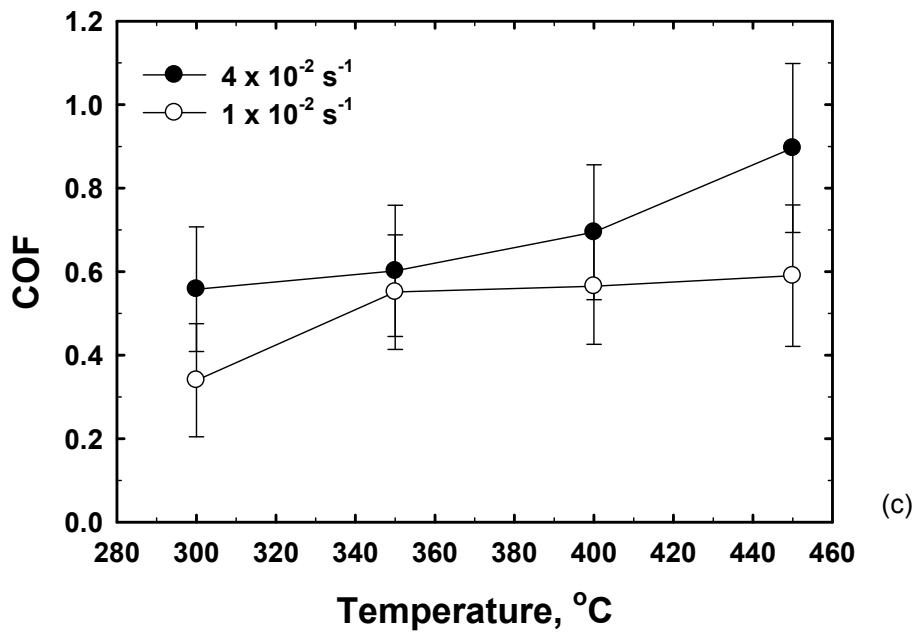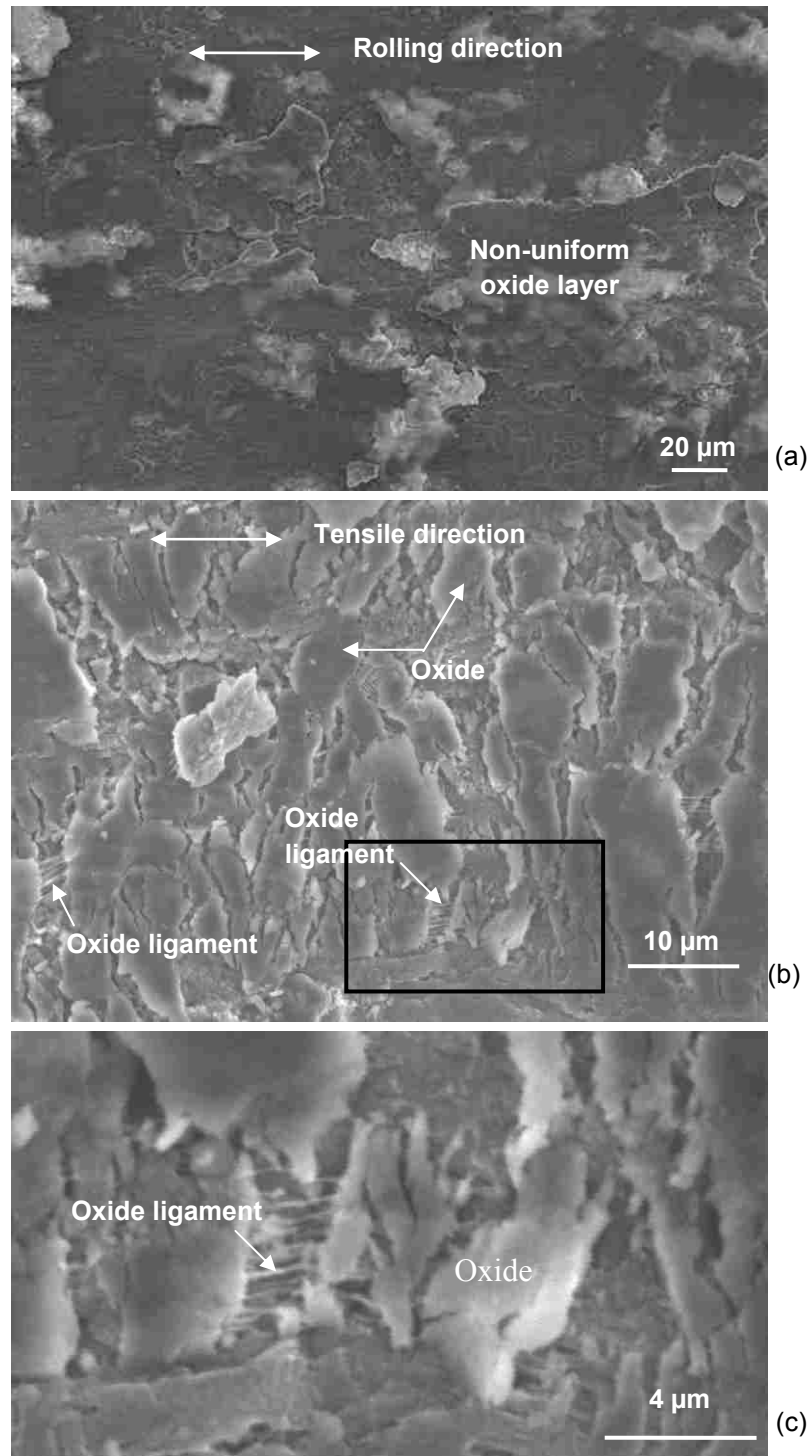
Figure 5. 2. (a) Surface morphology of the AZ31 strip in initial cold rolled condition. (b) SEM micrograph of the surface deformed at 450 °C and 4×10^{-2} s^{-1} and (c) a higher magnification image taken from plate (b); (d) SEM micrograph of the surface deformed at 450 °C and 4×10^{-2} s^{-1} showing the out-of-plane sliding of grains at some locations; (e) SEM micrograph of the surface deformed at 250 °C and 2×10^{-2} s^{-1}.

(d)

(e)

Tensile direction

(a)

(b)
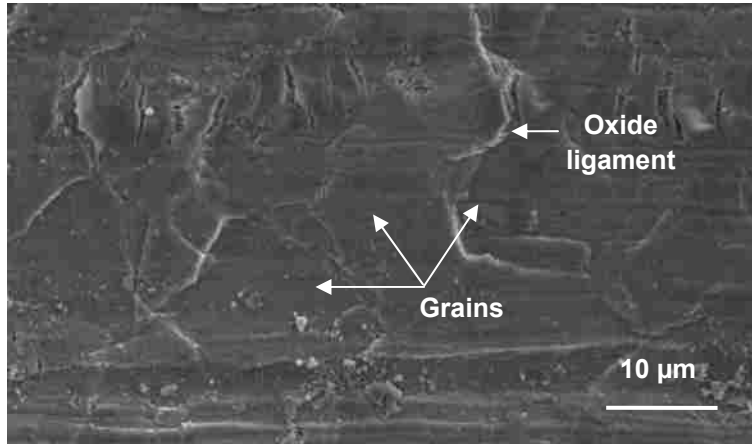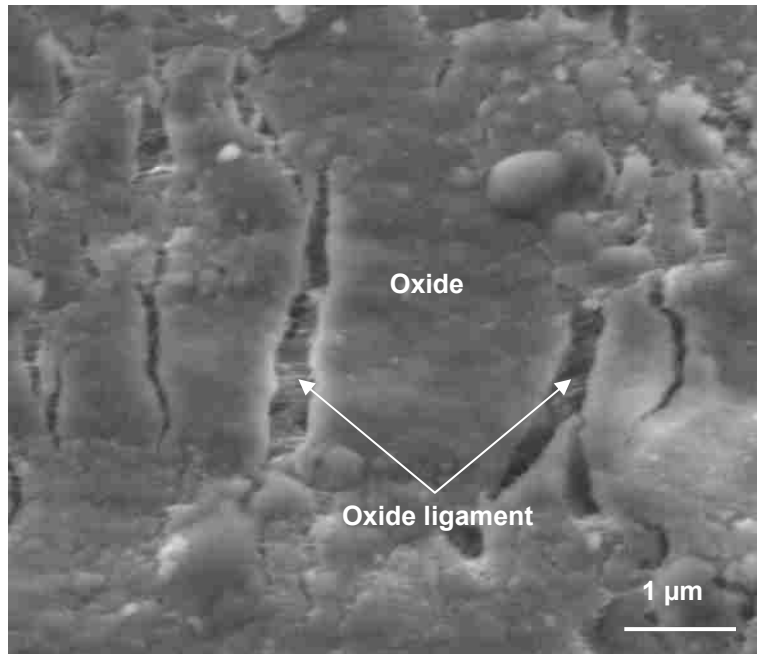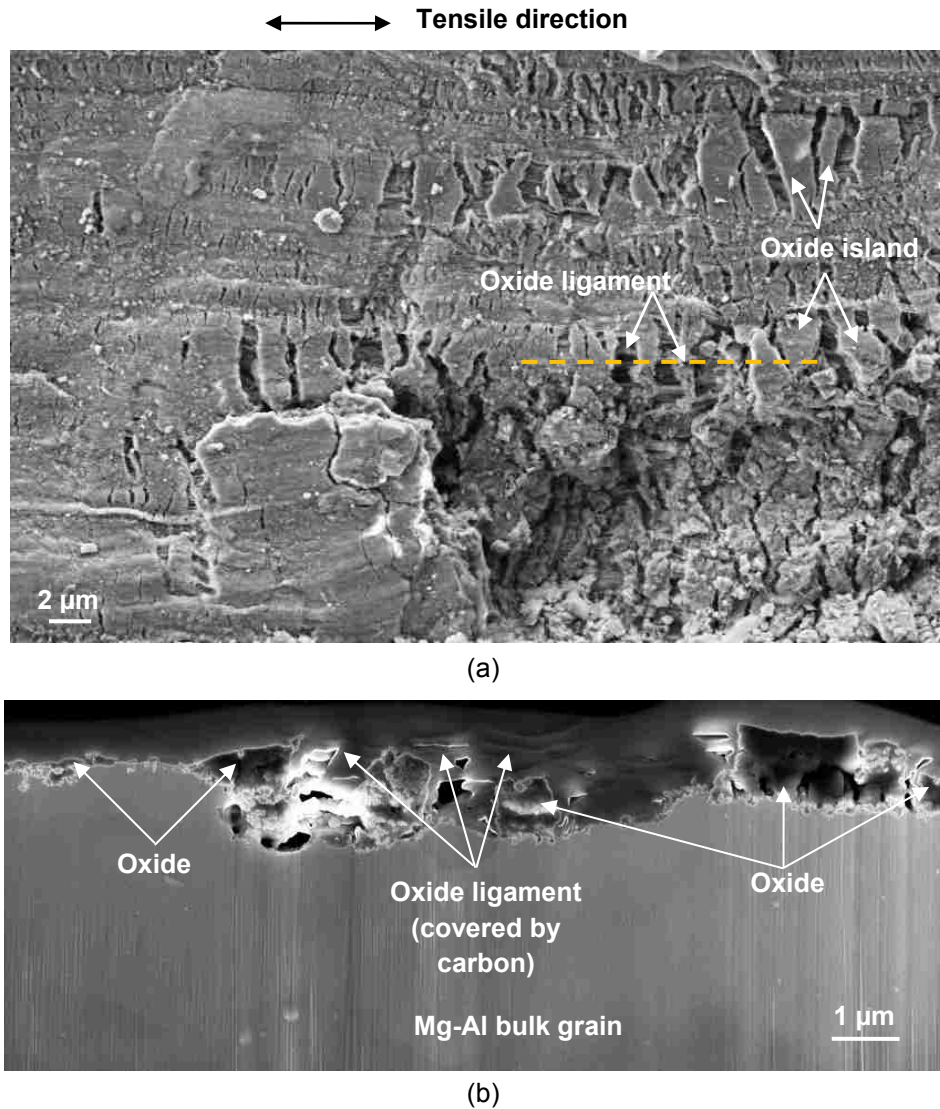
Figure 5. 3. (a) Surface micrograph of the AZ31 sample deformed at ace deformed at 450 °C and 4 × 10^{-2} s^{-1}, (b) FIB cross section taken along the dotted line in plate (a) showing the surface oxide and also ligaments covered with carbon; (c) TEM micrograph of deformed surface (at 450 °C) along the tensile axis (the dotted line shows the position of the surface); (d) high magnification image taken from plate (c) showing the area with superplastic ligament between the oxide island; (e) SADP pattern taken from the superplastic ligament in plate (d) (with different rings in the SADP pattern indexed as MgO).

Tensile direction

Carbon

Ligament
covered with
carbon

Mg-Al bulk grain

500 nm

(c)

Ligament
covered with
carbon

50 nm

(d)

111_{MgO}
200_{MgO}
220_{MgO}
311_{MgO}

(e)
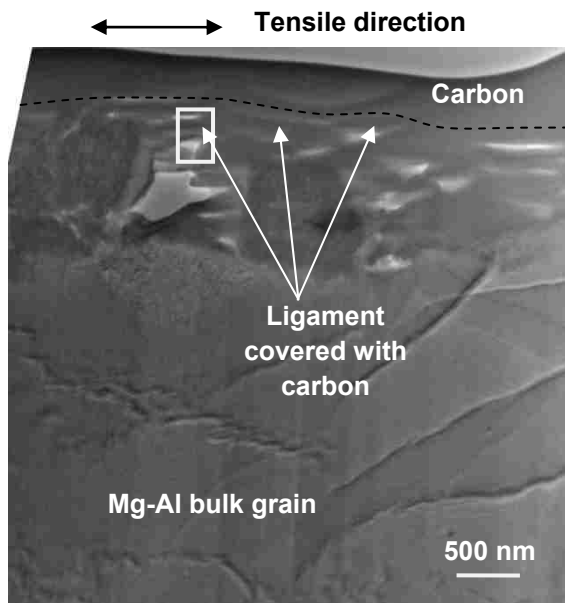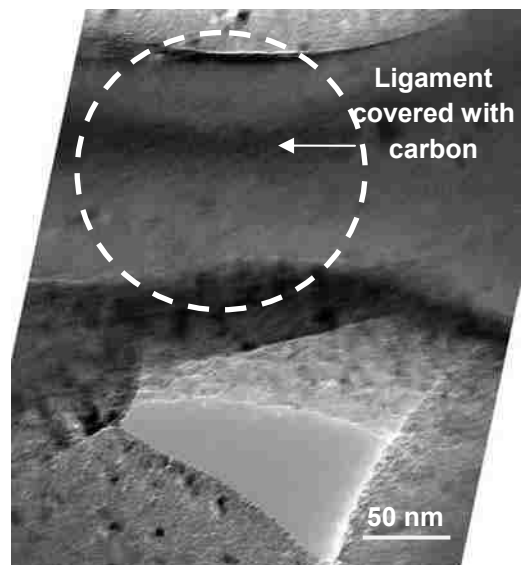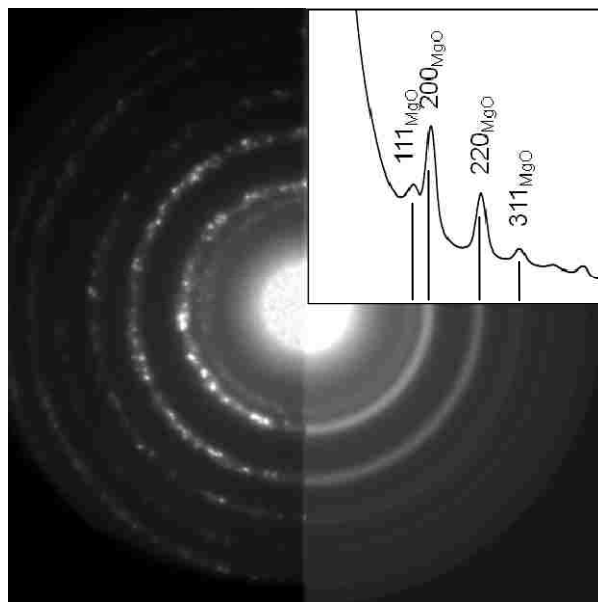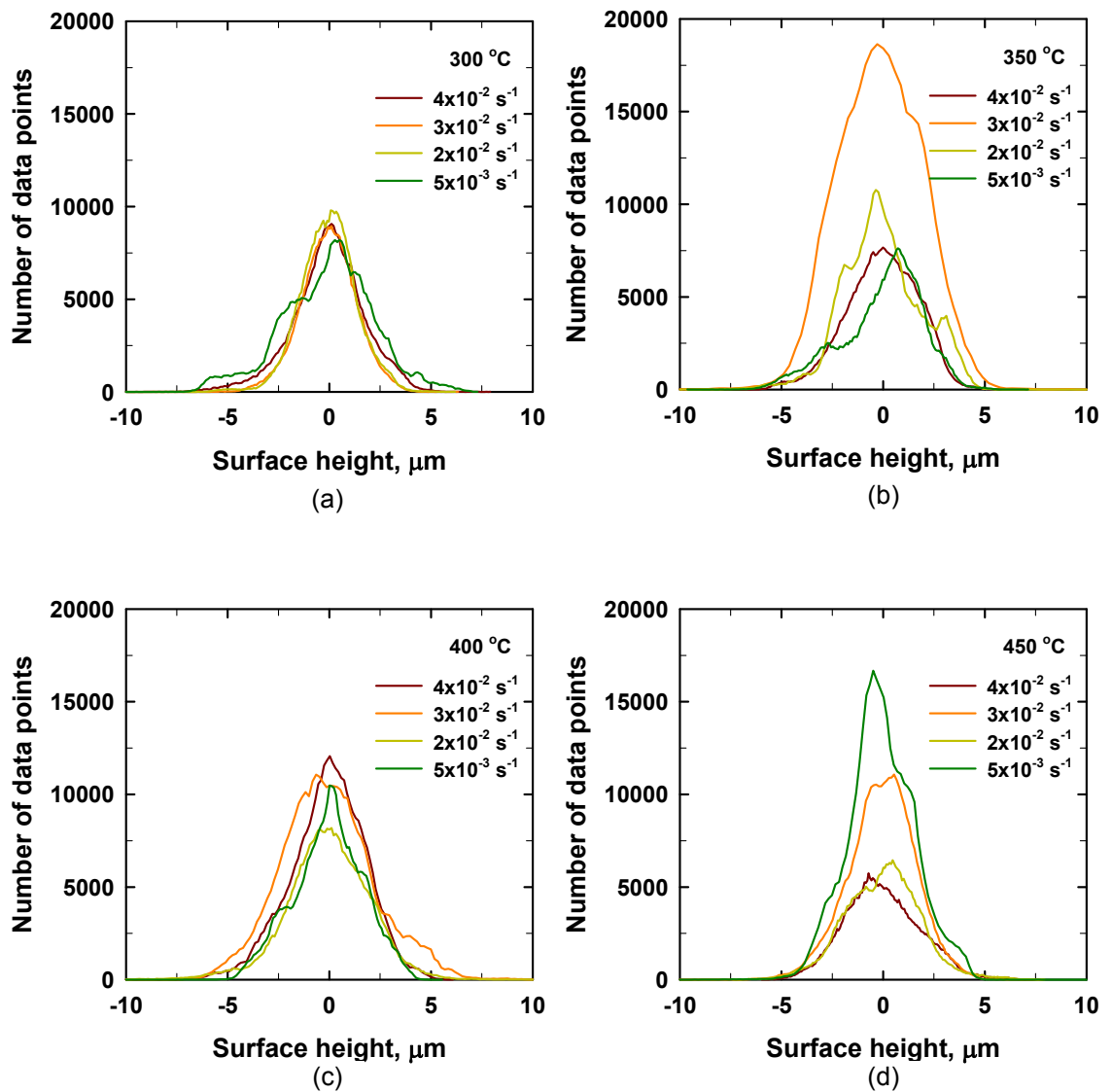
Figure 5. 4. (a) Surface height distribution profiles for surfaces deformed at four temperatures (a) $T = 300$ °C, (b) $T = 350$ °C, (c) $T = 400$ °C and (d) $T = 450$ °C. Measurements at each surface were taken from areas of 300 μm × 225 μm. (e) Average surface roughness data (in μm) plotted on temperature vs. strain rate axes and (f) roughness map generated based on the value in (e).
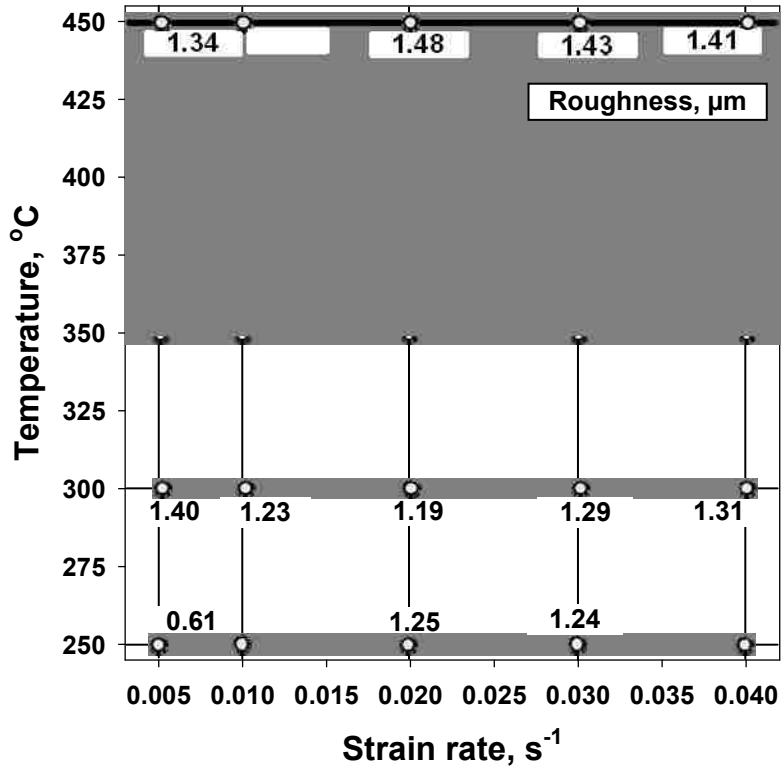
(e)
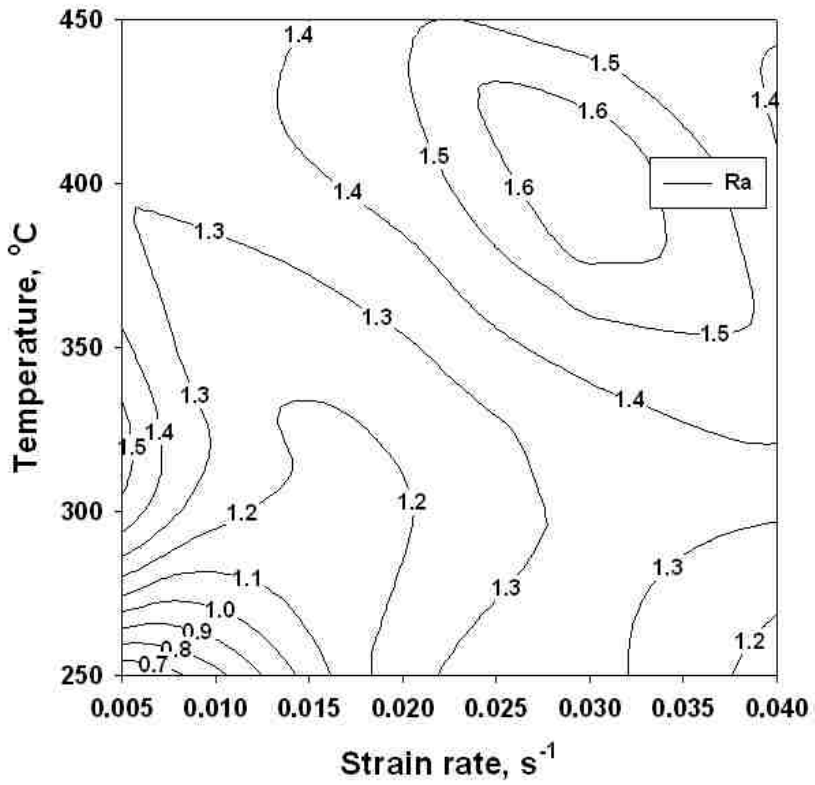
(f)
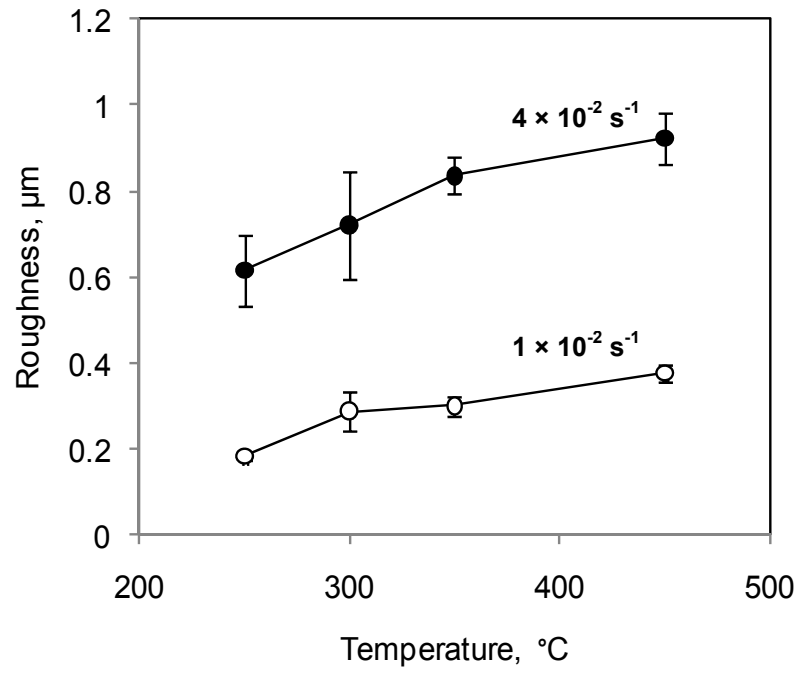
Figure 5. 5. Average surface roughness vs. temperature plot for polished surface after deformation at two strain rates of 1×10^{-2} s^{-1} and 4×10^{-2} s^{-1}.
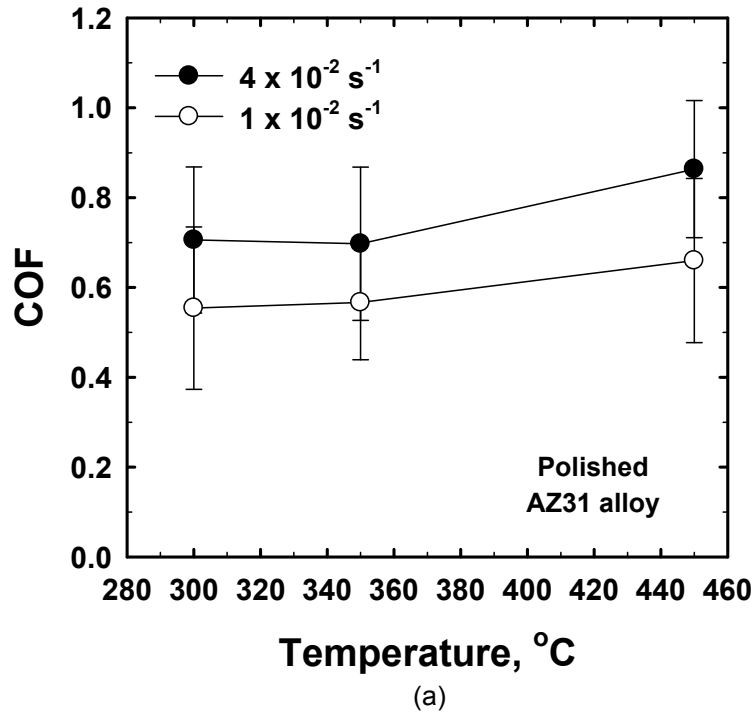
Figure 5. 6. (a) Variation in average COF between polished AZ31 sample and P20 steel pin with temperature, at two strain rates. Average COF vs. temperature plot for as-received and polished surface at two different strain rates show increase in COF value when the temperature is increased from 300 °C to 450 °C (b) 1×10^{-2} s^{-1} and (c) 4×10^{-2} s^{-1}. Error bars indicate range of fluctuations in mean COF values measured over 100 s time test period on each strip (following the initial 20 s heating period).

(b)

(c)
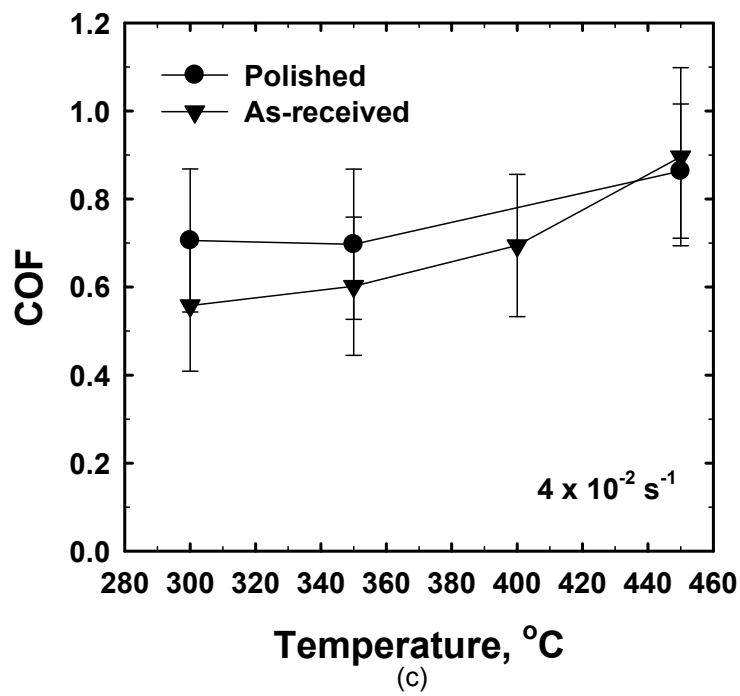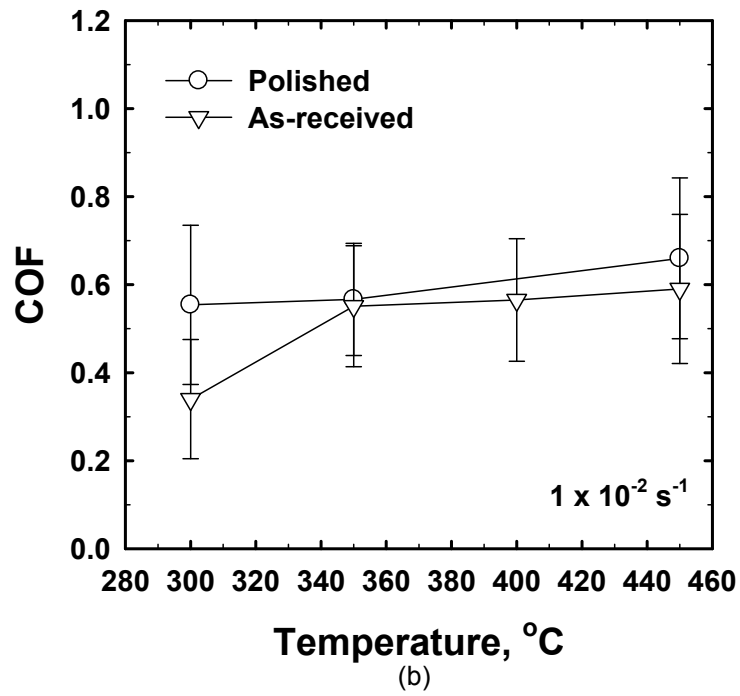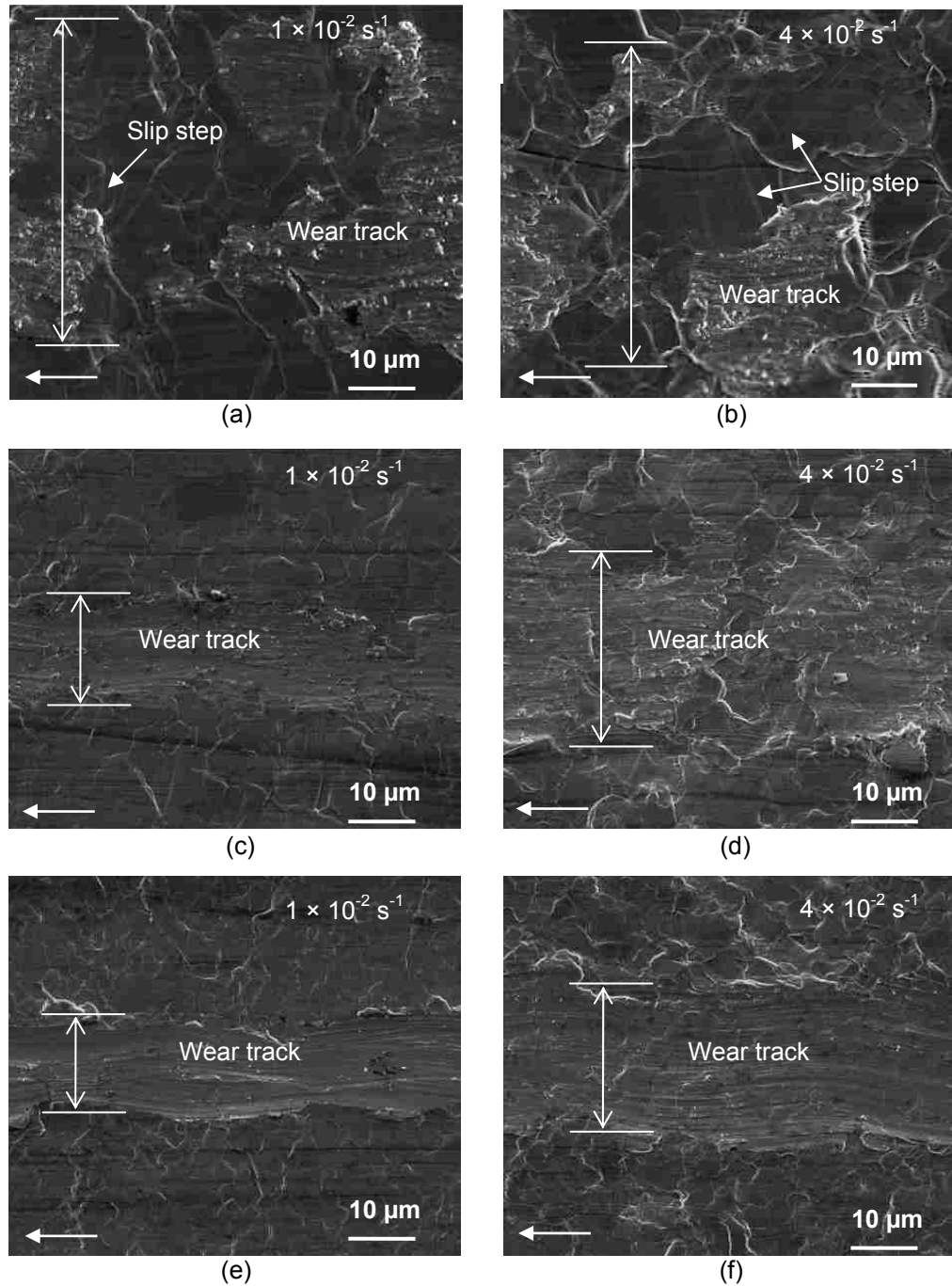
Figure 5. 7. SEM micrograph of the wear track on the deformed surface without any pre-existing oxide layer (a) and (b) at 450 °C, (c) and (d) 350 °C and (e) and (f) 300 °C. Strain rate applied during each experiments are given in the micrograph. The arrow placed in the bottom left corner of each image represents the sliding direction. (g) Width of the wear track vs. temperature plot after experiments at two strain rates of 1×10^{-2} s^{-1} and 4×10^{-2} s^{-1}.
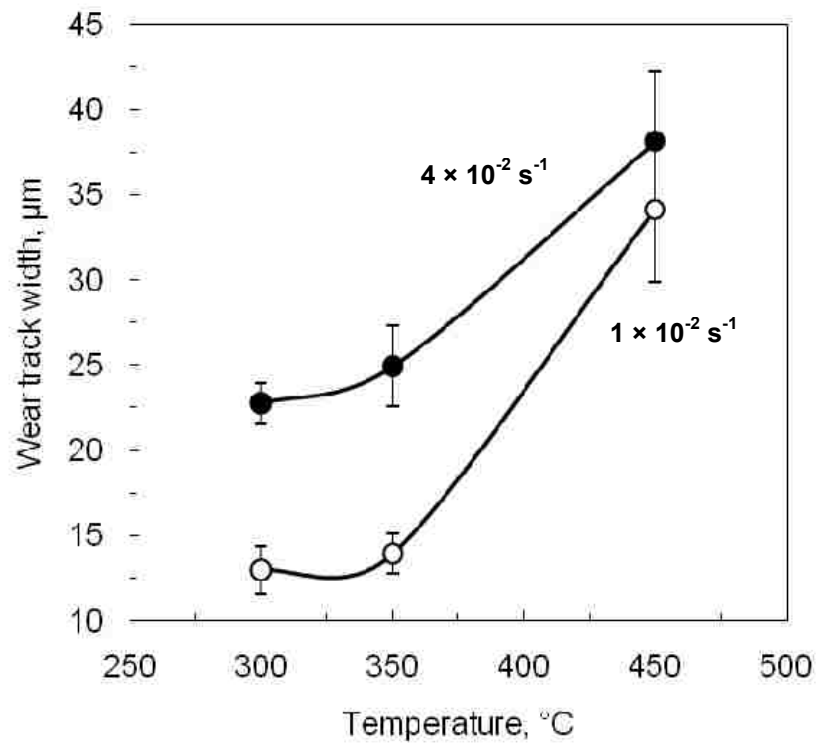
(g)
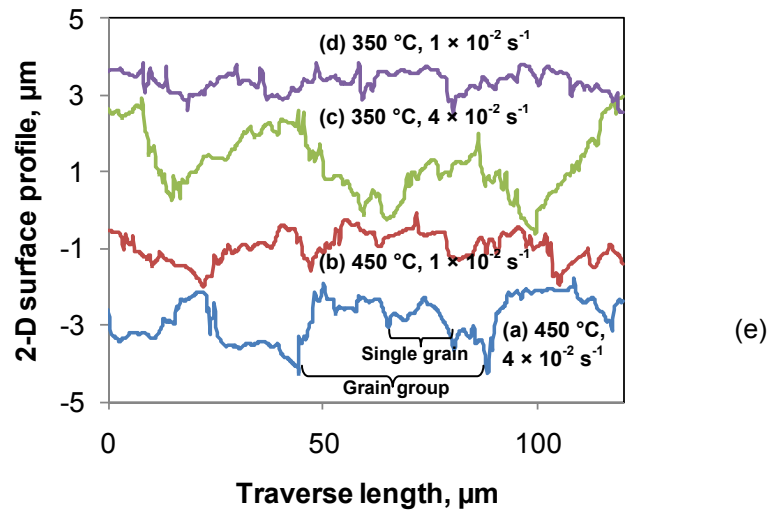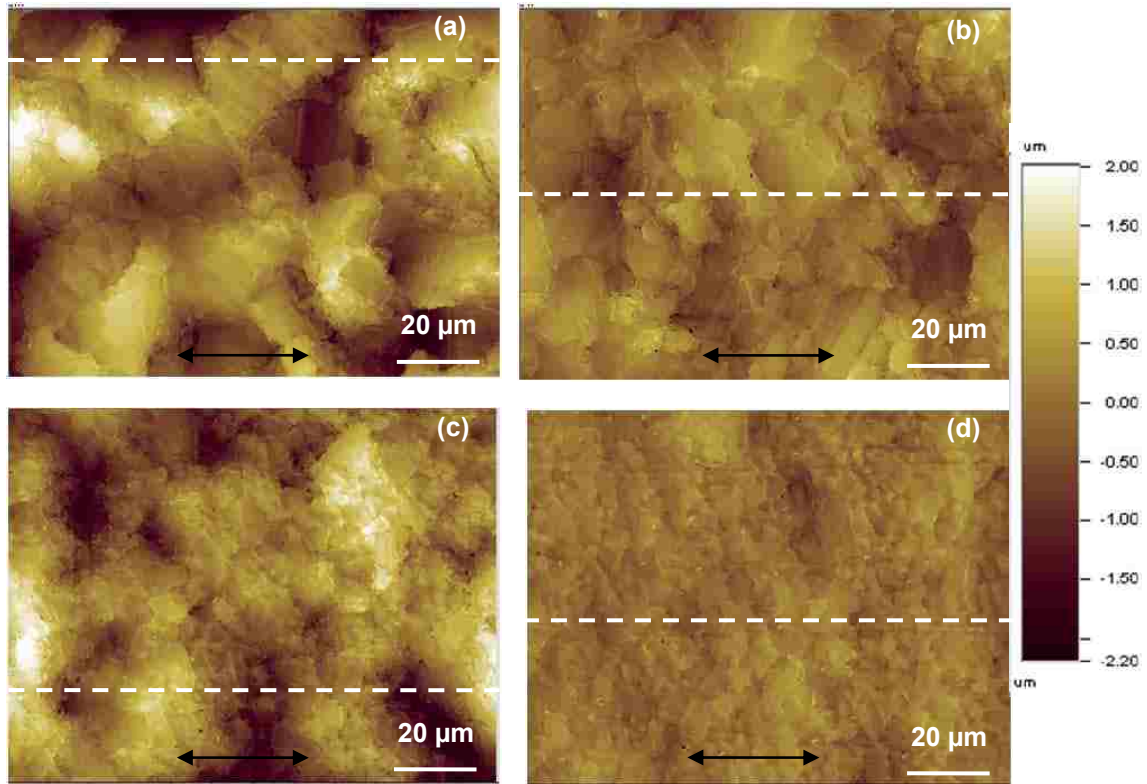
Figure 5. 8. Surface profile of polished surface after deformation at (a) 450 °C, 4×10^{-2} s^{-1}, (b) 450 °C, 1×10^{-2} s^{-1}, (c) 350 °C, 4×10^{-2} s^{-1}, and (d) 350 °C, 1×10^{-2} s^{-1}. (e) 2-D profiles taken along the dotted line in plates (a)-(d). The two sided arrow in the image indicates the tensile direction.

	0.005 s⁻¹	0.01 s⁻¹	0.03 s⁻¹	0.04 s⁻¹
450°C				
400°C				
350°C				
300°C				
250°C				50 μm
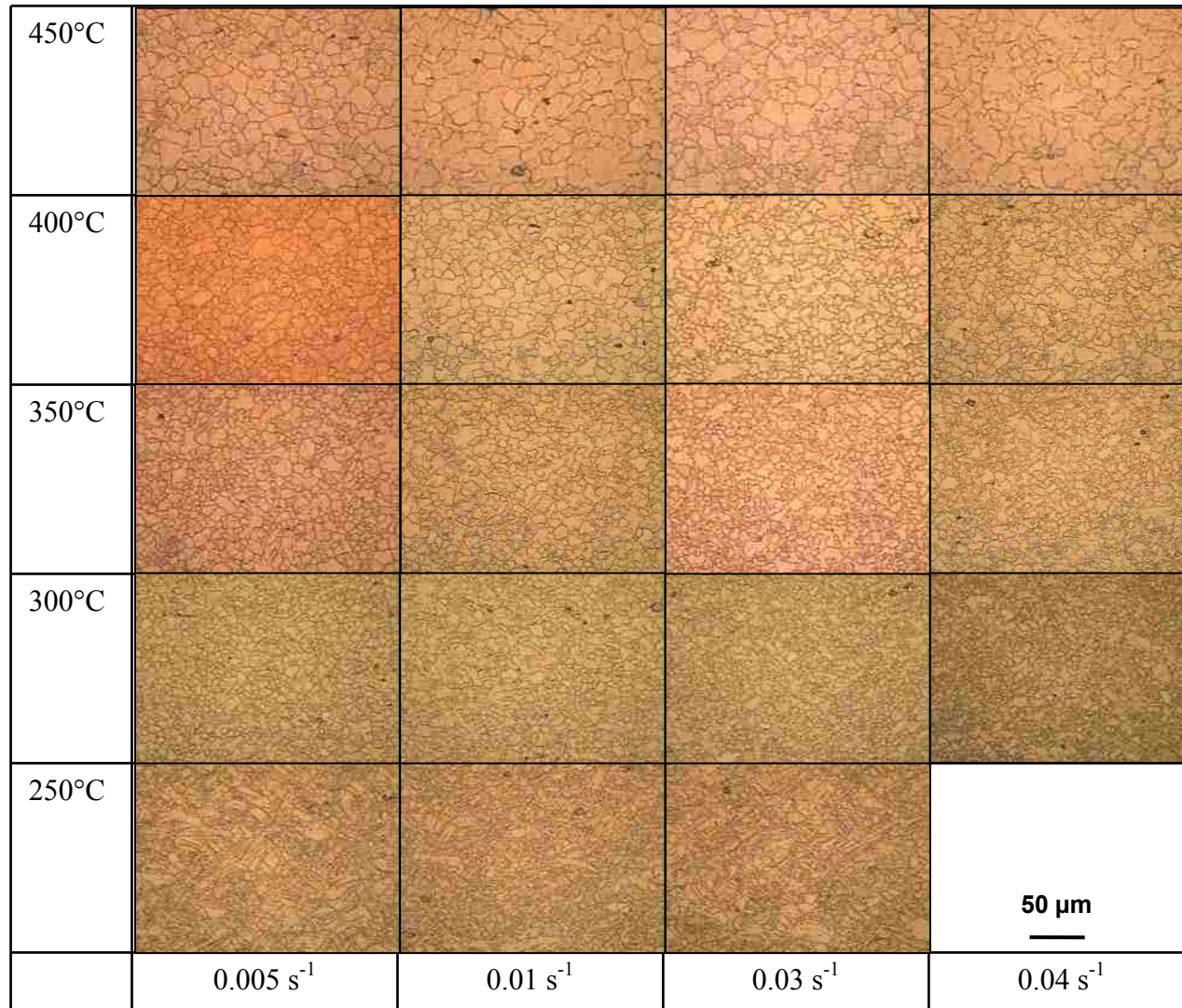
Figure 5. 9. Microstructure of AZ31 alloy after deformed at various temperature and strain rates.
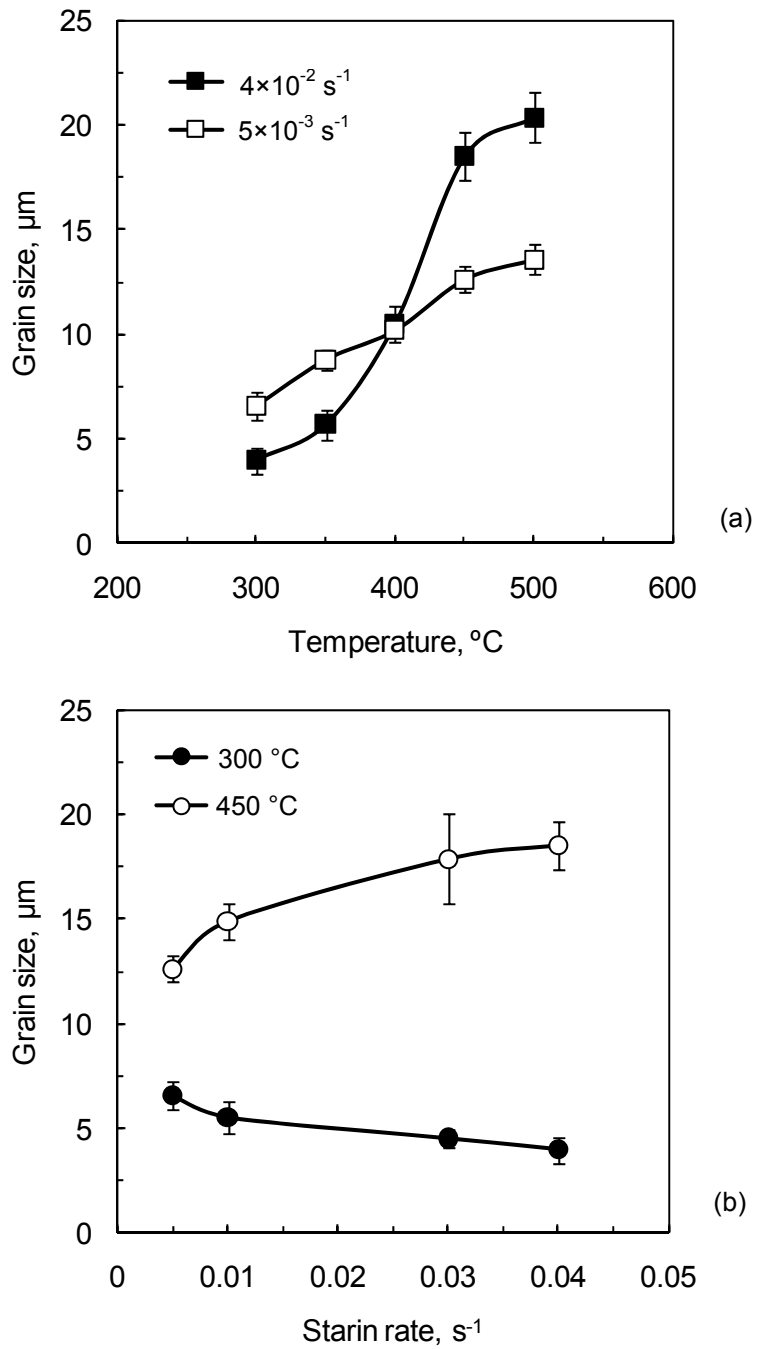
Figure 5. 10. (a) Average grain size vs. temperature plot at two strain rates of 1×10^{-2} s^{-1} and 4×10^{-2} s^{-1} and (b) grain size vs. strain rate plot at two temperatures of 300 °C and 450 °C. (c) Average grain size values (in μm) plotted on temperature vs. strain rate axes.
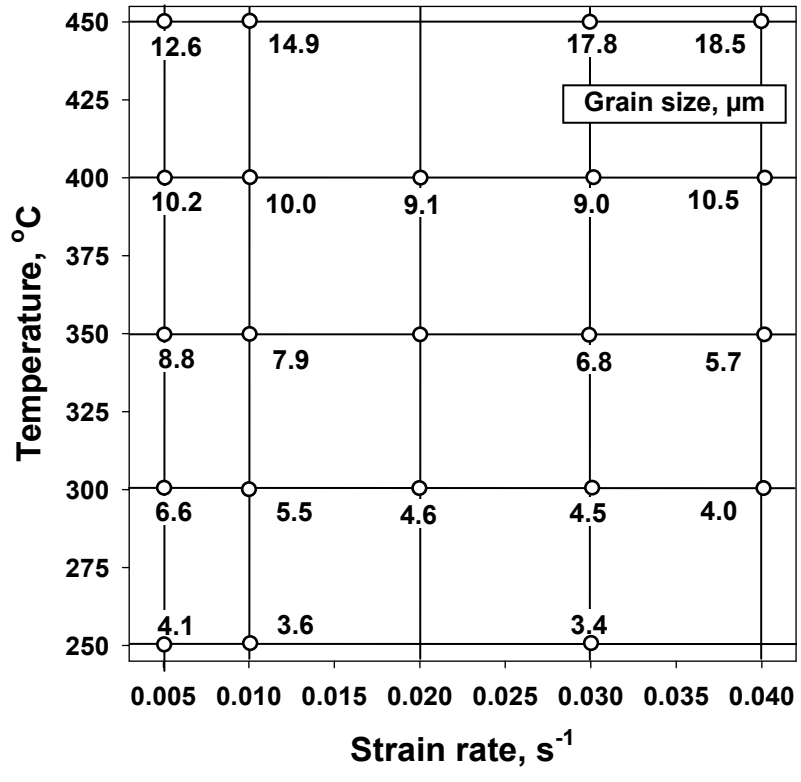
(c)
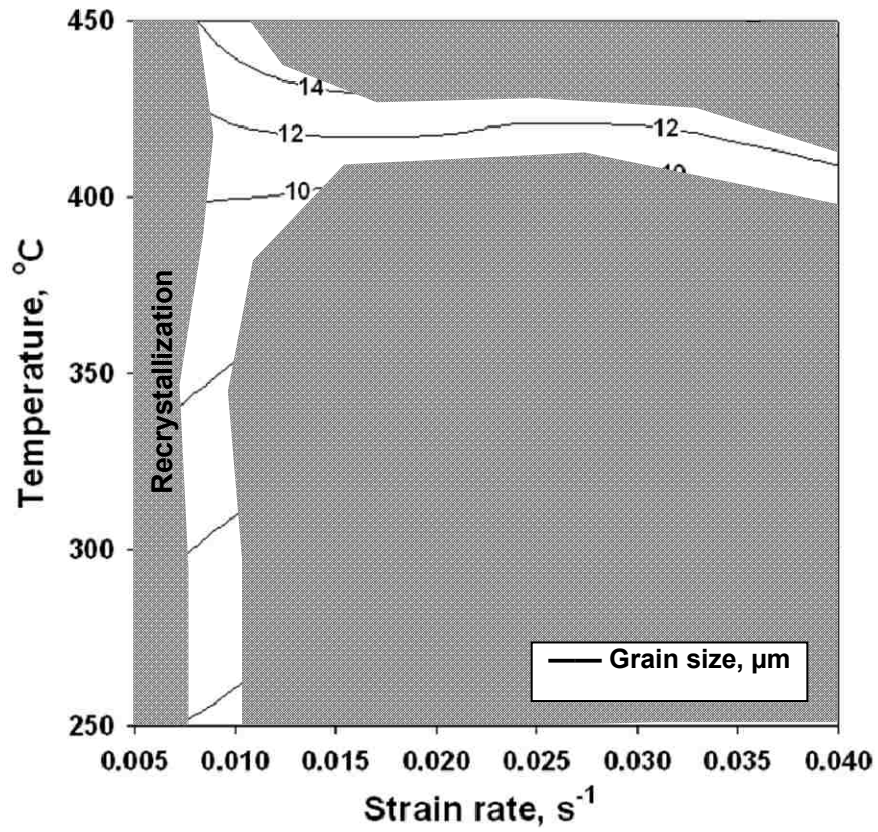
Figure 5. 11. Grain size (in μm) map generated on temperature vs. strain rate axes. The contours represent iso-grain size values in μm.
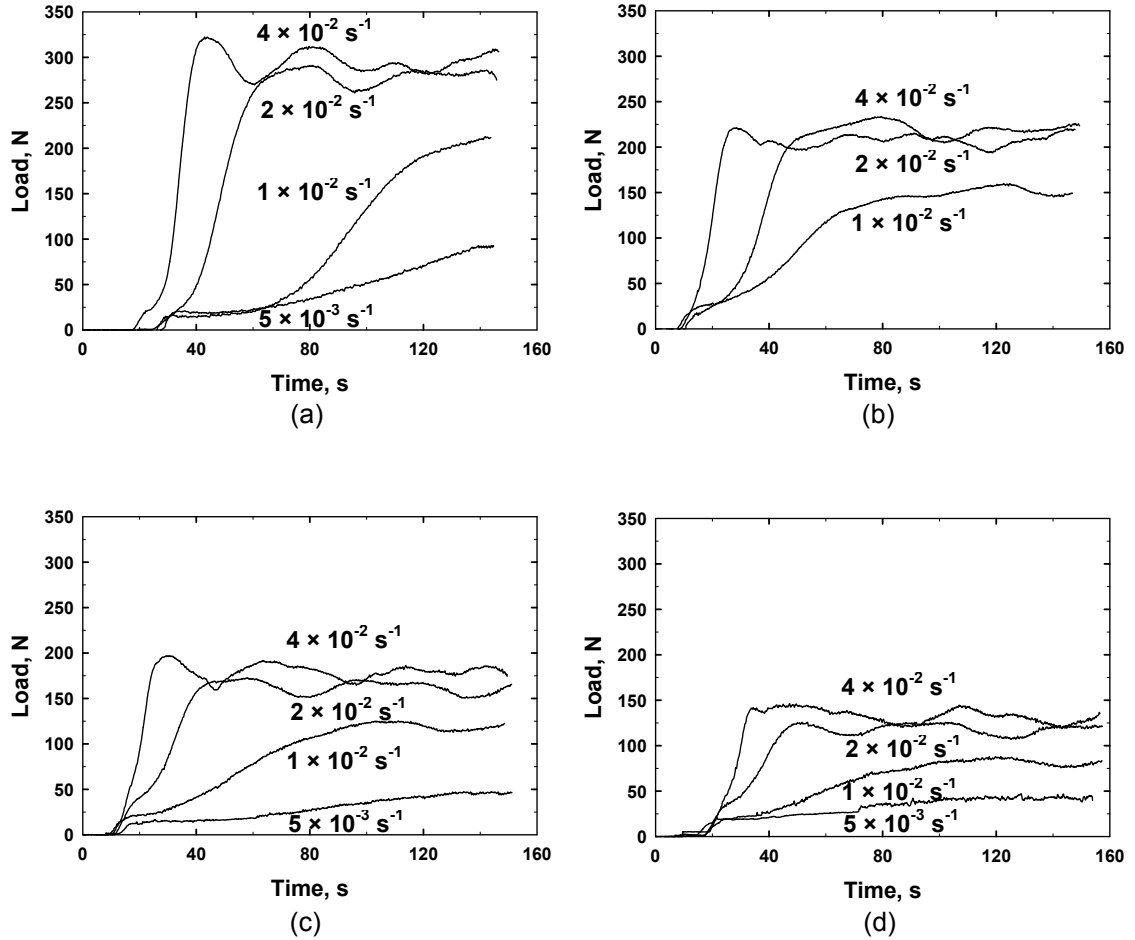
Figure 5. 12. (a) Tensile load applied to AZ31 strips vs. time plot at different strain rates and at (a) 300 °C, (b) 350 °C, (c) 400 °C and (d) 450 °C; (e) Average flow stress values (in MPa) plotted on temperature vs. strain rate axes.
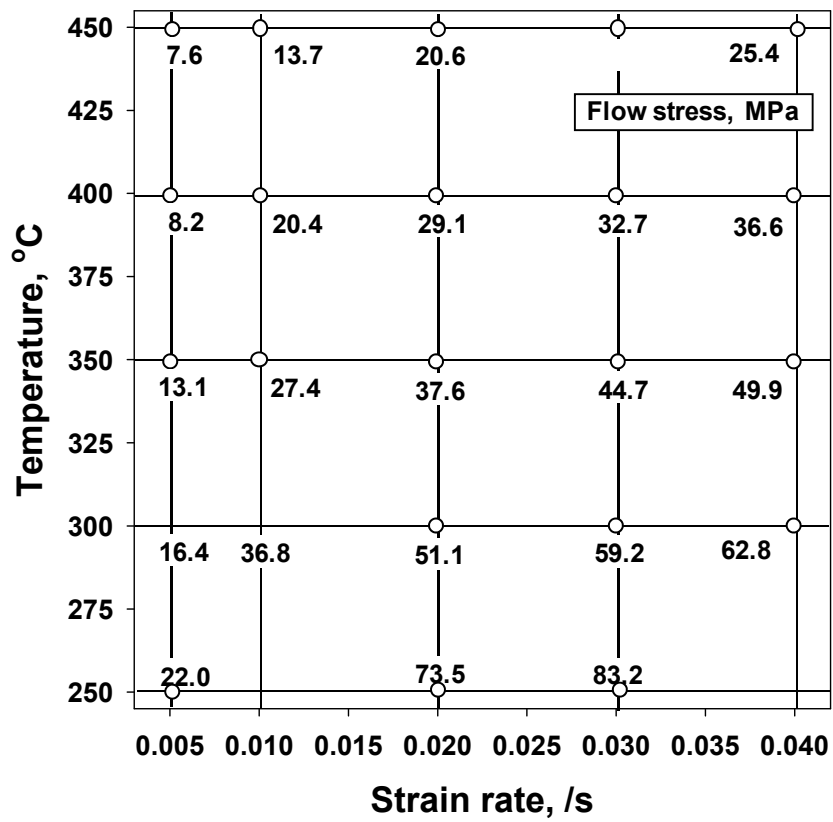
(e)
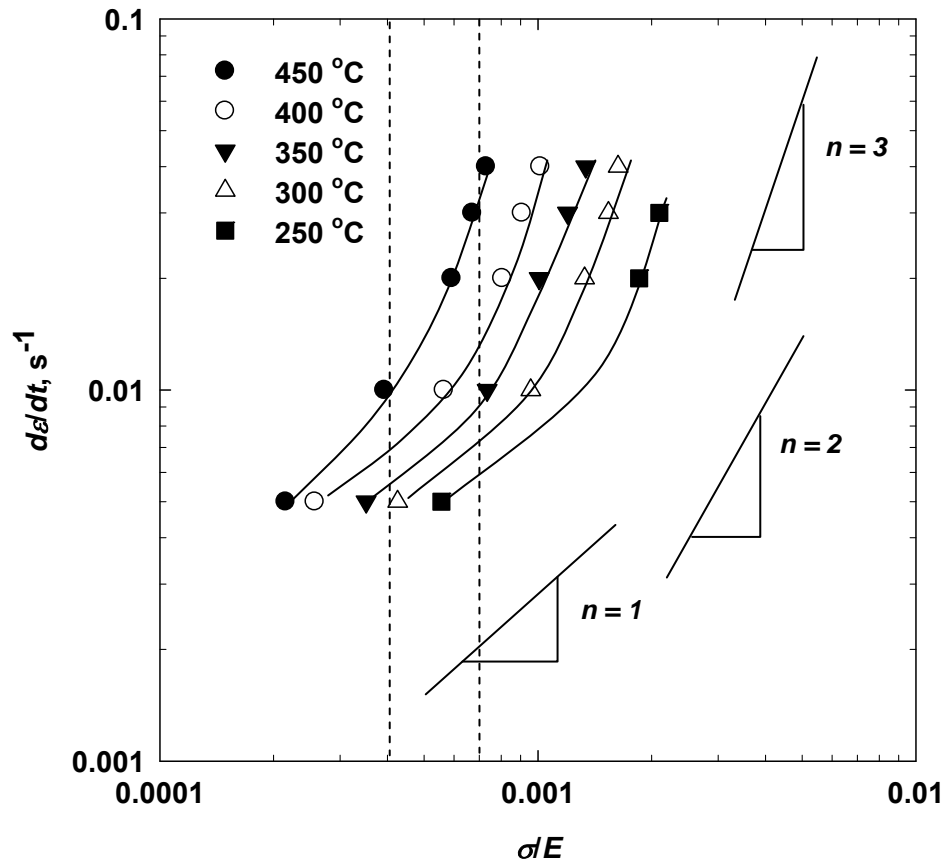
Figure 5. 13. Strain rate vs. modulus compensated flow stress plots following the general creep equation where '*n*' is the stress exponent.
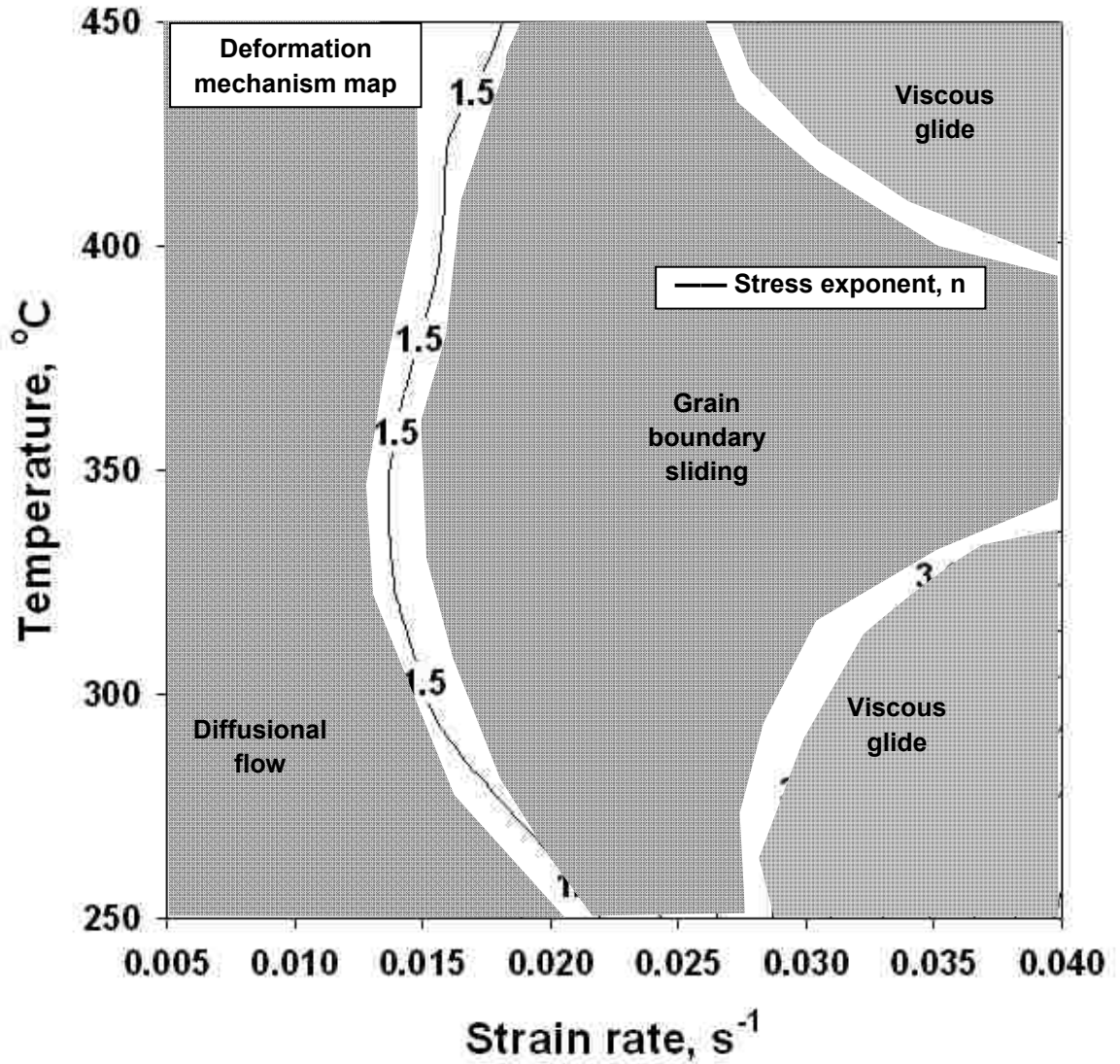
Figure 5. 14. Stress exponent map for AZ31 where contours of constant *n* values are plotted on temperature vs. strain rate axes.
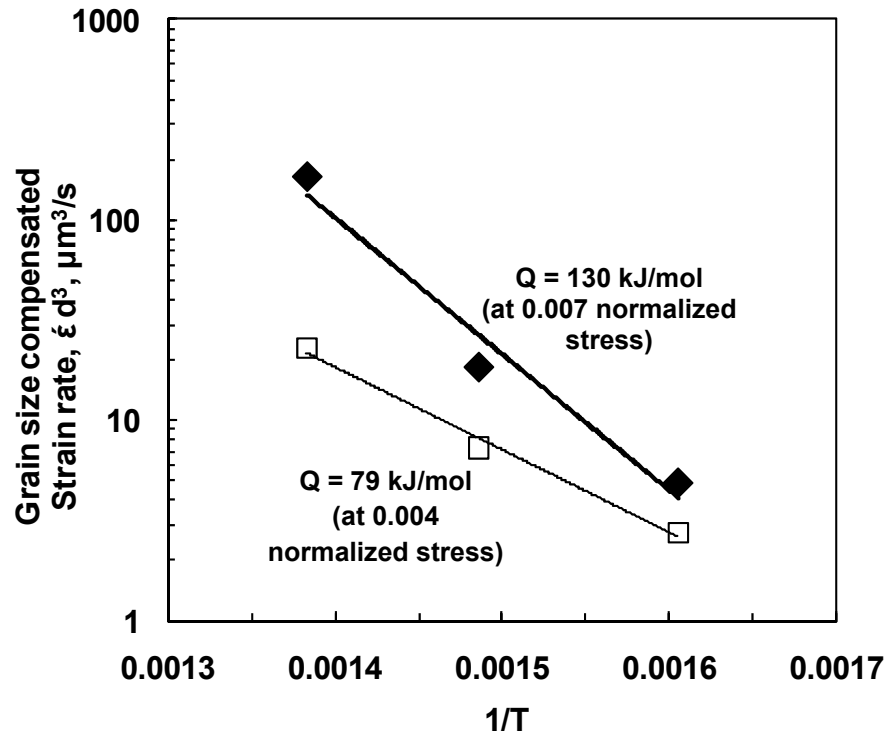
Figure 5. 15. Grain size compensated strain rate as a function of reciprocal temperature in AZ31 alloy. The plot is used to calculate the activation energy for deformation, *Q*, at two normalized stress value of 0.004 and 0.007 (see the dotted line in Figure 5.13).
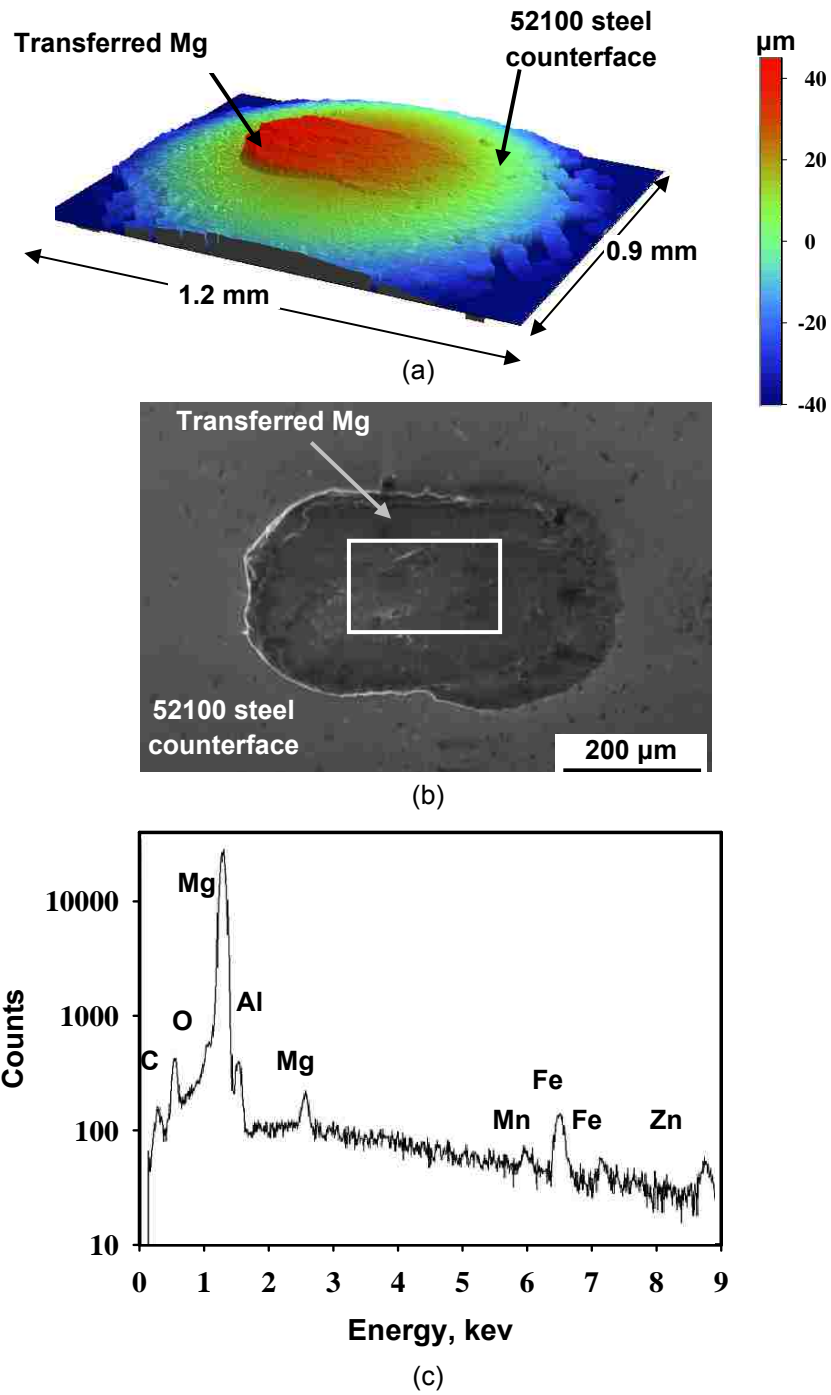
Figure 5. 16. (a) Three-dimensional surface contour of the counterface surface after one cycle of contact with AZ31 at 400 °C showing material transfer; (b) SEM micrograph of the corresponding area of the counterface and (c) the EDS analysis of transferred material from inside the area marked in (b).

(a)

Recrystallized grains

50 µm
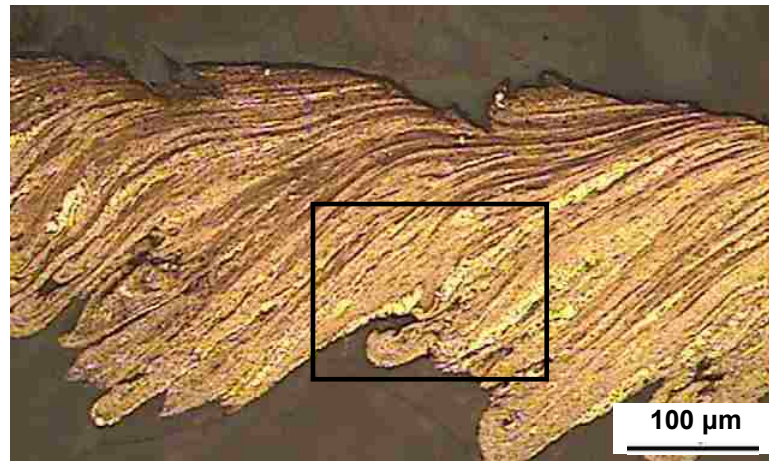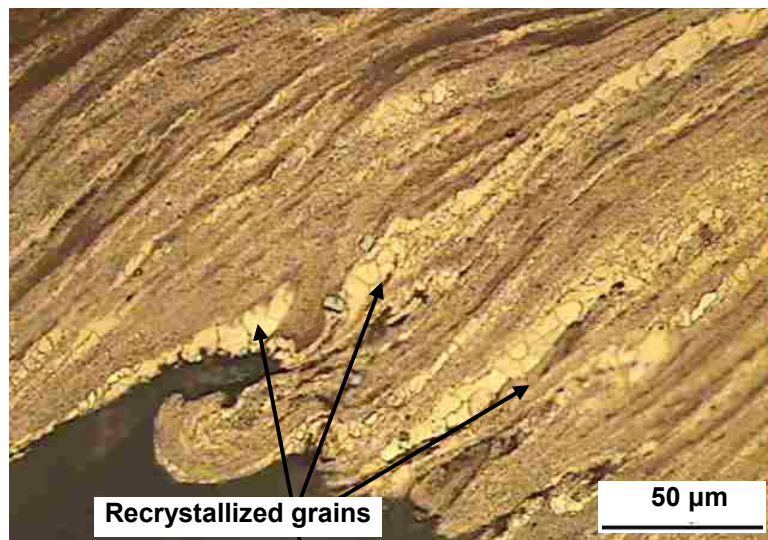
(b)

Figure 5. 17. (a) Optical micrograph showing general view of polished cross-section of transferred material after multiple cycles where deformation bands and zones of recrystallized grains can be seen; (b) higher magnification image of the rectangular area in (a) showing the recrystallized grains.
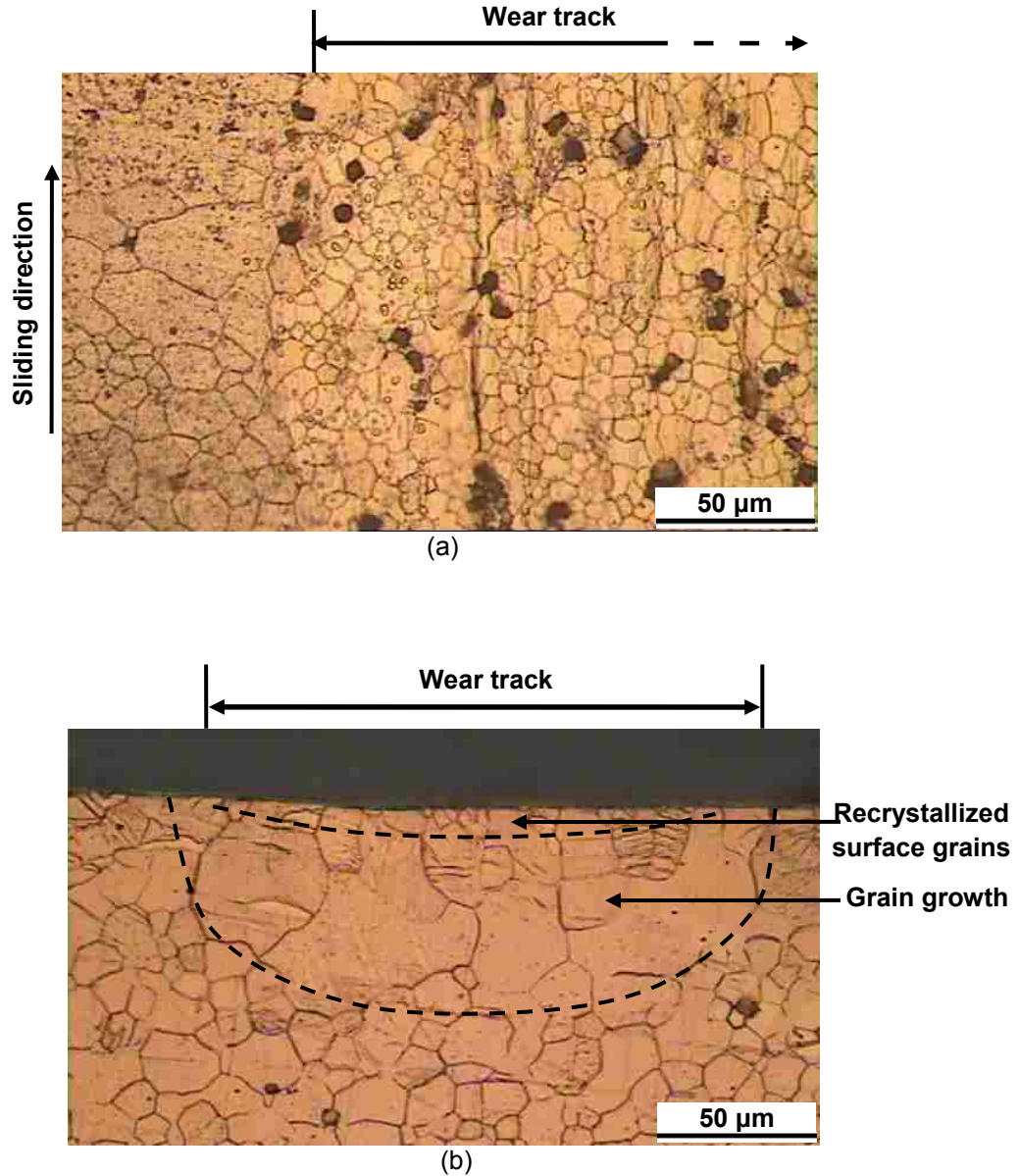
Figure 5. 18. Optical micrograph of worn sample after single cycle sliding at 400 °C: (a) Surface microstructure showing recrystallized grains inside the wear track. The track was etched with an acetic-picral solution for two seconds to remove the damaged surface layer; (b) Subsurface cross-sectional microstructure indicating recrystallized and grain growth zone.
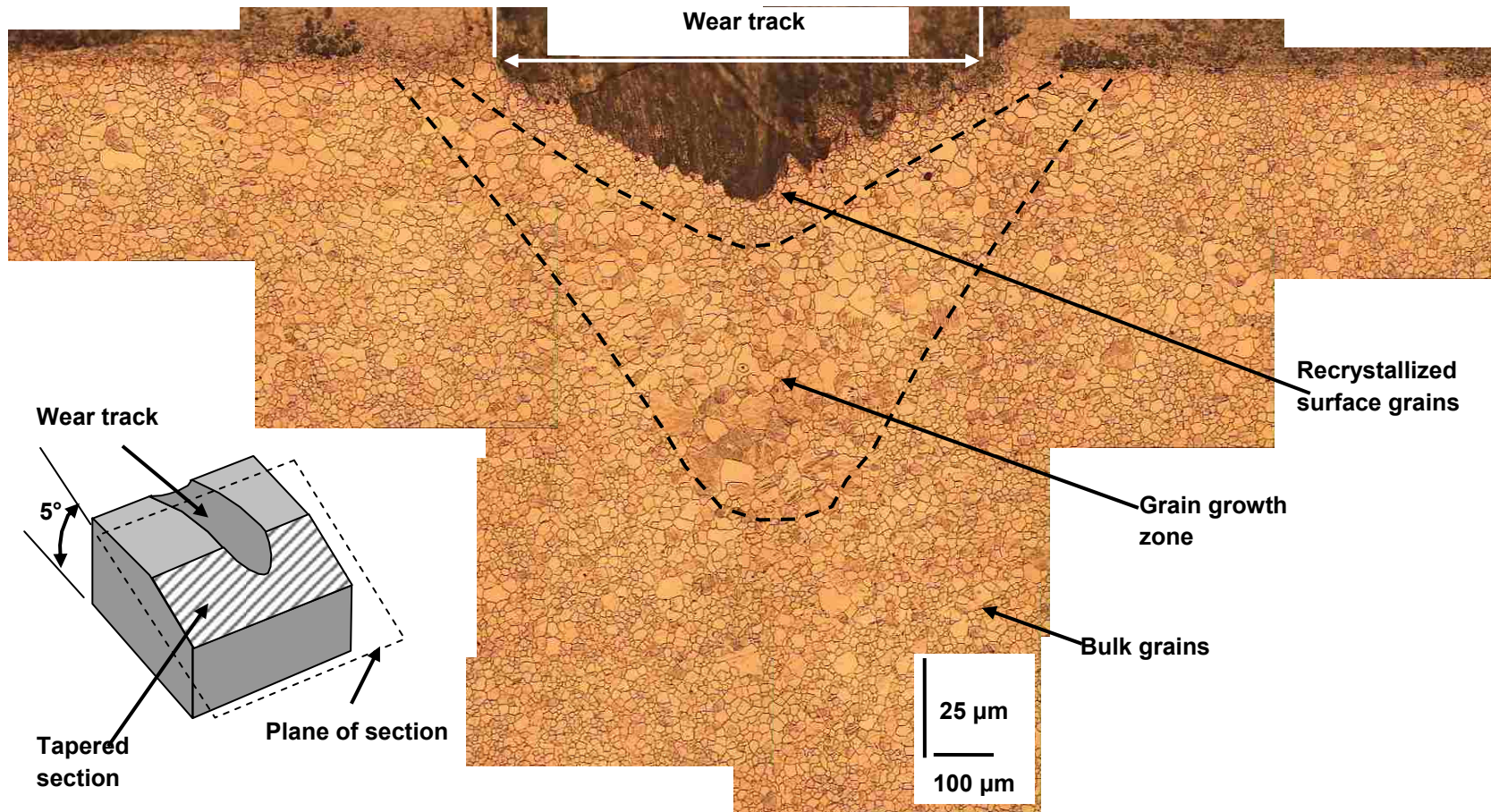
Figure 5. 19. Subsurface microstructure of the worn samples developed after sliding for 50 cycles at 400 °C. Micrograph indicates presence of a thin recrystallized zone and an extensive grain growth zone. This micrograph was taken from a tapered section of the wear track where the section plane was at a 5° angle to the horizontal axis (as indicated in the inserted schematic diagram).
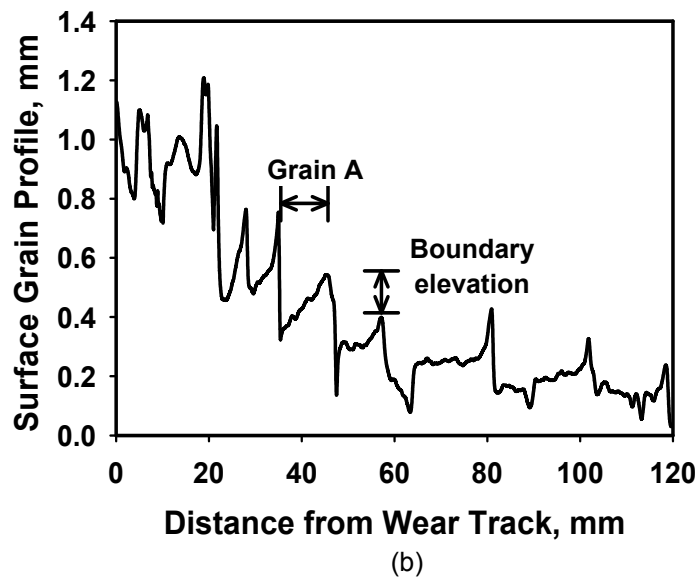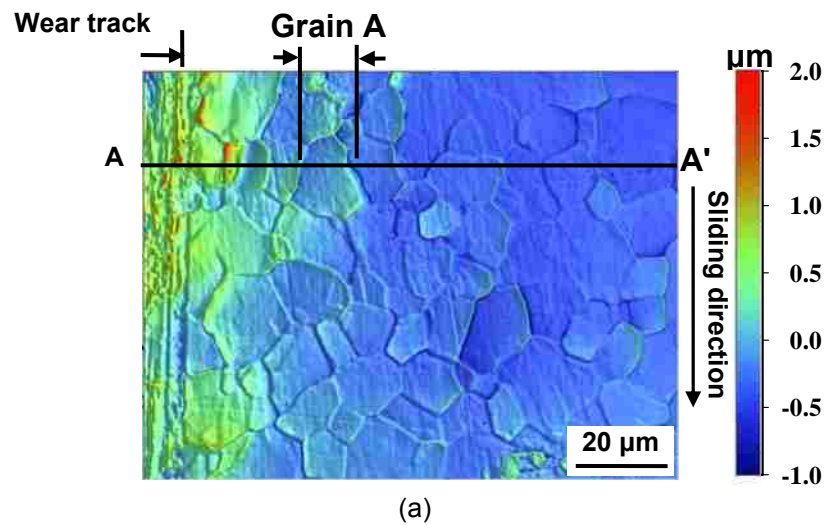
Figure 5. 20. (a) Worn surface profile of the plastically deformed zone adjacent to wear track after sliding for 50 cycles and (b) Two-dimensional profile of surface grains in the vicinity of wear track (from section AA' in (a)) indicating grains in the form of horizontal steps, and grain boundary elevations. The origin, i.e., '0' position on distance axis corresponds to the edge of wear track.

Chapter 6 General Discussion

6.1. Introduction

This chapter provides a general discussion of the deformation mechanisms that operate at elevated temperatures. It also discusses the relationships established between the deformation mechanisms and the measured COFs. **Section 6.2** focuses on the interpretation of the COF of AA5083 alloy in conjunction with its deformation behaviour. This section also discusses the surface damage caused by the high temperature deformation behaviour. **Section 6.3** describes the effect of dynamic recrystallization on deformation mechanisms of AZ31 alloy and the ways the dynamic recrystallization and deformation mechanisms could affect COF. In **Section 6.4**, a discussion of surface microstructure and morphology of the work piece material and adhesion of AA5083 and AZ31 alloy materials to steel surface is provided. The section also includes a discussion on the strength of the interface generated at first contact between the working material and P20 steel. This chapter also discusses the characteristic features developed on the surface as a result of high temperature deformation and the role of the surface morphologies and the surface oxide in contributing towards adhesion and friction.

6.2. Relationships between COF and deformation mechanisms

The delineation of deformation mechanisms that operate at elevated temperatures and their effect on surface conditions constitute an important step towards rationalizing the friction behaviour of AA5083. By analyzing the COF values simultaneously with the principal deformation mechanisms, a COF-deformation mechanism map (COF-DMM)

was developed as shown in **Figure 6.1**. This map incorporates iso-COF contours plotted together with the dominant deformation mechanism regimes. The map indicates the effects of different deformation mechanisms on the COF values. Accordingly, within a narrow temperature and strain rate region where plastic deformation occurs by SD creep, COF is comparatively low, that is, it varies between 1.2 and 1.4. Deformation by SD does not induce the roughening of the strip surface (**Figures 4.19c and d**) to the same extent as the GBS, which is evident from the comparison of R_a values (**Table 4.2**). Furthermore, the flow stress (hardness) of the alloy is the highest in the SD controlled region (**Figure 4.15c**). Thus, the relatively low COF can be attributed to two factors: (i) high hardness and (ii) low average roughness of the strip. At low strain rates, where diffusional flow occurs, the COF increases from 0.95 (420 °C and 5×10^{-3} s^{-1}) to 1.6 (545 °C and 1×10^{-2} s^{-1}), which corresponds to a 65 % increase in COF in a temperature range of 120 °C. Diffusional flow is not expected to induce surface roughening, and in fact, the R_a values measured vary only between 0.29 μm (420 °C and 5×10^{-3} s^{-1}) and 0.37 μm (545 °C and 1×10^{-2} s^{-1}) (**Table 4.2**). The increase in COF that occurs with temperature could be attributed to the softening of the alloy as its flow stress decreases from 16.9 at 420 °C to 5.5 MPa at 545 °C (**Figure 4.15c**).

The GBS deformation operates in the widest temperature and strain rate region in the COF-DMM (**Figure 6.1**) and embraces COF values that are as low as 1.2 (440 °C and $2.0 \times 10^{-2} - 2.5 \times 10^{-3}$ s^{-1}) to over 2.0 (540 °C and 4.0×10^{-2} s^{-1}). GBS has proven responsible for the high surface roughness values due to the formation of grain boundary offsets on the surfaces. The exposed surfaces were covered with an oxide layer of non-uniform thickness. In order to determine the contribution of GBS to the formation of

surface offsets, these oxide layers on the surfaces of AA5083 strips were removed by mechanically polishing the surfaces to an initial roughness of R_a = 0.04 μm, and the polished strips were subjected to the plastic deformation under temperatures and strain rates of interest. Although a (thinner) oxide layer again formed on the surfaces, the surface grain topography could be distinctly observed using optical interferometry (**Figures 6.2a to c**). As shown in **Figure 6.2d**, an increase in the strain rate increased the average grain boundary step height on the free surface.

A thorough quantification of the grain boundary step height is provided by conducting a statistical analysis that included the step heights formed at the grain boundaries of $100 - 150$ grains at each temperature and strain rate. As shown in the histograms in **Figures 6.3a and b**, GBS induced plastic flow at T = 420 °C and $d\varepsilon/dt$ = 4×10^{-2} s^{-1} (**Figure 6.3a**) resulted in a mean grain boundary step height of 0.90 ± 0.12 μm on the surface, whereas at T = 545 °C and $d\varepsilon/dt$ = 4×10^{-2} s^{-1}, the average step height increased to 1.45 ± 0.19 μm (**Figure 6.3b**). When the COF values are plotted against the grain boundary step height together with the range of operating deformation mechanisms (**Figure 6.4a**), the role of GBS in controlling the COF becomes evident. The COF values increased when the deformation temperature was increased while maintaining the same strain rate, whereas the flow stress of the material followed the opposite trend of COF behaviour, that is, flow stress decreased with increase in temperature. COF values are plotted against the grain boundary step heights normalized by the flow stress of the material deformation and shown in **Figure 6.4b**. The data points in the plot are fitted with a strain line, which indicates that the COF in AA5083 alloy is a function of grain boundary step height (or surface roughness) and flow stress of

deformation.

GBS, which was one of the dominant operating deformation mechanisms in AA5083 alloy, was found to have a role in controlling friction under the present deformation conditions. **Section 6.3.1** discusses the effect of dynamic recrystallization (DRX) on the COF of AZ31 alloy.

6.3. Effect of dynamic recrystallization (DRX) on COF of AZ31 alloy

6.3.1. DRX and grain growth

Low stacking fault energy material AZ31 alloy is very prone to undergo DRX upon deformation at $T > 250\,°C$. Therefore to establish a relation between plastic deformation mechanism and COF, DRX and its role on deformation behaviour were analyzed and will be discussed in this section.

The evolution of microstructure (that is, grain size and morphology) with the temperature and strain rate in AZ31 alloy is shown in **Figure 5.9**. Finer DRX grains were formed when the strain rates were high (see **Figures 5.9 to 5.11**). Lowest grain size of 3.6 μm was observed for the deformation at 250 °C and 1×10^{-2} s^{-1}. Finer DRX grains with increased strain rate were also observed by Zhang et al. [175] in Mg-Zn-Y alloy. This was attributed to the higher dislocation density when the alloy was deformed at high strain rate. Fine subgrains and DRX grains could form as more dislocations were absorbed into high-angle boundaries. For temperature ~ 400 °C in the present investigation, the grain size remained constant (~10 μm) irrespective of the applied strain rate (see **Figures 5.10 and 5.11**). At temperature (> 400 °C), grain growth in the material

resulted in an increase in grain size, the lowest being 13 μm at 450 °C and 5 × 10^{-3} s^{-1}. At the same temperature of 450 °C, when the applied strain rate was increased to 4 × 10^{-2} s^{-1}, the grain size in the material became as large as 20 μm. An increase in grain size with the strain rate was also reported previously by Rabinovich and Trifonov [176]. Cao et al. [177] claimed that the lattice diffusion is the grain growth mechanism in magnesium-lithium alloys.

The flow stress of AZ31 alloy was influenced by the concurrent grain growth during the experiments. By plotting the grain size values simultaneously with the principal deformation mechanisms, a 'grain size-DMM' was developed as shown in **Figure 6.5**. This map incorporates iso-grain size contours (see **Figures 5.10 and 5.11**) plotted on the dominant deformation mechanism regimes (**Figure 5.14**) that were identified based on the stress exponent values over the experimental temperature and strain rate range. The grain size of AZ31 alloy varied between 3.6 μm (250 °C and 1 × 10^{-2} s^{-1}) and 18.5 μm (450 °C and 4 × 10^{-2} s^{-1}) as in **Figure 6.5**. It can be suggested that a dynamic change in the grain size could control the operating mechanisms of deformation. GBS is the dominant mechanism for fine grain material only [6]. With the increase in the grain size, the material tends to deform more readily by glide controlled dislocation creep (viscous glide or solute drag) [25,107,111] which can be described by the following equation [70]:

$$\dot{\varepsilon} = k_5 \left(\frac{D_s}{b^2}\right)\left(\frac{\sigma}{E}\right)^3 \tag{6.1}$$

Where D_s is solute atom diffusion coefficient, b is the Burgers vector, E is the Young's modulus, k is Boltzmann's constant, and k_5 is material constant.

At temperatures > 400 °C, the DMM (see **Figure 5.14**) shows a stress exponent value > 3 indicating the change in the operating mechanism from GBS to viscous glide (solute drag) creep. The grain coarsening at high temperature (> 400 °C) and high strain rate (> 2×10^{-2} s^{-1}) was responsible for the increase in stress exponent value (to 3.5) and the change in deformation mechanism to dislocation dominated flow. The stress exponent value 2 usually represents GBS mechanism, occurrence of which depends on the fine grain size of the material (usually < 10 µm) as previously indicated [91,99,105-107]. Viscous glide creep mechanism also operated in the region of low temperature (≤ 300 °C) and high strain rate (≥ 3×10^{-2} s^{-1}) as shown in **Figure 6.5**.

The deformation mechanisms were related to the COF data for an interpretation of the tribological behaviour of AZ31 alloy during high temperature deformation and will be discussed in **Section 6.3.3**.

6.3.2. Elevated temperature COF of AZ31 alloy

Regardless of testing conditions, AZ31 magnesium alloy always showed lower COF compared to aluminum AA5083 alloy under the same homologous temperature and strain rate conditions as shown in **Figure 6.6**. For AA5083 alloy, plastic deformation mechanism at elevated temperature influences the surface characteristics, such as formation of grain boundary step heights at the surface (as a consequence of GBS mechanism operating in the bulk material). In addition to the effect of flow stress that changed with temperature, COF of AA5083 alloy is also affected by the variation in GB step heights that caused surface roughening and also by the oxide composition and mechanical properties. The COF of AZ31 alloy increased with temperature and strain rate. However, unlike AA5083 alloy, the surface roughening in AZ31 alloy (see **Figures**

5.4e and f) induced by the deformation in bulk material under the temperature (250 °C –
450 °C) and strain rate (5×10^{-3} s^{-1} – 4×10^{-2} s^{-1}) did not have a straight forward
relationship with the change in COF (in **Figures 5.1d**). GBS in AZ31 alloy operates in
the largest temperature and strain rate range (**Figure 5.14**). GBS and CGBS have proven
responsible for the increase in surface roughness in AZ31 alloy (see **Figures 5.5 and
5.8**). The surface of the AZ31 alloy which was covered with an oxide layer was broken
and formed oxide islands when the roughness increased due to the formation of elevated
grains at 450 °C and 4×10^{-2} s^{-1}. These oxide islands acted as abrasive and caused an
increase in COF.

6.3.3. COF-DMM

To delineate the role of the deformation on the COF of the AZ31 alloy, the COF
values (**Figure 5.1**) are plotted together with the regime of dominant deformation
mechanisms (**Figure 5.14**) as shown in **Figure 6.7**. At low strain rates ($< 1.5 \times 10^{-2}$ s^{-1}),
where diffusional flow dominates, COF increased from 0.34 (300 °C and 1×10^{-2} s^{-1}) to
0.59 (450 °C and 1×10^{-2} s^{-1}). This increase in COF is due to the decrease in flow stress
of the material. At low temperatures ($\leq$ 300 °C) and high strain rates ($\geq 3 \times 10^{-2}$ s^{-1}),
viscous glide creep mechanism operates (**Figure 6.7**), where the COF value remained
low (0.47 at 250 °C and 3×10^{-2} s^{-1}) due to the high strength of the material. For a wide
range of temperature and strain rate, GBS operates as in **Figure 6.7**, and the increase in
COF could be attributed to the increase in surface roughness and to the decrease in flow
stress. At temperature > 400 °C and strain rate > 2×10^{-2} s^{-1}, the stress exponent value
(see **Figure 5.14**) identified the mechanism as viscous glide (or solute drag) creep
mechanism. However, the surface profilometry data (see **Figure 5.8**) and the surface

micrographs (see **Figure 5.7**) in this viscous glide (or solute drag) regime also showed the occurrence of CGBS in addition to the glide mechanism. CGBS mechanism in the material caused surface roughening, which changed the surface oxide morphology that increased the COF.

As mentioned previously, at temperatures lower than 400 °C, upon increasing the applied strain rate, the grain size decreased as a result of dynamic recrystallization. Accordingly, increase in COF with strain rate at these temperatures is attributed to the surface roughening due to the GBS mechanism, which was also supported by decreased grain size. At temperatures beyond 400 °C, dislocation dominated flow took over (**Figure 6.7**). However, in this regime of the DMM, along with the glide controlled creep, the grains underwent cooperative grain boundary sliding (CGBS) mechanism, and generated elevated areas on the deformed surface. This CGBS deformation behaviour of the material was supported by the microstructural evidence from the worn surface as shown in **Figures 5.7a and b**. The micrograph in **Figure 5.7b** shows intermittent wear tracks, which was formed when the rough surface (generated by CGBS mechanism under the deformation condition of 450 °C and 4×10^{-2} s^{-1}) of AZ31 alloy was in contact against the P20 counterface.

6.3.4. Sliding induced deformation processes in AZ31 alloy

The deformation and damage process during high temperature sliding contact was studied using pin-on-disk type setup (without the application of external strain). The multiple sliding cycle experiments were done in order to establish a relation between the sliding induced deformation behaviour and the material removal during high temperature

sliding contact. In such experiments, the plastic strain in the material (localized beneath the wear track) was induced by sliding contact and excluded the effect of external strain. This section discusses the evolution of microstructures during sliding contact by referring to the stress and strain states developed below the wear track.

The metallographic evidence presented in **Figures 5.17 and 5.18** suggests that at 400 °C, the contact surface of AZ31 was subjected to severe damage and underwent dynamic recrystallization as well as grain growth. Material transfer to the counterface occurred simultaneously, and the transferred material exhibited features consistent with severe deformation and dynamic recrystallization. A description of the development of sliding-induced deformation microstructures is illustrated in **Figure 6.8** based on static pin-on-disk tests. The schematic diagram identifies grain boundary sliding (GBS) in the vicinity of the wear track.

The generic DMM constructed to represent the deformation mechanisms of magnesium at 400 °C was shown in **Figure 2.16** [91,106]. For the sliding experiments that were performed under a normal load of 5.0 N, a contact stress of 70 MPa was estimated when considering a contact area of 7×10^{-2} mm^2 (for which the contact diameter was assumed equal to the wear track width). As a result, a normalized stress (σ/E) of $\sim 2 \times 10^{-3}$ was obtained (with $E = 36$ GPa [67]). Using these values, the DMM in **Figure 2.16** suggests that GBS should be the main deformation mechanism for magnesium with an initial grain size of 14 μm. GBS can occur by lattice diffusion or grain boundary diffusion, for which the strain rates are given by **Equations 6.2 and 6.3**.

$$\dot{\varepsilon} = k_3 \left(\frac{D_L}{d^2}\right) \left(\frac{\sigma}{E}\right)^2 \text{ (lattice diffusion controlled)} \qquad (6.2)$$

$$\dot{\varepsilon} = k_4 \left(\frac{D_{gb}b}{d^3}\right) \left(\frac{\sigma}{E}\right)^2 \text{(boundary diffusion controlled)} \tag{6.3}$$

From **Equations 6.2 and 6.3**, strain rates of 4×10^{-3} s^{-1} and 2×10^{-3} s^{-1} can be calculated using the parameters listed in **Table 6.1**. Both strain rates are in general agreement with those used to carry out the hot-forming of magnesium alloys.

Table 6. 1.   Material constants used for calculation of strain rates for diffusional flow and GBS. (*$E_{673K} = E_{RT}[1-5.3 \times 10^{-4}(T\text{-}300)]$, and $E_{RT} = 45 \times 10^9$ N/m^2).

Material Parameters	Reported Values [47,91]
Material constant, k_3	7.59×10^8
Material constant, k_4	7.04×10^7
Grain boundary diffusion coefficient, D_{gb}	1.5×10^{-10} m^2/s
Lattice diffusion coefficient, D_L	4.8×10^{-16} m^2/s
Burgers vector, b	3.21×10^{-10} m
*Young's modulus at 673 K, E_{673K}	36×10^9 N/m^2

While evidence of GBS was found in the deformed material adjacent to the wear track, fine recrystallized grains were observed immediately below the contact surface, a location subjected to high plastic strains. The low stacking fault energy (60 – 78 kJ/mol) of magnesium alloys facilitates dynamic recrystallization [48], which normally occurs at higher temperatures than 400 °C. An increase in the imposed strain is expected to decrease the recrystallization temperature. For example, application of 60% tensile strain

(at a stain rate of 10^{-4} s^{-1}) reportedly reduced the recrystallization temperature of AZ31 alloy to a temperature of 250 °C [25]. Thus an effort has been made in this work to estimate the plastic strains under the worn surfaces. The experimentally determined equivalent (effective) plastic strain distribution under the wear track of the AZ31tested at 400 °C is shown in **Figure 6.9**. The measurements were made using the artificial marker method described in **Chapter 3**. The subsurface plastic strains exceed 100 % ($\varepsilon = 1$) at about 10 μm below the surface and reached as high as 3 or 300 % at depths less than 5 μm. The attainment of these large strains makes dynamic recrystallization possible during sliding at 400 °C. The recrystallized grains were confined to a narrow zone in the regions immediately below the contact surface, where the strains were the highest.

Underneath the recrystallization zone a grain growth zone was present. The kinetics of growth can be analyzed starting from examination of the grain size in data shown in **Figure 6.10a** which was obtained from quantitative analysis of microstructures in **Figures 5.18 and 5.19. Figure 6.10a** indicates an increase in the (largest) grain size from 36 ± 11 μm after one sliding cycle of sliding to 78 ± 13 μm after sliding for 50 cycles at 400 °C. No further increase in grain size was observed for a higher number of sliding cycles. The average maximum grain size (d_g) is re-plotted as a function of the sliding time (t) in **Figure 6.10b**, which reveals an initial high growth rate and subsequent decrease. Hence, the grain growth data can be expressed using the following parabolic equation:

$$d_g^2 - d_i^2 = C'.t$$

(6.4)

where d_i is the initial grain size, and d_g is the grain size at sliding time t. C' is a constant, and is equal to 24.1 μm^2 s^{-1} at 400 °C. Grain growth measurements performed at

other temperatures have shown that the parabolic relationship was maintained, so that the activation energy, Q, for grain growth can be obtained from a $(d_g^2 - d_i^2)$ plot against $(1/T)$ in a semi-logarithmic scale (**Figure 6.10c**) in the range between 300 °C and 400 °C, as follows:

$$d_g^2 - d_i^2 = C.t.exp\left(\frac{-Q}{RT}\right)$$

(6.5)

Accordingly, the activation energy for grain growth (calculated from the slope of the plot in **Figure 6.10c**) is determined as 35 kJ/mol. This value is lower than the activation energy for the self-diffusion of pure magnesium (for which Q_L = 135 kJ/mol for lattice diffusion, and Q_{gb} = 92 kJ/mol for grain boundary diffusion [67]). Consequently, the value of activation energy for grain growth during the sliding contact of AZ31 corresponds to ~ 0.38 Q_{gb}. The activation energy value determined for sliding induced grain growth in AZ31 can be compared with that from other high-strain deformation processes. For example, data generated during equal channel angular pressing experiments performed on AZ31, with a strain of ε = 3.0 [178,179] provided an activation energy of 33.5 kJ/mol for grain growth. Comparative activation energy data in the literature on high temperature sliding wear is rare, but the lower activation energy value of 35 kJ/mol for AZ31 is in agreement with the activation energy of 33 kJ/mol calculated for the severe wear of a 6061 aluminum alloy subjected to sliding contact at T = 200-500 °C and ε = 10 [143]. This value, too, is lower than that of the activation energy for the grain boundary diffusion of pure aluminum, Q_{gb} = 84 kJ/mol [67].

The progression of dynamic microstructural evolution events leading to material detachment from the surface of AZ31 can be considered as part of the cyclical damage

process that repeats itself during the course of sliding at 400 °C. During each cycle, high subsurface plastic strain gradient was generated immediately after the initiation of sliding contact (ε >3). This strain gradient in the subsurface caused recrystallization of grains within a zone of 10 μm in thickness below the contact surface. Recrystallized grains became detached from the underlying grain growth zone. It is conceivable that the material delamination process would be assisted by strain incompatibility between the two zones with different grain sizes. Once the material is removed and transferred to the counterface, fresh AZ31 surface became exposed so that another cycle of strain accumulation, deformation, and damage events recur. In this way, the microstructure would reach a dynamic equilibrium, and consequently, a constant wear rate (see **Figure 3.9**) is maintained.

The investigation on sliding induced damage in AZ31 alloy revealed that DRX and grain growth resulting from the strain accumulation controls the material transfer process during sliding contact experiments. In addition, evidence of high temperature deformation process such as GBS was also found in the vicinity of the wear track. The finding of the sliding experiments (without the application of external strain) provided a basic understanding of the role of the deformation mechanism on the tribological behaviour. Therefore, this was considered to be an important step towards understanding the friction and adhesion of AZ31 alloy during elevated temperature deformation.

6.4. Surface oxidation and adhesion

In previous sections (**Sections 6.2 and 6.3**), the temperature and strain rate dependence of COF has been discussed for both aluminum AA5083 and magnesium

AZ31 alloy materials. Also, a relation between the governing mechanisms of deformation and COF has been established. This section provides a few thoughts on adhesion of the material to the counterface. The characteristic features that developed on the surface of AA5083 and AZ31 alloys as a result of high temperature deformation, as well as the way these surface oxides interact with the counterface in nano-metric scale contributing towards adhesion and friction, are also provided here.

6.4.1. Junction strength

The maximum force required to break the asperity junction formed at the first contact is termed as 'junction strength'. The strength vs. time plots of junction strength experiments conducted on AZ31 alloy and AA5083 alloy are shown in **Figure 6.11**. The tangential force required to slide the workpiece materials against P20 counterface increased until a maximum value was reached, after which the force dropped. The maximum tangential force or junction strength values for AZ31 and AA5083 alloys (indicated using the dotted lines in **Figure 6.11**) are 0.30 N and 0.57 N respectively.

Static sliding experiments using ball-on-disk apparatus as well as dynamic sliding experiments using hot-forming simulator showed lower COF in AZ31 alloy than in AA5083 alloy (**Figure 6.6**) under the same homologous deformation temperature. The junction strength experiments conducted on AZ31 alloy and AA5083 alloy confirmed that the strength of AZ31 alloy is lower than the strength of AA5083 alloy as in **Figure 6.11.** In this figure, the junction strength of magnesium alloy with higher with higher aluminum content (AZ91) than that present in AZ31 was also plotted. The junction strength of AZ91 was found to be between AA5083 and AZ31 alloys. Accordingly, it can be inferred that junction strength in AA5083 is high because of its

low magnesium content. The existence of magnesium rich surface oxide reduced junction strength, and hence low COF is expected in AZ31 alloy. From the in-situ observation of the contact surface while the material was in sliding contact against 2 mm thick quartz glass disk, oxide formation at the contact surface was observed. **Figure 6.12a** shows chronological changes in the contact surface of magnesium AZ91 alloy slid against quartz glass. Oxidation of the material at first contact is evident from the microstructure in **Figure 6.12a**. Also, the contact area became larger and the oxidation continued until the whole contact surface was completely oxidized, which is the reason for the darker appearance. **Figure 6.12b** shows chronological changes in the contact surface of aluminum AA5083 alloy slid against quartz glass. The surface contact became enriched with this oxide (as seen by the dark areas in **Figures 6.12a and b**). In AZ31 alloy, once the surface became completely oxidized (MgO), material transfer to counterface disk was reduced. However, in AA5083 alloy, the formation of MgO was not sufficient to reduce the material transfer and COF. The junction strength experiments provided a better understanding of the COF behaviour of alloys with different magnesium content.

The surfaces of both as-received AA5083 and AZ31 alloy materials that produce the dynamic contact interface with the die surface were covered with a layer of oxide. The alloy with high magnesium content would provide a high amount of magnesium rich oxides and is therefore very important factor which ultimately determines COF at elevated temperature.

6.4.2. Surface oxide layers: role on COF

6.4.2.1. *Surface damage mechanisms in AA5083 alloy at 420 – 545 °C*
In this section the damage mechanisms that occurred in the oxide layer that

covered the surface of the AA5083 alloy during plastic deformation in the 420 – 545 °C temperature range were considered. Thin, fibrous structures or ligaments are observed in samples subjected to plastic deformation, especially at high temperatures and high strain rates. Typically, ligaments were between 1.5 – 2.5 μm long and were elongated to more than ten times their diameter of 0.1 – 0.2 μm without necking, suggesting superplastic behaviour. It has been shown [138,141] that the test environment has a crucial effect on ligament formation because ligaments are observed only on surfaces exposed to air. In addition, the results of this work have shown that the ligaments form directly from the oxide layer on the material and not from the bulk alloy. Distinction should be made between the plastic deformation of bulk alloy and the deformation of the oxide layer. When the grains of the alloy are subjected to GBS, they form surface steps on the surface. The sliding grain boundaries apply plastic strain to the oxide stretching over these sliding grain boundaries. The oxide is subjected to superplastic deformation at those locations. The superplasticity of the oxide ligaments could be attributed to diffusional flow and will be discussed in **Section 6.4.2.2**.

At T ≤ 450 °C, oxide layers fractured, with only a very few ligaments observed, while an increase in strain rate for $T \geq 460$ °C increased both the length and the area fraction of the ligaments on the deformed oxide layer. The deformation mechanisms operating in the AA5083 alloy in the same temperature (420 °C – 545 °C) and strain rate regime (2×10^{-2} s^{-1} – 4×10^{-2} s^{-1}) were described in **Section 6.2**. In the temperature range of 420 °C – 545 °C and a strain rate range of 2×10^{-2} s^{-1} – 4×10^{-2} s^{-1}, GBS was the dominant deformation mechanism. The surface offsets at 420 °C – 440 °C were low, with a mean grain boundary step height of 0.90 μm that increased with the temperature to

1.45 μm at 545 °C. GBS of AA5083 grains adjacent to the surface imposed a plastic strain on the oxide layer extending layer over their boundaries, resulting in ligament formation. In fact, ligaments were always found to occur on the oxide patches extending along the grain boundaries of the near surface bulk grains that had undergone sliding. The length of the ligaments was equal to the length of the grain boundary steps, and the rows of ligaments generally formed across the entire width of the grain boundary surface steps. The increase in the length of the ligament with the increase in temperature and strain rate is as expected because GBS in the AA5083 alloy becomes more prominent at higher temperatures and strain rates.

At low temperatures between 420 °C and 450 °C and high strain rates greater than 3×10^{-2} s^{-1}, deformation by solute drag becomes dominant. Since this mechanism does not promote the formation of surface offsets, oxide ligaments are not expected to form at the grain boundaries. On the other hand, diffusional flow becomes the main deformation mechanism at low strain rates. The alloy surface is flat without any grain boundary facets, and consequently, there is no local strain condition caused by GBS. Thus the GBS of the surface grains of the AA5083 alloy caused large elongations stretching oxide ligaments, and this is consistent with the observation that the location of the ligaments always corresponded to the grain boundaries of the bulk alloy, and the ligament length increased with increasing the grain boundary step height. The two types of oxide damage mechanisms are schematically illustrated in **Figures 6.13a and b**.

6.4.2.2. *Oxide ligament formation within the oxide layer*

The oxide ligaments within the oxide layer were able to accommodate the imposed strains and exhibited superplastic behaviour because of the nanocrystalline oxide

grains of 3 – 7 nm in diameter observed in their cross-sections. The size and geometry of these grains promote superplastic behaviour by grain boundary diffusion. More information regarding the formation of the ligaments can be obtained from **Figure 4.12**. It shows that the boundaries around the fine grains forming the ligaments are of significant size in relation to the grain diameters. This suggests that the ligaments are formed by Coble creep in which the diffusion in the material occurs mainly along the grain boundaries. The results of this work agree with the fine grain superplasticity model proposed by Zelin [134] and Claey [141] in which the superplastic deformation of the material is promoted by the small grain size in the ligaments.

Superplasticity has been observed in a number of nanocrystalline materials with grain sizes in the range of 10 – 100 nm tested at low temperatures ($< 0.4T_m$) [180,181]. Gleiter [182] suggested that grain boundary diffusion (Coble creep) should be the principal deformation mechanism in nanocrystalline materials even at $T = 0.1T_m$ (room temperature). The strain rate in a material experiencing Coble creep [56] is given by:

$$\frac{d\varepsilon}{dt} = \frac{\alpha_1 D_{gb}\delta\sigma\Omega}{d^3 kT}$$
(6.6)

Where α_1 is a constant, D_{gb} is the grain boundary diffusion coefficient, σ is the applied stress, Ω is the atomic volume, k is Boltzmann's constant, T is temperature, d is the average grain size and δ is the thickness of the grain boundary over which diffusion takes place.

A schematic diagram illustrating the possible microscopic processes responsible for the large elongations of the oxide ligaments is given in **Figure 6.14**. Nanocrystalline oxide grains with short diffusion distances and large grain boundary areas promote

diffusional flow when subjected to a local plastic strain gradient. This strain gradient is provided by the local increase of the surface roughness due to GBS of the underlying AA5083 grains. This is reflected in **Figure 6.14**, where the section of the oxide layer is being stretched as a result of the formation of a surface step by sliding of adjacent grains, and the oxide can accommodate the imposed strains due to the enhanced diffusional flow because of its nanocrystalline microstructure. In addition, dynamic oxide resulting from the reaction of atmospheric oxygen with the outward diffused magnesium during high temperature plastic deformation may contribute to ligament formation [134,183].

The area fractions of the oxide surface covered by the ligaments (termed ligament exposure) under the different temperature and strain rate conditions were used to generate an oxide damage map as shown previously in **Figure 4.10**. Apparently, both COF and ligament exposure increased with temperature and strain rate, when comparing COF-DMM in **Figure 6.1** with the oxide damage map in **Figure 4.10**. However, the increase in ligament exposure from 0.1% (at 420 °C and 5×10^{-3} s^{-1}) to 42.0% (at 545 °C and 4×10^{-2} s^{-1}) with the increase in temperature and strain was due to the higher grain boundary step heights resulting from GBS mechanism. These ligaments consisted of magnesium rich oxides (see **Sections 4.4.4 and 6.4.2.2**). Previously in **Sections 4.4.5 and 6.4.1**, it was shown that material with high magnesium contact provided a high amount of magnesium rich oxide (MgO), which reduced the COF of the material by reducing the junction strength of the contact. Therefore, the ligament exposure may not be the reason for the increasing behaviour of COF.

An interpretation of COF data at elevated temperatures required a detailed characterization of the material transferred to the P20 steel pin counterface. Further

investigations of the aluminum-steel interface are expected to shed light on the adhesion behaviour of the material and will be discussed in the next section.

6.4.3. Some comments on material transfer and adhesion

The interface between transferred material and the P20 steel surface showed the formation of very small junctions (< 100 nm). These appeared as miniature tensile samples as shown previously in **Figure 4.13c**. A high magnification micrograph taken from the same interface (**Figure 6.15a**) clarifies that the tensile samples at the interface are attached to the two surfaces as shown with the schematic representation in **Figure 6.15b**. The length and width of these interface features are not more than 60 nm and 20 nm respectively. Based on the angles made by these nano-tensile samples at the interface with the transferred material and the P20 steel surface (as in **Figure 6.15c**), the work of adhesion and the strength of the interface can be measured subsequently. The work of separation of these nano-tensile structures from either side can be calculated using **Equation 6.7** [184].

$$W = \gamma(1 + \cos\theta) \tag{6.7}$$

From the work of separation, the interface strength can be measured using **Equation 6.8** [184].

$$s = \frac{2W}{b} \tag{6.8}$$

Where W is the work of separation, γ is the surface energy, θ is the inside angle that was formed at the interface of the nano-tensile structures (see **Figure 6.15**) and the materials,

and *b* is the Burgers vector. Surface energy and Burgers vector values of Mg, Al, and their oxides (MgO and Al_2O_3) are given in **Table 6.2**.

Table 6. 2.   Surface energy and Burgers vector of different materials

Material	Surface energy, γ, J/m^2 [67,185]	Burgers vector, *b*, m [67]
Mg	0.79	3.21×10^{-10}
Al	1.14	2.86×10^{-10}
MgO	1.00	2.98×10^{-10}
Al_2O_3	0.90	4.76×10^{-10}

The angle, θ, on both sides of the nano-tensile sample was measured from the high magnification micrograph in **Figure 6.15a**, where the average value of interface angle θ was found to be $37.22 \pm 10.70°$ and $61.09 \pm 13.93°$ for side A and side B (as indicated in **Figure 6.15c**) respectively. The work of adhesion and interface strength values calculated using **Equations 6.7 and 6.8** for different materials are given in **Tables 6.3a and 6.3b**. Although the interface angles are not quite consistent at all locations, the average strength was found to be higher on side A than that of side B. Deformation behaviour of these nano-scaled structures is quite complex in nature due to the high surface to volume ratio of these structures. As shown on T**able 6.2**, the surface energy of metallic aluminum is the highest among Mg, MgO, Al_2O_3, and Al, hence providing high work of adhesion and interfacial strength as in **Table 6.3**. However, as discussed previously, the surface of AA5083 alloy is covered by MgO upon elevated temperature exposure. The interface strength for MgO was found to be 12.05 GPa and 9.95 GPa for

side A and side B (**Figure 6.15c**) respectively. Depending on the strength, the interface will break either on the side of the transferred material or on the side of the P20 steel surface.

Table 6. 3.   Work of adhesion (W) and interface strength (s) for different material at (a) side A, considering the average angle of 37.22° and (b) side B, considering the average angle of 61.09°.

(a)

Material	Work of adhesion, W, N/m (Calculated)	Interface strength, s, GPa (Calculated)
Mg	1.42	8.84
Al	2.05	14.32
MgO	1.80	12.05
Al$_2$O$_3$	1.62	6.79

(b)

Material	Work of adhesion, W, N/m (Calculated)	Interface strength, s, GPa (Calculated)
Mg	1.17	7.30
Al	1.69	11.82
MgO	1.48	9.95
Al$_2$O$_3$	1.33	5.61

The surface energy, and therefore the work of adhesion of the nano scaled structures formed at the surface and at the interface with the counterface material, contributes towards the microscopic friction behaviour.

6.5.   Factors determining the value of COF

The value of coefficient of friction under a dynamic tribological condition, which was created by the simultaneous effect of temperature and strain rate, depends on various factors as follows:

A. The strength of the material: Decrease in strength of the material as a consequence of temperature rise, increased the value of COF.

B. Magnesium content of the alloy: The alloy which had higher magnesium content provided lower COF. This is due to the fact that the alloy containing higher bulk magnesium showed more outward diffusion of magnesium which resulted in higher amount of MgO formation at the surface. Formation of MgO is the responsible for the low COF observed in the material with high magnesium content.

C. Nature of the oxide: It was expected that with the increase in temperature the higher amount of magnesium rich oxide formation at the surface would reduce COF of the material. However, with the increase in temperature the oxide layer, which consisted of nanocrystalline oxide grains, becomes viscous in nature and tends to stick to the counterface and hence increases COF value.

D. Surface roughness: Increase in temperature also has an influence on the possibility of GBS mechanism operating in the bulk material. GBS mechanism was found to induce surface roughening of the deformed material. Increased surface roughness due to GBS mechanism at high temperature and high strain rate contributed to high COF values.

Though presence of higher MgO at the contact surface at higher temperature is expected to reduce friction of the deforming material; however, low strength of the bulk material, dynamic surface roughening induced by GBS, and the sticky nature of the oxide at 545 °C have adverse affect on the tribological behaviour and increased the value of COF.
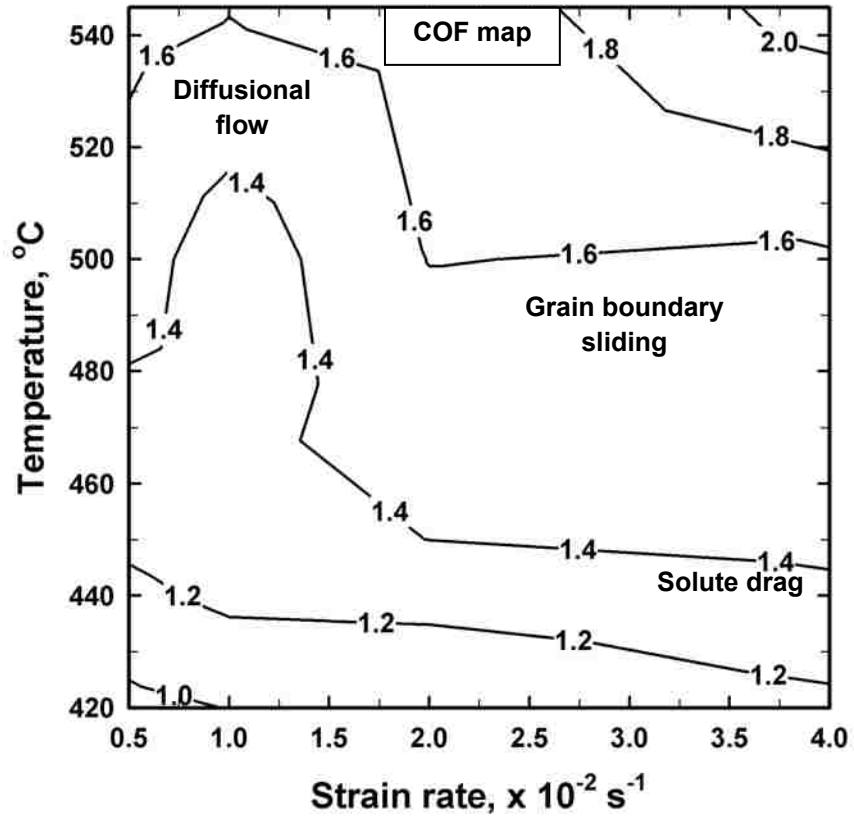
Figure 6. 1. Coefficient of friction-deformation mechanism map (COF-DMM) for AA5083 alloy plotted on temperature vs. strain rate axes, where the COF values from Figure 4.1c are superimposed on the DMM from Figure 4.17. The contours represent iso-COF values.
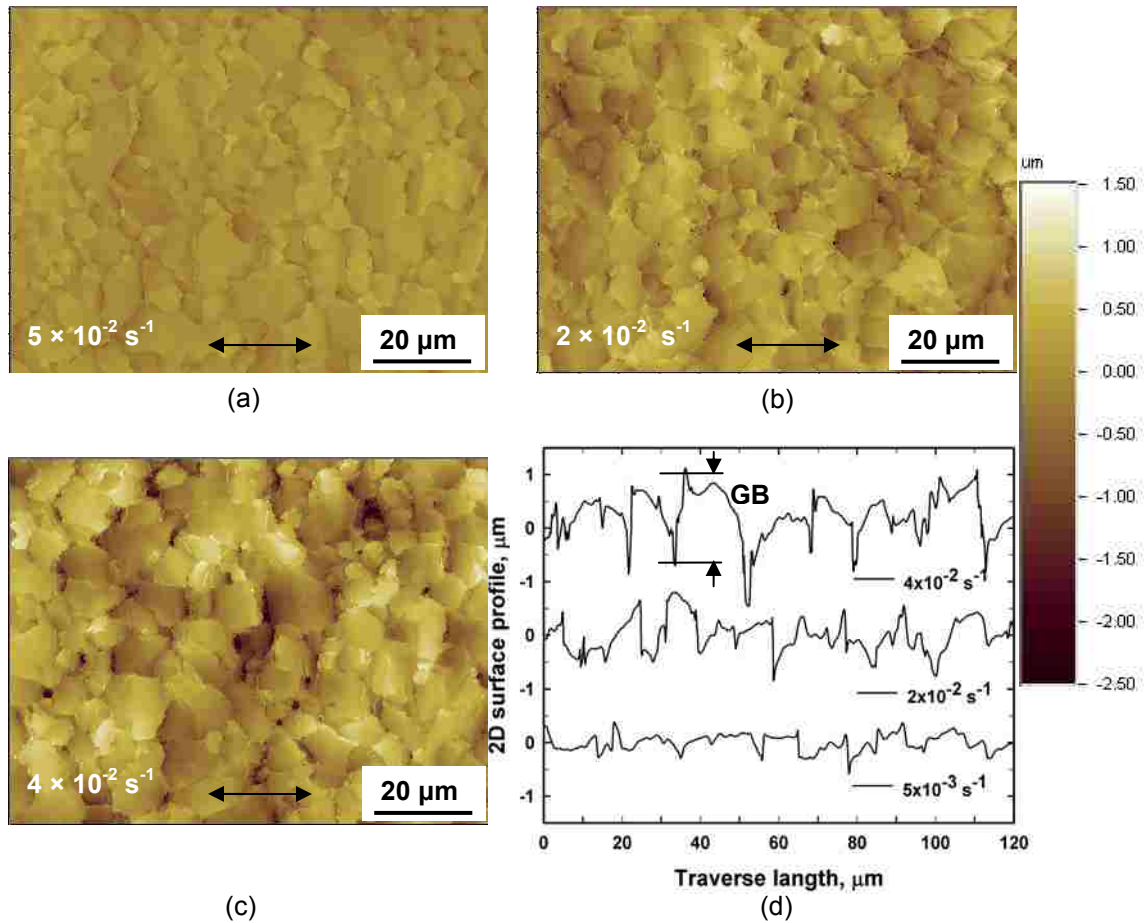
Figure 6. 2. 3-D optical surface interferometry profiles of the polished surfaces of AA5083 alloy strips deformed at 545 °C and (a) 5×10^{-3} s^{-1}, (b) 2×10^{-2} s^{-1} and (c) 4×10^{-2} s^{-1}; (d) 2-D profiles that show grain boundary step heights on the strip surface. The two sided arrow in the image indicates the tensile direction.
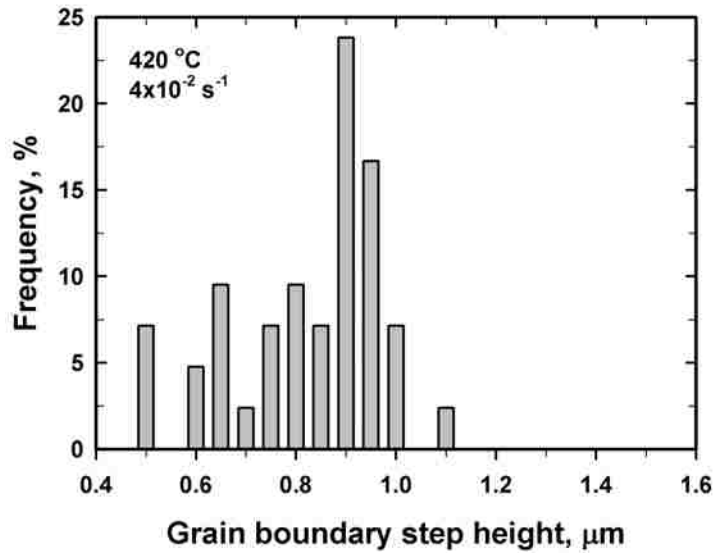
(a)
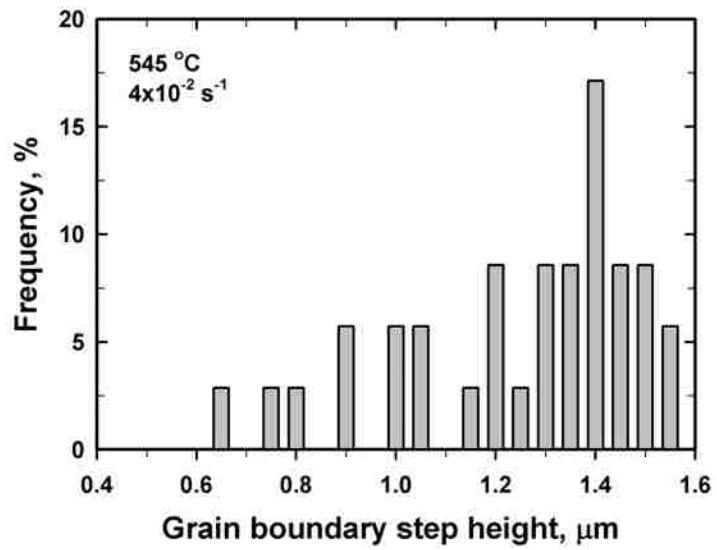
(b)

Figure 6. 3. Histograms showing the distribution of grain boundary (GB) step height on the surface of samples deformed at (a) 420 °C and 4×10^{-2} s^{-1}; and (b) 545 °C and 4×10^{-2} s^{-1}.
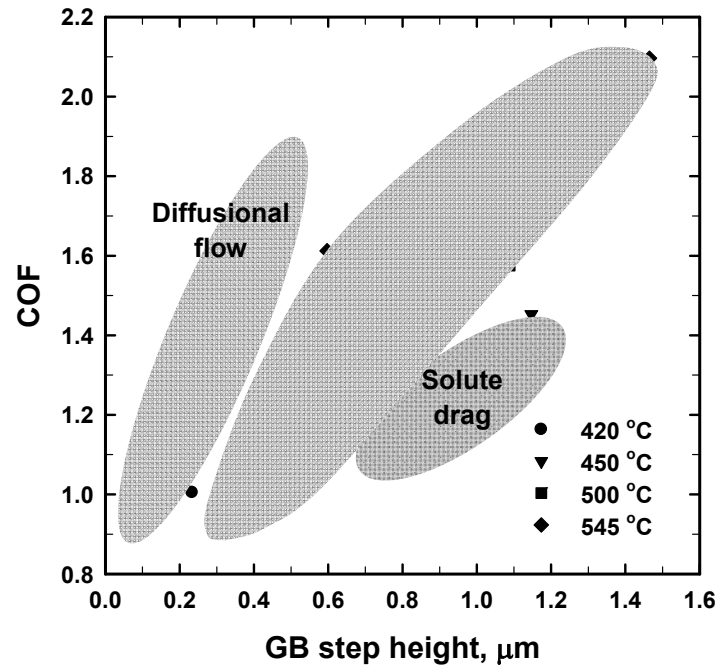
(a)
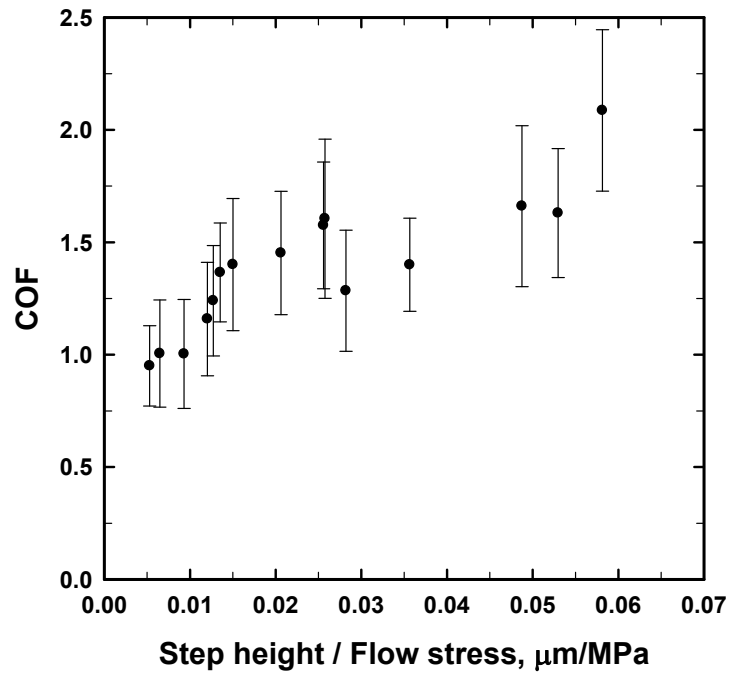
(b)

Figure 6. 4. (a) COF as a function of grain boundary (GB) step heights measured on strips deformed at various temperatures and (b) COF as a function of (step height/ flow stress) showing the combined effect of surface characteristics and mechanical behaviour on COF.
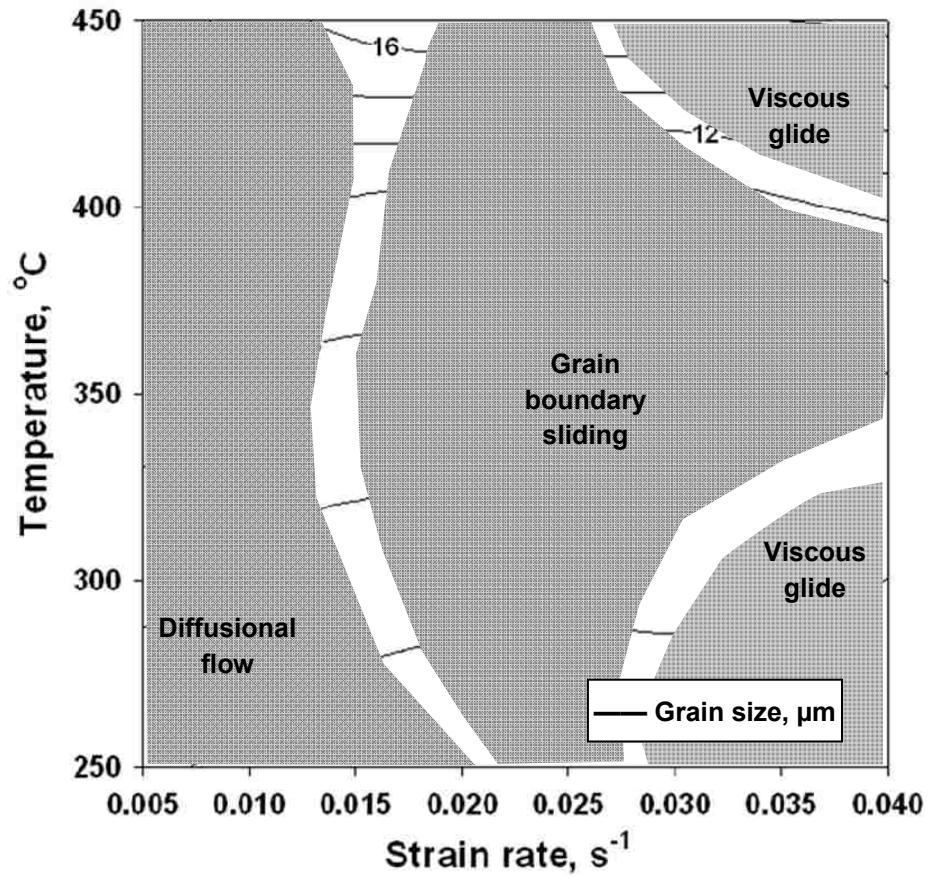
Figure 6. 5. Grain size (μm) of AZ31 alloy plotted along with the deformation mechanisms on temperature vs. strain rate axes.
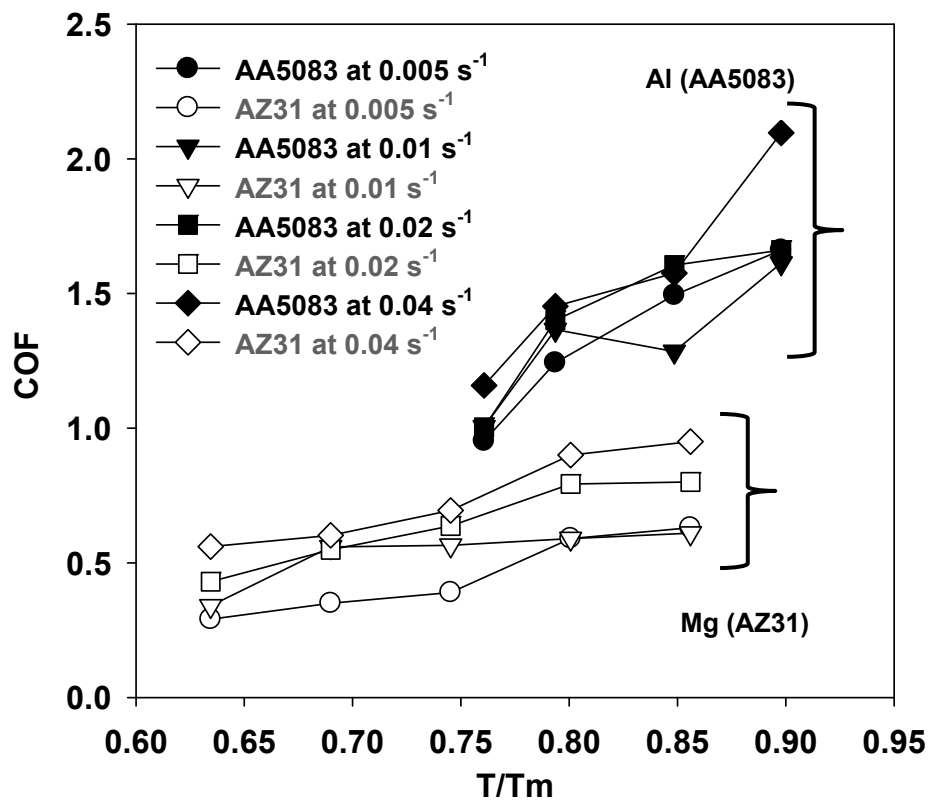
Figure 6. 6. COF of AA5083 and AZ31 alloys for same homologous temperatures at different strain rates.
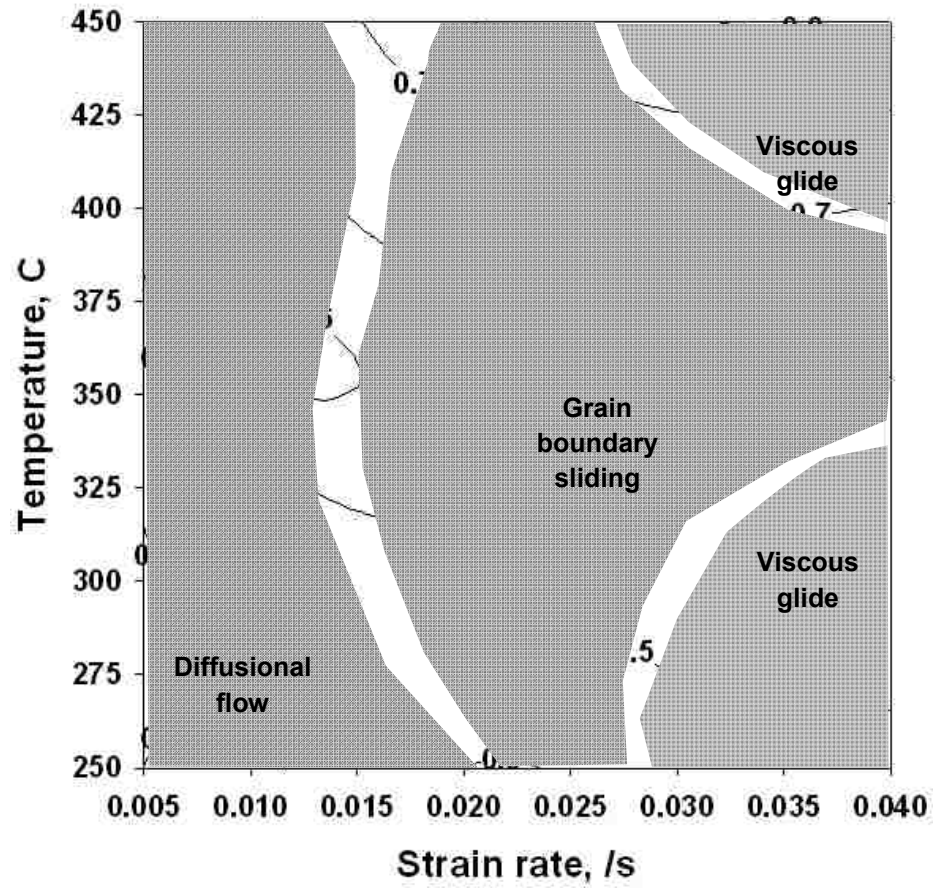
Figure 6. 7. COF-DMM for AZ31 alloy plotted on temperature vs. strain rate axes.
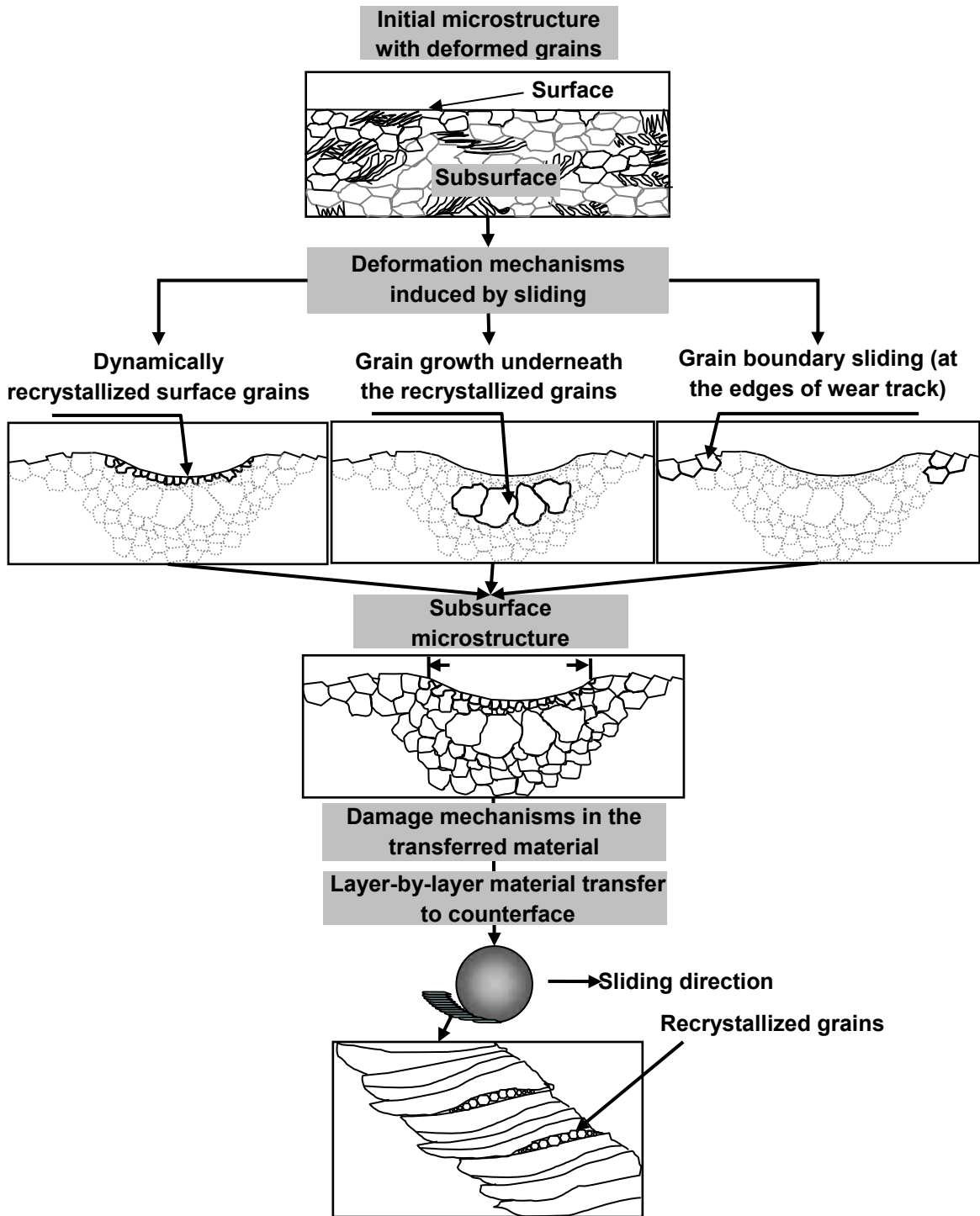
Figure 6. 8. Schematic diagram summarizing sliding induced microstructural events observed under the contact surfaces as well as in the debris fragments generated at 400 °C (constructed according to the Figures 5.17 to 5.20).
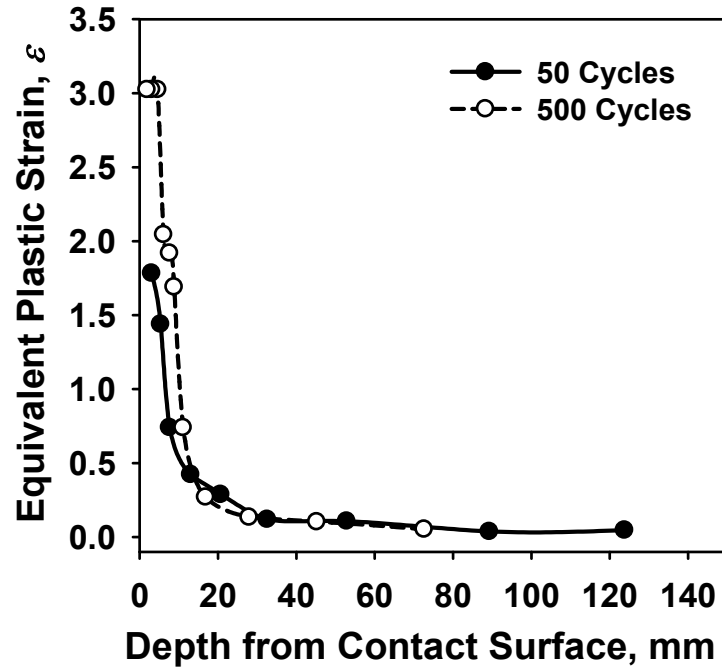
Figure 6. 9. The variation of equivalent plastic strain as a function of depth from the contact surface for samples tested for two different sliding cycles at 400 °C. See the Chapter 3 for details of the marker technique used for the stain measurements.
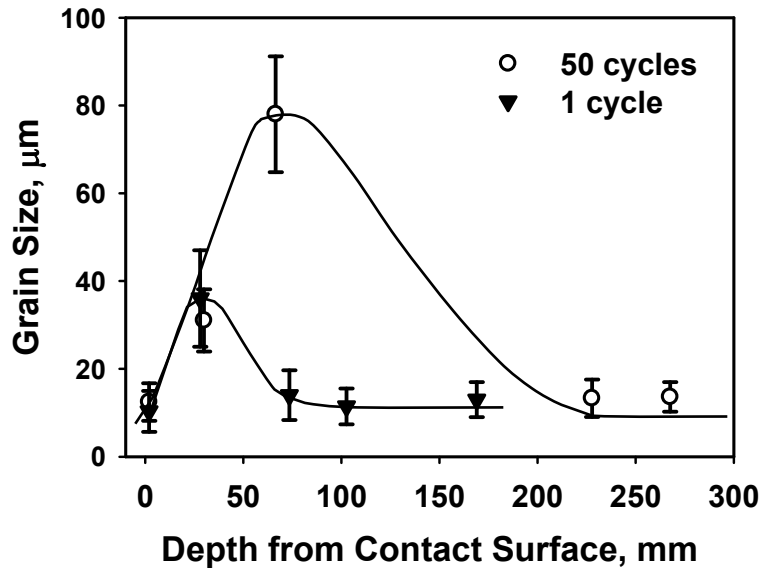
(a)
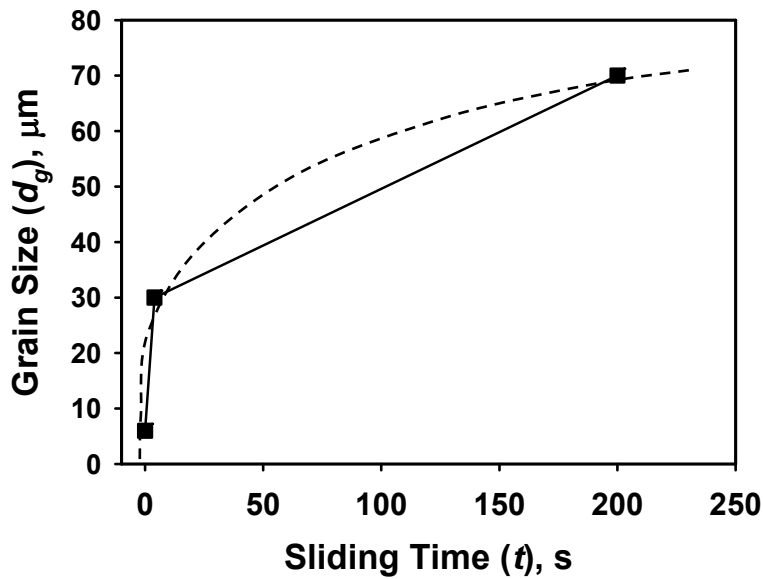
(b)

Figure 6. 10. (a) Grain size versus depth below the contact surface plot at one cycle (▼) and 50 cycles (●) at 400 °C; (b) The maximum grain size from (a) plotted against sliding time and (c) Plot of log $(d_g^2-d_i^2)$ against $1/T$ for the estimation of activation energy of grain growth during sliding in the temperature range of 300 and 400 °C.
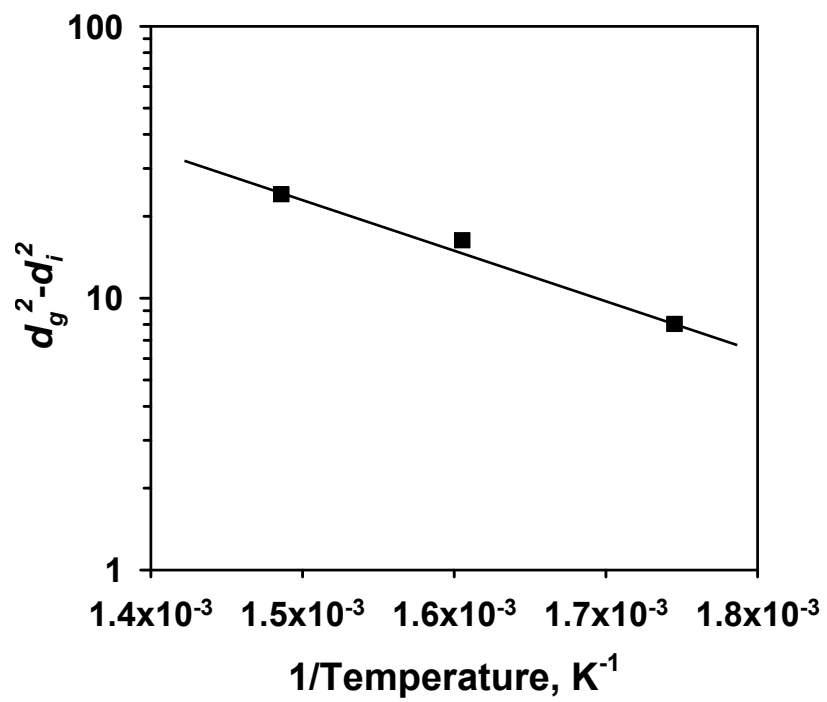
(c)
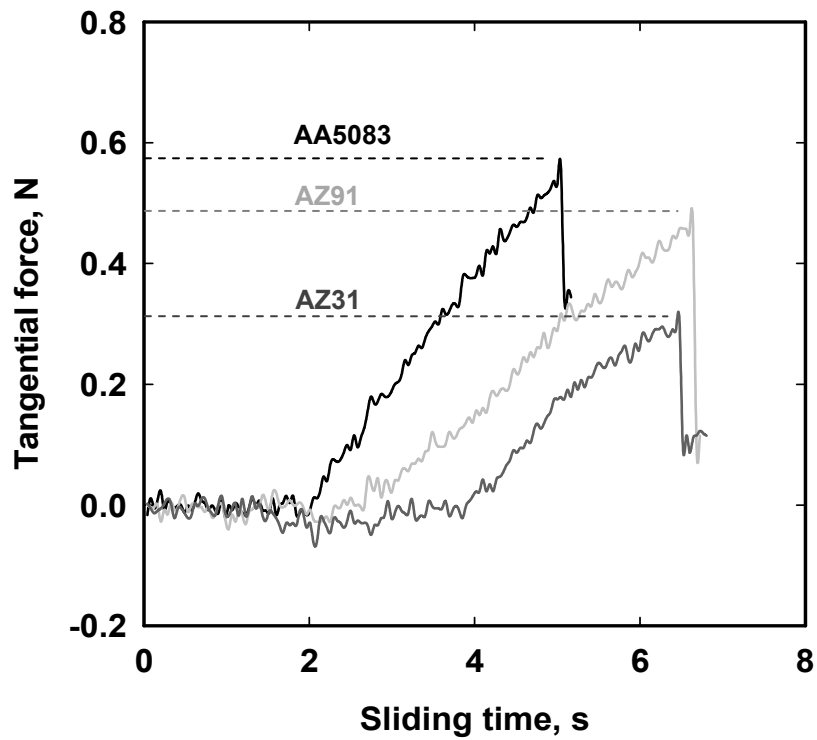
Figure 6. 11. Tangential force vs. sliding time plot for AA5083 and AZ31 alloys sliding against P20 steel at 390 °C under 0.5 N normal load. The plot shows that the junction strength of AZ31 alloy is lower than that of AA5083 alloy.
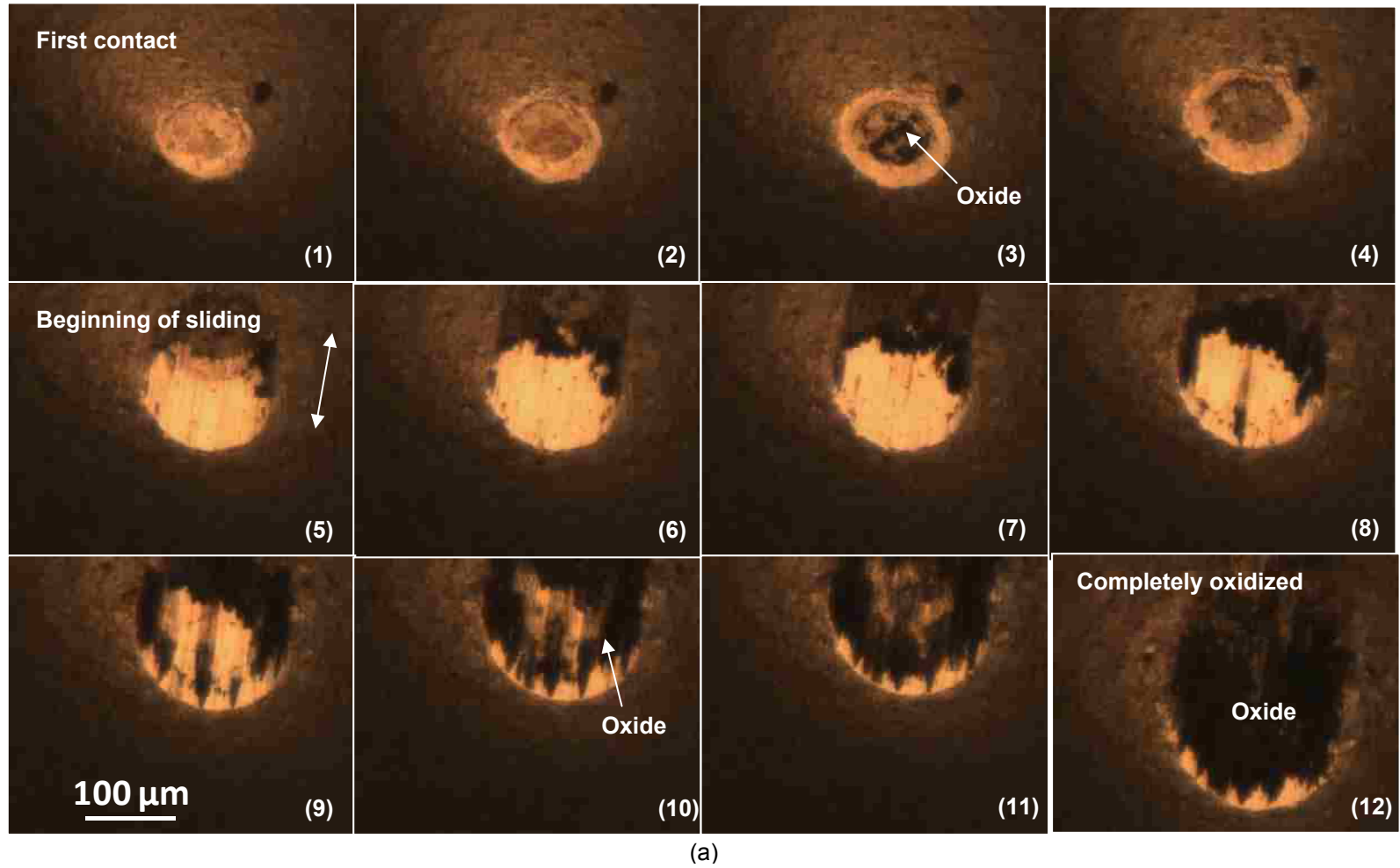
Figure 6. 12. (a) Sequential image of the AZ31 contact surface generated during a sliding experiment against glass using in-situ observation. Both sided arrow indicates the sliding direction. (b) Sequential image of the AA5083 contact surface generated during a sliding experiment against glass.

(b)

Brittle oxide

Crack in oxide layer

Surface layer - Cracks appear on the oxide layer, Al-Mg grains are exposed

(a)

Superplastic oxide

Surface offset due to GBS

Superplastic oxide ligaments

Surface layer - Ductile oxide layer, local superplasticity
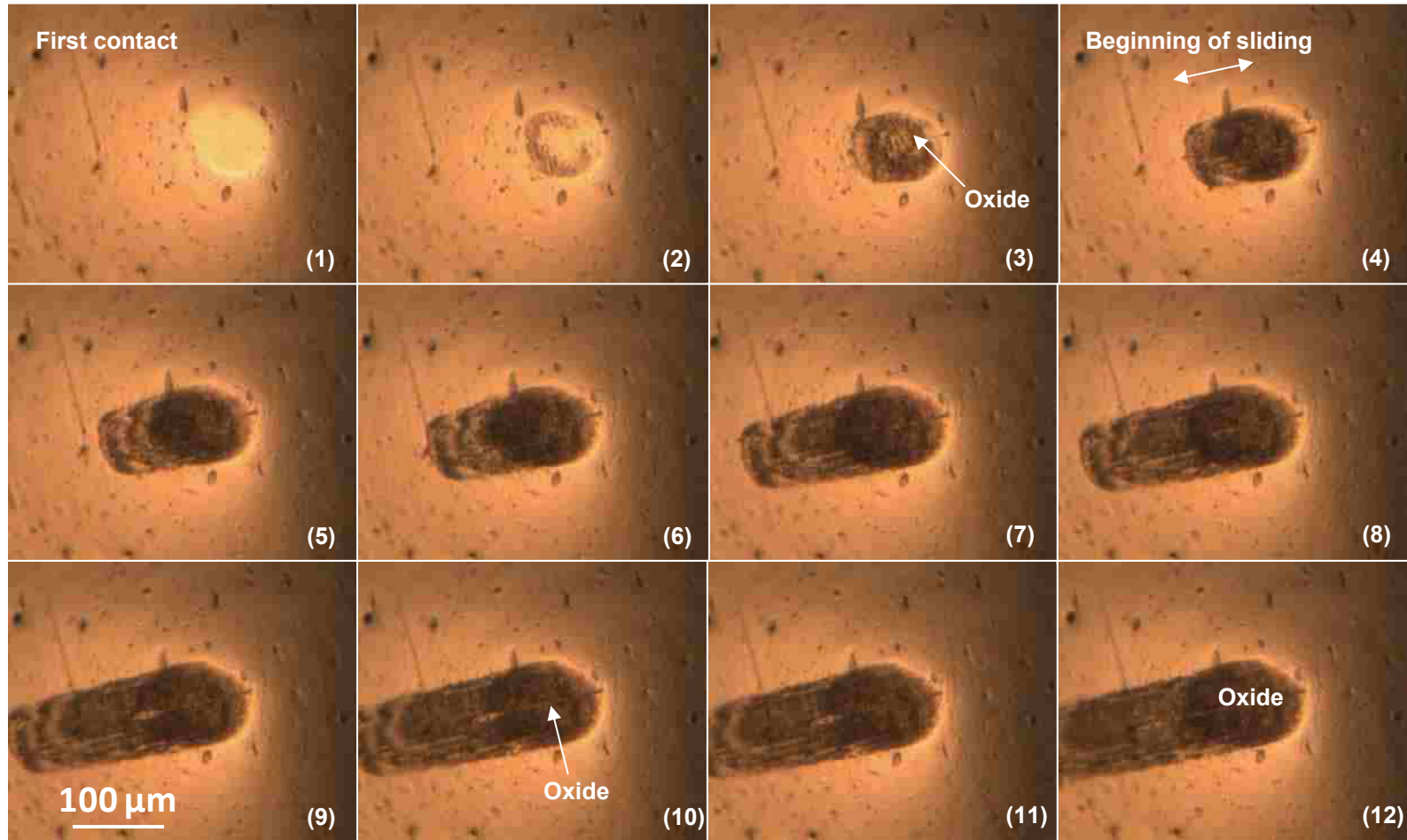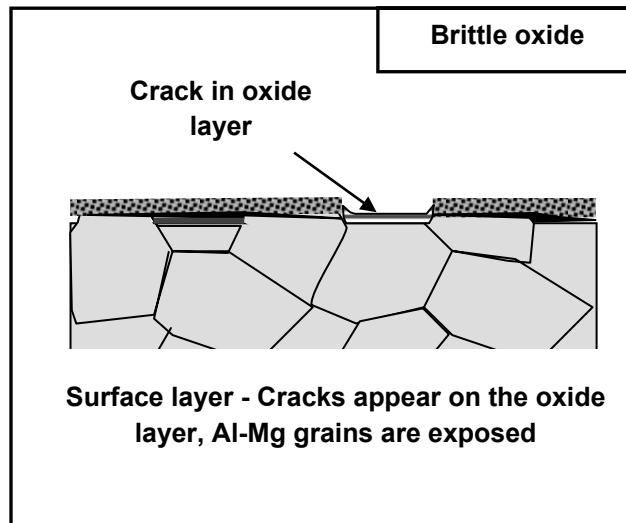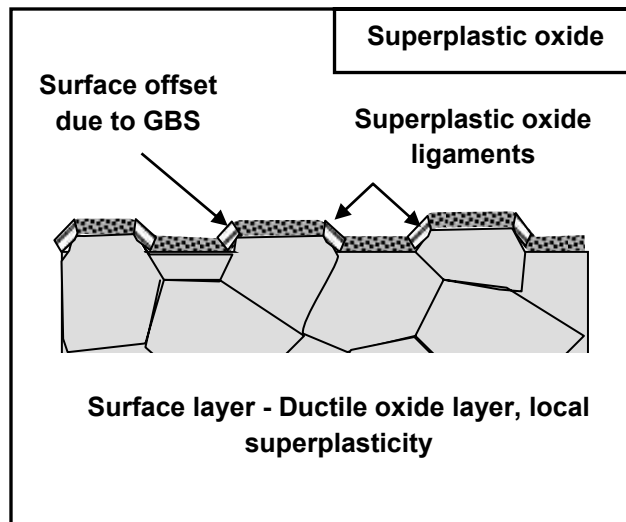
(b)

Figure 6. 13. The schematic representation of two types of surface damage features at two temperatures (a) cracks appeared on the oxide layer at 420 °C and (b) superplastic oxide ligaments, triggered by surface offset due to GBS, observed at 545 °C.
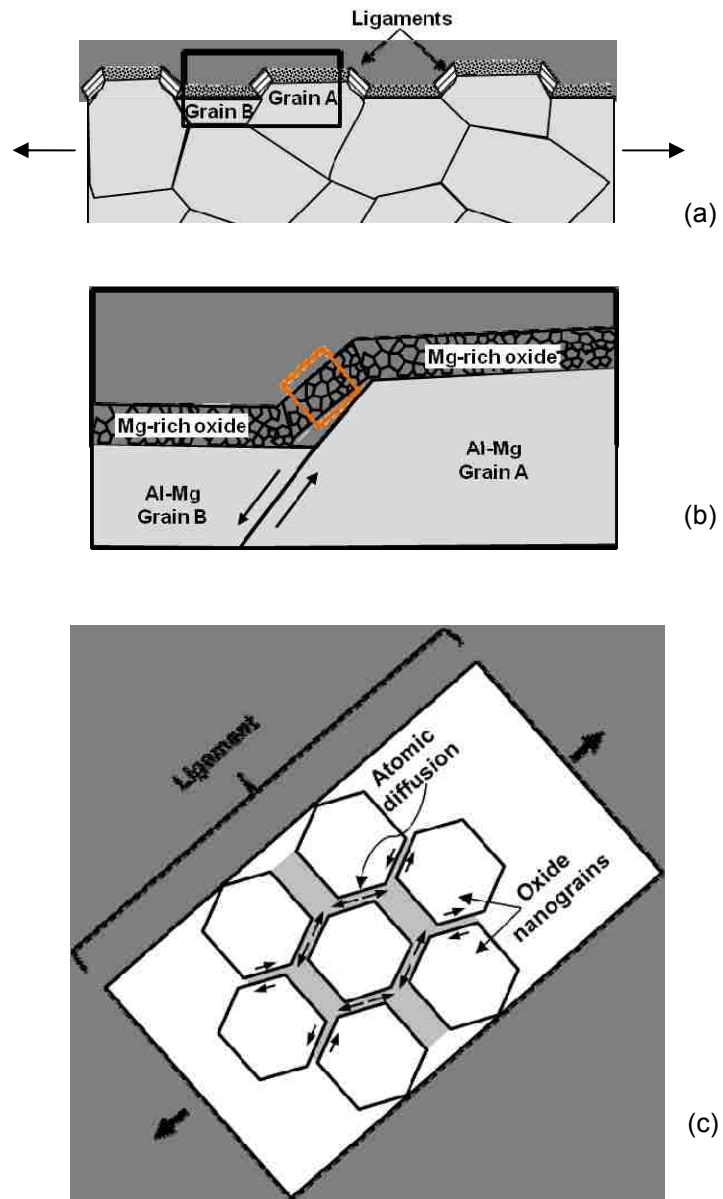
Figure 6. 14. (a) GBS of bulk grains leads to the formation of steps at the surface; (b) Step at the grain boundary due to relative sliding between grain A and grain B; (c) Suggested model for the formation of ligaments in the hot deformed AA5083 alloy.
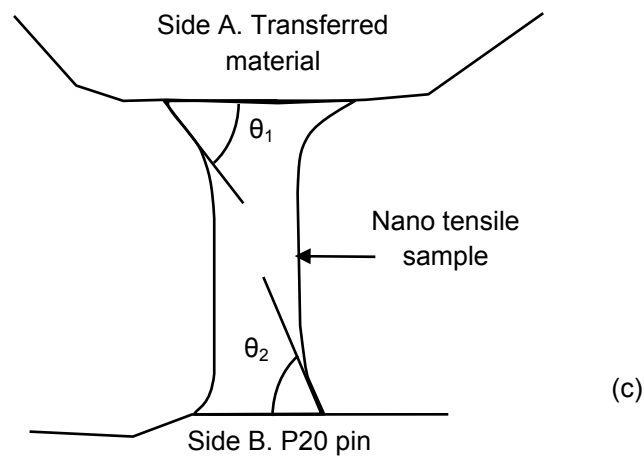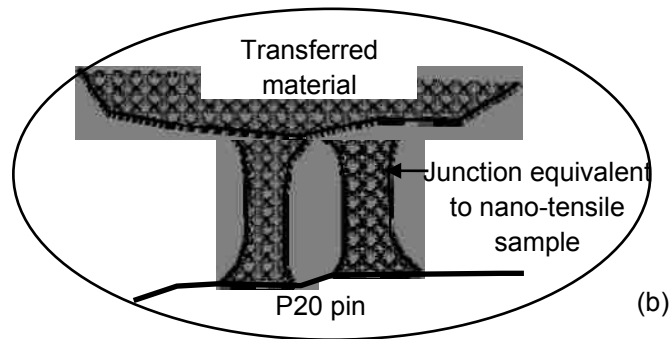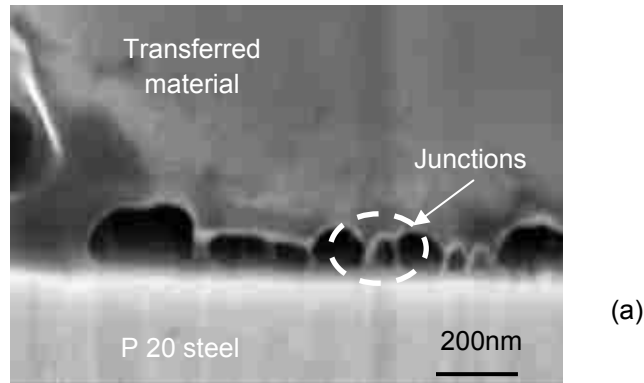
Figure 6. 15. (a) A high magnification view of the interface showing the formation of nano-tensile structures; (b) Schematic representation showing the both ends of nano-tensile samples are attached to the transferred material and P 20 steel surface; and (c) Schematic representation of the interface angle formed by the nano-tensile samples at side A and side B.

Chapter 7 Summary and Conclusions

7.1. Friction and plastic deformation mechanism of AA5083 alloy

1. Friction experiments conducted on the AA5083 strips showed that the coefficient of friction (COF) increased from 0.95 at 420 °C and 5×10^{-3} s^{-1}, to 2.09 at 545 °C and 4×10^{-2} s^{-1}.

2. The measured COF values were plotted on temperature and strain rate axes to create COF-DMM that represent the dynamic nature of friction. Three types of operating bulk deformation mechanisms (diffusional flow, grain boundary sliding (GBS) and solute drag (SD) creep) were identified within the temperature and strain rate ranges studied. The COF maps described the correlations between the dominant creep mechanisms and the COF values.

3. The largest variation in COF occurred in the region where GBS was the dominant bulk deformation mechanism. GBS increased with increasing temperature and strain rate and led to a higher surface roughness, and thus higher COF, due to steps that formed at the grain boundaries on the surface.

4. Diffusional flow did not induce surface roughening, and the R_a values varied within a small range. The increase in COF that occurred with temperature in this regime was attributed to the softening of the alloy.

5. Low average roughness and retention of strength (hardness) during deformation, led to low COF values in SD regime.

7.2. Friction and deformation behaviour of AZ31 alloy

1. Friction experiments conducted on the AZ31 strips showed that the COF increased from 0.3 at 250 °C and 5×10^{-3} s^{-1}, to 0.89 at 450 °C and 4×10^{-2} s^{-1}. Under the same homologous temperature and strain rate conditions AZ31 alloy showed lower COF than that of AA5083 alloy.

2. The COF map for AZ31 alloy was generated, which showed the regions of dominant creep mechanisms operating in the bulk and the corresponding COF values.

3. It was found that dynamic recrystallization and the grain growth are the additional factors to be considered while describing the tribological behaviour of AZ31 alloy. Upon deformation, dynamic recrystallization (DRX) refined the grains and made the material favorable for GBS. The process of DRX enhanced with the increase in strain rate.

4. At temperatures > 400 °C, grain growth became dominant and deformation mechanism changed to glide controlled dislocation creep (viscous glide). A clear distinction between the DMM for AA5083 and AZ31alloy materials is the glide controlled dislocation creep operating in AZ31 alloy at high temperature and high strain rate as a result of large grain size.

5. Along with the viscous glide creep, occurrence of cooperative grain boundary sliding (CGBS) mechanism was also found at $T > 400$ °C. CGBS mechanism influenced the COF behaviour by changing surface characteristics.

7.3. Sliding induced deformation in AZ31 alloy

1. During sliding wear at 400 °C, AZ31 material layers were detached and transferred to the counterface, which indicates that adhesion was the main material removal process. The transferred material was both highly deformed, and dynamically recrystallized.

2. Dynamic recrystallization occurred in the AZ31 close to the contact surface, where high strains (~ 200 – 300%) were generated. The subsurface below the contact surface experienced grain growth. Grain growth kinetics obeyed a parabolic law with an activation energy of 35 kJ/mol, which is comparable to other high-strain deformation processes at similar temperatures. Evidence of GBS was found in the deformed material at the edges of the wear track.

3. The large subsurface plastic strain under the wear track caused recrystallization of a thin layer of material, which was detached from the underlying grain growth zone and transferred to the counterface. The deformation and damage events repeated themselves in a cyclic form leading to the attainment of a dynamic equilibrium microstructure and a steady-state wear rate.

7.4. Surface oxide damage during high temperature deformation

1. Surface oxide damage mechanisms were found to be sensitive to the operating bulk deformation mechanisms. The creation of GBS-induced steps in AA5083 alloy led to the formation of micro-superplastic fibrous structures (ligaments) at high temperatures. At low temperatures, the surface oxide layer damage involved oxide cracks that formed along the grain boundaries normal to the tensile direction

2. Surface characterization of AA5083 revealed that fibres or ligaments up to 2.5 µm long and about 200 nm in diameter were formed on the surface of the oxide layer of an AA5083 alloy deformed between 420°C and 545°C. The main constituents of the ligaments were magnesium rich oxides (MgO and $MgAl_2O_4$).

3. Magnesium rich oxide was also found at the interface generated between the transferred material and the P20 steel surface.

4. The ligaments in AA5083 alloy always formed at locations extending above the grain boundaries of bulk alloy grains that experienced sliding during plastic deformation. The ligaments had an average grain size of 4.5 ± 0.7 nm. Diffusional flow promoted by nano-size grains was concluded to be responsible for oxide ligaments' superplasticity.

5. The appearance of the thin ligaments that showed uniform extension of up to 10 times their diameter, suggested superplastic behaviour of the oxide. The results agreed with the fine grain superplasticity model where the superplastic deformation of the material is promoted by the small grain size in the fibres. An understanding of the formation of these ligaments was important since they will

have a bearing on the fracture of these sheets following large-scale plasticity and on the friction during high temperature deformation.

6. The ligaments were also formed on the surface of AZ31 during high temperature (> 250 °C) deformation. The main constituent of the oxide ligaments that were found in AZ31 alloy as well as AA5083 alloy was MgO.

7. Magnesium rich surface oxides that were observed on the contact surface during junction strength experiments revealed that the adhesion tendency of Al-Mg alloys depends on the alloy's magnesium content. Magnesium- rich surface oxide was the reason for lower COF observed in AZ31 than that of AA5083 under the same homologous temperature and strain rate conditions.

7.5. General conclusions

1. Role of plastic deformation and damage mechanisms on COF of aluminum AA5083 and magnesium AZ31 alloy is established by generating COF-DMM for these materials. Also, the influence of surface oxide characteristics on the COF of these materials is identified.

2. By knowing the relation between friction and deformation behaviour, a desirable friction characteristics during hot-forming operation can be maintained by manipulating the deformation behaviour.

3. The friction maps generated for AA5083 and AZ31 alloy materials are important findings and could be used as an input parameter to improve the process modeling of hot-forming of these alloys.

7.6. Suggestions for future work

1. TEM investigations can be done on the AZ31 material, which was transferred to P20 steel pin under the same homologous temperature as in AA5083 alloy. The structure and composition of the interface generated between the transferred material and the P20 steel surface would led to the identification of the interface material and calculation of the strength of the interface. Also, a better understanding of the low COF in AZ31 alloy than that of AA5083 alloy can be obtained from the study.

2. The experiments can be extended to develop COF-DMM map for another experimental working window where a very high strain can be applied to the material, and, COF can be measured using different strain rate range or different sliding velocity. Extension of the map would lead to the data being more comparable to the actual conditions QPF or SPF where the strain can reach up to 300 %.

3. Using the COF maps developed in this work, generation of friction constitutive models for elevated temperature forming operation involving aluminum and magnesium alloys and rigid tools can be considered. These models can be implemented into the commercial finite element code and can be used to validate the actual hot-forming operations.

List of References

1. P.E. Krajewski, Research opportunities for automotive superplastic forming alloys, in: Taleff E.M., Friedman P.A., Krajewski P.E., Mishra R.S., Schrith J.G. (Eds.), Advances in Superplasticity and Superplastic Forming, Charlotte, NC. ed., 2004, pp. 173-183.

2. N. Ridley, Superplastic forming, in: Totten GE, MacKenzie DS (Eds.), Handbook of Aluminum, vol. 1, 1st ed., Marcel Dekker, New York, 2003, pp. 1105-1158.

3. A.A. Luo. Magnesium: Current and potential automotive applications, JOM. 54 (2002) 42-48.

4. R. Verma, P.A. Friedman, A.K. Ghosh, S. Kim, C. Kim. Characterization of superplastic deformation behavior of a fine grain 5083 AI alloy sheet, Metall Mat Trans A Phys Metall Mat Sci. 27 (1996) 1889-1898.

5. R.M. Cleveland, A.K. Ghosh, J.R. Bradley. Comparison of superplastic behavior in two 5083 aluminum alloys, Mat Sci Eng A. 351 (2003) 228-236.

6. O.D. Sherby, J. Wadsworth. Superplasticity-Recent advances and future directions, Prog Mater Sci. 33 (1989) 169-221.

7. M.S. Rashid, E.F. Ryntz, C. Kim, F.I. Saunders, R. Verma, S. Kim. Quick plastic forming of aluminum alloy sheet metal, US Patent US6253588 B1. (2001).

8. J.G. Schroth, General motors' quick plastic forming process, Adv. Superplasticity Superplastic Forming. (2004) 9-20.

9. A.T. Morales, Evaluation of die coatings for superplastic forming processes, Adv. Superplasticity Superplastic Forming. (2004) 51-64.

10. P.E. Krajewski, A.T. Morales. Tribological issues during quick plastic forming, J Mater Eng Perform. 13 (2004) 700-709.

11. R. Benzing, I. Goldblatt, V. Hopkins, W. Jamison, K. Mecklenburg, M. Peterson, Friction and wear devices, 2nd ed., American Society of Lubrication Engineers, Park Ridge, Ill, 1976, pp. 1-458.

12. J.A. Schey, Tribology in Metal Working: Friction, Fabrication and Wear, ASM, Metals Park, OH, 1983,.

13. J.A. Schey, M.K. Smith, Report of NADDRG friction committee on reproducibility of friction tests within and between laboratories, SAE Spec Publ. (1993) 261-267.

14. L. Wang, Y. He, J. Zhou, J. Duszczyk. Effect of temperature on the frictional behaviour of an aluminium alloy sliding against steel during ball-on-disc tests, Tribol Int. 43 (2010) 299-306.

15. M.D. Hanna. Tribological evaluation of aluminum and magnesium sheet forming at high temperatures, Wear. 267 (2009) 1046-1050.

16. S. Kalpakjian. Recent progress in metal forming tribology, CIRP Ann.Manuf.Technol. 34 (1985) 585-592.

17. M.A. Kulas, W.P. Green, E.M. Taleff, P.E. Krajewski, T.R. McNelley. Deformation mechanisms in superplastic AA5083 materials, Metall Mat Trans A Phys Metall Mat Sci. 36 (2005) 1249-1261.

18. E.M. Taleff, An overview of creep deformation behaviors in 5000-series and Al-Mg alloys, Adv. Superplasticity Superplastic Forming. (2004) 85-94.

19. E.M. Taleff, W.P. Green, M.-. Kulas, T.R. McNelley, P.E. Krajewski. Analysis, representation, and prediction of creep transients in Class I alloys, Mat Sci Eng A. 410-411 (2005) 32-37.

20. W.P. Green, M.-. Kulas, A. Niazi, K. Oishi, E.M. Taleff, P.A. Krajewski, et al. Deformation and failure of a superplastic AA5083 aluminum material with a Cu addition, Metall Mat Trans A Phys Metall Mat Sci. 37 (2006) 2727-2738.

21. T.R. McNelley, K. Oh-Ishi, A.P. Zhilyaev, S. Swaminathan, P.E. Krajewski, E.M. Taleff. Characteristics of the transition from grain-boundary sliding to solute drag creep in superplastic AA5083, Metall Mat Trans A Phys Metall Mat Sci. 39 (2008) 50-64.

22. T.R. McNalley, D.J. Michel, A. Salama. The Mg-concentration dependence of the strength of A1Mg alloys during glide-controlled deformation, Scripta Metall. 23 (1989) 1657-1662.

23. E.M. Taleff, G.A. Henshall, T.G. Nieh, D.R. Lesuer, J. Wadsworth. Warm-temperature tensile ductility in Al-Mg alloys, Metall Mat Trans A Phys Metall Mat Sci. 29 (1998) 1081-1091.

24. E.M. Taleff, P.J. Nevland, P.E. Krajewski. Tensile ductility of several commercial aluminum alloys at elevated temperatures, Metall Mat Trans A Phys Metall Mat Sci. 32 (2001) 1119-1130.

25. J.C. Tan, M.J. Tan. Superplasticity and grain boundary sliding characteristics in two stage deformation of Mg-3Al-1Zn alloy sheet, Mat Sci Eng A. 339 (2003) 81-89.

26. J.K. Solberg, J. Tørklep, Ø. Bauger, H. Gjestland. Superplasticity in magnesium alloy AZ91, Mat Sci Eng A. 134 (1991) 1201-1203.

27. H. Somekawa, H. Hosokawa, H. Watanabe, K. Higashi. Diffusion bonding in superplastic magnesium alloys, Mat Sci Eng A. 339 (2003) 328-333.

28. J.C. Tan, M.J. Tan. Dynamic continuous recrystallization characteristics in two stage deformation of Mg-3Al-1Zn alloy sheet, Mat Sci Eng A. 339 (2003) 124-132.

29. H. Takuda, S. Kikuchi, N. Hatta. Possibility of grain refinement for superplasticity of a Mg-AI-Zn alloy by pre-deformation, J Mater Sci. 27 (1992) 937-940.

30. X. Wu, Y. Liu. Superplasticity of coarse-grained magnesium alloy, Scripta Mater. 46 (2002) 269-274.

31. SuperformUSA, http://www.superform-aluminium.com/susa/. 2010.

32. M.D. Hanna, P.E. Krajewski, J.G. Schroth. Tribological testing of graphite and boron nitride lubricant formulations for high temperature aluminum sheet forming processes, Proceedings of the STLE/ASME Int'l Joint Tribology Conference, IJTC2007-44043. (2007).

33. P.E. Krajewski. Lubrication System for Hot Forming, Lubrication System for Hot Forming. (1998).

34. B. Navinšek, P. Panjan. Novel applications of CrN (PVD) coatings deposited at 200 °C, Surf Coat Technol. 74-75 (1995) 919-926.

35. B. Navinšek, P. Panjan, I. Milošev. Industrial applications of CrN (PVD) coatings, deposited at high and low temperatures, Surf Coat Technol. 97 (1997) 182-191.

36. J. Edwards, Coating and surface treatment systems for metals, 1997.

37. T.G. Nieh, J. Wadsworth, O.D. Sherby, Superplasticity in metals and ceramics, 1st ed., Cambridge University Press, UK, 1997, pp. 22-90.

38. E.E. Underwood. A review of superplasticity and related phenomenon, J.Met. 14 (1962) 914-919.

39. W.A. Backofen, I.R. Turner, D.H. Avery. Superplasticity in an Al-Zn alloy, Trans.ASM. 57 (1964) 980-990.

40. O.D. Sherby, J. Wadsworth, Development and characterization of fine-grain superplastic materials, Deformation, Processing, and Structure, ASM Materials Science Seminar. (1984) 355-389.

41. R. Verma, J.T. Carter. Quick Plastic Forming of a Decklid Inner Panel with Commercial AZ31 Magnesium Sheet. (2006).

42. G.E. Dieter. Mechanical Metallurgy. (1986).

43. R. Verma, A.K. Ghosh, S. Kim, C. Kim. Grain refinement and superplasticity in 5083 Al, Mat Sci Eng A. 191 (1995) 143-150.

44. O.D. Sherby. Advances in superplasticity and in superplastic materials, ISIJ Int. 29 (1989) 698-716.

45. D. Lee. The nature of superplastic deformation in the Mg-Al eutectic, Acta Metall. 17 (1969) 1057-1069.

46. R.Z. Valiev, O.A. Kaibyshev. Mechanism of superplastic deformation in a magnesium alloy - 1. Structural changes and operative deformation mechanisms. Phys Status Solidi (A) Appl Res. 44 (1977) 65-76.

47. R.E. Reed-Hill, W.D. Robertson. Deformation of magnesium single crystals by nonbasal slip, Trans.AIME. 209 (1957) 496-502.

48. S.E. Ion, F.J. Humphreys, S.H. White. Dynamic recrystallisation and the development of microstructure during the high temperature deformation of magnesium, Acta Metall. 30 (1982) 1909-1919.

49. A.A. Luo. Recent magnesium alloy development for elevated temperature applications, Int Mater Rev. 49 (2004) 13-30.

50. W. Rosenhain, J.C.W. Humfrey. The Crystalline Structure of Iron at Higher Temperature, Proc Royal Soc London. 83 (1910) 200-209.

51. W.A. Rachinger. Relative grain translations in the plastic flow of aluminium, J.Inst.Metals. 81 (1952) 33-41.

52. T.G. Langdon. A unified approach to grain boundary sliding in creep and superplasticity, Acta Metall Mater. 42 (1994) 2437-2443.

53. I.M. Lifshitz. On the theory of diffusion-viscous flow of polycrystalline bodies, Soviet Phys.JETP. 17 (1963) 909-920.

54. F.R.N. Nabarro. Deformation of crystals by the motion of single ions, Report of a Conference on the Strength of Solids.The Physical Society, London, U.K., 1948. (1948) 75-90.

55. C. Herring. Diffusional viscosity of a polycrystalline solid, J.Appl.Phys. 21 (1950) 437-445.

56. R.L. Coble. A model for boundary diffusion controlled creep in polycrystalline materials, J.Appl.Phys. 34 (1963) 1679-1682.

57. A.H. Chokshi. On the emergence of new surface grains during superplastic deformation, Scripta Mater. 44 (2001) 2611-2615.

58. M.F. Ashby, R.A. Verrall. Diffusion-accommodated flow and superplasticity, Acta Metall. 21 (1973) 149-163.

59. J.R. Spingarn, W.D. Nix. Diffusional creep and diffusionally accommodated grain rearrangement, Acta Metall. 26 (1978) 1389-1398.

60. D. Lee. Structural changes during the superplastic deformation, MT. 1 (1970) 309-311.

61. R.C. Gifkins. Grain rearrangements during superplastic deformation, J Mater Sci. 13 (1978) 1926-1936.

62. P.M. Hazzledine, D.E. Newbury, Grain boundary structure and properties, Academic Press, London, 1976, pp. 235-264.

63. T.G. Langdon. Significance of grain boundary sliding in creep and superplasticity, Metals forum. 4 (1981) 14-23.

64. H. Lüthy, R.A. White, O.D. Sherby. Grain boundary sliding and deformation mechanism maps, Materials Science and Engineering. 39 (1979) 211-216.

65. A. Ball, M.M. Hutchison. Superplasticity in aluminium-zinc alloy, Metal Sci J. 3 (1969) 1-7.

66. A.K. Mukherjee. The rate controlling mechanism in superplasticity, Materials Science and Engineering. 8 (1971) 83-89.

67. H.J. Frost, M.F. Ashby, Deformation-mechanism maps, Pergamon Press, Oxford, UK, 1982, pp. 22-110.

68. H. Fukuyo, H.C. Tsai, T. Oyama, O.D. Sherby. Superplasticity and newtonian-viscous flow in fine-grained class I solid solution alloys, ISIJ International. 31.1 (1991) 76-85.

69. R.C. Gifkins. Grain boundary sliding and its accomodation during creep and superplasticity, Metall Trans A. 7 A (1976) 1225-1232.

70. P. Yavari, T.G. Langdon. An examination of the breakdown in creep by viscous glide in solid solution alloys at high stress levels, Acta Metall. 30 (1982) 2181-2196.

71. F.A. Mohamed. Correlation between creep behavior in Al-based solid solution alloys and powder metallurgy Al alloys, Mat Sci Eng A. 245 (1998) 242-256.

72. T.G. Langdon. Transitions in creep behavior, Mater Trans, JIM. 37 (1996) 359-362.

73. O.D. Sherby, P.M. Burke. Mechanical behavior of crystalline solids at elevated temperature, Prog.Mater.Sci. 13 (1967) 325-390.

74. J. Weertman. Creep of indium, lead, and some of their alloys with various metals, Trans.AIME. 218 (1960) 207-218.

75. A.H. Cottrell, M.A. Jaswon. Distribution of solute atoms round a slow dislocation, Proc Royal Soc London. 199 A (1949) 104-114.

76. J.C. Fisher. On the strength of solid solution alloys, Acta Metall. 2 (1954) 9-10.

77. P. Yavari, D.A. Miller, T.G. Langdon. An investigation of harper-dorn creep-I. Mechanical and microstructural characteristics, Acta Metall. 30 (1982) 871-879.

78. J. Weertman. Steady-state creep through dislocation climb, J.Appl.Phys. 28 (1957) 362-364.

79. K. Linga Murty. Transitional creep mechanisms in Al-5Mg at high stresses, Scripta Metall. 7 (1973) 899-903.

80. W.J. Kim, E. Taleff, O.D. Sherby. A proposed deformation mechanism for high strain-rate superplasticity, Scripta Metallurgica et Materiala. 32 (1995) 1625-1630.

81. J. Harper, J.E. Dorn. Viscous creep of aluminum near its melting temperature, Acta Metall. 5 (1957) 654-665.

82. T.G. Langdon, P. Yavari. An investigation of Harper-Dorn creep-II. The flow process, Acta Metall. 30 (1982) 881-887.

83. J.N. Wang, T.G. Langdon. An evaluation of the rate-controlling flow process in Harper-Dorn creep, Acta Metall Mater. 42 (1994) 2487-2492.

84. F.A. Mohamed. Analysis of creep data on aluminum at very low stresses, Mat Sci Eng A. 32 (1978) 37-40.

85. R.Z. Valiev, O.A. Kaibyshev. On the quantitative evaluation of superplastic flow mechanisms, Acta Metall. 31 (1983) 2121-2128.

86. T.G. Langdon. The physics of superplastic deformation, Mat Sci Eng A. 137 (1991) 1-11.

87. M.T. Pérez-Prado, G. González-Doncel, O.A. Ruano, T.R. McNelley. Texture analysis of the transition from slip to grain boundary sliding in a discontinuously recrystallized superplastic aluminum alloy, Acta Mater. 49 (2001) 2259-2268.

88. E.A. El-Danaf, A.A. Almajid, M.S. Soliman. High-temperature deformation and ductility of a modified 5083 Al alloy, J Mater Eng Perform. 17 (2008) 572-579.

89. M.A. Kulas, W.P. Green, E.M. Taleff, P.E. Krajewski, T.R. McNelley. Failure mechanisms in superplastic AA5083 materials, Metall Mat Trans A Phys Metall Mat Sci. 37 (2006) 645-655.

90. D.E. Cipoletti, A.F. Bower, Y. Qi, P.E. Krajewski. The influence of heterogeneity in grain boundary sliding resistance on the constitutive behavior of AA5083 during high-temperature deformation, Mat Sci Eng A. 504 (2009) 175-182.

91. W.J. Kim, S.W. Chung, C.S. Chung, D. Kum. Superplasticity in thin magnesium alloy sheets and deformation mechanism maps for magnesium alloys at elevated temperatures, Acta Materialia. 49 (2001) 3337-3345.

92. T. Mohri, M. Mabuchi, M. Nakamura, T. Asahina, H. Iwasaki, T. Aizawa, et al. Microstructural evolution and superplasticity of rolled Mg-9Al-1Zn, Mat Sci Eng A. 290 (2000) 139-144.

93. T. Mukai, H. Watanabe, K. Higashi. Grain refinement of commercial magnesium alloys for high-strain-rate-superplastic forming, Mater Sci Forum. 350 (2000) 159-170.

94. H. Somekawa, H. Watanabe, K. Higashi. The grain size dependence on diffusion bonding behavior in superplastic Mg alloys, Materials Transactions. 44 (2003) 496-503.

95. J.A. Del Valle, M.T. Pérez-Prado, O.A. Ruano. Deformation mechanisms responsible for the high ductility in a Mg AZ31 alloy analyzed by electron backscattered diffraction, Metall Mat Trans A Phys Metall Mat Sci. 36 (2005) 1427-1438.

96. S.B. Yi, S. Zaefferer, H.-. Brokmeier. Mechanical behaviour and microstructural evolution of magnesium alloy AZ31 in tension at different temperatures, Mat Sci Eng A. 424 (2006) 275-281.

97. M. Mabuchi, T. Asahina, H. Iwasaki, K. Higashi. Experimental investigation of superplastic behaviour in magnesium alloys, Mater Sci Technol. 13 (1997) 825-831.

98. M. Mabuchi, H. Iwasaki, K. Yanase, K. Higashi. Low temperature superplasticity in an AZ91 magnesium alloy processed by ECAE, Scripta Mater. 36 (1997) 681-686.

99. H. Watanabe, T. Mukai, M. Kohzu, S. Tanabe, K. Higashi. Effect of temperature and grain size on the dominant diffusion process for superplastic flow in an AZ61 magnesium alloy, Acta Materialia. 47 (1999) 3753-3758.

100. Y.N. Wang, J.C. Huang. Comparison of grain boundary sliding in fine grained Mg and Al alloys during superplastic deformation, Scripta Mater. 48 (2003) 1117-1122.

101. H.K. Lin, J.C. Huang. High strain rate and/or low temperature superplasticity in AZ31 Mg alloys processed by simple high-ratio extrusion methods, Mater.Trans. 43 (2002) 2424-2432.

102. C.J. Lee, J.C. Huang. Cavitation characteristics in AZ31 Mg alloys during LTSP or HSRSP, Acta Mater. 52 (2004) 3111-3122.

103. M.T. Pérez-Prado, J.A. Del Valle, O.A. Ruano, Superplastic behavior of a fine grained AZ61 alloy processed by large strain hot rolling, Mater Sci Forum. 447-448 (2004) 221-226.

104. D.L. Yin, K.F. Zhang, G.F. Wang, W.B. Han. Superplasticity and cavitation in AZ31 Mg alloy at elevated temperatures, Mater Lett. 59 (2005) 1714-1718.

105. N. Srinivasan, Y.V.R.K. Prasad, P. Rama Rao. Hot deformation behaviour of Mg-3Al alloy-A study using processing map, Mat Sci Eng A. 476 (2008) 146-156.

106. S.W. Chung, K. Higashi, W.J. Kim. Superplastic gas pressure forming of fine-grained AZ61 magnesium alloy sheet, Mat Sci Eng A. 372 (2004) 15-20.

107. H. Somekawa, K. Hirai, H. Watanabe, Y. Takigawa, K. Higashi. Dislocation creep behavior in Mg-Al-Zn alloys, Mat Sci Eng A. 407 (2005) 53-61.

108. H. Watanabe, T. Mukai, M. Mabuchi, K. Higashi. Superplastic deformation mechanism in powder metallurgy magnesium alloys and composites, Acta Materialia. 49 (2001) 2027-2037.

109. T. Mukai, H. Tsutsui, H. Watanabe, K. Ishikawa, Y. Okanda, M. Kohzu, et al. Experimental study of the mechanical properties at elevated temperatures in commercial Mg-Al-Zn alloys for superplastic forming, Key Eng Mat. 171-174 (2000) 337-342.

110. A. Galiyev, R. Kaibyshev, Dynamic recrystallization and grain growth in a ZK60 magnesium alloy sheet produced by isothermal rolling, Mater Sci Forum. 467-470 (2004) 1175-1180.

111. H. Watanabe, H. Tsutsui, T. Mukai, M. Kohzu, S. Tanabe, K. Higashi. Deformation mechanism in a coarse-grained Mg-Al-Zn alloy at elevated temperatures, Int J Plast. 17 (2001) 387-397.

112. A. Mwembela, E.B. Konopleva, H.J. McQueen. Microstructural development in Mg alloy AZ31 during hot working, Scr.Mater. 37 (1997) 1789-1795.

113. M.M. Myshlyaev, H.J. McQueen, A. Mwembela, E. Konopleva. Twinning, dynamic recovery and recrystallization in hot worked Mg-Al-Zn alloy, Mat Sci Eng A. 337 (2002) 121-133.

114. Y. Zhang, X. Zeng, C. Lu, W. Ding. Deformation behavior and dynamic recrystallization of a Mg-Zn-Y-Zr alloy, Mat Sci Eng A. 428 (2006) 91-97.

115. R.S. Kottada, A.H. Chokshi, Hot working of an as-cast Mg-2%Al alloy, Mater Sci Forum. 426-432 (2003) 4417-4422.

116. A. Galiyev, R. Kaibyshev, G. Gottstein. Correlation of plastic deformation and dynamic recrystallization in magnesium alloy ZK60, Acta Mater. 49 (2001) 1199-1207.

117. F.J. Humphreys, M. Hatherly, Recrystallization and related annealing phenomena, 2nd ed., Elsevier, Oxford, UK, 2004.

118. J.A. del Valle, O.A. Ruano. Influence of texture on dynamic recrystallization and deformation mechanisms in rolled or ECAPed AZ31 magnesium alloy, Mater Sci Eng A. 487 (2008) 473-80.

119. T. Al-Samman, G. Gottstein. Dynamic recrystallization during high temperature deformation of magnesium, Mat Sci Eng A. 490 (2008) 411-420.

120. R. Panicker, A.H. Chokshi, R.K. Mishra, R. Verma, P.E. Krajewski. Microstructural evolution and grain boundary sliding in a superplastic magnesium AZ31 alloy, Acta Mater. 57 (2009) 3683-3693.

121. M. Fishkis, J.C. Lin. Formation and evolution of a subsurface layer in a metalworking process, Wear. 206 (1997) 156-170.

122. G. Buytaert, H. Terryn, S. Van Gils, B. Kernig, B. Grzemba, M. Mertens. Study of the near-surface of hot- and cold-rolled AlMg0.5 aluminium alloy, Surf Interface Anal. 37 (2005) 534-543.

123. Y. Liu, M.F. Frolish, W.M. Rainforth, X. Zhou, G.E. Thompson, G.M. Scamansc, et al. Evolution of near-surface deformed layers during hot rolling of AA3104 aluminium alloy, Surf Interface Anal. 42 (2010) 180-184.

124. D.J. Field, G.M. Scamans, E.P. Butler. High temperature oxidation of Al-4.2 wt pct Mg alloy, Metall Trans A. 18 A (1987) 463-472.

125. C. Lea, J. Ball. The oxidation of rolled and heat treated Al-Mg alloys, Appl Surf Sci. 17 (1984) 344-362.

126. M.H. Zayan, O.M. Jamjoom, N.A. Razik. High-temperature oxidation of Al-Mg alloys, Oxid Met. 34 (1990) 323-333.

127. M. Schutze, Protective oxide scales and their breakdown, John Wiley & Sons Ltd., Chichester, 1997, pp. 67-114.

128. S.Z. Bokstein, M.B. Bronfin, S.T. Kishkin, V.A. Marichev. Study of diffusion of magnesium through aluminum by the method of evaporation in a vacuum, Met Sci Heat Treat. 7 (1966) 242-244.

129. K.J. Holub, L.J. Matienzo. Magnesium diffusion in several aluminum alloys, Appl Surf Sci. 9 (1981) 22-38.

130. A.R. Riahi, A. Edrisy, A.T. Alpas. Effect of magnesium content on the high temperature adhesion of Al-Mg alloys to steel surfaces, Surf Coat Technol. 203 (2009) 2030-2035.

131. P. Hancock, J.R. Nicholls. Application of fracture mechanics of failure of surface oxide scales, Mater Sci Technol. 4 (1987) 398-406.

132. H.E. Evans. Spallation of oxide from stainless steel AGR nuclear fuel cladding: Mechanisms and consequences, Mater Sci Technol. 4 (1987) 415-420.

133. H.R. Le, M.P.F. Sutcliffe, P.Z. Wang, G.T. Burstein. Surface oxide fracture in cold aluminium rolling, Acta Mater. 52 (2004) 911-920.

134. M.G. Zelin. On micro-superplasticity, Acta Mater. 45 (1997) 3533-3542.

135. V.P. Poida, V.V. Bryukhovetskii, A.V. Poida, R.I. Kuznetsova, V.F. Klepikov, D.L. Voronov. Morphology and mechanisms of the formation of fiber structures upon high-temperature superplastic deformation of aluminum alloys, Phys.Met.Metallogr. 103 (2007) 414-423.

136. Y. Takayama, T. Tozawa, H. Kato. Superplasticity and thickness of liquid phase in the vicinity of solidus temperature in a 7475 aluminum alloy, Acta Mater. 47 (1999) 1263-1270.

137. W.D. Cao, X.P. Lu, H. Conrad. Whisker formation and the mechanism of superplastic deformation, Acta Mater. 44 (1996) 697-706.

138. J.K. Chang, E.M. Taleff, P.E. Krajewski, J.R. Ciulik. Effects of atmosphere in filament formation on a superplastically deformed aluminum-magnesium alloy, Scripta Mater. 60 (2009) 459-462.

139. J. Koike, M. Mabuchi, K. Higashi. In situ observation of partial melting in superplastic aluminum alloy composites at high temperatures, Acta Metall Mater. 43 (1995) 199-206.

140. W.J.D. Shaw. The role of microsuperplastic flow in high temperature fracture of AL-9021 mechanically alloyed aluminium, J Mater Sci. 24 (1989) 4114-4119.

141. S.F. Claeys, J.W. Jones, J.E. Allison, Dispersion strengthened aluminum alloys, TMS. Warrendale, PA. (1988) 323-336.

142. J.S. McFarlane, D. Tabor. Relation between friction and adhesion, Proceedings of the Royal Society of London, Series A (Mathematical and Physical Sciences). 202 (1950) 244-253.

143. J. Singh, A.T. Alpas. High-temperature wear and deformation processes in metal matrix composites, Metall Mat Trans A Phys Metall Mat Sci. 27 (1996) 3135-3148.

144. C. Jin, K. Cho, I. Park, Wear properties of high temperature Al alloys, (1995) 43-55.

145. Z. Chen, P.F. Thomson. Friction against superplastic aluminium alloys, Wear. 201 (1996) 227-232.

146. S. Wilson, A.T. Alpas. Effect of temperature on the sliding wear performance of Al alloys and Al matrix composites, Wear. 196 (1996) 270-278.

147. J. Singh, A.T. Alpas. Elevated temperature wear of Al6061 and Al6061-20%Al_2O_3, Scripta Metallurgica et Materiala. 32 (1995) 1099-1105.

148. D.K. Leu. A simple dry friction model for metal forming process, J Mater Process Technol. 209 (2009) 2361-2368.

149. P.J. Blau, M. Walukas. Sliding friction and wear of magnesium alloy AZ91D produced by two different methods, Tribol Int. 33 (2000) 573-579.

150. K. Hiratsuka, A. Enomoto, T. Sasada. Friction and wear of Al_2O_3, ZrO_2 and SiO_2 rubbed against pure metals, Wear. 153 (1992) 361-373.

151. H. Chen, A.T. Alpas. Sliding wear map for the magnesium alloy Mg-9Al-0.9 Zn (AZ91), Wear. 246 (2000) 106-116.

152. K.M. Asl, A. Tari, F. Khomamizadeh. Effect of deep cryogenic treatment on microstructure, creep and wear behaviors of AZ91 magnesium alloy, Mat Sci Eng A. 523 (2009) 27-31.

153. M. Habibnejad-Korayem, R. Mahmudi, H.M. Ghasemi, W.J. Poole. Tribological behavior of pure Mg and AZ31 magnesium alloy strengthened by Al_2O_3 nano-particles, Wear. 268 (2010) 405-412.

154. M. Bakhshi-Jooybari. A theoretical and experimental study of friction in metal forming by the use of the forward extrusion process, J Mater Process Technol. 125-126 (2002) 369-374.

155. B. Podgornik, S. Hogmark, O. Sandberg. Proper coating selection for improved galling performance of forming tool steel, Wear. 261 (2006) 15-21.

156. Standard test methods for determining average grain size, Standard Test Methods for Determining Average Grain Size. (1996).

157. A.T. Morales, A.R. Riahi, A.T. Alpas, Design and build of a hot-forming simulator, Collaborative report, GM R&D. (2008).

158. J.H. Dautzenberg, J.H. Zaat. Quantitative determination of deformation by sliding wear, Wear. 23 (1973) 9-19.

159. M.A. Moore, R.M. Douthwaite. Plastic deformation below worn surfaces, Metallurgical Transactions A. 7 (1976) 1833-1839.

160. J. Zhang, A.T. Alpas. Delamination wear in ductile materials containing second phase particles, Mat Sci Eng A. 160 (1993) 25-35.

161. J. Kang, X. Hu, S.I. Wright, P. Wu, D.S. Wilkinson, R.K. Mishra. On the calculation of volume fraction of texture components in AA5754 sheet materials, Metall Mat Trans A Phys Metall Mat Sci. 39 (2008) 2007-2013.

162. W.C. Oliver, G.M. Pharr. Improved technique for determining hardness and elastic modulus using load and displacement sensing indentation experiments, J.Mater.Res. 7 (1992) 1564-1580.

163. W.C. Oliver, G.M. Pharr. Measurement of hardness and elastic modulus by instrumented indentation: Advances in understanding and refinements to methodology, J.Mater.Res. 19 (2004) 3-20.

164. X. Meng-Burany, T.A. Perry, A.K. Sachdev, A.T. Alpas. Subsurface sliding wear damage characterization in Al-Si alloys using focused ion beam and cross-sectional TEM techniques, Wear. 270 (2011) 152-162.

165. W.J.D. Shaw. Microsuperplastic behavior, Mater Lett. 4 (1985) 1-4.

166. S. Bhaduri, S.B. Bhaduri. Microstructural and mechanical properties of nanocrystalline spinel and related composites, Ceram.Int. 28 (2002) 153-158.

167. R.E. Reed-Hill, R. Abbaschian, Physical Metallurgy Principles, 3rd ed., PSW Publishing Company, Boston, MA, 1994, pp. 362-363.

168. W.B. Hutchinson, M. Hatherly. An introduction to texture in metals, The Institution of Metallurgist, Monograph 5.

169. Z.N. Farhat. Contribution of crystallographic texturing to the sliding friction behaviour of fcc and hcp metals, Wear. 250-251 (2001) 401-408.

170. T.R. Chen, J.C. Huang. Observations of grain-boundary sliding and surface topography in an 8090 Al alloy after uniaxial and biaxial superplastic deformation, Metall Mat Trans A Phys Metall Mat Sci. 30 (1999) 53-64.

171. M.G. Zelin, T.R. Bieler, A.K. Mukherjee. Cooperative grain-boundary sliding in mechanically alloyed in 90211 alloy during high strain rate superplasticity, Metallurgical Transactions A. 24 (1993) 1208-1212.

172. S. Tian, L. Wang, Y.S. Keun, H.K. Kyung, Y. Xu, Z. Hu. Microstructure evolution and deformation features of AZ31 Mg-alloy during creep, Materials Science & Engineering A (Structural Materials: Properties, Microstructure and Processing). 415 (2006) 309-16.

173. M. Mabuchi, K. Higashi. Constitutive equation of a superplastic Al-Zn-Mg composite reinforced with Si3N4 whisker, Mater.Trans.JIM. 36 (1995) 420-5.

174. R.S. Kottada, A.H. Chokshi. Grain boundary sliding during diffusion and dislocation creep in a Mg-0.7 Pct Al alloy, Metall Mat Trans A Phys Metall Mat Sci. 38 (2007) 1743-1749.

175. Y. Zhang, X. Zeng, C. Lu, W. Ding. Deformation behavior and dynamic recrystallization of a Mg-Zn-Y-Zr alloy, Mat Sci Eng A. 428 (2006) 91-97.

176. M.K. Rabinovich, V.G. Trifonov. Dynamic grain growth during superplastic deformation, Acta Materialia. 44 (1996) 2073-2078.

177. F.R. Cao, H. Ding, Y.L. Li, G. Zhou, J.Z. Cui. Superplasticity, dynamic grain growth and deformation mechanism in ultra-light two-phase magnesium-lithium alloys, Mat Sci Eng A. 527 (2010) 2335-2341.

178. H.O.K. Kim. Activation energies for the grain growth of an AZ31 Mg alloy after equal channel angular pressing, J Mater Sci. 39 (2004) 7107-7109.

179. Y. Iwahashi, J. Wang, Z. Horita, M. Nemoto, T.G. Langdon. Principle of equal-channel angular pressing for the processing of ultra-fine grained materials, Scr.Mater. 35 (1996) 143-146.

180. S.X. McFadden, R.S. Mishra, R.Z. Vallev, A.P. Zhilyaev, A.K. Mukherjee. Low-temperature superplasticity in nanostructured nickel and metal alloys, Nature. 398 (1999) 684-686.

181. C. Suryanarayana, C.C. Koch. Nanocrystalline materials - Current research and future directions, Hyperfine Interact. 130 (2000) 5-44.

182. H. Gleiter. Nanocrystalline materials, Prog Mater Sci. 33 (1989) 223-315.

183. J.H. Robinson, M.A. Rust, R.I. Todd, Mechanisms of microsuperplasticity, Mater Sci Forum. 551-552 (2007) 135-145.

184. A.H. Cottrell. The Mechanical Properties of Matter. (1964) 231-261.

185. C.B. Carter, M.G. Norton, Ceramic Materials: Science and Engineering, Springer, New York, 2007, pp. 226.

Appendix

Copyright clearance form I

License Number	2658880161276
License date	Apr 30, 2011
Licensed content publisher	Springer
Licensed content publication	Metallurgical and Materials Transactions A
Licensed content title	Role of Plastic Deformation on Elevated Temperature Tribological Behavior of an Al-Mg Alloy (AA5083): A Friction Mapping Approach
Licensed content author	S. Das
Licensed content date	Jan 1, 2011
Type of Use	Thesis/Dissertation
Portion	Full text
Number of copies	1
Author of this Springer article	Yes and you are the sole author of the new work
Order reference number	
Title of your thesis / dissertation	Plastic Deformation and Surface Damage Mechanisms during Hot-forming of Al and Mg Alloy Sheets
Expected completion date	Apr 2011
Estimated size(pages)	230
Total	0.00 USD

Copyright clearance form II

License number	2630821411070
License date	Mar 16, 2011
Licensed content publisher	Elsevier
Licensed content publication	Wear
Licensed content title	Microstructural evolution during high temperature sliding wear of Mg–3% Al–1% Zn (AZ31) alloy
Licensed content author	S. Das, A.T. Morales, A.T. Alpas
Licensed content date	4 January 2010
Licensed content volume number	268
Licensed content issue number	1-2
Number of pages	10
Start Page	94
End Page	103
Type of Use	reuse in a thesis/dissertation
Intended publisher of new work	other
Portion	full article
Format	both print and electronic
Are you the author of this Elsevier article?	Yes
Will you be translating?	No
Order reference number	
Title of your thesis/dissertation	Plastic Deformation and Surface Damage Mechanisms during Hot-forming of Al and Mg Alloy Sheets
Expected completion date	Apr 2011
Estimated size (number of pages)	230
Elsevier VAT number	GB 494 6272 12
Permissions price	0.00 USD
VAT/Local Sales Tax	0.0 USD / 0.0 GBP
Total	0.00 USD

Vita Auctoris

Name	Sarmistha Das
Place of birth	Agartala, Tripura, India
Education	Bachelor of Engineering (B.E.), Mechanical Engineering National Institute of Technology, Karnataka, India 1997-2001
	Materials Science and Engineering (M.Sc.Engg.), Mechanical Engineering Indian Institute of Science, Bangalore, India 2003-2006
	PhD, Engineering Materials University of Windsor, Ontario, Canada 2006-2011

Scholarly publications based on this work

1. **S. Das**, A. R. Riahi, X. Meng-Burany, A. T. Morales and A. T. Alpas "Friction and deformation mechanisms of AZ31 alloy deformed at elevated temperature" (to be submitted), 2011.

2. **S. Das**, A. R. Riahi, X. Meng-Burany, A. T. Morales and A. T. Alpas "High temperature deformation and fracture of tribo-layers on the surface of AA5083 sheet aluminum-magnesium alloy" (submitted to Materials Science and Engineering: A), 2011.

3. **S. Das**, A.T. Morales, A.R. Riahi, X.Meng-Burany and A.T. Alpas. "Role of plastic deformation on elevated temperature tribological behaviour of an Al-Mg alloy (AA5083): A friction mapping approach" Metallurgical and Materials Tansactions A, 2011, DOI: 10.1007/s11661-011-0649-4.

4. **S. Das**, A.T. Morales and A.T. Alpas. "Microstructural evolution during high temperature sliding wear of Mg–3% Al–1% Zn (AZ31) alloy" Wear, 268, 2010, 94-103.

Conference presentations based on this work

1. **S. Das**, A. Riahi, X. Meng-Burany, A.T. Morales, A.T. Alpas, Materials Science & Technology 2010 Conference, Houston, Texas, Oct. 2010.

2. **S. Das**, A. Riahi, X. Burany, A. Morales, A. Alpas, SAE 2010 World Congress & Exhibition, Session: Magnesium Technologies (Part 1 of 2), Detroit, Michigan, April 2010.

3.   **S. Das**, A. Riahi, A. T. Morales and A. T. Alpas, Materials Science & Technology 2009 Conference, Pittsburgh, Pennsylvania, Oct. 2009.

4.   **S. Das**, A. Riahi, A. T. Morales and A. T. Alpas, Materials Science & Technology 2009 Conference, Pittsburgh, Pennsylvania, Oct. 2009.

5.   **S. Das**, A. T. Morales and A. T. Alpas, 2nd International Conference on Advanced Tribology, 3-5 December 2008, Singapore.

6.   **S. Das,** A. T. Morales and A. T. Alpas, Materials Science & Technology 2008 Conference, Pittsburgh, Pennsylvania, Oct. 2008.

7.   **S. Das,** A. T. Morales and A. T. Alpas, STLE 2008 Annual meeting, Cleveland, Ohio, May 2008.

8.   **S. Das,** A. T. Morales and A. T. Alpas, Materials Science & Technology 2007 Conference, Detroit, Michigan, Sept. 2007.

9.   **S. Das,** A. T. Morales and A. T. Alpas, 19th Canadian Materials Science Conference, McMaster University, Hamilton, June 2007.

Internal reports based on this work

1.   **S. Das**, A. T. Morales A. R. Riahi, X. Meng-Burany and A. T. Alpas "Friction and Deformation Mechanisms of AZ31 Alloy Deformed at Elevated Temperature" General Motors Collaborative Report (to be submitted), 2011.

2.   **S. Das**, A. T. Morales A. R. Riahi, X. Meng-Burany and A. T. Alpas "Ligament Formation between Grains of AA5083 Subjected to Deformation at High Temperature" General Motors Collaborative Report, 2011, CL – 11/147/CML.

3.   **S. Das**, A. T. Morales A. R. Riahi and A. T. Alpas "Coefficient of Friction Map for AA5083 Deformed at Elevated Temperatures", General Motors Collaborative Report, 2010, CL – 10/081/CML.

4.   **S. Das**, A. T. Morales and A. T. Alpas "Deformation Mechanisms during High Temperature (673 K) Sliding of AZ31 Magnesium Alloy", General Motors Collaborative Report, 2008.